JAIST Repository
https://dspace.jaist.ac.jp/

| | |
|---|---|
| Title | n型結晶シリコン用高品質Cat-CVD窒化シリコンパッシベーション層の開発とその裏面コンタクト結晶シリコン太陽電池への応用 |
| Author(s) | Trinh, Thi Cham |
| Citation | |
| Issue Date | 2015-03 |
| Type | Thesis or Dissertation |
| Text version | ETD |
| URL | http://hdl.handle.net/10119/12772 |
| Rights | |
| Description | Supervisor:大平　圭介，マテリアルサイエンス研究科，博士 |

JAIST
JAPAN
ADVANCED INSTITUTE OF
SCIENCE AND TECHNOLOGY

Japan Advanced Institute of Science and Technology

Doctoral Dissertation

# Development of high-quality Cat-CVD $SiN_x$ passivation layer for n-type c-Si and its application to back-contact c-Si solar cells

TRINH THI CHAM

Japan Advanced Institute of Science and Technology

# Development of high-quality Cat-CVD $SiN_x$ passivation layer for n-type c-Si and its application to back-contact c-Si solar cells

TRINH THI CHAM

Submitted to

Japan Advanced Institute of Science and Technology

In partial fulfillment of the requirements

For the degree of

Doctor of Philosophy

Supervisor: Associate Professor Keisuke Ohdaira

School of Materials Science

Japan Advanced Institute of Science and Technology

March, 2015

Referee in Chief:

**Associate Professor Keisuke Ohdaira**

Japan Advanced Institute of Science and Technology

Referees:

**Professor Tatsuya Shimoda**

Japan Advanced Institute of Science and Technology

**Professor Toshikazu Suzuki**

Japan Advanced Institute of Science and Technology

**Professor Hideyuki Murata**

Japan Advanced Institute of Science and Technology

**Professor Hironobu Umemoto**

Shizuoka University

**ABSTRACT**

Nowadays, besides the trends of innovating high technical products to take human life to the top luxury comfortable life, scientists have paid much attention to solving two problems: shortage of energy and environmental pollution. Solar cell, an electric device which can directly convert light to electricity, is a novel product to solve both problems. The ways to improve solar cell efficiency and decrease its cost are the most concerning for scientists in this field.

The purpose of my study is to increase solar cell efficiency by improving the passivation quality and transparency of passivation layers formed by catalytic chemical vapor deposition (Cat-CVD), aiming at application to back-contact crystalline silicon (c-Si) solar cells. Passivation layers play important roles in realizing high-efficiency solar cells because they can reduce optical loss caused by the reflection of coming sun-light and electrical loss caused by the recombination of photo-generated carriers on c-Si surfaces. To meet this purpose, my study aims to improve the passivation quality and transparency of Cat-CVD anti-reflective silicon nitride ($SiN_x$) films.

I have succeeded to obtain Cat-CVD high-transparency $SiN_x$ films with high-passivation quality on n-type c-Si surfaces, and to significantly improve the passivation quality by doping phosphorous (P) on a n-type c-Si surface. This doping is performed by exposing a c-Si surface to P-related radicals generated by the catalytic cracking of $PH_3$ (Cat-doping), called P Cat-doped layer, before the passivation with the Cat-CVD $SiN_x$ single layer. By using the $SiN_x$/P Cat-doped layer structure, an extremely low surface recombination velocity (SRV) is obtained to be 2 cm/s on flat c-Si wafers. A SRV of 6.7 cm/s is also obtained for textured c-Si wafers, which are essential for high-performance solar cells due to its ability of lowering optical reflectance and enhancing light trapping inside c-Si absorber. For $SiN_x$/P Cat-doped layer/c-Si textured samples, optical reflectance less than 10% in visible range can be achieved.

The obtained results indicate that Cat-CVD have potential application in passivation technique for high-efficiency solar cells, particularly for n-type back-junction solar cells. Based on the remarkable results for the passivation of n-type c-Si surfaces, I will investigate the application of these passivation layers to n-type back-contact solar cells. The solar cells which will be realized in my research have several advantages as below:

High transparency and high passivation quality by using $SiN_x$/P Cat-doped layers.

No shading effect by metal grids on the front side.

Fabrication processes at low temperature (< 200 °C).

By these advantages, the solar cells with the highest efficiency ever should be expected.

*Keywords: Catalytic chemical vapor deposition (Cat-CVD), Phosphorus Cat-doping, surface recombination velocity, silicon nitride ($SiN_x$), passivation quality.*

# Acknowledgements

First of all, I would like to express my deepest gratitude to my supervisor: Associate Professor Keisuke Ohdaira for his instructions and financial support. Thanks to him, I have a chance to study an interesting topic of solar cell in one of the most beautiful countries in all over the world-Japan. Thanks to him, I have a chance to open my knowledge of not only science but also Japanese culture as well as estimable Japanese behavior. Special thanks to him for his kindness and enthusiasm, for providing me valuable suggestions in research as well as in English writing to improve my English skill and quality of this thesis. Without his help, my thesis would not have been possible.

I would like to acknowledge my honest gratitude to Professor Hideki Matsumura for his guidance and financial support. Professor H. Matsumura is the one who takes me to the world of science; gives me opportunity to study on application of Cat-CVD in solar cell passivation technique and teaches me how to become a real scientist. Thanks to his valuable instruction, precious suggestion and cheerful enthusiasm, I am able to complete my research and improve my ability to embark on science career.

I would like to give sincere thanks to Doctor Koichi Koyama for his guiding of experimental processes and for his sharing his knowledge and exciting discussion. I want to thank him for a lot of helping and encouragement during my study. Dr. Koyama was always on the way to help me whenever and whatever I got trouble during experiment. I really highly appreciate his kind helps and enthusiasm.

I would like to thank Professor Tatsuya Shimoda and Professor Toshikazu Suzuki for allowing me using measurement systems in their lab.

I would like to give my honest gratitude to Professor Tatsuya Shimoda, Professor Toshikazu Suzuki, and Professor Hideyuki Murata of School of Materials Science, JAIST, and Professor Hironobu Umemoto of Shizuoka University for reviewing my doctoral thesis and my presentation of doctoral dissertation and for spending their specious time.

My deepest appreciation to Doctor Le The Anh in Mizuta Lab and Doctor Nguyen Quy Tuan in Suzuki Lab in always being helpful and sharing his physics knowledge with me.

I am heartily thankful to my Lab members: Yoo Sakuma, Shogo Tsuzaki, Takafumi Oikawa, Taiki Watanabe, Cheng Guo, Junichi Seto, Takaki Nozawa and Seira Yamaguchi; and three assistant researchers: Lin Yang, Taichi Tsujino and Shigeki Terashima for their helps during my research. I would like to give my deepest thanks to Y. Sakuma, S. Tsuzaki, T. Oikawa and T. Watanabe san for their help of accommodation and travelling arrangement during my business trip.

I would like to give my sincere thanks to Associate Professor Susumu Horita for his kindness and his helping during my business trip. Special thanks to him for taking me to many special places in Japan to learn about Japanese culture and enjoy Japanese sightseeing and food.

I would like to thank my dear friends: Pham Anh Son, Huynh Thi Cam Tu, Mai Thi Kieu Lien, Nguyen Thuc Phuong, Nguyen Thi Kim Thanh, Phan Thanh Huong, Le Hoang Linh, Nguyen Duc Hieu, Le The Anh, Nguyen Duyen An, Pham Kieu Chinh…and all of Vietnamese group members in JAIST for always being beside me, encourage me, sharing joys and sorrow with me and helping me with a lot of things.

From bottom of my heart, I would like to express my honest gratitude to my family for love and encouragement. Thank for them, I always be on the right track.

Finally, I would like to thank school of Materials Science and Japan Science and Technology Agency (JST) CREST for financial support for my research and living life.

# Table of Contents

**Chapter 1 Introduction of solar cells and the background of the research** ........................ 1

**1.1 Current status of c-Si solar cells and its perspective** ................................................ 1

**1.2 Back-contact solar cells and the importance of surface passivation** ......................... 5

**1.3. Application of catalytic chemical vapor deposition to passivation technique for c-Si solar cells** ................................................................................................................... 10

***1.3.1 Introduction of Cat-CVD system*** ..................................................................... 11

***1.3.2 Cat-CVD application in passivation technique for c-Si solar cells*** ..................... 13

**1.4. Purpose of this study** ........................................................................................... 14

**References** ............................................................................................................... 16

**Chapter 2 Passivation mechanism of Cat-CVD Si-rich $SiN_x$/$SiN_x$ stacked layers on c-Si** ..........................................................................................................19

**2.1. Introduction** ............................................................................................................. 19

**2.2. Experimental Procedure** ......................................................................................... 20

***2.2.1 Sample Preparation*** ........................................................................................ 20

***2.2.2 Characterization of Prepared Samples*** ............................................................ 21

**2.3. Results and discussion** ........................................................................................... 23

***2.3.1. The role of fixed charges*** .................................................................................. 23

***2.3.2 The role of hydrogen*** ......................................................................................... 25

**2.4. Addition of $H_2$ during Si-rich $SiN_x$ deposition** ....................................................... 28

**2.5. Conclusion** ............................................................................................................... 32

**References** ............................................................................................................... 33

**Chapter 3 Passivation quality of a Cat-CVD $SiN_x$ single layer on n-type c-Si** .................. 35

**3.1. Introduction** ............................................................................................................. 35

**3.2. Experimental procedure** .......................................................................................... 36

***3.2.1. Sample preparation*** ........................................................................................... 36

***3.2.2. Characterization of prepared samples*** ............................................................... 37

**3.3. Results and discussion** ........................................................................................... 38

*3.3.1. Chemical composition of $SiN_x$ films* ..... 38

*3.3.2. Passivation quality of $SiN_x$ films on c-Si wafers* ..... 41

*3.3.3. Role of H content and fixed charge density on passivation quality of films* ..... 47

*3.3.4. Interface state density of $SiN_x$/c-Si structures* ..... 54

**3.4. Conclusions** ..... 59

**References** ..... 60

**Chapter 4 Improvement in the passivation quality of a Cat-CVD $SiN_x$ single layer by applying P Cat-doping** ..... 63

**4.1 Introduction: The role of a P Cat-doped layer in the passivation of a c-Si surface** . 63

**4.2 Experimental procedure** ..... 65

**4.3 Results and discussion** ..... 68

*4.3.1 The effect of annealing on P activation as donors and the passivation characteristic of $SiN_x$/P Cat-doped layer/c-Si structures* ..... 68

*4.3.2 Effect of $T_{s\text{-}dope}$ on the passivation characteristic of a $SiN_x$/P Cat-doped layer/c-Si structure* ..... 81

*4.3.3 Effect of $T_{s\text{-}dope}$ and doping duration on the passivation characteristic of $SiN_x$/P Cat-doped layer/c-Si structure* ..... 83

*4.3.4 The effect of light soaking on $\tau_{eff}$ of $SiN_x$/P Cat-doped layer/c-Si structure.* ..... 85

**4.4 Conclusion** ..... 89

**References** ..... 90

**Chapter 5 Passivation quality of a Cat-CVD $SiN_x$ single layer and Cat-CVD $SiN_x$/ P Cat-doped layers on textured c-Si** ..... 93

**5.1 Introduction** ..... 93

**5.2 c-Si texturing and cleaning processes** ..... 94

**5.3 Morphology of textured c-Si surfaces and their optical reflectance** ..... 98

**5.4 Conclusion** ..... 104

**References** ..... 105

**Chapter 6 Application of Cat-CVD $SiN_x$ and $SiN_x$/ P Cat-doped layers on back contact back junction solar cells** ..... 106

**6.1. Introduction** ..... 106

**6.2. Theory of solar cell and its characteristics** ..... 106

*6.2.1. Working principle of solar cell* ..... 106

*6.2.2. Solar cell parameters* ..... 108

**6.3. Application of $SiN_x$ and $SiN_x$/P Cat-doped layers on back contact solar cells** ..... 112

*6.3.1. Simulation data* ..... 112

*6.3.2. Back contact solar cell fabrication* ..... 121

**6.4. Conclusion** ..... 127

**References** ..... 128

**Chapter 7 General conclusion** ..... 129

**Appendix** ..... 131

***A-1. Spectroscopic ellipsometry*** ..... 131

***A-2. X-ray photoelectron spectroscopy*** ..... 136

***A-3. Ultraviolet-visible-near infrared spectrophotometry*** ..... 138

***A-4. Lifetime measurement*** ..... 139

***A-5. Electron spin resonance*** ..... 141

***A-6. Hall effect measurement.*** ..... 143

***A-7. X-ray reflectivity*** ..... 145

***A-8. Secondary ion mass spectrometry*** ..... 150

***A-9. Scanning electron microscopy*** ..... 152

***A-10. $D_{it}$ Calculation*** ..... 154

***A-11. Deviration equation of $J_{sc}$ and $V_{oc}$*** ..... 179

**References** ..... 182

**Matlab code** ..... 183

# Chapter 1 Introduction of solar cells and the background of the research

## 1.1 Current status of c-Si solar cells and its perspective

The outrace development of science and technology has given human a comfortable life with many amazing inventions that human could not even imagine it could be. However, together with it, human beings are facing two serious problems. They are air pollution caused by exhausting when burning coal produce electricity and the shortage of energy sources. Figure 1.1a shows an increase in the world energy consumption according to BP statistical review of the world energy 2013 [1]. The main energy sources are oil, coal, and gas, as shown in Figure 1.1b. All of them are limited sources. Based on the energy consumption and the cavity of these energy sources, it is estimated that current oil and coal reserves will be completely depleted in 2050 and 2155, respectively. The pollution is increasing day by day mainly due to pollutant disperse. In particular, pollution gases such as carbon dioxide ($CO_2$) which are produced form vehicle and industry are the most concerning. $CO_2$ pollution causes environment degradation such as green house effect and global warming, which affects harmful on human lives.

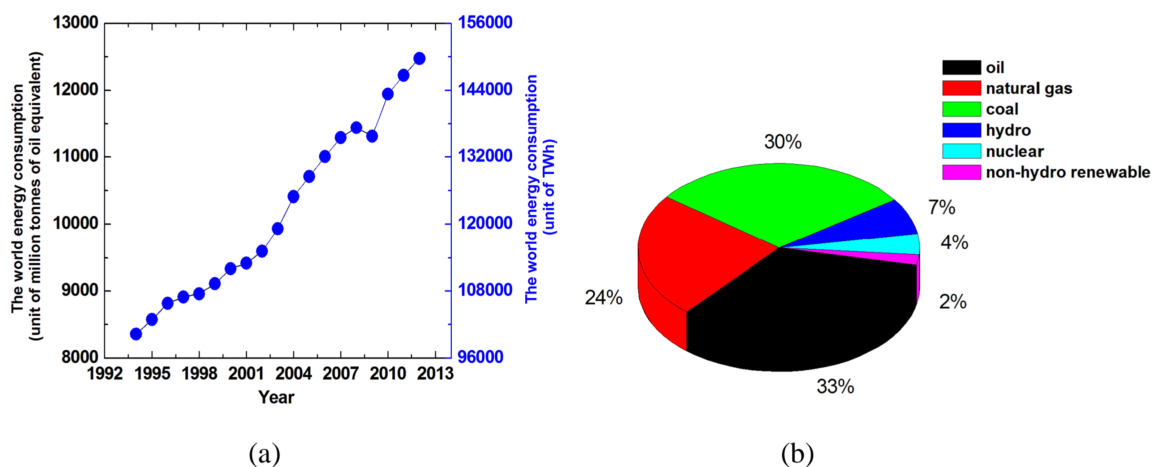


*Figure 1.1: The world energy consumption (a) by year and (b) by energy source*

Figure 1.2 shows a drastic increase in $CO_2$ emission in recent years, which is calculated by BP Statistical Review of World energy 2013 [1]. Many traffic accidents including train, car, and air-plane crash were recorded, related to bad-weather. Until now, nuclear power may be the most efficient to solve energy shortage. There are now 440 nuclear reactors which provide a fifth of world electricity consumption [2]. However, benefit of the energy source comes together with unfortunate risk. The world has faced to two nuclear crisis, which are Chernobyl nuclear disaster in 1986 and Fukushima Daiichi nuclear disaster in 2011. The serious consequence of the disasters still make people scare even just thinking about it. Additionally, it requires much cost, geologic conditions as well as high techniques to build one nuclear plant. They are reasons why nuclear energy production is lower compared to other energy sources.

Seriously talking, if we bring a comfortable life for our coming generation, we should firstly bring their lives long enough to enjoy it.

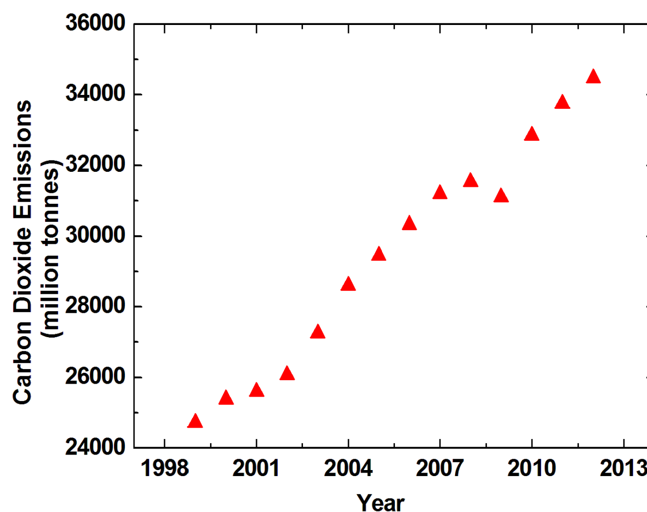


*Figure 1.2. $CO_2$ emissions*

To solve these above problems, using renewable energy sources are extremely necessary. Solar energy is the biggest potential energy candidate. It is abundant and widely available energy. Total energy the earth receives from the sun is about 3850000 exajoules per year, corresponding to 10700000000 TWh/year [3]. The amount of solar energy reaching the surface of our planet is so vast that solar energy that the earth receives in one hour is much more than the world energy consumption per year, as shown in Figure 1.1. In solar technology, solar cells are useful products because they can directly convert sun-light to electricity, based on photovoltaic effect. The production of solar cells is growing rapidly

and widely applied in many industrial products such as vehicles, calculator...as well as supporting electric power for housing furniture. The great increase in worldwide solar cell production from 1999 to 2013 is shown in Figure 1.3 [4]. Many scientists believe that it is just the matter of time that solar cells will become power for all industrial products and vehicles.

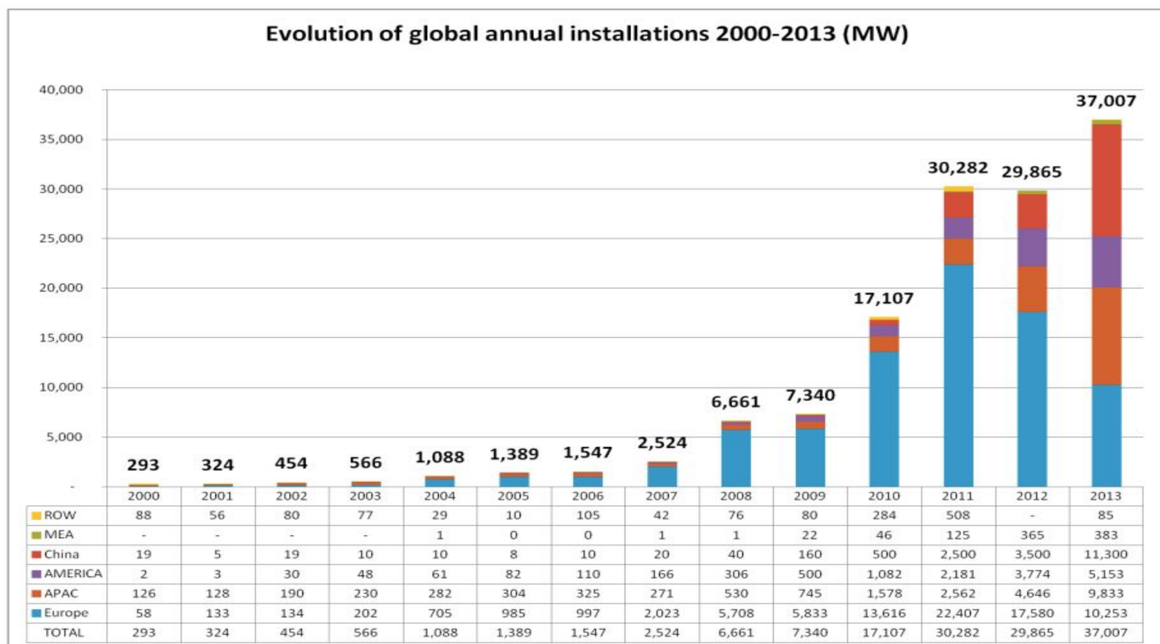


| | 2000 | 2001 | 2002 | 2003 | 2004 | 2005 | 2006 | 2007 | 2008 | 2009 | 2010 | 2011 | 2012 | 2013 |
|---|---|---|---|---|---|---|---|---|---|---|---|---|---|---|
| ROW | 88 | 56 | 80 | 77 | 29 | 10 | 105 | 42 | 76 | 80 | 284 | 508 | - | 85 |
| MEA | - | - | - | - | 1 | 0 | 0 | 1 | 1 | 22 | 46 | 125 | 365 | 383 |
| China | 19 | 5 | 19 | 10 | 10 | 8 | 10 | 20 | 40 | 160 | 500 | 2,500 | 3,500 | 11,300 |
| AMERICA | 2 | 3 | 30 | 48 | 61 | 82 | 110 | 166 | 306 | 500 | 1,082 | 2,181 | 3,774 | 5,153 |
| APAC | 126 | 128 | 190 | 230 | 282 | 304 | 325 | 271 | 530 | 745 | 1,578 | 2,562 | 4,646 | 9,833 |
| Europe | 58 | 133 | 134 | 202 | 705 | 985 | 997 | 2,023 | 5,708 | 5,833 | 13,616 | 22,407 | 17,580 | 10,253 |
| TOTAL | 293 | 324 | 454 | 566 | 1,088 | 1,389 | 1,547 | 2,524 | 6,661 | 7,340 | 17,107 | 30,282 | 29,865 | 37,007 |

*Source: EPIA*

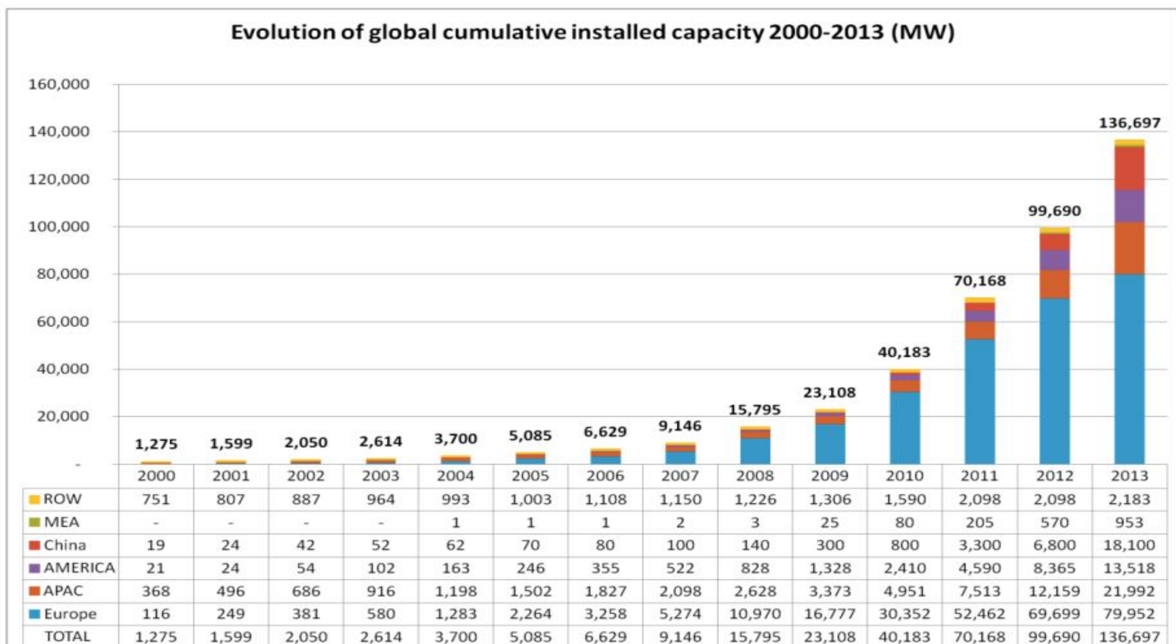


| | 2000 | 2001 | 2002 | 2003 | 2004 | 2005 | 2006 | 2007 | 2008 | 2009 | 2010 | 2011 | 2012 | 2013 |
|---|---|---|---|---|---|---|---|---|---|---|---|---|---|---|
| ROW | 751 | 807 | 887 | 964 | 993 | 1,003 | 1,108 | 1,150 | 1,226 | 1,306 | 1,590 | 2,098 | 2,098 | 2,183 |
| MEA | - | - | - | - | 1 | 1 | 1 | 2 | 3 | 25 | 80 | 205 | 570 | 953 |
| China | 19 | 24 | 42 | 52 | 62 | 70 | 80 | 100 | 140 | 300 | 800 | 3,300 | 6,800 | 18,100 |
| AMERICA | 21 | 24 | 54 | 102 | 163 | 246 | 355 | 522 | 828 | 1,328 | 2,410 | 4,590 | 8,365 | 13,518 |
| APAC | 368 | 496 | 686 | 916 | 1,198 | 1,502 | 1,827 | 2,098 | 2,628 | 3,373 | 4,951 | 7,513 | 12,159 | 21,992 |
| Europe | 116 | 249 | 381 | 580 | 1,283 | 2,264 | 3,258 | 5,274 | 10,970 | 16,777 | 30,352 | 52,462 | 69,699 | 79,952 |
| TOTAL | 1,275 | 1,599 | 2,050 | 2,614 | 3,700 | 5,085 | 6,629 | 9,146 | 15,795 | 23,108 | 40,183 | 70,168 | 99,690 | 136,697 |

*Source: EPIA*

*Figure 1.3. World solar power installation and corresponding capacity from 2000 to 2013 [4].*

Among photovoltaic cell types, crystalline silicon (c-Si) solar cells are overwhelming share of 80-90% of the photovoltaic market [5]. This is because silicon is the second most abundant element in the earth's crust and has the advantage of being available in sufficient quantities. Additionally, producing process of the material does not burden the environment. Another advantage of the c-Si solar cell is that manufacturing technology has been developed from the huge knowledge base of the microelectronics industry. Therefore, c-Si solar cells have good efficiency performance and are cost-effective.

With the development of science and technology, the efficiency of c-Si solar cells has been improving significantly. By 1954, Chapin et al. [6] at Bell Labs has demonstrated the first silicon single-crystal solar cell with 6% efficiency. After a few year, Si solar cell efficiency increases up to 15% [7]. In 2014, the highest efficiency c-Si solar cell with an efficiency of 25.6% has been realized [8]. It is close to theoretical maximum efficiency of 29% [9].

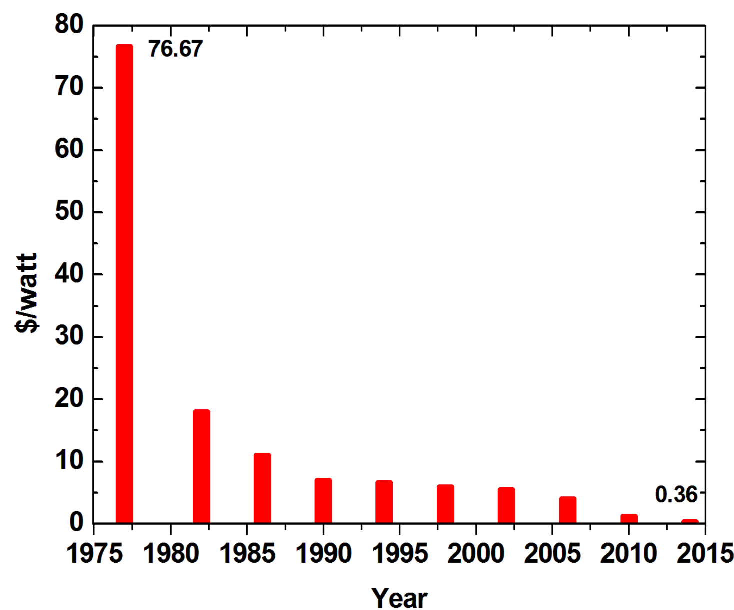


*Figure 1.4. Price history of silicon solar cells[11]*

However, there are two problems that photovoltaic technology needs to overcome. One is that the cost of the product is still high. According to calculation of Bloomberg New energy finance, photovoltaic prices have fallen dramatically. The price of c-Si solar cells was 76.67 $ per watt in 1977 [11]. About 10 year later, it fell to about 1 $ per watt and it is estimated to be 0.36 $ per watt in 2014, as shown in Figure 1.4 [11]. However, its cost is

still higher than conventional energy sources. The second one is that solar cell efficiency is not high enough to balance its cost. As I mentioned above, c-Si solar cell efficiency increases significantly and reached a high value. But when applying in solar panel, and to industrial products, power price is still very high, becoming a barrier for the expansion of solar cell's market.

Due to easier fabrication processing, p-type wafer c-Si solar cells are the most dominant c-Si solar cell. n-type wafer c-Si solar cells are available, but their market share is at very low level (around 4%) [11]. However, because of many advantages compared to p-type wafer c-Si, n-type wafer c-Si has recently become more and more attractive to photovoltaic research, raising forecast of switch from p-type to n-type wafer c-Si solar cells on photovoltaic industry [11-12]. For p-type c-si which uses boron (B) dope exhibit light-induced degradation. Illumination enhances interstitial oxygen dimers ($O_{2i}$) diffusivity in this cell. The $O_{2i}$ can combine with substitutional $B_s$; forming $B_sO_{2i}$ complexes which can act as trap centers for carriers. For n-type c-si, no light-induced degradation is observed. Additionally, a survey of the recombination effect of metallic impurities on c-Si has showed that p-type c-Si has higher recombination strength than n-type because the capture cross section of these impuries for electron is lager than that for hole [13]. Moreover, phosphorus doping for back surface field for n-type is easier than boron doping for p-type c-Si, resulting to higher diffusion length and better back surface reflectance for n-type. Thus, efficiency of p-type based c-Si solar cell is lower and less stable than that of n-type based c-Si solar cell [14]. The highest-efficiency solar cell of 25.6% has been recorded for an a-Si/n-type wafer c-Si hetero-junction back-contact solar cell in 2014 [8].

## 1.2 Back-contact solar cells and the importance of surface passivation

There are many types of c-Si-based solar cells categorized based on the structure of the cells or techniques used for the cells [12]. Among these cells, back-contact solar cells are the most interest for scientist and industry because they have many advantages such as [14]:

- No shading loss due to the absence of the metallization grid on the front side, thus high short circuit current can be obtained. The benefit of no metallization grid on

the front is not only high short circuit current but also decreasing grid resistance due to wider coverage and reducing stringing costs.

- Avoiding the trade-off between series resistance and reflectance.
- Simpler and easier module fabrication.

There are several types of back-contact solar cells such as metallization wrap-around, metallization wrap-through (MWT), emitter wrap-through (EWT), back-contact back-junction solar cell or interdigitated back-contact solar cell. Some examples of these cell structures are shown in Figures 1.5 and 1.6. For the first three types, because of emitter wrap through or around cell, they do not require high quality c-Si wafers. It has reported an efficiency of up to 19.7% with low cost industrial techniques on n-type Czochralski (CZ) wafers. Bifacial modules using MWT back-contact technology can have conversion efficiencies of above 20% [11]. Back-junction back-contact solar cell is realized as the most promising cell among back-contact cells. It has easier fabrication process and higher efficiency. Back-junction back-contact solar cell has paid much attention by scientist and industry. Its efficiency is more and more improved. The A-300 back-junction back-contact solar cell was first manufactured and reported by SunPower in 2004 on a large area having a maximum cell efficiency of 21%. In 2010, SunPower reported a new record efficiency of 24.2% at R&D level. [12-15]. Recently, Panasonic HIT back-contact solar cell has achieved highest world level of cell efficiency of 25.6% [8].

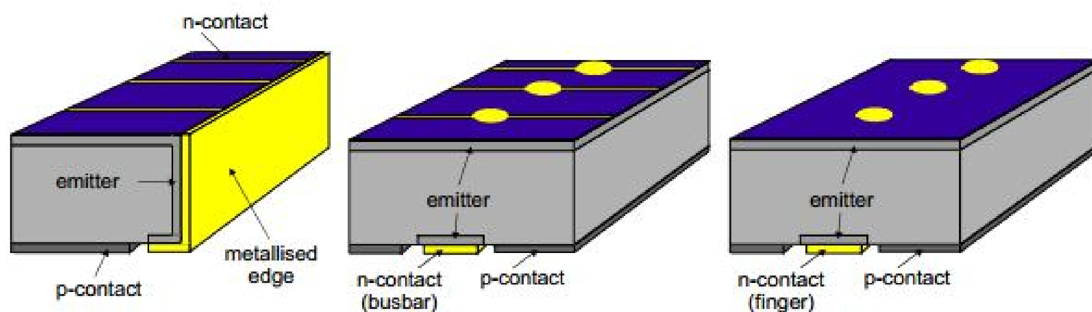


*Figure 1.5. From left to right: Metallization wrap around, metallization wrap through, emitter wrap through cells [16]*

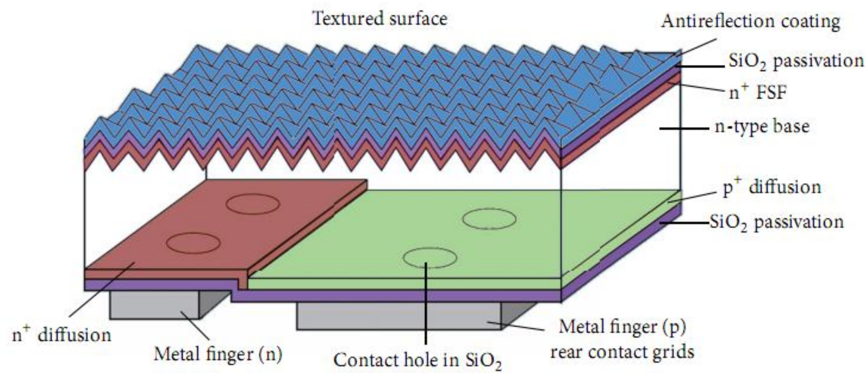


*Figure 1.6. Schematic of a back-junction back-contact solar cell from SunPower [17].*

However, back-junction back-contact solar cell requires high c-Si base quality. For this cell, photo-generated carriers should not be trapped on a c-Si surface and have high diffusion length to pass from front to rear side to reach collector electrodes. In other words, high bulk carrier lifetime and low surface recombination velocity (SRV) are critical parameters for a high efficiency cell. Figure 1.7 shows the Liebig Law of the Minimum applied to describe the efficiency potential of a solar cell [18]. The shortest stave will decide the capacity of barrel with unequal-length staves. There are many factors affecting efficiency of solar cells such as optical loss due to reflection, non-absorbed region, electrical loss due to surface recombination, bulk trap recombination, series resistance, shunt resistance… Here, SRV is the shortest stave due to the fact that passivation layers for c-Si solar cell are not well-optimal at this moment. If this factor will be improved more, a solar cell with highest efficiency ever would be expected. Reported simulation data shown in Figure 1.8 indicates that front SRV of <10 cm/s and a bulk carrier lifetime of >1000 μs are required for back-junction solar cells [19].

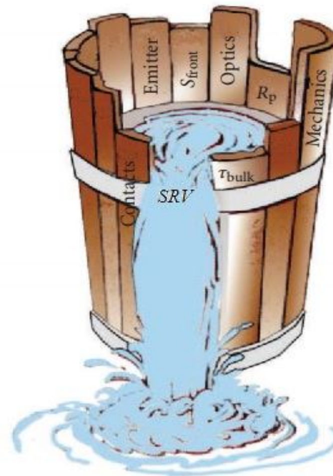


Liebig's law adapted to solar cells.

*Figure 1.7. Law of minimum applied to describe the potential efficiency of a solar cell [18].*

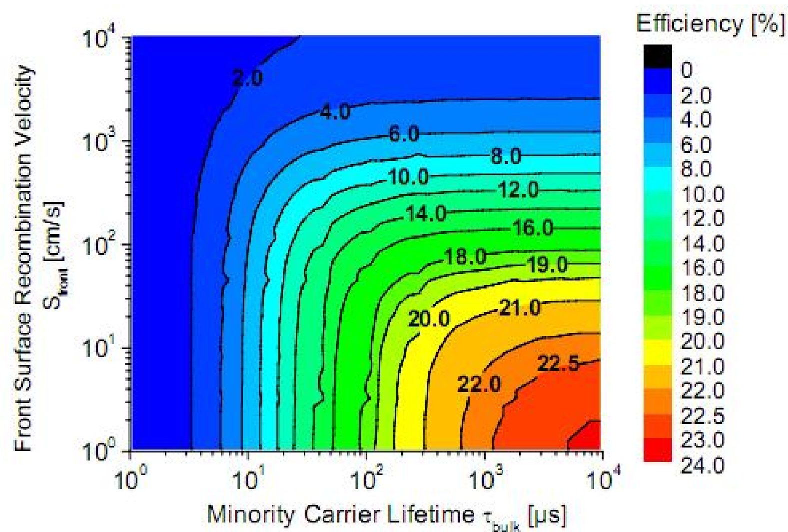


*Simulations of the efficiency of a one-dimensional back-junction solar cell structure in a wide range of carriers lifetime and front surface recombination velocity. The thickness of the simulated device is 200 µm. The resistivity of the n-type base is 1 Ωcm and the p-type rear emitter has a sheet resistance of 30 Ω/sq. Simulations were performed using PC1D*

*Figure 1.8. Relationship of front SRV, bulk lifetime and the efficiency of a back-junction solar cell [19].*

There are various types of passivation layers and passivation stacked layers for c-Si solar cells, such as $Al_2O_3$, $SiN_x$, SiO…[15,20-27]. These passivation layers contribute significantly to reduction in the surface recombination of minority carriers on both n- and p-type c-Si. There are two mechanisms for passivation technique to reduce surface

recombination:

- ❖ Reduction of interface states density ($D_{it}$) by terminating dangling bonds on a c-Si surface. In this mechanism, hydrogen (H) atoms play a critical role (see Figure 1.9).
- ❖ Reduction in the amount of excess carriers on the surface of c-Si by means of field effect passivation. Fixed charges in passivation layers cause band-bending which can act as a barrier preventing minority carriers coming close to a c-Si surface. Thus, the probability of carrier capturing at defects on the c-Si surface is reduced (see Figure 1.10).

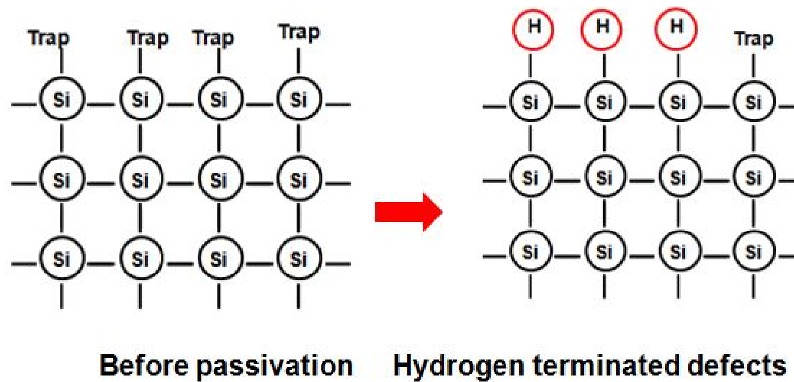


*Figure 1.9. Defect termination by H atoms.*

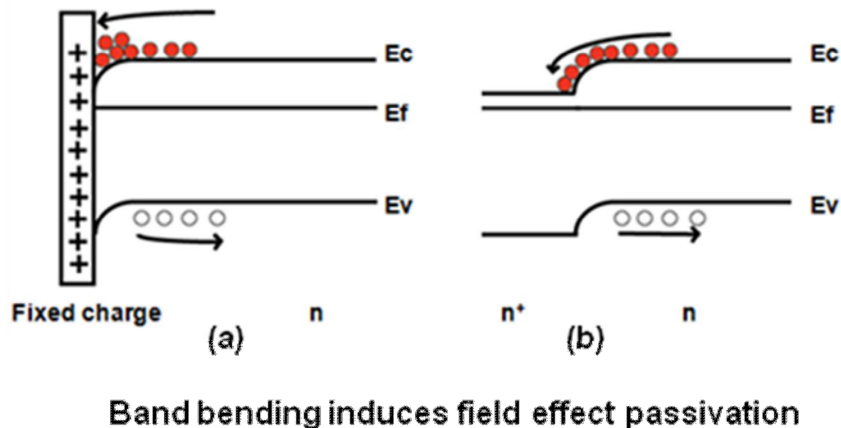


*Figure 1.10. Minority carriers (hole) in n-type c-Si wafer are pushed away from c-Si surface by band bending caused by (a) fixed charges and (b) a $n^+$ layer.*

Thermally-grown silicon dioxide ($SiO_2$) layers can significantly reduce interface state density, while passivation mechanism of plasma enhanced chemical vapor deposition (PECVD) $SiN_x$ layers are mostly based on field effect passivation. Typical values of $D_{it}$ and fixed charge density are $10^{10}$ $cm^{-2}eV^{-1}$ and $10^{10}$ $cm^{-2}$ for $SiO_2$ and $10^{11}$ $cm^{-2}eV^{-1}$ and $10^{11}$ $cm^{-2}$ for PECVD $SiN_x$ layers [27]. $SiN_x$ passivation layers are paid much attention by researchers and industry because they have not only high passivation quality but also excellent anti-reflective property. They can thus reduce both electrical loss and optical loss and $SiN_x$ becomes potential passivation layers for high-efficiency solar cells.

Therefore, in this study, I would like to introduce the passivation quality of high-transparency $SiN_x$ layers and its application for back-contact n-type c-Si solar cells.

### 1.3. Application of catalytic chemical vapor deposition to passivation technique for c-Si solar cells

As I mentioned above, excellent passivation techniques are very important in producing high-efficiency solar cells. It is well known that $SiN_x$ layers are effective anti-reflection and good passivation layers for c-Si to gain high efficiency of c-Si solar cells. They act as an anti-reflection coating; thus, reducing the optical loss. Furthermore, $SiN_x$ layers have high H content, which can terminate defects on the surface as well as in the bulk of Si substrates, and consequently, reduce recombination of carriers. Schmidt *et al.* [28] reported that outstandingly low SRV below 10 cm/s can be achieved when mirror-polished 1 Ωcm p-type float-zone (FZ) silicon wafers are passivated with $SiN_x$ films fabricated by high-frequency direct PECVD. However, it is known that direct contact between $SiN_x$ and c-Si makes P-centers [29], which are defect centers caused by nitrogen dangling bonds in Si network. If this problem can be solved, extremely low SRV can be obtained. The combination of $SiN_x$ layers and other passivation layers can improve passivation ability. It was reported that stacked structures consisting of thermally-grown $SiO_2$ films and PECVD $SiN_x$ films show excellent passivation ability on a 2.5 Ωcm n-type CZ Si wafers with a SRV lower than 2.4 cm/s [23]. Focsa *et al.* [25] reported that a SRV for $SiN_x$/intrinsic amorphous silicon (a-Si) stacked layers which are formed at 50 $^oC$ by remote PECVD on n-type FZ Si wafers reaches 11 cm/s and for p-type FZ Si wafers 14 cm/s. Nevertheless, PECVD uses plasma to activate precursor gases into radical species; it can cause plasma damage on c-Si substrates. Therefore, an excellent method

preventing plasma damage is favorable for application in passivation technique for c-Si. Catalytic chemical vapor deposition (Cat-CVD), also referred to as hot-wire CVD [30], is one of the most promising methods satisfying the requirement. In Cat-CVD system, radicals are formed by decomposing gas sources on a heated catalyzing wire, and thus no plasma damage occurs; high passivation quality of Cat-CVD films on c-Si is expected. The results obtained by Cat-CVD passivation films have proved this prediction. In particular, $SiN_x$/a-Si stacked layers formed by Cat-CVD have demonstrated excellent passivation ability with a SRV of lower than 1.5 cm/s for n-type c-Si wafers and a SRV of lower than 9.0 cm/s for p-type wafers [31]. The obtained SRV is the best world level for n-type c-Si passivation.

In the next part of the chapter, I would like to describe Cat-CVD system and explain the reason why high passivation quality can be obtained by using films prepared by Cat-CVD system.

### *1.3.1 Introduction of Cat-CVD system*

Cat-CVD is a novel method to prepare thin films with high film quality and high film/c-Si interface quality. In this method, gas sources are decomposed to radicals on a heated catalyzing wire (usually at very high temperature, more than 1000 $^{o}$C). During the deposition process, no energetic ions can be formed, and thus there is no serious damage on c-Si surfaces or film/c-Si interfaces. Therefore, Cat-CVD is very suitable for application in semiconductor devices.

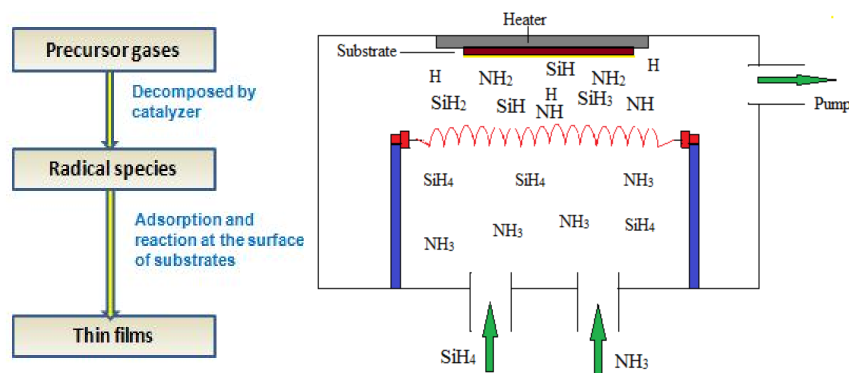


*Figure 1.11. Working principle scheme of Cat-CVD*

The working principle scheme of Cat-CVD is shown in Figure 1.11. The key point of this method is the way of forming activated radicals. In Cat-CVD system, radical species are formed by decomposing gas sources on a heated catalyzing wire such as tungsten and tantalum. Compared to conventional PECVD, in which energetic ions are formed when source gases pass through plasma reactors, Cat-CVD film/c-Si interfaces can have better quality due to no damage from plasma.

Cat-CVD has been firstly introduced by Wiesmann *et al.* [31, 32] in 1979 as a method of producing hydrogenated amorphous silicon (a-Si) films at a high deposition rate. Until 1985, H. Matsumura has found the catalytic role of a heated filament (tungsten (W)) and firstly succeeded in preparing device-quality a-Si by using only Si source gas and a heated W wire by adjusting deposition parameters, and he named the method catalytic CVD [33-35]. He has also succeeded in preparing high quality amorphous silicon germanium (a-SiGe) in 1987 [36], $SiN_x$ in 1989 [37] and polycrystalline silicon (poly-Si) at low temperatures in 1991 [38], which showed the large feasibility of the method. In 1991, Mahan *et al.* [39] reported the comparison of Cat-CVD a-Si films with PECVD films, and indicated the superiority of Cat-CVD technique for the preparation of excellent quality a-Si films. Since this report was so clear to understand the feasibility of Cat-CVD, many researchers started to study this new exciting topic. Since they used the term of hot-wire CVD (HWCVD) in their reports, many people also started to use this term instead of Cat-CVD. Since 1991, the properties of Cat-CVD films have been widely investigated particularly in Europe in addition to USA and Japan, and various results of device application such as solar cells [40] and thin-film transistors (TFTs) [41- 44] have been reported. Since the discovery of Cat-CVD, there are also many new methods developed based on the working principles of Cat-CVD, such as initiated CVD, organic catalytic CVD, plasma-assisted HWCVD…

Since 2000, the international conference on Hot-wire CVD was held biennially. An increase in participants in this conference indicates an increase in interest of this method as well as the expanding of its application.

### *1.3.2 Cat-CVD application in passivation technique for c-Si solar cells*

Due to the absence of energetic ions during deposition process, Cat-CVD film/c-Si interfaces with high interface quality are realized. Therefore, this method has high potential for application in passivation technique for c-Si solar cells. It has been reported by Koyama *et al*. that an extremely low SRV of 1.5 cm/s can be obtained for $SiN_x$/a-Si stacked layers passivating on a 2-5 Ωcm FZ (100) n-type c-Si wafer [30]. The insertion of an a-Si layer contributes greatly to improvement in lowering SRV for $SiN_x$/a-Si/c-Si structures. This layer plays a critical role in lowering defect centers forming during $SiN_x$ deposition, which is clearly indicated as the observation of a damage layer in a scanning transmission electron microscopy (STEM) image [45].

Moreover, Cat-CVD system can also be used for impurity doping to c-Si. A shallow phosphorus (P) doped layer with high doping concentration can be obtained when $PH_3$ or mixed $PH_3/H_2$ was introduced to a Cat-CVD chamber with a heated catalyzing wire. This doping process is performed at low substrate temperature as low as room temperature. Sheet carrier density of the shallow doped layers is in a range from $10^{12}$ to $10^{13}$ $cm^{-2}$, depending on substrate temperature. This shallow P Cat-doped layer with suitable donor concentration is a promising layer for creating field effect passivation for a n-type c-Si wafer. Applying the P Cat-doped layer to passivation technique for a c-Si wafer has been reported by Hayakawa *et al.* [46]. They investigated the passivation quality of a-Si films, a-Si/n-type a-Si and a-Si/P doped layers on n-type c-Si. a-Si films play important roles in reducing trapping centers on a c-Si surface, and n-type a-Si and P Cat-doped layers causes band bending, sending minority carriers away from a c-Si surface. The use of these passivation layers can improve greatly minority carrier lifetime.

However, the use of a-Si films is not desirable since a-Si has high optical absorption property. This parasitic absorption in a-Si causes reduction in solar cell efficiency. The materials with high transparency and high passivation quality are more favorable. Si-rich $SiN_x$, which is more transparent than a-Si, is one of the promising layers for replacing a-Si. In my master thesis, I have reported that a low SRV of 4.4 cm/s can be obtained for 2-5 Ωcm FZ (100) n-type c-Si passivated by Cat-CVD $SiN_x$/Si-rich $SiN_x$ layers and the use of Cat-CVD Si-rich $SiN_x$ film can enhance significantly optical transparency [47]. In particular, I achieved 30% improvement in the optical transparency at

the wavelength of 400 nm compared to that of the $SiN_x$/a-Si stacked layers. In Cat-CVD, Si-rich $SiN_x$ film properties can easily change by changing $SiH_4/NH_3$ flow rate ratio. However, the more Si-rich, the lower SRV, but the lower transparency can be obtained.

### 1.4. Purpose of this study

For both study of Koyama and my master thesis, top Cat-CVD $SiN_x$ films is stoichiometric films which was optimized for excellent oxidation resistance applying in ultralarge scale integrated circuits [48]. The deposition conditions of Cat-CVD $SiN_x$ films for the best passivation quality have not been optimized yet. A SRV of the $SiN_x$/c-Si structure is high, more than 100 cm/s. In my master thesis, I found that post-annealing process is also effective in improving the passivation quality of Cat-CVD $SiN_x$/Si-rich $SiN_x$ films. The diffusion of H atoms in Si-rich $SiN_x$ films to a c-Si surface is a key point for the SRV improvement. Therefore, in this dissertation, my aim is to optimize deposition conditions for Cat-CVD $SiN_x$ passivation layers, improve its passivation quality and then, apply it to n-type c-Si back-contact solar cells.

Due to the purpose of my study, I would like to divide my dissertation in 7 chapters.

Chapter 1 is introduction. In this chapter, I would like to briefly mention the current status of solar cells and its perspective. The role of passivation layers, achievement of applying Cat-CVD for passivation technique on c-Si as well as research motivation are also described to point out the main purpose of the study.

In Chapter 2, based on the obtained results from master thesis, which shows that c-Si wafers passivated with $SiN_x$/Si-rich $SiN_x$ stacked layers have low SRV and a drastic reduction in SRV is realized after post-annealing, in this study, I firstly investigate the role of H and fixed charge on passivation quality of $SiN_x$/Si-rich $SiN_x$ stacked layers on c-Si. We found that H contributes significantly to improvement in the passivation quality of the Cat-CVD stacked layers. The effect of adding $H_2$ into Si-rich $SiN_x$ films on their passivation quality is also examined.

The results from Chapter 2 suggest that, if $SiN_x$ films contain high amount of H, the passivation quality of the films might be enhanced greatly by annealing. The optical

transparency of the film is very important for a passivation layer. Thus, in the next step, I investigated the passivation quality of high-transparency single Cat-CVD $SiN_x$ films. H content of $SiN_x$ films (with a refractive index of ~2) were varied by changing substrate temperature and pressure during the film deposition. The details of this study are clearly expressed in Chapter 3.

As I mentioned above, a P Cat-doped layer can lower SRV by field effect passivation. In order to reduce SRV for $SiN_x$/c-Si structure, a P Cat-doped layer is introduced before depositing $SiN_x$ films. Chapter 4 describes a drastic reduction in SRV in $SiN_x$/c-Si when a P Cat-doped layer is introduced.

My aim is to apply passivation films into back-contact solar cell application. For this cell, textured c-Si has a critical role in reducing reflection and enhancing light trapping. Therefore, the passivation quality of optimized $SiN_x$ films on textured Si should be investigated. The details of this investigation are presented in Chapter 5.

Chapter 6 focuses on the application of Cat-CVD $SiN_x$ and $SiN_x$/P-Cat doped layers in back-contact solar cells. Cell characteristics and how enhancement in cell efficiency by using films prepared Cat-CVD technique is clearly discussed.

Finally, Chapter 7 gives conclusive summary of the dissertation.

**References**

[1] http://www.bp.com/en/global/corporate/about-bp/energy-economics/statistical-review-of-world-energy.html

[2] http://www.ncbi.nlm.nih.gov/pmc/articles/PMC1310946/

[3] http://www.renewable-energy-info.com/solar-energy

[4]http://cleantechnica.com/2014/04/13/world-solar-power-capacity-increased-35-2013-charts/

[5] http://www.solarbuzz.com/going-solar/understanding/technologies

[6] D. M. Chapin, C. S. Fuller and G. L. Pearson, *J. Appl. Phys.* **25** (1954) 676.

[7] P. Gevorkian, The only complete design resource for sustainable energy systems geared towards engineers, (2007) 499.

[8] http://news.panasonic.net/stories/2014/0416_26881.html

[9]R. M. Swanson, Proc. 31st IEEE Photovoltaic Specialists Conference (2005) 889.

[10] http://en.wikipedia.org/wiki/Solar_cell

[11] International Technology Roadmap for Photovoltaic (ITRPV), SEMI PV Group Europe, 2013, http://www.itrpv.net/

[12] A. U. Rehman and S. H. Lee, The Scientific World Journal, 2013, 470347

[13] J. Schmidt, *Solid State Phenomena* **95-96** (2004) 187.

[14]U.K. Das, S. Bowden, M. Lu, M.A. Burrows, O. Jani, D. Xu, S.S. Hegedus, R.L. Opila, and R.W. Birkmire, Proc. 18th Workshop on Crystalline Silicon Solar Cells and Modules: Materials and Processes, Vail, Colorado, August 3-6, 2008, p. 70.

[15] W. Zhao, J. Wang, Y. Shen, Z. Wang, Y. Cheng, Z. Hu, G. Li, J. Chen, J. Xiong, N. Guillevin, B. J. B. Heurtault, L. J. Geerligs, A. W. Weeber And J. H. Bultman, Proc. 38th IEEE, Photo-voltaic Specialists Conference (Austin, Texas), Jun 3-8th, 2012, pp. 2289.

[16] W. Jooß, dotoral thesis, 2002

[17] W.P. Mulligan, D. H. Rose, M. J. Cudzinovic, D. M. De Ceuster, K. R. McIntosh, D. Smith, R. M. Swanson, Proc. 19th European Photovoltaic Solar energy conference, Paris, France, 2014, p. 387

[19] F. Granek, doctoral thesis, 2009.

[20] R. Hezel, K. Jaeger, *J. Electrochem. Soc.* **136** (1989) 518.

[21] J. Schmidt, A. Merkle, R. Brendel ,B. Hoex, MCM. Van de Sanden, WMM. Kessels, *Prog. Photovolt. Res. Appl.* **16** (2008) 461.

[22] J. Schmidt and M. Kerr, *Sol. Energy Mater. Sol. Cells* **65** (2001) 585.

[23] P. Aubert, F. Delmotte, M. C. Hugon, B. Agius, J. L. Cantin, H. J. Von Bardeleben, *Phys. Rev. B* **59** (1999) 10677.

[24] Y. Larionova, V. Mertens, N. Harder, and R. Brendel, *Appl. Phys. Lett*. **96** (2010) 032105.

[25] A. Focsa, A. Slaoui, H. Charifi, J. P. Stocquert and S. Roques, *Mater. Sci. Eng.* B **159-160** (2009) 242.

[26] J. Benick, B. Hoex, M. C. M. vande Sanden, W. M. M. Kessels, O. Schultz and S. W. Glunz, *App. Phys. Lett.* **92** (2008) 253504.

[27] S. W. Glunz, *Advances in OptoElectronics* **2007** (2007) 2.

[28] J. Schmidt and M. Kerr, *Sol. Energy Mater. Sol. Cells* **65** (2001) 585.

[29] Y. Larionova, V. Mertens, N. Harder, and R. Brendel, *Appl. Phys. Lett*. **96** (2010) 032105.

[30] H. Matsumura, *J. Appl. Phys.* **65** (1989) 4396.

[31] K. Koyama, K. Ohdaira, and H. Matsumura, *Appl. Phys. Lett*. **97** (2010) 082108.

[32] H. Wiesmann, A.K. Ghosh, T. McMahon and M. Strongin. *J. Appl. Phys.* **50** (1979) 3752.

[33] H. Matsumura, H. Ihara, H. Tachibana, Proc. 18th IEEE Photovoltaic Specialists Conf., Las Vegas, 1985, p. 1277

[34] H. Matsumura and H. Tachibana, *Appl. Phys. Lett.* **47** (1985) 833.

[35] H. Matsumura, *Jpn. J. Appl. Phys.* **25** (1986) L949.

[36] H. Matsumura, *Appl. Phys. Lett.* **51** (1987) 804.

[37] H. Matsumura, *J. Appl. Phys.* **66** (1989) 3612.

[38] H. Matsumura, *Jpn. J. Appl. Phys.* **30** (1991) L1522.

[39] A.H. Mahan, J. Carapella, B.P. Nelson, R.S. Crandall and I. Balberg. *J. Appl. Phys.* **69** (1991) 6728.

[40] B. Schroeder, *Thin Solid Films* **430** (2003) 1.

[41] H. Matsumura, K. Mimura, H. Makino, Dig. Tech. Papers 1995 Int. Workshop Active-Matrix Liquid-Crystal Displays, Osaka, 1995, p. 89

[42] H. Meiling and R.E.I. Schropp, *Appl. Phys. Lett.* **69** (1996) 1062.

[43] J.K. Rath, F.D. Tichelaar, H. Meiling and R.E.I. Schropp, *Mater. Res. Soc. Symp. Proc.* **507** (1998) 879.

[44] M. Sakai, T. Tsutsumi, T. Yoshioka, A. Masuda and H. Matsumura, *Thin Solid Films* **395** (2001) 330.

[45] K. Koyama, Trinh Cham Thi, K. Higashimine, K. Ohdaira, and H. Matsumura, Proc. 39th IEEE Photovoltaic Specialists Conference, 2014, p. 3304.

[46] T. Hayakawa, T. Ohta, Y. Nakashima, K. Koyama, K. Ohdaira, and H. Matsumura, *Jpn. J. Appl. Phys.* **51** (2012) 101301.

[47] Trinh Cham Thi, Koichi Koyama, K. Ohdaira, and H. Matsumura, *Sol. Energy Mater. Sol. Cells* **93** (2012) 169.

[48] R. Morimoto, C. Yokomori, A. Kikkawa, A. Izumi and H. Matsumura, *Thin Solid Films* **430** (2003) 230.

# Chapter 2 Passivation mechanism of Cat-CVD Si-rich $SiN_x$/$SiN_x$ stacked layers on c-Si

## 2.1. Introduction

It is very important to provide an excellent coating layer for high-efficiency c-Si solar cells. The important roles of the coating layers are to decrease optical and electrical losses on a c-Si surface which cause reduction in c-Si solar cell efficiency. As I mentioned in Chapter 1, Cat-CVD system can be utilized as a promising method to prepare passivation layers for c-Si because of its advantage of no plasma damage to a c-Si surface. As a result, an extremely low SRV of 1.5 cm/s is obtained for n-type c-Si passivated with $SiN_x$/a-Si stacked layers prepared by Cat-CVD [1]. However, a-Si absorbs sun-light, causing reduction in c-Si solar cell efficiency. In order to overcome this problem, in my master thesis, I have attempted to use Si-rich $SiN_x$ films, instead of a-Si films. Here, Si-rich $SiN_x$ is defined as $SiN_x$ whose composition ratio [Si]/[N] is larger than 1.3 (in other word, its refractive index ($n$) at wavelength of 630 nm is larger than that of stoichiometric SiN ($n$~2)). I have found that the $SiN_x$/Si-rich $SiN_x$ stacked layer structure prepared by Cat-CVD is a promising candidate for a coating structure on a c-Si surface with a low SRV of 3 cm/s and higher transparency than a-Si [2]. However, the passivation mechanism of the stacked layers has not been investigated yet.

In this chapter, in order to clarify the passivation mechanism of the staked layers, I focus on the effect of fixed charges and H concentration in Si-rich $SiN_x$ films on the passivation quality of the stacked films. The obtained results suggest that the amount of H atoms formed in a Cat-CVD chamber during film deposition can be an important factor to enhance the passivation quality of the stacked layers. Si-rich $SiN_x$ films are thus deposited using $SiH_4$, $NH_3$ and $H_2$ as gas sources to improve more passivation quality of the stacked layers.

## 2.2. Experimental Procedure

### *2.2.1 Sample Preparation*

After cleaning c-Si wafers by diluted (5%) hydro-fluoric acid (HF) solution to remove native oxide on c-Si surfaces, 10-nm-thick Si-rich $SiN_x$ films and 100-nm-thick $SiN_x$ films were deposited by Cat-CVD in this order. The films were formed also on glass substrates for optical transmission measurement. Si-rich $SiN_x$ films and $SiN_x$ films were deposited in the same chamber. Source gases introduced to the chamber were decomposed on a heated tungsten catalyzer, which has a length of 210 cm and a diameter of 0.5 mm. The distance between substrate and catalyzer ($D_{cs}$) was 8 cm. Substrate temperature ($T_s$) and catalyzer temperature ($T_{cat}$) during deposition process were kept unchanged at 250 and 1800 $^oC$, respectively. The deposition conditions and composition ratios ([Si]/[N]) of the films, which were evaluated by X-ray photoelectron spectroscopy (XPS), are summarized in Table 2.1. For Fourier-transform infrared (FTIR) spectroscopy, Si-rich $SiN_x$ films with a thickness of about 150 nm were deposited on n-type (100) c-Si substrates with a resistivity of 3460 Ωcm. The reason for choosing the high resistivity c-Si substrate is to prevent infrared absorption by free electrons.

*Table 2.1. Deposition conditions of Si-rich $SiN_x$ and $SiN_x$ films.*

| Films | $SiH_4$ (sccm) | $NH_3$ (sccm) | $H_2$ (sccm) | Pressure (Pa) | $D_{cs}$ (cm) | $T_s$ ($^oC$) | $T_{cat}$ ($^oC$) | [Si]/[N] |
|---|---|---|---|---|---|---|---|---|
| Si-rich $SiN_x$ (without $H_2$) | 10 | 250 | 0 | 10 | 8 | 250 | 1800 | 1.4 |
| | 12.5 | 250 | 0 | 10 | 8 | 250 | 1800 | 1.8 |
| | 15 | 250 | 0 | 10 | 8 | 250 | 1800 | 2.0 |
| | 17.5 | 250 | 0 | 10 | 8 | 250 | 1800 | 2.7 |
| | 20 | 250 | 0 | 10 | 8 | 250 | 1800 | 3.5 |
| $SiN_x$ | 6.9 | 200 | 0 | 10 | 8 | 250 | 1800 | 0.8 |
| Si-rich $SiN_x$ (with $H_2$) | 15 | 20-50 | 50-200 | 10 | 8 | 250 | 1800 | |

### 2.2.2 *Characterization of Prepared Samples*

The thickness and refractive index ($n$) of $SiN_x$ and Si-rich $SiN_x$ films were measured on J. A. Woollam Co., HS-190™ spectroscopic ellipsometer, using the Cauchy model for data analysis [3]. More details of the working principle of spectroscopic ellipsometry and Cauchy model using for fitting data are described in Appendix A-1. Optical transmission spectra were observed on an Ultraviolet-visible-near infrared spectrophotometer, SHIMAZU Co. Ltd., UV-3150. The film density was measured by X-ray reflectivity. In order to investigate the passivation quality of the stacked layers on c-Si, microwave photo-conductivity decay (μ-PCD) measurement was carried out on KOBELCO LTA-1510EP using a pulse laser with a wavelength of 904 nm and a photon density of $5\times10^{13}$ $cm^{-2}$. For this measurement, $SiN_x$/Si-rich-$SiN_x$ stacked layers were deposited on both sides of 290-μm-thick n-type (100) floating-zone (FZ)-grown Si wafers with a resistivity of 2.5 Ωcm. Therefore, an excess carrier density of $1.7\times10^{15}$ $cm^{-3}$ is estimated. The cross-sectional schematic of the structure is shown in Figure 2.1(a). $\tau_{eff}$ is determined from the exponential decay of microwave reflection intensity and can be expressed as below:

$$\frac{1}{\tau_{eff}} = \frac{1}{\tau_{bulk}} + \frac{2S}{W} , \qquad (2.1)$$

where $\tau_{bulk}$, $W$, and $S$ represent minority carrier lifetime in c-Si bulk, wafer thickness, and SRV, respectively. In this study, I calculate the maximum value of SRV ($SRV_{max}$) by assuming $\tau_{bulk}=\infty$ .

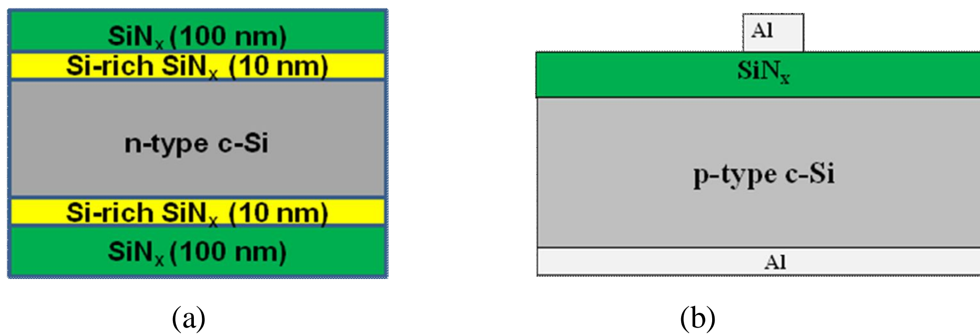


*Figure 2.1. Cross-sectional schematic of samples for (a) lifetime measurement and (b) C-V measurement*

For capacitance-voltage (C-V) measurement, a 100-nm-thick aluminum (Al) layer was deposited on one side of 2 Ωcm p-type (100) FZ c-Si wafers by evaporation method. To obtain Ohmic contact, the Al/c-Si structure was annealed at 400 $^{o}$C for 15 minutes in $N_2$ atmosphere. Then, Si-rich $SiN_x$ films and $SiN_x$ films were deposited on the other surface of the c-Si wafer. Finally, 2-mm-diameter Al electrodes were evaporated on $SiN_x$ layers through a hard mask. The cross-sectional schematic of a sample for C-V measurement is shown in Figure 2.1(b). C-V characteristics were obtained in the dark at a high frequency of 1 MHz using Keithley 6517A. Fixed positive charges density $Q_f$ was calculated by:

$$Q_f = Q_{total} - Q_m .$$

Here, $Q_{total}$ and $Q_m$ are determined by:

$$Q_{total} = \frac{C_i}{A}(\Delta\varphi_{ms} - V_{FB_1}) \ ,$$

$$Q_m = \frac{C_i}{2A}(V_{FB_1} - V_{FB_2}) ,$$

where $C_i$ is an insulator capacitance, $A$ is the area of electrodes, $\Delta\varphi_{ms}$ is work function difference between the metal and the silicon, and $V_{FB1}$ and $V_{FB2}$ are flat band voltages for forward and reverse C-V curves, respectively. They are determined through flat band capacitance, which is calculated to be $6\times10^{-9}$ F [4].

The concentration of bonded H ($C_H$) in Si-rich $SiN_x$ films is determined from the integrated areas of a Si-H stretching mode peak ($A_{Si-H}$) and a N-H stretching mode peak ($A_{N-H}$) in FTIR spectra using the following equation:

$$C_H = 1.36\times10^{17} \times (1.4\times A_{N-H} + A_{Si-H}) \times \frac{1}{d} \ (\text{cm}^{-3}),$$

where $d$ is a thickness of the film [5].

## 2.3. Results and discussion

### *2.3.1. The role of fixed charges*

It is reported that both H atoms included during deposition process and fixed charges contribute to improvement in the passivation quality of $SiN_x$ layers on c-Si [6]. Fixed charges in $SiN_x$ layers can prevent the recombination of photo-generated carriers by field effect passivation, while H atoms can decrease recombination centers by passivating dangling bonds on the surface of c-Si. In order to investigate clearly which factor is more significant in the passivation quality of the stacked layers, I evaluated fixed charge density and H content in the films. For this study, the composition of Si-rich $SiN_x$ films was varied by adjusting the ratio of the silane ($SiH_4$)-to-ammonia ($NH_3$) gas flow rates ($R$= $[SiH_4]/[NH_3]$) from 0.04 to 0.08. $R$ was varied by changing the $SiH_4$ flow rate from 10 to 20 sccm at a fixed $NH_3$ flow rate of 250 sccm.

Figure 2.2(a) shows the C-V curves of an Al/$SiN_x$/Si-rich $SiN_x$/c-Si structures before and after annealing at an annealing temperature ($T_a$) of 350 and 500 °C for 30 minutes. One can see large hysteresis for all the C-V curves. I consider that the hysteresis originates from mobile positive charges. The mobile charges are ionic impurities such as $Na^+$, $K^+$, $Li^+$ and $H^+$ [7], and I believe that the main mobile charges are $H^+$ ions because a large amount of H atoms must be captured in the films during deposition process due to the dissociation of $SiH_4$ and $NH_3$. Hysteresis becomes smaller after annealing, which may be because the H atoms can bond with Si dangling bonds or bond together to form $H_2$ molecules. Figure 2.2(b) shows the fixed charge density of the films before and after annealing at 350 °C for 30 min as a function of $R$. The highest value of $Q_f$ is $2.29\times10^{12}$ $cm^{-2}$ for only stoichiometric $SiN_x$ film. With Si-rich $SiN_x$ film insertion, $Q_f$ tends to decrease with increase in $R$ and reaches $1.54\times10^{12}$ $cm^{-2}$ when Si-rich $SiN_x$ films with $R$=0.08 ($n$=2.92) is used. The positive fixed charges are probably Si dangling bond defects with a configuration of $N_3{\equiv}Si^+$ in $SiN_x$ films, generally referred to as $K^+$ centers [8, 9]. Although $Q_f$ decreases after annealing, the values of $Q_f$ are still sufficiently high for effective field effect passivation [8], and can partially contribute to suppression in the surface recombination of minority carriers. However, $SRV_{max}$ rather decreases with increase in $R$,

that is, with decrease in $Q_f$, as shown in Figure 2.2(b). This means that there is a more significant factor to reduce SRV other than field effect induced by fixed charge.

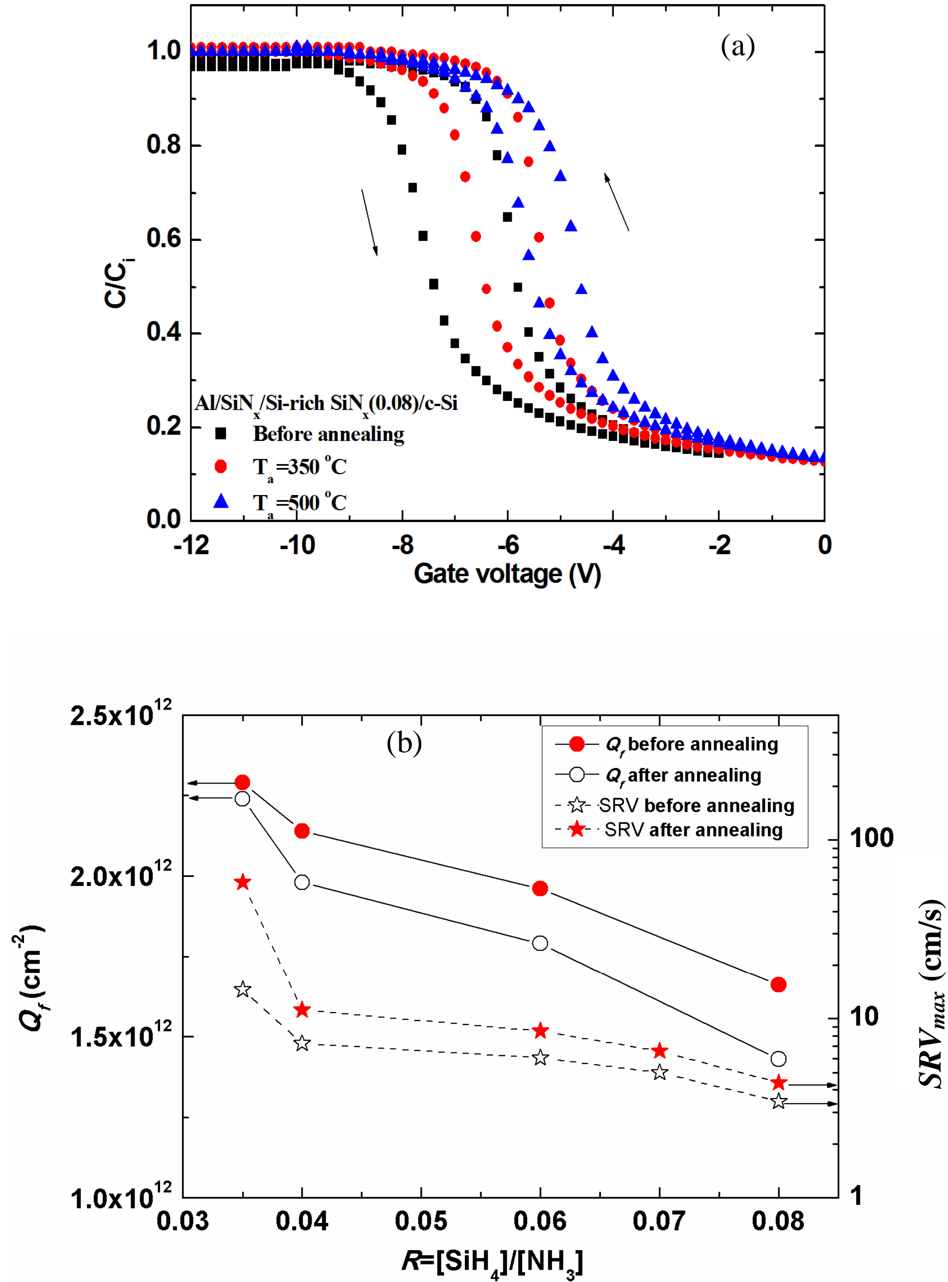


*Figure 2.2. (a) C-V curves of Al/$SiN_x$/Si-rich $SiN_x$/c-Si structures before and after annealing at $T_a$ of 350 and 500 $^oC$ for 30 minutes, and (b) $Q_f$ and $SRV_{max}$ before and after annealing at 350 $^oC$ for 30 min as a function of R.*

### *2.3.2 The role of hydrogen*

H atoms formed during deposition process can contribute greatly to improvement in the passivation quality of the $SiN_x$/Si-rich $SiN_x$ stacked films. For more detailed understanding of this effect, H content in Si-rich $SiN_x$ films is investigated.

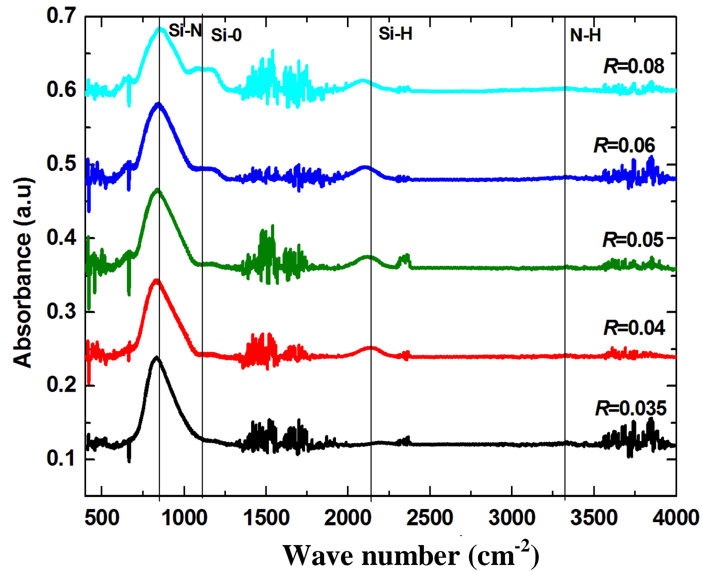


*Figure 2.3. FTIR spectra of 150-nm-thick Si-rich $SiN_x$ films deposited with various R.*

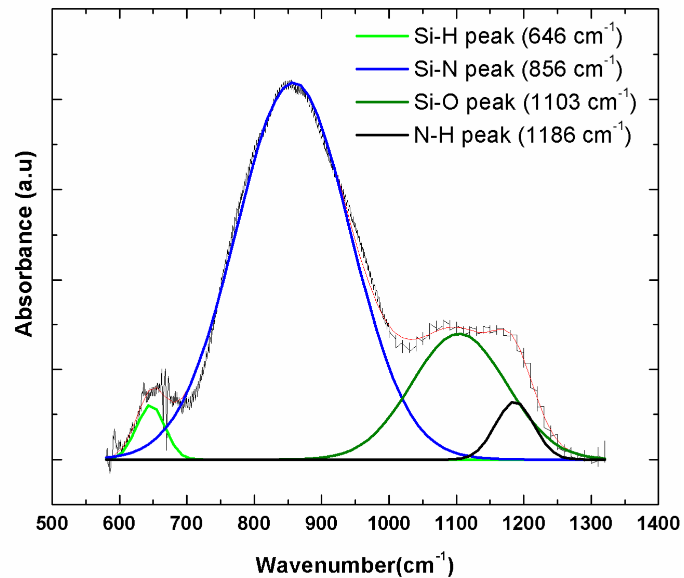


*Figure 2.4. Splitting of FTIR peaks of Si-rich $SiN_x$ films (R=0.08) using Gaussion fitting method.*

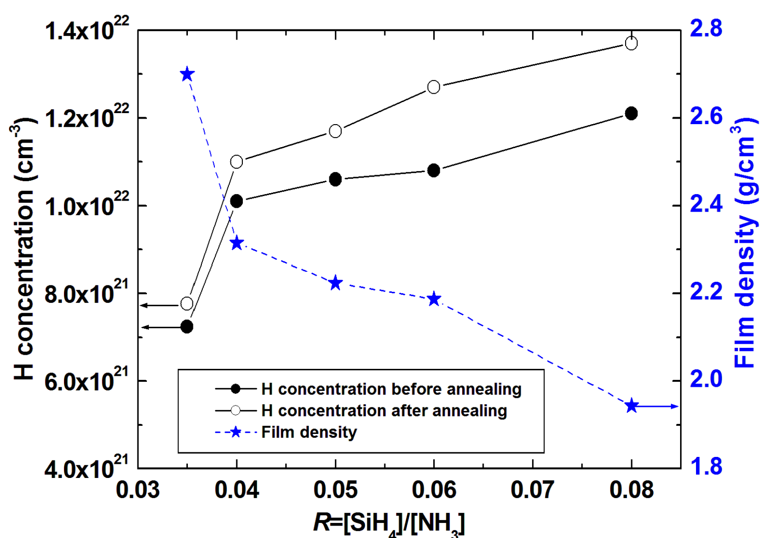


*Figure 2.5. H concentration of Si-rich $SiN_x$ films before and after annealing at $T_a$ of 350 °C and film density as a function of R.*

Figure 2.3 shows the FTIR spectra of 150-nm-thick Si-rich $SiN_x$ films deposited with various *R*. A Peak corresponding to N-H stretching mode is located at around 3326 $cm^{-1}$ and Si-H stretching mode is around 2140 $cm^{-1}$. One can see the increase of Si-H peak area with increase in *R*. The position of Si-H peak shifts to high wavelength in less Si-rich $SiN_x$ films may be due to the increase in electro-negativity of the backboned Si atoms when N content in the film increases [10]. At high *R*, there are two peaks beside the Si-N peak. By Gaussion fitting to split this spectrum, I obtain four peaks corresponding the Si–O–Si asymmetric stretching mode, N-H bending mode, Si-N stretching mode and Si-H wagging mode, as shown in Figure 2.4. The presence of the Si-O peak suggests that the films deposited with high *R* have low film density, and thus, oxygen in ambient can be absorbed easily into the films. To support this suggestion, film density was measured by X-ray reflectivity method. Film density as a function of *R* is shown in Figure 2.5. One can see that film density decreases when *R* increases. This fact supports the hypothesis that Si-rich $SiN_x$ films deposited with high *R* can allow more diffusion of H atoms into c-Si wafers during $SiN_x$ deposition and during annealing process, resulting high passivation quality. Figure 2.5 also shows the H content in Si-rich $SiN_x$ films as a function of *R* before and after annealing at 350 °C for 30 min. The film density of Si-rich $SiN_x$ films is also plotted in the same Figure. H concentration increases with *R* due to increase in Si-H bondings. Increase in H concentration in Si-rich $SiN_x$ films after annealing at a $T_a$ of 350 °C may be because Si-rich $SiN_x$ films have low density, as shown in Figure 2.5, and H

atoms existing in the voids of the films can diffuse and bond with Si dangling bonds, forming Si-H bondings. However, Si-H peak around 2100 $cm^{-1}$ disappears after annealing at a $T_a$ of 500 $^oC$, as shown in Figure 2.6, which means that Si-H bonds are broken and H atoms are released to environment in form of $H_2$. I have previously reported that $SRV_{max}$ drastically increases to 50 cm/s after annealing at a $T_a$ of 500 °C, as shown in Figure 2.7 [2], the reason of which is probably the desorption of H atoms from the films observed in this study.

The above results show the important role of H content in the passivation quality of the $SiN_x$/Si-rich $SiN_x$ stacked layers on c-Si wafers. The H atoms may passivate dangling bonds on a c-Si surface not only during the deposition of Si-rich $SiN_x$ films but also during $SiN_x$ film deposition and annealing. Therefore, rich H content is an important factor to realize the good passivation quality of $SiN_x$/Si-rich $SiN_x$ stacked films.

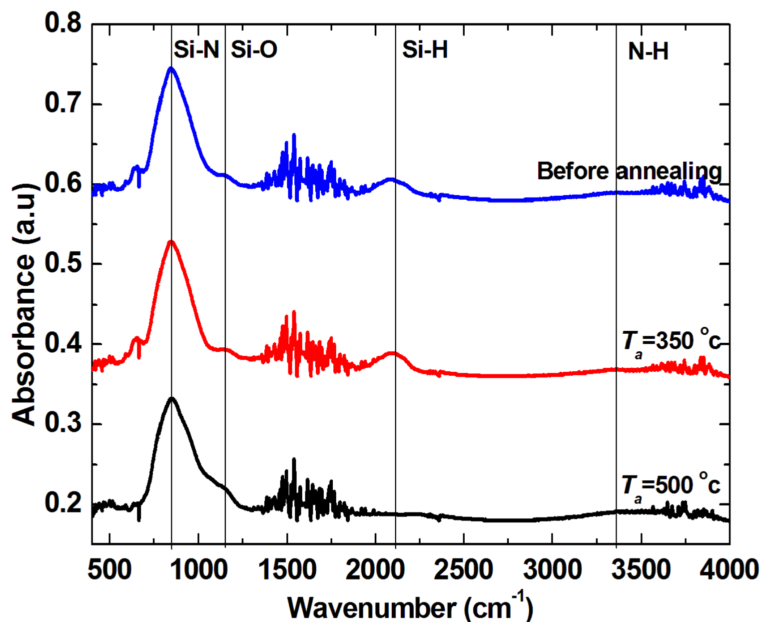


*Figure 2.6. FTIR spectra of a Si-rich $SiN_x$ films before and after annealing at 350 and 500 $^oC$.*

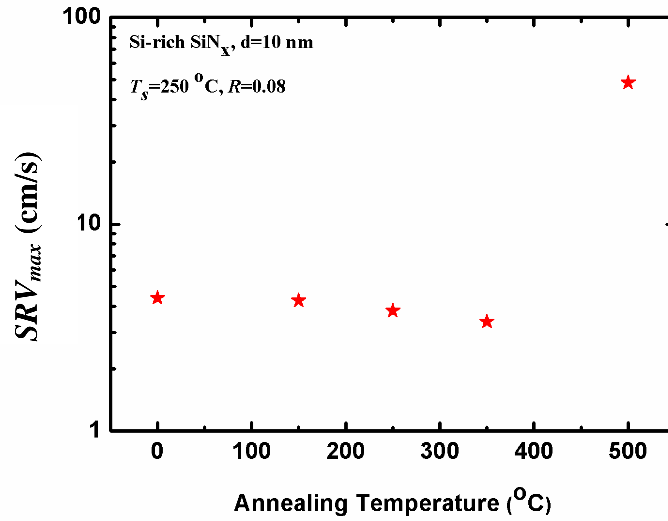


*Figure 2.7. $SRV_{max}$ of c-Si passivated with $SiN_x$/Si-rich $SiN_x$ stacked layers as a function of annealing temperature (data obtained in my master thesis).*

### 2.4. Addition of $H_2$ during Si-rich $SiN_x$ deposition

Before starting the investigation of the passivation quality of $SiN_x$/Si-rich $SiN_x$ stacked layers on c-Si, I firstly discuss gas phase reaction occurring during film deposition in Cat-CVD system. Si and H radicals are produced by the catalytic decomposition of $SiH_4$ gas, while $SiH_3$ formed by a gas phase reaction betwee H and $SiH_4$ is one of the most important deposition species [11-14]. H and $NH_2$ radicals are primary decomposition products on catalyzer surface when only $NH_3$ is gas source [15]. NH radicals are formed in gas phase reaction such as:

$NH_2+H \rightarrow NH+H_2$

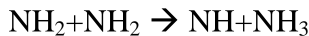

$NH_2+NH_2 \rightarrow NH+NH_3$

The addition of $SiH_4$ can strongly decrease the catalytic decomposition efficiency of $NH_3$. $SiH_4$ is decomposed into Si and 4H at catalyzer surface, causing Si-contaminated tungsten surface [16], which leads to reduction in the decomposition efficiency of $NH_3$. It has been reported that the reaction of radicals forming aminosilane molecules is dominant to form $SiN_x$ films prepared by PECVD and photo-assisted CVD [17-19]. For example, $SiH_3$ and $NH_2$ species reacts to form $SiNH_5$ [19]. Possible aminosilanes ($SiH_x(NH_2)_{4-x}$ (x=0-3)) were also observed [18]. It has been found that increase in the amount of $NH_3$ gas

leads to the formation of aminosilanes over disilane and trisilane. The mechanism of the formation of aminosilanes from $SiH_{3-x}(NH_2)_x$ (x=0-3) was proposed as below [18]:

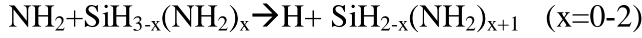

$$NH_2+SiH_{3-x}(NH_2)_x \rightarrow H+ SiH_{2-x}(NH_2)_{x+1} \quad (x=0\text{-}2)$$

$$SiH_{2-x}(NH_2)_{x+1}+H \rightarrow SiH_{3-x}(NH_2)_{x+1} \quad (x=0\text{-}2)$$

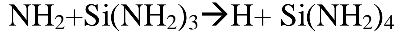

$$NH_2+Si(NH_2)_3 \rightarrow H+ Si(NH_2)_4$$

However, in Cat-CVD system, it was found that the densities of $SiH_3$ and $NH_2$ radicals are much larger than NH density and no aminosilane signal is obtained [16]. This implies that not aminosilane molecules but $NH_2$ and $SiH_3$ are major deposition radicals to form a $SiN_x$ film in Cat-CVD system. The addition of $H_2$ as gas source can significantly improve the decomposition efficiency of $NH_3$ due to the cleaning of a catalyzer surface by $H_2$ [20]. Quality of $SiN_x$ films deposited with $H_2$ dilution is found to be higher than that in the case of without $H_2$ dilution [21-22]. Additionally, as mentioned above, the amount of H atoms formed during a deposition process is a key point for improvement in the passivation quality of the $SiN_x$/Si-rich $SiN_x$ stacked films. Therefore, in this study, $H_2$ gas was added during the deposition of Si-rich $SiN_x$ films.

Various Si-rich films with different $n$ were deposited by changing $R$. $H_2$ flow rate was fixed at 100 sccm. Figure 2.8 shows $SRV_{max}$ of c-Si wafers passivated by $SiN_x$/Si-rich $SiN_x$ stacked layers as a function of $n$ when Si-rich $SiN_x$ films were deposited with and without $H_2$. One can see reduction in $SRV_{max}$ when Si-rich $SiN_x$ films are deposited with $H_2$ addition. In particular, I obtained a $\tau_{eff}$ of 5.1 ms for a Si-rich $SiN_x$ film with a $n$ of 2.92 deposited with $H_2$ dilution, corresponding to a $SRV_{max}$ of as low as 2.9 cm/s, which is much better than a $SRV_{max}$ for a Si-rich $SiN_x$ films deposited without $H_2$ dilution showing $\tau_{eff}$ of 3.3 ms, corresponding to $SRV_{max}$ of 4.4 cm/s. One possible reason for this tendency is that higher amount of H atoms a $SRV_{max}$ re formed in the Cat-CVD chamber during deposition process with $H_2$ dilution, and therefore, more H atoms passivate dangling bonds on the surface of c-Si. In order to support this hypothesis, Si-rich $SiN_x$ films were deposited at various $H_2$ gas flow rate with keeping $n$ of the films.

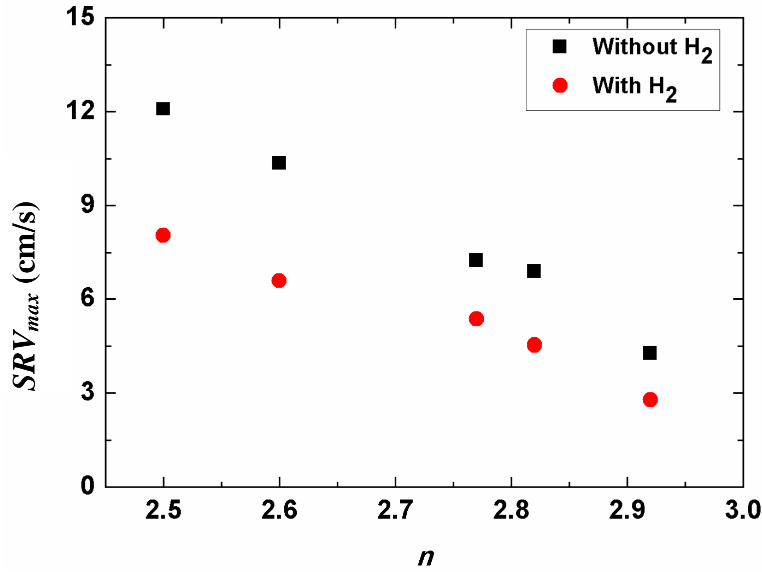


*Figure 2.8. $SRV_{max}$ of c-Si wafers passivated with $SiN_x$/Si-rich $SiN_x$ stacked layers as a function of n.*

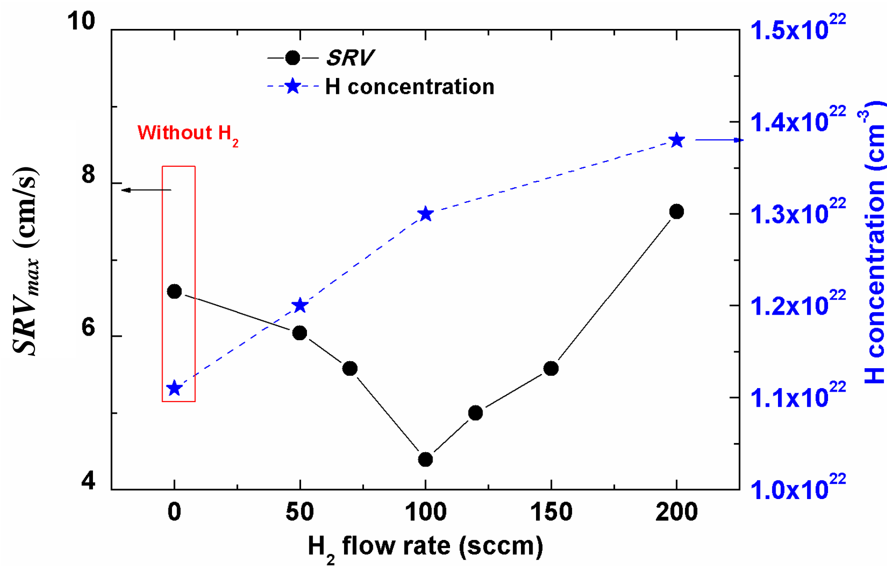


*Figure 2.9. $SRV_{max}$ of c-Si wafers passivated with $SiN_x$/Si-rich $SiN_x$ stacked layers (n=2.82) and H content in Si-rich $SiN_x$ films at various $H_2$ flow rate*

Figure 2.9 shows $SRV_{max}$ of c-Si wafers passivated with $SiN_x$/Si-rich $SiN_x$ stacked layers ($n$=2.82) and H concentration in Si-rich $SiN_x$ films at various $H_2$ flow rate. $SiH_4$ and $NH_3$ flow rate was fixed at 15 and 30 sccm, respectively. One can see that H concentration in the films increases monotonically with increase in $H_2$ gas flow rate. The data can also be confirmed in H concentration profiles measure by elastic recoil detection analysis

(ERDA), as shown in Figure 2.10. $SRV_{max}$ also tends to decrease with $H_2$ flow rate up to a $H_2$ flow rate of 100 sccm, while starts to increase after reaching the lowest $SRV_{max}$. Decrease in $SRV_{max}$ is probably due to higher H content during film deposition which acts to terminate dangling bonds on c-Si surface. At $H_2$ gas flow rate of 200 sccm, $SRV_{max}$ becomes higher compared to $SRV_{max}$ in case of without $H_2$ dilution even higher H contents. One possible reason for increased $SRV_{max}$ is that very large amount of H atoms come onto the surface of c-Si wafers during film deposition, and cause damage by the etching of Si leading to increase in $SRV_{max}$.

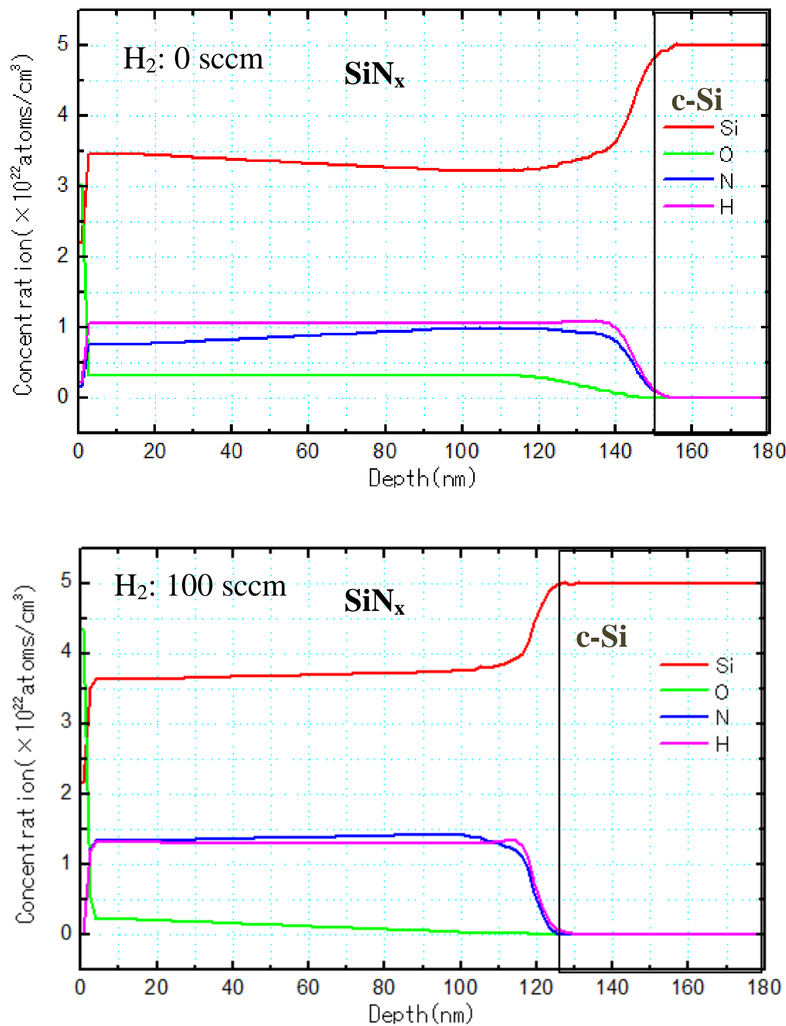


*Figure 2.10. Concentration profiles of Si-rich $SiN_x$ samples with and without $H_2$ addition.*

Figure 2.11 shows the transmission spectra of Si-rich $SiN_x$ ($n$=2.92) films deposited with and without $H_2$. Although Si-rich $SiN_x$ films deposited with $H_2$ dilution can improve passivation quality, transparency of the films seems not to be different from Si-rich $SiN_x$

films deposited without $H_2$ dilution at the same *n*. This result demonstrates the benefit of the addition of proper amount of $H_2$ gas for Si-rich $SiN_x$ deposition. However, $SRV_{max}$ may reach the limited value for each Si-rich $SiN_x$ film. It does not improve significantly even after the sample is annealed. For example, for Si-rich $SiN_x$ films with n=2.92, $SRV_{max}$ of c-Si wafers passivated by $SiN_x$/Si-rich $SiN_x$ stacked layers is 4.4 cm/s for as deposited sample and decreases to 3.0 cm/s after annealing. With addition of $H_2$, $SRV_{max}$ of 2.8 cm/s for as deposited sample and slightly decreases to 2.7 cm/s after annealing.

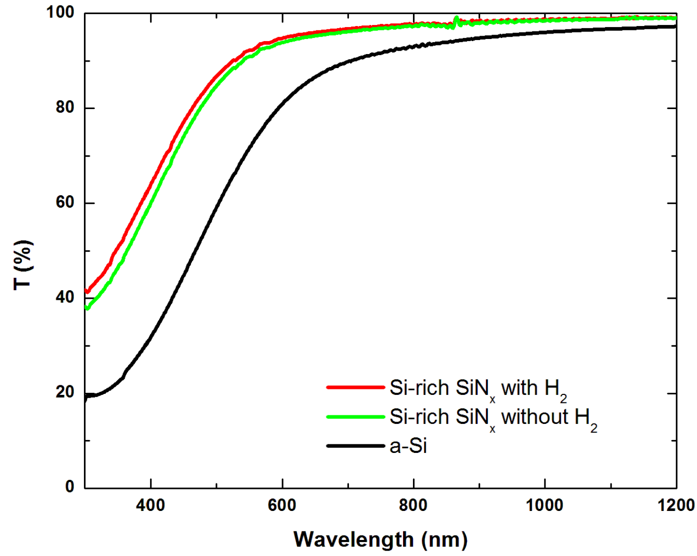


*Figure 2.11. Transmission spectra of Si-rich $SiN_x$ (n=2.92) deposited with and without $H_2$. Transmission spectrum of an a-Si film was shown for comparison.*

## 2.5. Conclusion

In this chapter, the roles of fixed charges and H in Cat-CVD Si-rich $SiN_x$ films for the passivation of c-Si surface are elucidated. Fixed charge density in the stacked layers is sufficiently high and can contribute to field passivation effect; however, it does not contribute to improve in passivation quality by annealing. H content is found to be more important in the passivation quality of the $SiN_x$/Si-rich $SiN_x$ stacked layers on c-Si wafers. H atoms terminate c-Si defects not only during deposition process but also during annealing. The addition of $H_2$ during the deposition of Si-rich $SiN_x$ films improves significantly the passivation quality of the stacked layers. The best $\tau_{eff}$ obtained for Si-rich $SiN_x$ film (*n*=2.92) deposited with $H_2$ dilution is 5.1 ms, corresponding to a $SRV_{max}$ of 2.8 cm/s, which is much larger than the case of using a Si-rich $SiN_x$ film with the same *n* deposited without $H_2$ dilution showing $\tau_{eff}$ of 3.3 ms, corresponding to $SRV_{max}$ of 4.4 cm/s.

**References**

[1] K. Koyama, K. Ohdaira and H. Matsumura, *Appl. Phys. Lett.* **97** (2010) 082108.

[2] T. T. Cham, K. Koyama, K. Ohdaira and H. Matsumura, *Sol. Energy Mater. Sol. Cells* **93** (2012) 169.

[3] Guide to Using WVASE32$^{TM}$: Software for Vase and M-44 Ellipsometers. J.A. Woollam Co., Inc., 1989, p. 159.

[4] E. H. Nicollian and J. A. Brews, MOS physics and Technology, Wiley-Interscience publication, New York, 1982, p. 83.

[5] W. A. Lanford, *J. Appl. Phys.* **49** (1978) 2473.

[6] A. G. Aberle, *Sol. Energy Mater. Sol. Cells* **65** (2001) 239.

[7] D. K. Schroder, "Semiconductor Material and Device Characterization", 3rd Edition, Wiley-IEEE Press, New York, 2006, p. 321.

[8] J. -F. Lelièvre, E. Fourmond, A. Kaminski, O. Palais, D. Ballutaud and M. Lemiti, *Sol. Energy Mater. Sol. Cells* **93** (2009) 1281.

[9] J. Robertson, W. L. Warren and J. Kanicki, *J. Non-Cryst. Solids* **187** (1995) 297.

[10] G. Lucovsky, *Solid State Commun.* **29** (1978) 571.

[11]. Y. Nozaki, K. Kongo, T. Miyazaki, M. Kitazoe, K. Horii, H. Umemoto, A. Masuda and H. Matsumura, *J. Appl. Phys.* **88** (2000) 5320.

[12]. Y. Nozaki, M. Kitazoe, K. Horii, H. Umemoto, A. Masuda and H. Matsumura, *Thin Solid Films* **395** (2001) 47.

[13]. H. Umemoto, Y. Nozaki, M. Kitazoe, K. Horii, K. Ohara, D. Morita, K. Uchida, Y. Ishibashi, M. Komoda, K. Kamesaki, A. Izumi, A. Masuda and H. Matsumura, *J. Non-Cryst. Solids* **299–302** (2002) 9.

[14]. H. Umemoto, K. Ohara, D. Morita, Y. Nozaki, A. Masuda and H. Matsumura, *J. Appl. Phys.* **91** (2002) 1650.

[15]. H. Umemoto, K. Ohara, D. Morita, M. Yamawaki, A. Masuda and H. Matsumura, *J. Appl. Phys.* **42** (2003) 5315.

[16] H. Umemoto, T. Morimoto, M. Yamawaki, Y. Masuda, A. Masuda and H. Matsumura, *Thin Solid Films* **430** (2003) 24.

[17] D. L. Smith, A. S. Alimonda, C. C. Chen, S.E. Ready and B. Wacker, *J. Electrochem. Soc.* **137** (1990) 614.

[18] D. B. Beach and J. M. Jasinski, *J. Phys. Chem.* **94** (1990) 3019.

[19] M. Yoshimoto, K. Takubo, T. Ohtsuki, M. Komoda and H. Matsunami, *J. Electrochem. Soc*. **142** (1995) 1976.

[20] T. Morimoto, S. A. A. G. Ansari, K. Yoneyama, H. Umemoto, A. Masuda and H. Matsumura, *Thin Solid Films* **501** (2006) 31.

[21] A.H. Mahan, A.C. Dillon, L.M. Gedvilas, D.L. Williamson and J.D. Perkins, *J. Appl. Phys*. **94** (2003) 2360.

[22] Q. Wang, S. Ward, L. Gedvilas, B. Keyes, E. Sanchez and S. Wang, *Appl. Phys. Lett.* **84** (2004) 338.

# Chapter 3 Passivation quality of a Cat-CVD $SiN_x$ single layer on n-type c-Si

## 3.1. Introduction

The obtained results from Chapter 2 indicate that c-Si passivated with $SiN_x$/Si-rich $SiN_x$ stacked layer has lower SRV but higher transparency than in the case of $SiN_x$/a-Si stacked layers. However, Si-rich $SiN_x$ films still have considerable light absorption. Ideally, further improvement in transparency should be achieved. Stoichiometric $SiN_x$ films do not only have high transparency but also act as anti-reflective coating layers on c-Si [1]. For both study of Koyama and my master thesis, top Cat-CVD $SiN_x$ films were stoichiometric films which was optimized as excellent oxidation resistance applying in ultralarge scale integrated circuits [2-4]. Deposition conditions of Cat-CVD $SiN_x$ films for the best passivation quality have not been optimized yet. A $SRV_{max}$ of the $SiN_x$/c-Si structure is high, more than 100 cm/s. In the previous chapter, I elucidated that annealing process is effective in improving the passivation quality of Cat-CVD $SiN_x$/Si-rich $SiN_x$ films, and the diffusion of H in Si-rich $SiN_x$ films to a c-Si surface is a key point for the passivation quality improvement [5]. These results suggest that passivation films with high transparency and high H content may passivate significantly a c-Si surface and become excellent passivation layers for application to c-Si solar cells. Therefore, in this study, I study the passivation quality of a high-transparency Cat-CVD $SiN_x$ single layer ($n$ of ~ 2 at a wavelength of 630 nm) on c-Si. The obtained results demonstrate that passivation quality of the films is improved significantly by annealing. Samples prepared at lower substrate temperature during deposition ($T_s$) show more significant improvement in $\tau_{eff}$ by annealing, probably due to higher H content. The highest $\tau_{eff}$ obtained for the sample deposited at a $T_s$ of 100 $^{o}$C and a pressure ($P$) of 10 Pa is about 3 ms, corresponding to a $SRV_{max}$ of 5.0 cm/s.

## 3.2. Experimental procedure

### *3.2.1. Sample preparation*

After cleaning c-Si wafers in diluted (5%) HF solution to remove native oxide on c-Si surfaces, 100-nm-thick $SiN_x$ films were deposited by Cat-CVD. $SiN_x$ films with an approximately the same $n$ of ~ 2 at a wavelength of 630 nm were deposited at various $T_s$ and $P$. $SiN_x$ films were also deposited onto glass substrates for optical transmission measurements. I also formed 100-nm-thick $SiN_x$ films on quartz substrates to measure the defect density of the films. The deposition conditions of the $SiN_x$ films are summarized in Table 3.1.

***Table 3.1.*** *Deposition conditions of $SiN_x$ films. n and thickness of deposited films are also summarized.*

| Film | $SiH_4$ (sccm) | $NH_3$ (sccm) | Pressure (Pa) | $T_s$ ($^oC$) | $T_{cat}$ ($^oC$) | Deposition time (s) | $n$ | Thickness (nm) |
|---|---|---|---|---|---|---|---|---|
| 1 | 8.7 | 150 | 10 | 50 | 1800 | 144 | 2.01 | 103 |
| 2 | 8.4 | 150 | 10 | 70 | 1800 | 160 | 2.04 | 103 |
| 3 | 8.2 | 150 | 10 | 90 | 1800 | 180 | 2.02 | 103 |
| 4 | 8 | 150 | 10 | 100 | 1800 | 190 | 1.99 | 103 |
| 5 | 7 | 150 | 10 | 150 | 1800 | 220 | 2.01 | 98 |
| 6 | 6 | 150 | 10 | 200 | 1800 | 240 | 1.99 | 100 |
| 7 | 5.6 | 150 | 10 | 250 | 1800 | 250 | 2.06 | 102 |
| 8 | 5.3 | 150 | 10 | 300 | 1800 | 300 | 2.02 | 96 |
| 9 | 3 | 60 | 3.5 | 150 | 1800 | 520 | 2.01 | 102 |
| 10 | 5.5 | 150 | 7 | 150 | 1800 | 300 | 1.99 | 102 |
| 11 | 8.5 | 150 | 13 | 150 | 1800 | 180 | 2.02 | 101 |
| 12 | 9.5 | 150 | 15 | 150 | 1800 | 170 | 2.01 | 98 |
| 13 | 11.5 | 150 | 18 | 150 | 1800 | 130 | 2.01 | 105 |

To measure H content by FTIR, $SiN_x$ films with a thickness of about 100 nm were deposited on c-Si substrates with a high resistivity of 3460 Ωcm. The method used to calculate H content is the same as described in Chapter 2. $Q_f$ of $SiN_x$ films was calculated based on the results of C-V measurement for metal-insulator-semiconductor (MIS) structures. The sample structure and the method to calculate $Q_f$ are the same as described in Chapter 2. 100-nm-thick $SiN_x$ films were deposited on both sides of 290-μm-thick n-type (100) FZ Si wafers with a resistivity of 2.5 Ωcm to measure $\tau_{eff}$. Figure 3.1 shows the cross-sectional schematic of a sample for $\tau_{eff}$ measurement. The samples were then annealed in $N_2$ atmosphere to investigate the effect of annealing on the passivation quality of $SiN_x$ films.

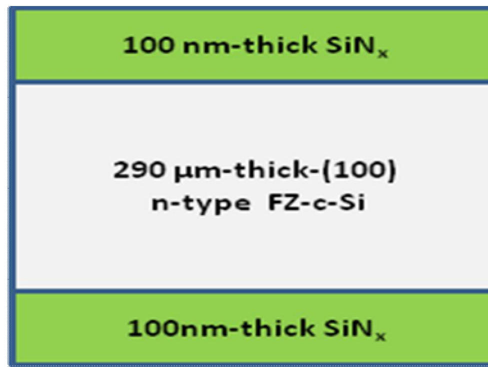


*Figure 3.1 Cross-sectional schematic of a sample for $\tau_{eff}$ measurement.*

### *3.2.2. Characterization of prepared samples*

The thickness and *n* of all the $SiN_x$ films were measured on J. A. Woollam, HS-190™ spectroscopic ellipsometry, using Cauchy model for data analysis. The film density was measured by X-ray reflectivity. Atomic contents of the $SiN_x$ films were measured by XPS. The transmission spectra of $SiN_x$ films were measured in a Shimadzu, UV-3150 ultraviolet-visible-near infrared spectrophotometer. Defect density of the $SiN_x$ films was calculated by using electron spin resonance (ESR). The details of the method and defect density calculation are given in Appendix B. In order to investigate the passivation quality of the $SiN_x$ layers on c-Si, I carried out μ-PCD measurement (Kobelco LTA-1510EP) using a 904 nm wavelength pulse laser with a photon density of $5\times10^{13}$ $cm^{-2}$. The method to determine $SRV_{max}$ has been described in the previous chapter.

Interface state density ($D_{it}$) of $SiN_x$/c-Si samples was estimated by using four methods: conductance method, Terman method, high-low frequency method, and low frequency method. I firstly estimated $D_{it}$ using Terman method, high-frequency C-V curves was obtained by using Keithley 6517A electrometer/high resistance meter and 6440B component analyzer. However, due to the limitation of this system, low frequency C-V shape curve could not be obtained. Therefore, for conductance method, I employed impedance measurement Solarstron 1296 and 1290 to obtain C-V curves.

## 3.3. Results and discussion

### *3.3.1. Chemical composition of $SiN_x$ films*

In order to form $SiN_x$ films with high transparency, I changed $SiH_4$ flow rate, substrate temperature ($T_s$) and gas pressure ($P$), as shown in Table 3.1. The variation of these factors will change Si and N content in $SiN_x$ films. I firstly measured chemical composition of these films. The chemical composition of $SiN_x$ films at various $T_s$ and $P$ are shown in Figure 3.2. Si content in the films decreases with increase in $T_s$ or decrease in $P$. Note that $SiH_4$ flow rate was also changed together with $T_s$ or $P$ to keep the $n$ of $SiN_x$ films to be ~2. Increase or decrease in Si content can thus be related to the change of $SiH_4$ gas flow rate during $SiN_x$ deposition.

Figure 3.3 describes [Si]/[N] composition ratio of $SiN_x$ films deposited at various $P$ and $T_s$. One can see all the samples show [Si]/[N]<1.33 and are thus not Si-rich $SiN_x$. All the samples have high optical transparency, as shown in Figure 3.4. The small difference and the shift of maximum peak may be due to the slight difference in thickness and/or $n$ of the samples (see Table 3.1). After the confirmation of the high-transparency property of the $SiN_x$ films, in the next step, I will examine the passivation quality of these layers on n-type c-Si.

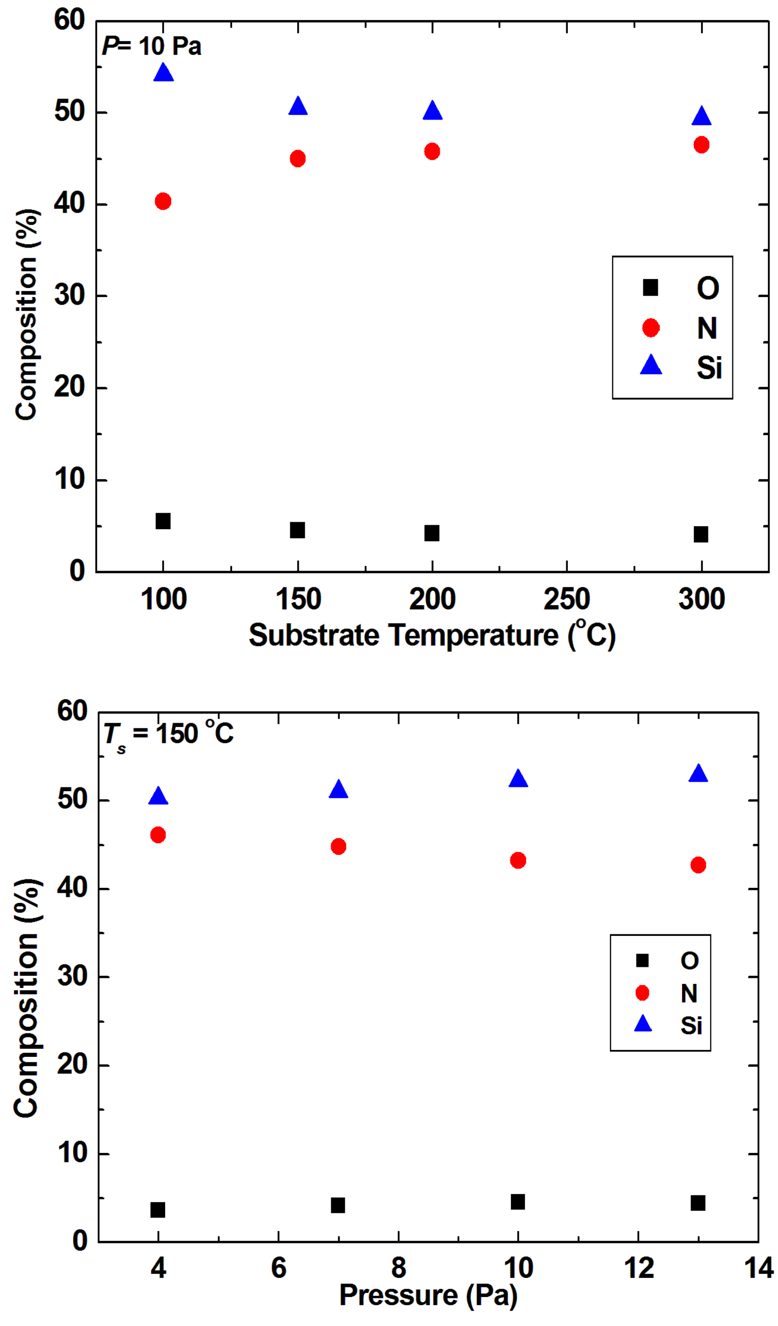


*Figure 3.2 Chemical composition of $SiN_x$ films deposited at various $T_s$ and P.*

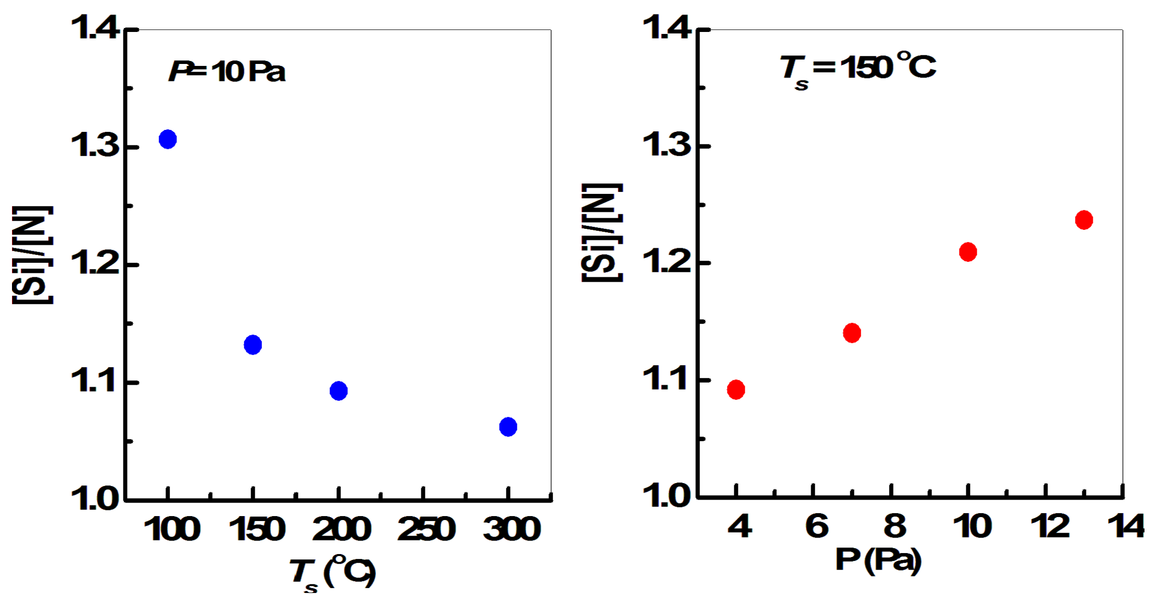


*Figure 3.3 [Si]/[N] composition ratio of $SiN_x$ films deposited at various P and $T_s$.*

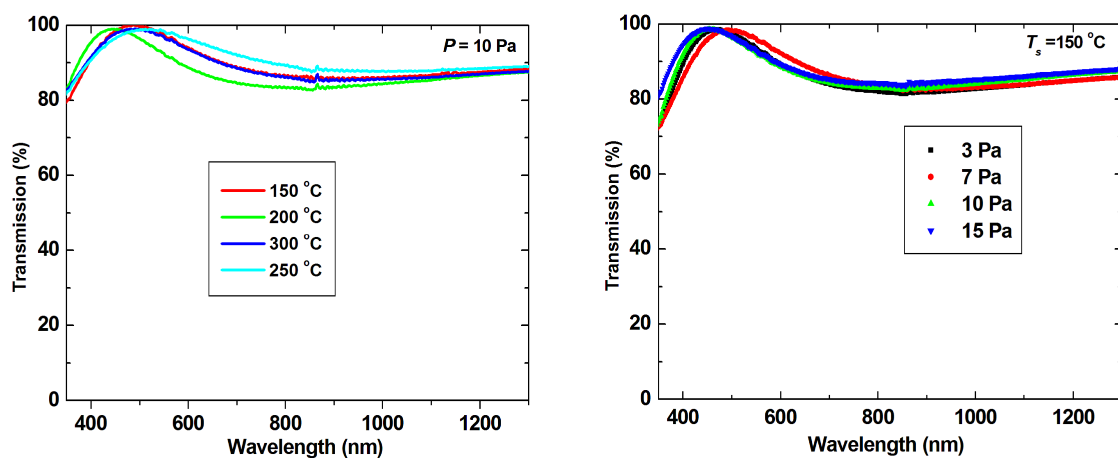


*Figure 3.4 Transmission spectra of $SiN_x$ films deposited at various $T_s$ and P.*

### 3.3.2. Passivation quality of $SiN_x$ films on c-Si wafers

The passivation quality of $SiN_x$ films on c-Si has been investigated by many researchers [6-29]. Sputtering $SiN_x$ film with excellent homogeneity, high-film density silane-free process and long-service cycle is promising-coating layer [27]. It has been used as passivation layer for c-Si solar cell fabrication and efficiency of 17.5% is obtained. Passivation quality of the sputtering films is not as high as PECVD method [28]. It is reported that addition of $H_2$ gas during sputtering can slight increase in passivation quality. However, there is also report that $H_2$ gas does not make any positive effect on improving passivation quality but also causes blister to $SiN_x$ films [29]. Therefore, it is not suitable to passivate surface which need high passivation quality film such as multi-crystalline Si solar cells. Most of $SiN_x$ films were prepared by PECVD and low SRVs have been achieved. It has been reported that a low *SRV* of 3.8 cm/s can be achieved when stoichiometric PECVD $SiN_x$ films are deposited on 3-5 Ωcm n-type Si wafers [11]. Schmidt *et al.* have achieved a *SRV* lower than 10 cm/s for 1.5 Ωcm p-type Si wafers passivated by stoichiometric $SiN_x$ films [14]. Like PECVD films, Cat-CVD $SiN_x$ films are formed by using $SiH_4$ and $NH_3$ gas sources. Therefore, film properties such as composition and H content in films are easily controlled by changing deposition condition such as gas flow rate, pressure… Cat-CVD $SiN_x$ films are found to have lower H content, higher density and thus, lower film stress compared to PECVD $SiN_x$ films. The Cat-CVD film properties are supposed to be superior to those of PECVD [10]. Due to advantages of the films, Cat-CVD $SiN_x$ with high passivation quality to c-Si would be expected. There are, however, few reports for the passivation of c-Si surfaces using Cat-CVD $SiN_x$ films [16, 17]. The work of Cat-CVD $SiN_x$/c-Si was already published from our institute in 2003 [17]. However, at that time, the effect of annealing and the role of H content in the films were not noticed, and the results obtained are not sufficiently good.

The effect of annealing on the passivation quality of various $SiN_x$ films has also been reported by many authors [9, 23, 24]. It is demonstrated that the rearrangement of $SiN_x$ network structure and H diffusion during annealing can terminate defects on a $SiN_x$/c-Si interface, which results in improvement in passivation quality. In my previous study, I also found that the passivation quality of Cat-CVD $SiN_x$/Si-rich $SiN_x$ films on a c-Si wafer is enhanced significantly after annealing [4,5]. In this study, I thus firstly

investigate the effect of annealing temperature ($T_a$) and annealing time ($t_a$) on the passivation quality of stoichiometric $SiN_x$ single films on c-Si wafers.

Figure 3.5 shows $SRV_{max}$ of $SiN_x$ films deposited at $T_s$ of 50, 100, and 150 °C at a fixed $P$ of 10 Pa, and their H concentration deposited at a $T_s$ of 150 °C as a function of $T_a$ with a fixed duration of 30 min. $SRV_{max}$ decreases with increase in $T_a$, reaches the minimum value, and then increases. The reduction in $SRV_{max}$ with $T_a$ may be related to the diffusion of H atoms from the films and the termination of defects on a $SiN_x$/c-Si interface by the H atoms during annealing. $T_a$ of 350 °C might be a proper temperature to support sufficient energy for H diffusion and defect termination, resulting in the formation of a good-quality $SiN_x$/c-Si interface.

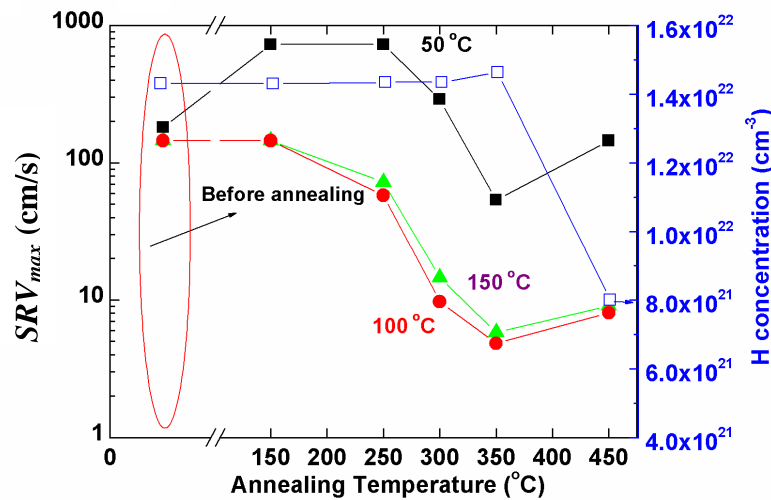


*Figure 3.5 $SRV_{max}$ of $SiN_x$ films deposited at $T_s$ of 50, 100, and 150 °C at a fixed P of 10 Pa. The blue-colored data shows H concentration of those films deposited at a $T_s$ of 150 °C as a function of $T_a$ with a fixed duration of 30 min.*

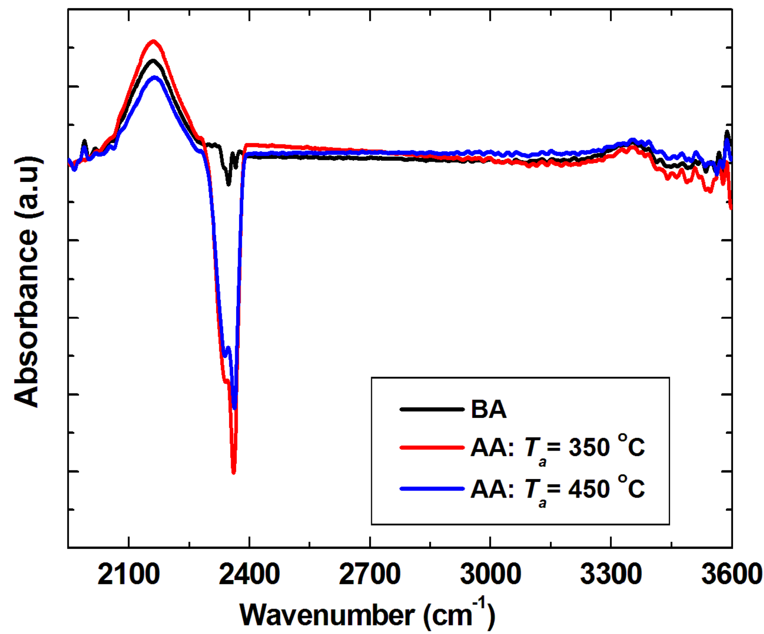


*Figure 3.6  FTIR spectra of $SiN_x$ films deposited at a $T_s$ of 150 °C annealed at various $T_a$ for 30 min.*

Figure 3.6 shows the FTIR spectra of $SiN_x$ films deposited at a $T_s$ of 150 °C at various $T_a$ for 30 min. Increase in H content after annealing at 350 °C, shown in the FTIR spectra, indicates increase in the number of Si-H bonds. This suggests that, during annealing, H atoms combine with Si defects inside $SiN_x$ films, and H atoms existing near the $SiN_x$/c-Si interface and/or inside the $SiN_x$ film diffuse to a c-Si substrate and recombine with dangling bonds on a c-Si surface. However, at excessively high $T_a$, H atoms can be released to environment and do not terminate defects, and *SRV* becomes high [15-25]. As shown in Figures 3.5 and 3.6, H concentration and Si-H bonding density decrease dramatically at a $T_a$ of 450 °C, which is a clear evidence for H loss to environment.

The passivation quality of $SiN_x$ films can be stable for long time annealing, as shown in Figure 3.7. Degradation of passivation quality for very long $t_a$ may be due to H desorption caused by the breaking of Si-H and N-H bonds. In the next steps, I used a $T_a$ of 350 °C and a $t_a$ of 30 min as optimized annealing conditions for high passivation quality after annealing.

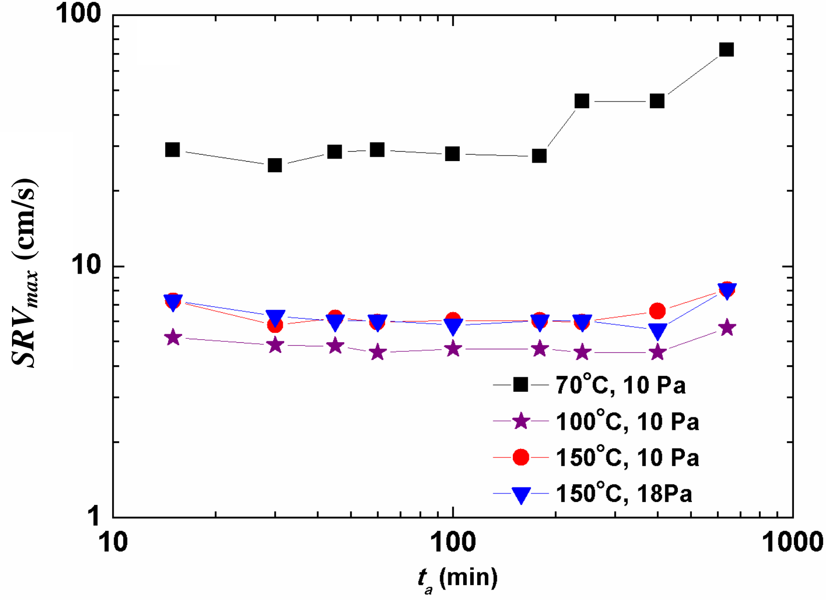


*Figure 3.7 $SRV_{max}$ as a function of $t_a$ at a $T_a$ of 350 °C.*

Figure 3.8 shows $SRV_{max}$ of c-Si wafers with $SiN_x$ films as functions of $T_s$ and $P$ before and after annealing at a $T_a$ of 350 °C for 30 min. $SRV_{max}$ of an as-deposited film before annealing decreases with increase in $T_s$, while increases with increase in $P$. The high $SRV_{max}$ obtained at low $T_s$ is considered to be due to low film quality or the effect of etching by atomic H, which is known to occur more significantly at lower $T_s$ [26]. The effect of etching may be negligible, because at low $T_s$ with high deposition rate, the rapid covering of a c-Si surface with a $SiN_x$ film can suppress H etching effect. In order to confirm it experimentally, the surface morphology of c-Si samples was observed by AFM. I firstly deposited a $SiN_x$ film at a $T_s$ of 100 °C, and the $SiN_x$ film was then removed by diluted HF (30%). After 5 seconds, the $SiN_x$ was completely removed. The removal of $SiN_x$ was confirmed by spectroscopic ellipsometry. Figure 3.9 shows the AFM image of c-Si surfaces after removing the $SiN_x$ film. The morphology of a c-Si surface etched by diluted HF is also shown for comparison. For the sample without a $SiN_x$ film, a root-mean-square roughness ($R_{rms}$) is 0.095 nm while for the sample with $SiN_x$ deposition, $R_{rms}$ is 0.15 nm. One can see that etching occurs during $SiN_x$ deposition, which is, however, not so serious. The fact that a low $SRV_{max}$ of 5 cm/s is obtained proves that the effect of etching by atomic hydrogen may be negligible.

However, films deposited with a high deposition rate (at low $T_s$ and high $P$) might leads to the insufficient coverage of c-Si surface, resulting in increase in $SRV_{max}$. The

reason of high $SRV_{max}$ under these conditions can also be explained by low $Q_f$, which will be discussed later. Figure 3.8 also shows that $SRV_{max}$ is improved significantly after annealing. For the annealed samples, $SRV_{max}$ reaches its lowest value at $T_s$ of 100 °C, then it increases with increase in $T_s$, while $SRV_{max}$ decreases with increase of $P$ and reaches a saturated value at $P \geq 10$ Pa. $\tau_{eff}$ obtained for the as-deposited sample at a $T_s$ of 100 °C and a $P$ of 10 Pa is about 0.1 ms, corresponding to a $SRV_{max}$ of 144 cm/s. $\tau_{eff}$ of the same samples increases up to 3 ms after annealing, which corresponds to a $SRV_{max}$ of 5.0 cm/s.

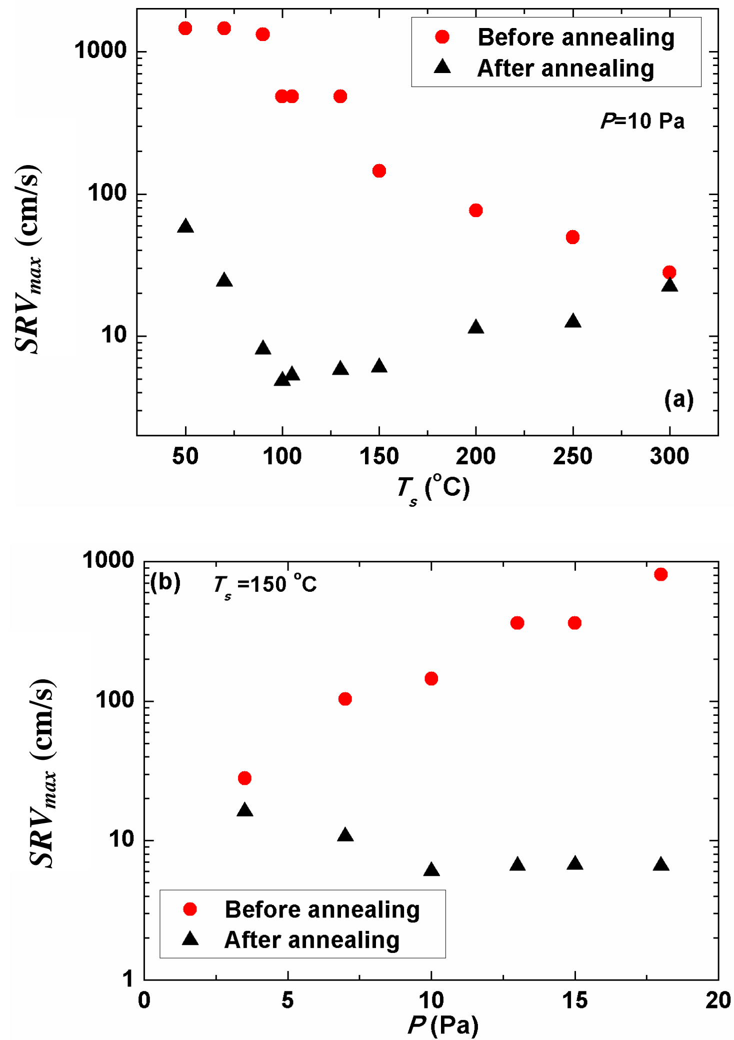


*Figure 3.8 $SRV_{max}$ as functions of (a) $T_s$ and (b) P before and after annealing at a $T_a$ of 350 °C for 30 min in $N_2$ atmosphere.*

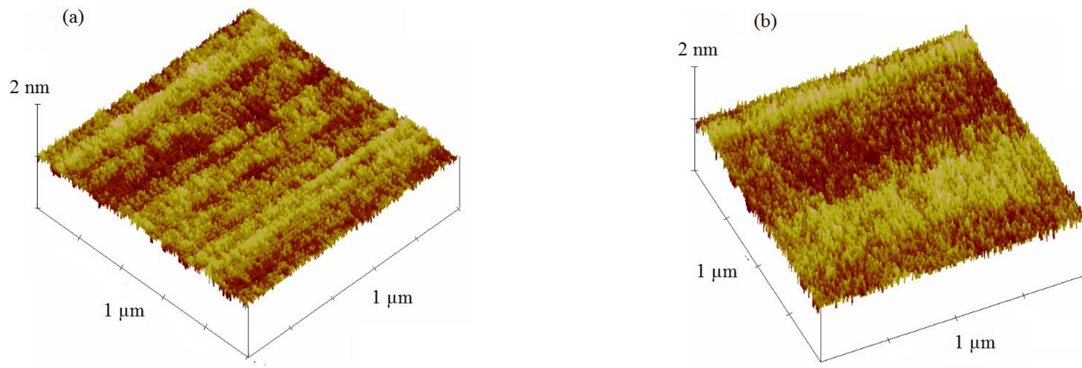


*Figure 3.9. Surface morphology of (a) c-Si etched by HF 30% for 5 s.*

*(b)c-Si after $SiN_x$ removing by HF 30% for 5 s.*

Figure 3.10 shows the optical transmission spectra of $SiN_x$ films deposited at a $T_s$ of 150 °C and a $P$ of 10 Pa before and after annealing at a $T_a$ of 350 °C for 30 min. The appearance of fringe in transmission spectra is probably due to the effect of interference. I also plotted the simulated transmission spectrum of the $SiN_x$ film evaluated by using Beer's equation [30]:

$$I = I_o \exp(-\alpha \times d),$$

where absorption coefficient (α) and film thickness ($d$) obtained by analyzing spectroscopic ellipsometry data using by the Cauchy mode are used. The stoichiometric $SiN_x$ films show sufficiently high optical transmission even in short wavelength region, unlike the case of a-Si or Si-rich $SiN_x$ films [3, 4]. Furthermore, the transparency of the films does not significantly change by annealing. The very small difference in the transparency in a short wavelength region might be related to the slight change of network structures such as Si-H bonds by annealing. The improvement in the passivation quality of stoichiometric $SiN_x$ films without decreasing transparency after annealing is of great advantage for the application of the films in c-Si solar cell fabrication.

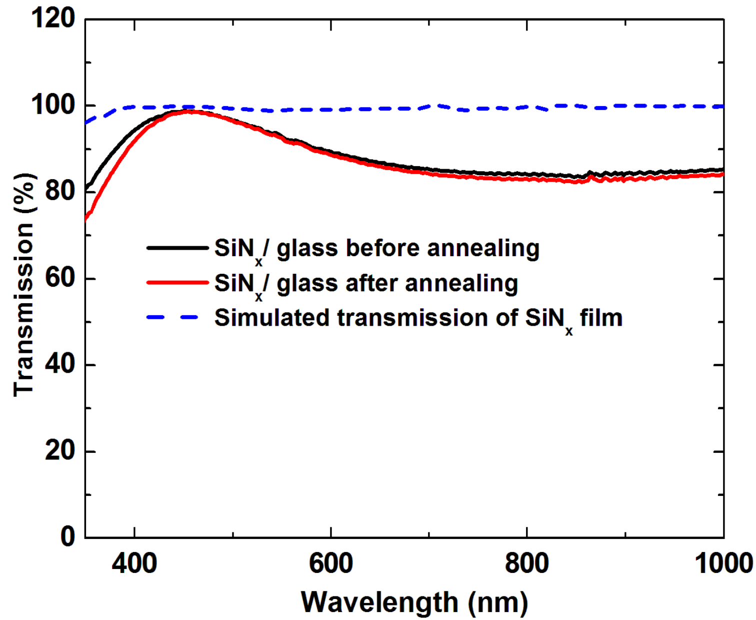


*Figure 3.10 Transmission spectra of $SiN_x$ films deposited at a $T_s$ of 150 $^oC$ and a P of 10 Pa before and after annealing at a $T_a$ of 350 $^oC$ for 30 min. The simulated transmission spectrum of the $SiN_x$ film is also shown.*

### 3.3.3. Role of H content and fixed charge density on passivation quality of films

In order to investigate the origin of the high passivation quality of $SiN_x$ films, I evaluated H content and $Q_f$ in the films [6, 12, 15]. Positive fixed charges send minority carriers (holes) back away from an n-type c-Si surface. They can therefore reduce the trapping probability of minority carriers (holes) at defects near the c-Si surface. Another way to reduce recombination is the termination of defects by H atoms.

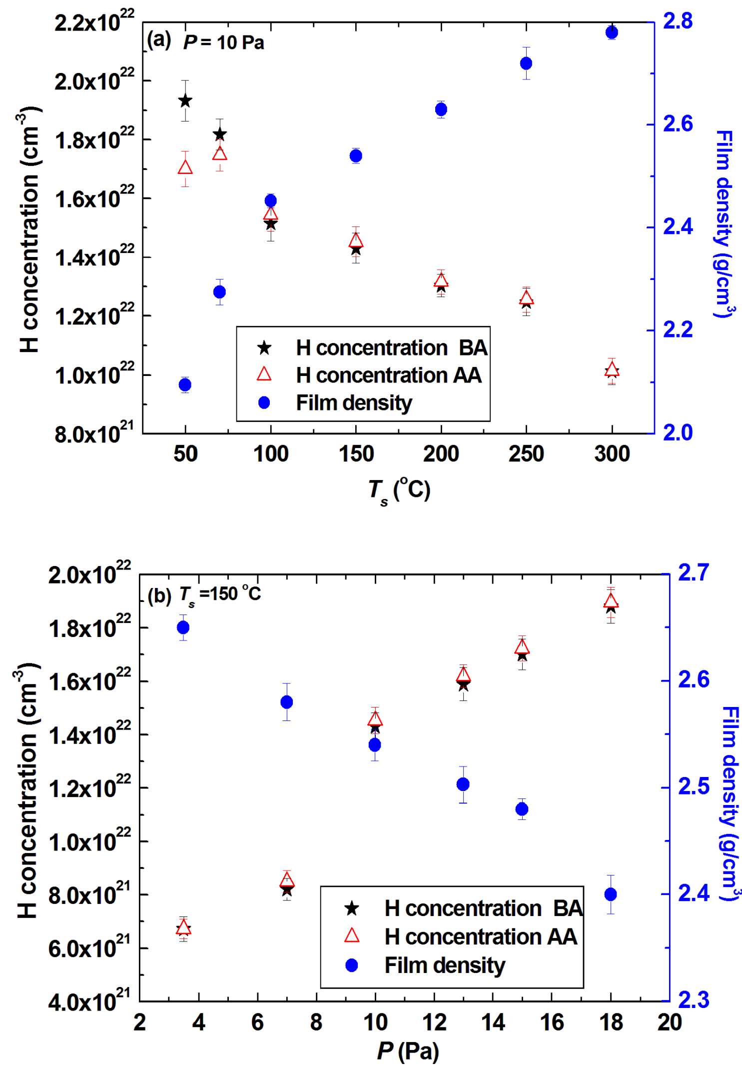


*Figure 3.11 Film density and H concentration of $SiN_x$ films before and after annealing at a $T_a$ of 350 °C for 30 min as functions of $T_s$ and P.*

Figure 3.11 shows $SiN_x$ film density and H concentration in $SiN_x$ films before and after annealing at a $T_a$ of 350 °C for 30 min as functions of $T_s$ and *P*. H concentration of $SiN_x$ films were determined from FTIR spectra, parts of which are shown in Figure 3.12. H concentration in $SiN_x$ films decreases with increase in $T_s$, which is probably due to more enhanced H desorption during deposition at higher $T_s$. Higher *P* leads to the inclusion of larger amount of H in $SiN_x$ films, while Si-H/N-H bond density ratio is kept almost constant. Compared to $SiN_x$ films deposited at higher $T_s$, the $SiN_x$ film deposited at a $T_s$ of 50 °C have a Si-H peak shifted to lower wavenumber. This might be related to the lower electro-negativity of backboned Si atoms for $SiN_x$ films with lower N content [31]. The number of Si-H bonds increases much with decrease in $T_s$ and increase in *P*, while that of

N-H bonds slightly increases with increase in $T_s$ and $P$. The samples with high H content show more effective decrease in $SRV_{max}$ by annealing, and H may contribute to improvement in passivation quality. Sample prepared at $T_s$ <100 °C exceptionally shows less significant improvement in passivation quality even with higher H content. This may be due to low film density. During annealing, low-density materials would release H in the molecular form, while denser films would make H desorption slower [16, 31]. Here, $SiN_x$ film density is ~2.1 g/cm$^3$ for the sample deposited at $T_s$ of 50 °C, while it is more than 2.4 g/cm$^3$ for the sample deposited at $T_s \geq$ 100 °C, as shown in Figure 3.11. H atoms might thus be released to atmosphere during annealing and not contribute to the passivation of a c-Si surface, resulting in a high $SRV_{max}$. Samples formed at higher $T_s$ with much higher film density can suppress H desorption, and H atoms can significantly contribute to passivating defects on a c-Si surface. I also similarly explain improvement in passivation quality after annealing samples deposited at various $P$. Improvement in film passivation quality may be related to H concentration and density of the films. Most of films deposited at various $P$ have sufficiently high film density and samples deposited at higher $P$ have higher H concentration, and passivation quality is improved more significantly after annealing for $SiN_x$ films deposited at high $P$.

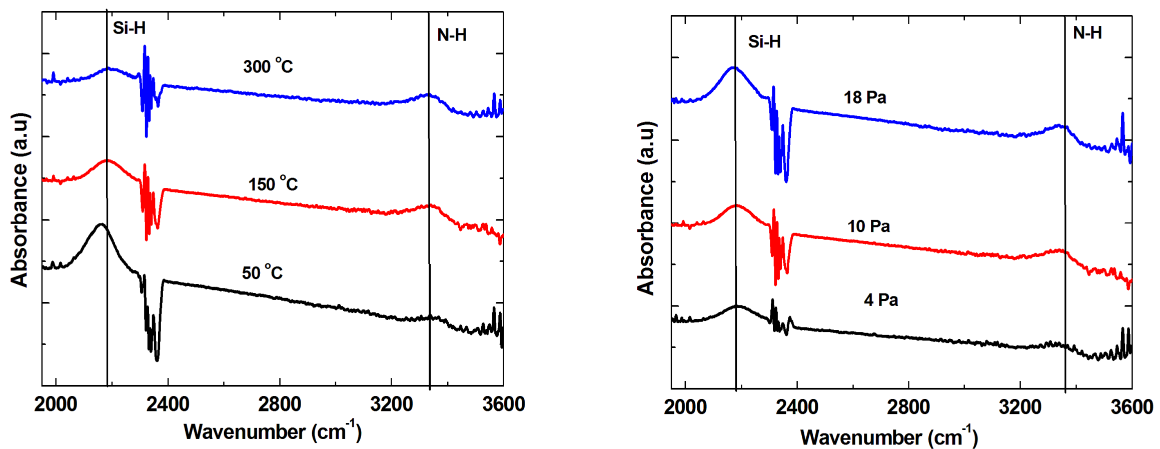


*Figure 3.12 FTIR spectra of $SiN_x$ films deposited at various $T_s$ (P=10 Pa) and P ($T_s$=150 °C).*

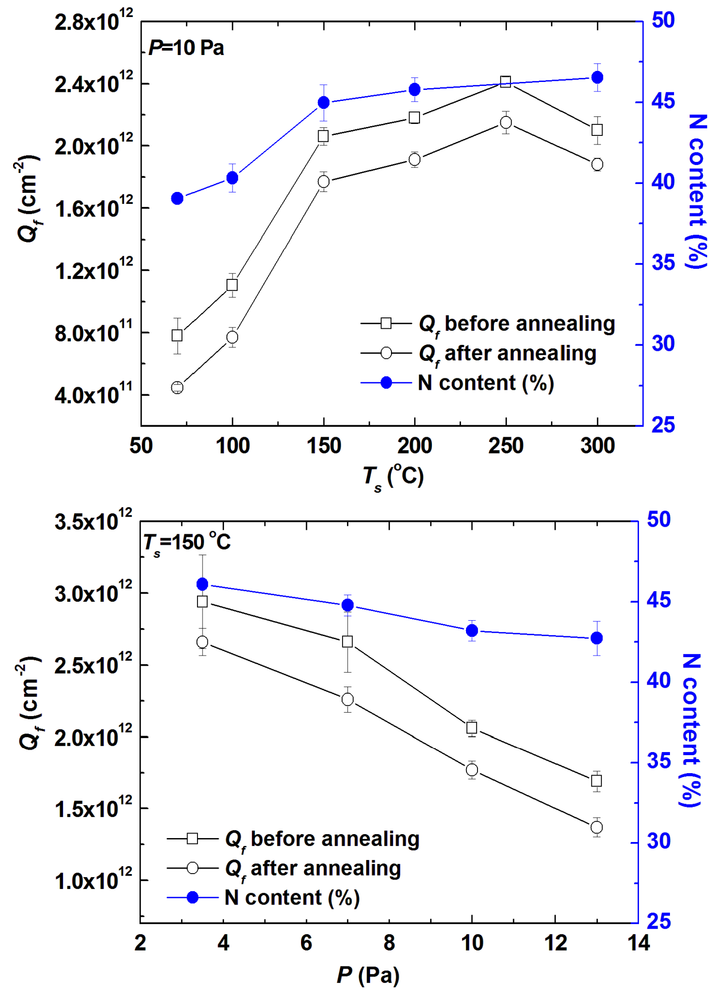


*Figure 3.13 N content and $Q_f$ of $SiN_x$ films as functions of $T_s$ and P before and after annealing at a $T_a$ of 350 °C for 30 min.*

Figure 3.13 shows N content and $Q_f$ of $SiN_x$ films as functions of $T_s$ and $P$ before and after annealing at a $T_a$ of 350 °C for 30 min. $Q_f$ increases with increase in $T_s$, and reaches highest value at a $T_s$ of 250 °C, then it slightly decreases at 300 °C. $Q_f$ of $7.5\times10^{11}$ $cm^{-2}$ is quite low for the $SiN_x$ films deposited at $T_s$ of 50 °C, which can be one of the possible reasons to explain high $SRV_{max}$ for the sample deposited at low $T_s$ and high $P$, as shown in Figure 3.8. N content increases with increasing $T_s$ or decreasing $P$. It may be correlative to film density, which is related to the migration of radicals on c-Si surface during film deposition. The origin of fixed charges is known to be Si-dangling bond defects whose configuration is $N_3 \equiv Si^+$ in $SiN_x$ films, generally called $K^+$ centers [15, 21, 32, 33]. From Figure 3.13, one can also see that $Q_f$ is proportional to N content in films. It is in good agreement with the suggestion of the origin of fixed charges as mentioned above.

Decrease in $Q_f$ at a $T_s$ of 300 $^{o}$C might be related to decrease in Si dangling bonds in $SiN_x$ films when they were deposited at sufficiently high $T_s$.

Figure 3.14 shows H distribution in $SiN_x$ films deposited at $T_s$ of 100 $^{o}$C before and after annealing at 350 $^{o}$C for 30 min. The profiles were obtained by secondary ion mass spectroscopy (SIMS). One can see that there is no difference in H concentration for sample before and after annealing. It is noted that H concentration calculated in previous part is relied on Si-H and N-H bonds in $SiN_x$ measured by FTIR spectra. Si-H bonds increases when sample is annealed at 350 $^{o}$C, H concentration thus increases. The obtained results suggest that not diffusion but the bonding –rearrangement during annealing assists defect termination, resulting in improvement in passivation quality. In order to confirmation of defect termination by annealing, in next part, I will investigate defect density in $SiN_x$ films and interface state density at $SiN_x$/c-Si interface.

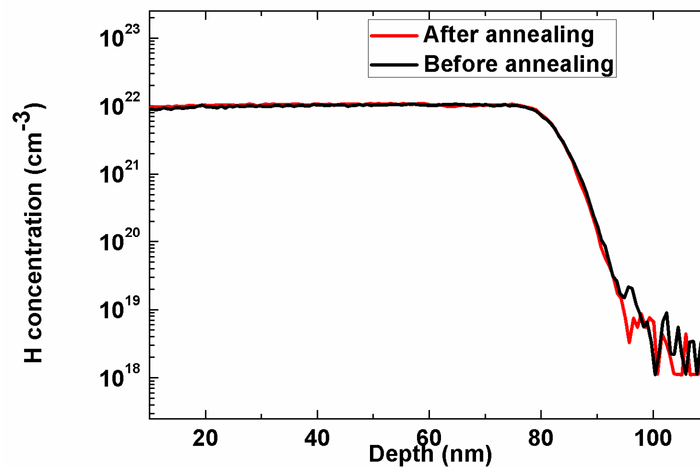


*Figure 3.14. H profiles of SiNx films deposited at 100 $^{o}$C before and after annealing at 350 $^{o}$C.*

Figure 3.15 shows the defect density of $SiN_x$ films as functions of $T_s$ and $P$ before and after annealing at a $T_a$ of 350 $^{o}$C for 30 min. One can see lower defect density at higher $T_s$. One possible reason for this tendency is more enhanced migration of radicals on a c-Si surface during film deposition at higher $T_s$. Dangling bonds in $SiN_x$ films are related to Si-dangling bonds back bonded to three N atoms, $N_3$≡Si·, generally called $K^0$ centers, which contain an unpaired electron and are observable by ESR [12, 13, 34]. The g value reported for the $K^0$ defects is 2.003. The g value for a-Si of 2.0055 is reported by Street [35]. In this study, the g value obtained is 2.0033~2.0047 for $SiN_x$ samples. For sample deposited at

100 $^{o}$C, g value is 2.0033 for both as-deposited and annealed samples. The shift in g value obtained in thus study implies that defects observed by ESR for $SiN_x$ films are both $K^0$ dangling bonds and dangling bonds exiting in i-a-Si films. The defect density of $SiN_x$ films deposited at low $T_s$ may thus be related to N content in the films. Defect density of the $SiN_x$ film deposited at low $T_s$ is relatively low, and higher $P$ leads to lower defect density, as shown in Figure 3.15. These trends are the same as those of N content in $SiN_x$ films. It has been reported, by Lelièvre *et al.*, that H atoms can combine with Si-dangling bond defects ($K^+$ centers) during annealing, resulting in the formation of neutralized dangling bonds (K centers) [15]. Other group has also reported that $K^0$ centers will be converted to $K^+$ and $K^-$ centers by annealing [30]. In this study, defect density ($K^0$ centers) and fixed charge $K^+$ decreases significantly by annealing, as shown in Figures 3.13 and 15. These are clear evidences of defect termination by H in $SiN_x$ films during annealing. I guess that H can terminate defects not only inside $SiN_x$ but also on a $SiN_x$/c-Si interface during annealing, and $SRV_{max}$ decreases significantly by annealing. The samples with lower film density and higher H content show small change in $Q_f$ and defect density by annealing, as shown in Figures 3.11 and 13. This may be because denser films can prevent more hydrogen atoms from releasing to atmosphere during annealing, which results in more H atoms combine with Si-dangling bonds in $SiN_x$ films, and more decrease in $Q_f$ and defect density. This consideration cannot explain the change of defect density and $Q_f$ by annealing for samples deposited at high $T_s$. The difference of H content in the films might be related to this phenomenon.

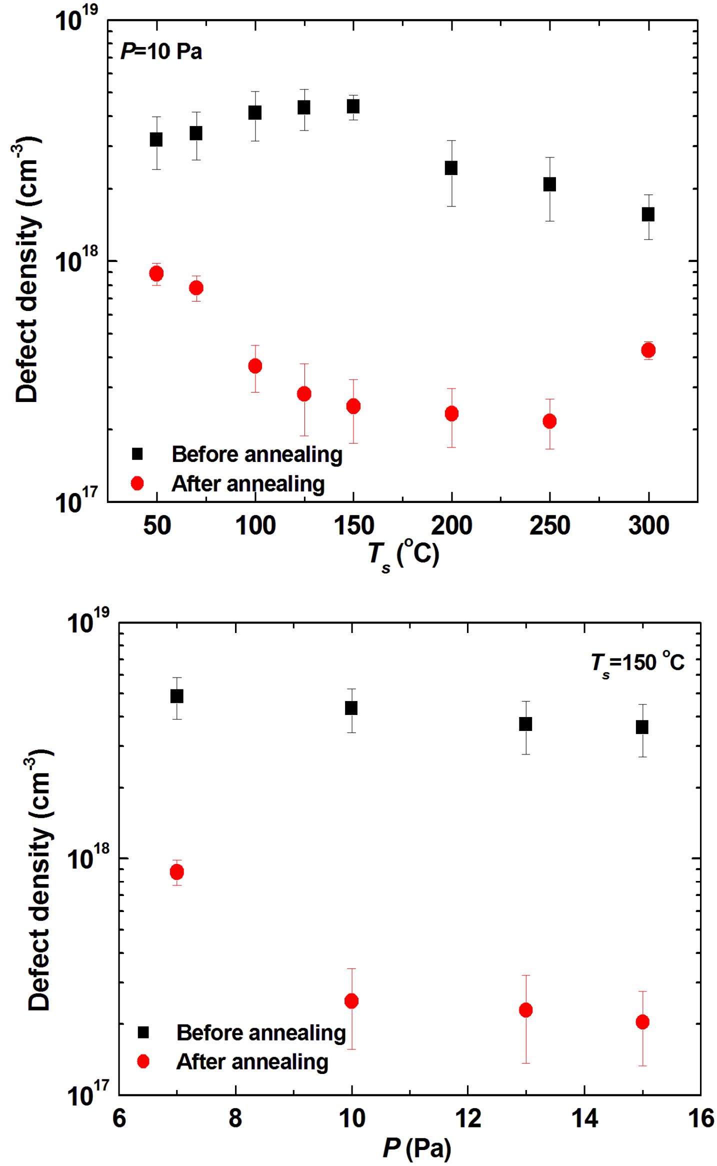


*Figure 3.15 Defect density of $SiN_x$ films as functions of $T_s$ and P before and after annealing at a $T_a$ of 350 °C for 30 min.*

Finally, I discuss the origin of remarkably low $SRV_{max}$ of Si wafers passivated with $SiN_x$ films. The value of $Q_f$ on the order of $10^{12}$ $cm^{-2}$ is high enough to induce field-effect passivation. Fixed charge in $SiN_x$ films can thus partially contribute to suppression in surface recombination. $Q_f$, however, decreases after annealing, while film passivation quality is significantly improved by annealing. This fact indicates that not $Q_f$ but defect termination by H atoms mainly contributes to improvement in the passivation quality of $SiN_x$ films, which is consistent with our previous results shown in the previous chapter [5].

### 3.3.4. Interface state density of $SiN_x$/c-Si structures

In order to demonstrate more clearly the effect of defect termination by H atoms on the passivation quality of $SiN_x$ films on a c-Si surface, I estimated $D_{it}$ of these samples from their C-V curves by using the following three methods: Terman method, conductance method, and low frequency method [36-39]. Details of three methods are summarized in Appendix A-10. Matlab codes using for calculation are also given there. However, for both low frequency and conductance method, the samples before and after annealing do not show so much different $D_{it}$. $D_{it}$ obtained for sample before and after annealing is $5.6\times 10^{11}$ and $6.8\times10^{11}$ $eV^{-1}cm^{-2}$, respectively. The value after annealing is comparable with value reported by other groups, at which the high $\tau_{eff}$ obtained for $SiN_x$/c-Si [40-42], but the one before annealing is not consistent with low $\tau_{eff}$. It may be because the accumulation capacitance of the sample before annealing varies greatly when frequency changes. Although corrected capacitance and conductance are taken into account, the result obtained is still unreasonable. See Appendix A-10 for more detail about this calculation and limitation problem.

Terman method may give the best simulation result for my samples. Frequency used for the calculation is 1 MHz. According to the analysis results by Terman method, $D_{it}$ of the sample before annealing is on the order of $10^{12}$ $eV^{-1}cm^{-2}$, while $D_{it}$ after annealing is on the order of $10^{11}$ $eV^{-1}cm^{-2}$. Figures 3.16 and 18 shows $D_{it-average}$ as a function of surface potential for $SiN_x$ samples deposited at 70 $^{o}$C and 100 $^{o}$C before and after annealing. $D_{it-average}$ is estimated as average $D_{it}$ values in low $D_{it}$ region from calculated $D_{it}$ - surface potential curve. One can see a significant decrease in $D_{it-average}$ for the samples after annealing. It is in agreement with the explanation of improvement in passivation quality. Figures 3.17 and 3.19 shows the experimental and theoretical C-V curves of the samples deposited at 70 and 100 °C before and after annealing. The theoretical C-V curves are drawn under the assumption of no $D_{it}$. One can see good overlap of the theoretical and experimental curves only for the samples after annealing. In particular, in the case of the sample deposited at 100 $^{o}$C which demonstrates low $SRV_{max}$ of 5 ms after annealing, the experimental and ideal C-V curves show the best coincidence and $D_{it-average}$ calculated is $1.0\times10^{11}$ $eV^{-1}cm^{-2}$. $SRV_{max}$ as a function of $D_{it-average}$ of the $SiN_x$/c-Si samples deposited at various $T_s$ before and after annealing at 350 $^{o}$C for 30 min are ploted in Figure 3.20. For the samples before annealing with large $SRV_{max}$, $D_{it-average}$ are on the order of $10^{12}$ $eV^{-1}cm^{-2}$.

$D_{it\text{-}average}$ decreases to the order of $10^{11}$ $eV^{-1}cm^{-2}$ after annealing, at which low $SRV_{max}$ less than 10 cm/s can be obtained. This fact strongly supports the suggestion that H atoms terminate defects at $SiN_x$/c-Si interface, resulting in low $SRV_{max}$ by annealing.

Figure 3.21 shows experimental results obtained by Wan *et al.* [36]. The dependence of $SRV_{max}$ on $D_{it}$ at mid-gap and $Q_f$ of $SiN_x$/c-Si samples are summarized in this graph. $D_{it}$ at mid-gap is calculated by using Terman method. From this data, one can see that $SRV_{max}$ becomes less than 10 cm/s when $D_{it}$ is around $10^{11}$ $eV^{-1}cm^{-2}$ and $Q_f \sim 10^{12}$ $cm^{-2}$. $SRV_{max}$ >100 cm/s corresponds to $D_{it} > 10^{12}$ $eV^{-1}cm^{-2}$. These are consistent with $D_{it}$ and $SRV_{max}$ obtained in my study.

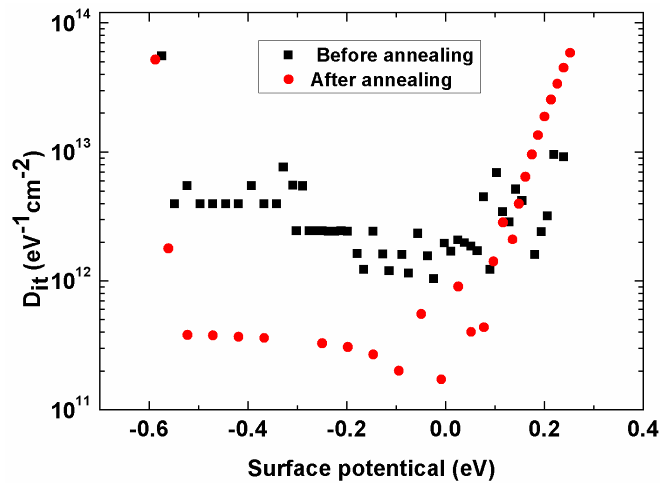


*Figure 3.16 $D_{it}$ of the sample deposited at 70 $^{o}$C as a function of surface potential .*

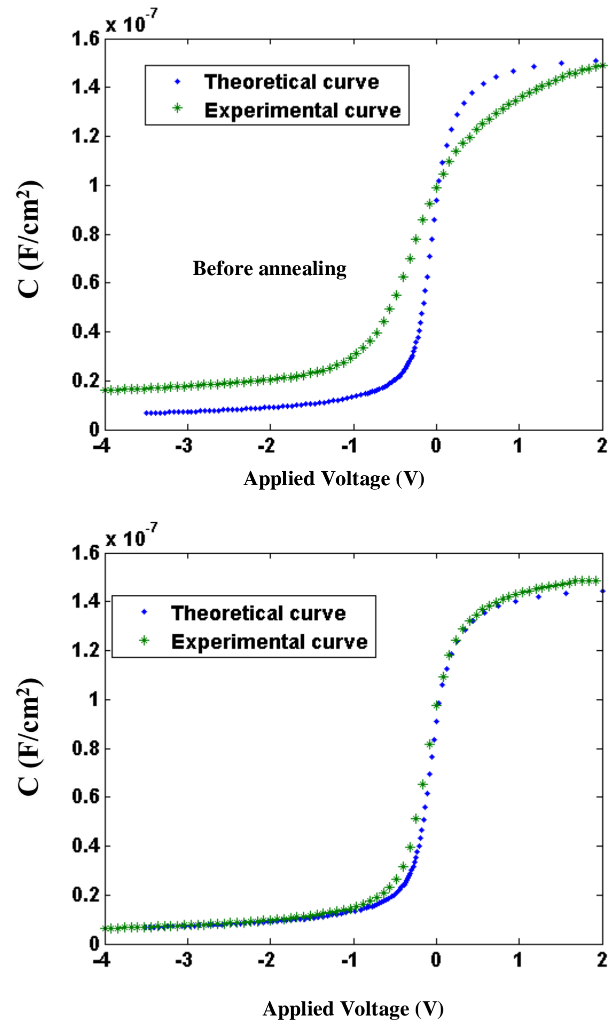


*Figure 3.17 C-V curves of the sample deposited at 70 $^{o}$C before and after annealing. Blue dot line is theoretical curve and green one is experimental curve.*

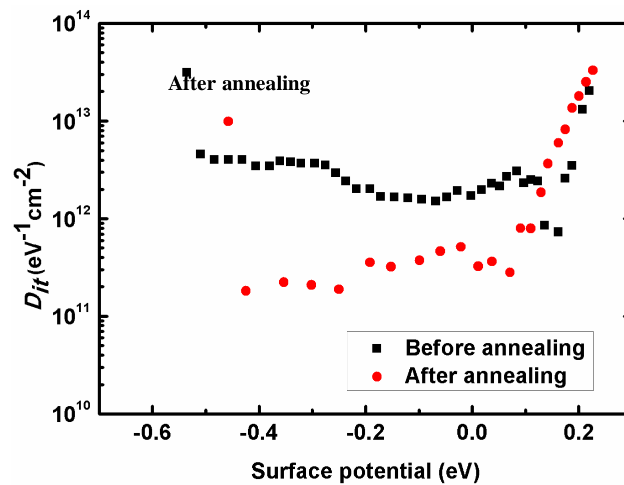


*Figure 3.18 $D_{it}$ of the sample deposited at 100 $^{o}$C as a function of surface potential.*

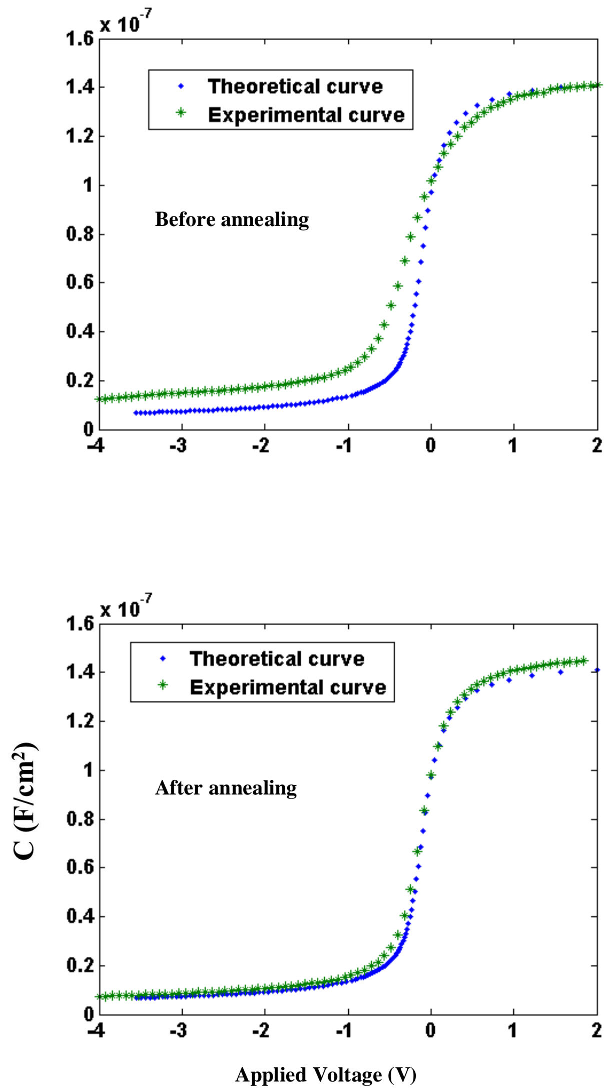


*Figure 3.19 C-V curves of the sample deposited at substrate temperature of 100 $^oC$ before and after annealing. Blue dot line is theoretical curve and green one is experimental curve.*

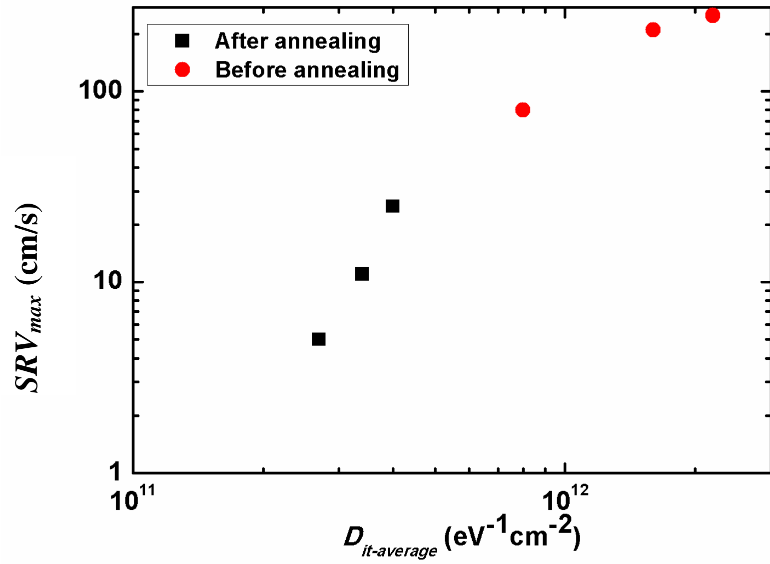


*Figure 3.20. $SRV_{max}$ as function of $D_{it\text{-}average}$ for $SiN_x$/c-Si samples before and after annealing.*

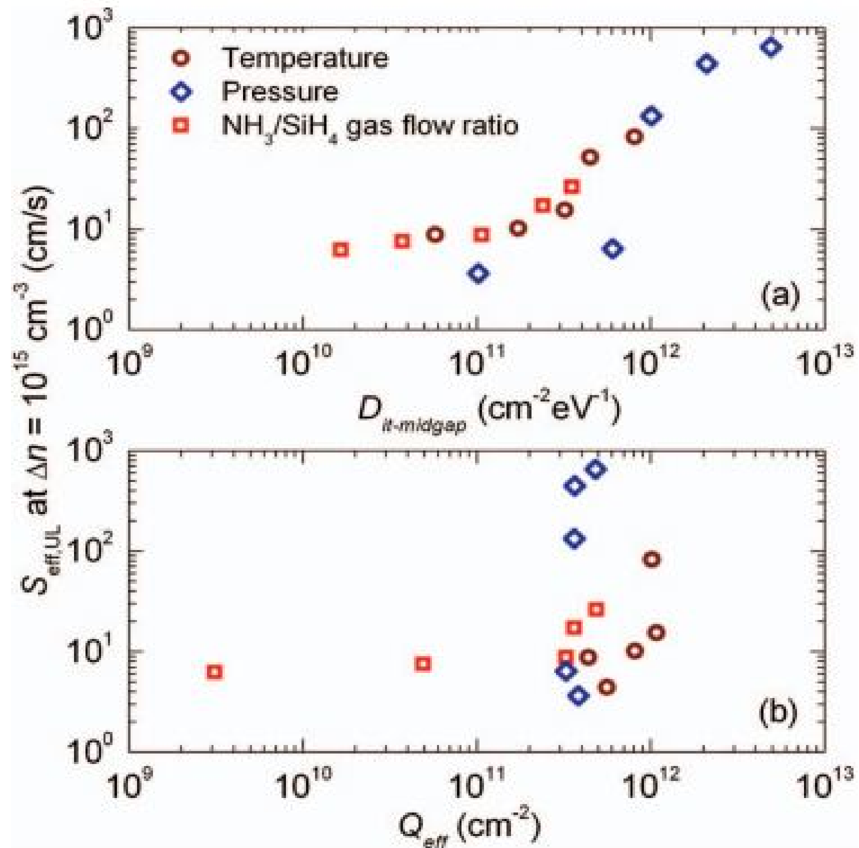


*Figure 3.21 $SRV_{max}$ (or $S_{eff,UL}$) as a function of $Q_f$ and $D_{it}$ at mid-gap of $SiN_x$/c-Si samples. (Experimental data from various $SiN_x$ deposition conditions) [35].*

### 3.4. Conclusions

Stoichiometric $SiN_x$ single films prepared by Cat-CVD have good passivation quality on c-Si wafers. Samples prepared at lower $T_s$ and high $P$ show more significant improvement in film passivation quality by annealing. The possible reason for this effect is related to the diffusion of H atoms in the films and the termination of defects on a $SiN_x$/c-Si interface by H atoms during annealing. H content in samples deposited at low $T_s$ or high $P$ is high, and more H atoms can contribute to SRV suppression. H content in the films thus plays an important role on improving passivation quality. Fixed charges in $SiN_x$ layers may affect the passivation quality of the films before annealing, while it does not contribute to improving $SiN_x$ film passivation quality after annealing. The highest $\tau_{eff}$ obtained is 3 ms, corresponding to a $SRV_{max}$ of as low as of 5.0 cm/s. This study highlights the feasibility of the Cat-CVD stoichiometric $SiN_x$ films as passivation layers for c-Si solar cells.

## References

[1] A. Goetzberger, J. Knobloch and B. Vob, *Crystalline Silicon Solar Cells* (Wiley, Chichester, U. K., 1998) p. 87.

[2] R. Morimoto, C. Yokomori, A. Kikkawa, A. Izumi and H. Matsumura, *Thin Solid Films* **430** (2003) 230.

[3] K. Koyama, K. Ohdaira and H. Matsumura, *Appl. Phys. Lett.* **97** (2010) 0821081.

[4] Trinh Cham Thi, K. Koyama, K. Ohdaira, and H. Matsumura, *Sol. Energy Mater. Sol. Cells* **93** (2012) 169.

[5] Trinh Cham Thi, K. Koyama, K. Ohdaira, and H. Matsumura, *Thin Solid Films* **575** (2015) 60.

[6] A.G. Aberle, *Sol. Energy Mater. Sol. Cells* **65** (2001) 239.

[7] F. Duerinckx and J. Szulfcik, *Sol. Energy Mater. Sol. Cells* **72** (2002) 231.

[8] T. Lauinger, A.G. Aberle, R. Hezel, Proc. 14th European Photovoltaic Solar Energy Conf., 1997, p. 853.

[9] V. Yelundur, A. Rohatgi, J.I. Hanoka, R. Reedy, Proc. 19th European Photovoltaic Solar Energy Conf., 2004, p. 951.

[10] J. K. Holt, D. G. Goodwin, A. M. Gabor, F. Jiang, M. Stavola and H. A. Atwater, *Thin Solid Films* **430** (2003) 37.

[11] S. Duttagupta, B.Hoex, A. G. Aberle, presented at 22nd Int. Photovoltaic Science and Engineering Conf., 2012.

[12] J. Schmidt and S. Dauwe, presented at Workshop Fundamentals of a-$SiN_x$:H in Industrial Solar Cell Processing, 2005.

[13] J. Schmidt and M. Kerr, *Sol. Energy Mater. Sol. Cells* **65** (2001) 585.

[14] J. Schmidt and A.G. Aberle, *J. Appl. Phys.* **85** (1998) 3626.

[15] J.-F. Lelièvre, E. Fourmond, A. Kaminski, O. Palais, D. Ballutaud and M. Lemiti, *Sol. Energy Mater. Sol. Cells* **93** (2009) 1281.

[16] H. Matsumura, *Jpn. J. Appl. Phys.* **37** (1998) 3175.

[17] H. Matsumura, A. Kikkawa, T. Tsutsumi, A. Masuda, A. Izumi, M. Takahashi, H. Ohtsuka and J. D. Moschner, Proc. 3rd World Conf. Photovoltaic Energy Conversion, 2003, p. 114.

[18] W. A. Lanford, *J. Appl. Phys.* **49** (1978) 2473.

[19] E. H. Nicollian, J. A. Brews, *MOS Physics and Technology* (Wiley, New York, 1982) p. 83.

[20] Guide to Using WVASE32$^{TM}$: Software for Vase and M-44 Ellipsometers (J.A. Woollam, Lincoln, NE, USA, 1989) p. 159.

[21] L. Xiangna, Z. Zhouyin and W. Yong, *Chin. Phys. Lett.* **7** (1990) 79.

[22] K. Lauer, A. Laades, H. bensee, H. Metzner and A. L awerenz, *J. Appl. Phys.* **104** (2008) 104503.

[23] B. Sopori, R. Reedy, K. Jones, Y. Yan and M. Al-Jassim, Proc. 31st Photovoltaic Specialists Conf., 2005, p. 1039.

[24] J. Hong, W. M. M. Kessels, M. J. Soppe, A. W. Weeber, W. M. Arnoldbik and M. C. M. Van de Sanden, *J. Vac. Sci. Technol. B* **21** (2003) 2123.

[25] H.F.W. Dekkers, G. Beaucarne, M. Hiller, H. Charifi and A. Slaoui, *Appl. Phys. Lett.* **89** (2006) 211914.

[26] H. Matsumura, K. Kamesaki, A. Masuda and A. Izumi, *Jpn. J. Appl. Phys.* **40** (2001) L289.

[27] K. Seshan, *Handbook of thin film deposition (*Oxford, 2012) p. 324.

[28] O. Hégr, J. Boušek, J. Sobota, T. Fořt, Radim Bařinka and A. Poruba Proc. 23rd European Photovoltaic Solar Energy Conf., 2009, p. 1495.

[29] S. Scholz, S. Voser, G. Dovids, H. Haverkamp and G. Hahn, Proc. 23rd European Photovoltaic Solar Energy Conf., 2008, p. 1717.

[30] H. Fujiwara, *Spectroscopic Ellipsometry Principles and Application* (Wiley, Chichester, U. K., 2007) p. 22.

[31] G. Lucovsky, *Solid State Commun.* **29** (1978) 571.

[32] J. Robertson, W.L. Warren, J. Kanicki, *J. Non-Cryst. Solids* **187** (1995) 297.

[33] W. L. Warren, J. Robertson, and J. Kanicki, *Appl. Phys. Lett.* **6** (1993) 2685.

[34] E.H. Nicollian, J. R. Brews, MOS physic and technology, John Wiley &Sons, 1982.

[35] E.H. Nicollian, A. Goetzberger and A. D. Lopez, *Solid-State Electron.* **12** (1968) 937.

[36] K. H. Zaininger, member, IEEE and G. Warfield, *IEEE Trans. Electron Dev.* **ED-12** (1965) 179.

[37] C. N. Berglund, *IEEE Trans. Electron Dev.* **ED-13** (1966) 701.

[38] Y. Wan, K. R. McIntosh and A. F. Thomson, *AIP Advances* **3** (2013) 032113.

[39] Y. Wan, K. R. McIntosh, A. F. Thomson and A. Cuevas, *IEEE. J. Photovolt.* **3** (2013) 554.

[40] S. Duttagupta, F. Lin, M. Wilson, M. B. Boreland, B. Hoex and A. G. Aberle, *Prog. Photovolt: Res. Appl.* **22** (2014) 641.

# Chapter 4 Improvement in the passivation quality of a Cat-CVD $SiN_x$ single layer by applying P Cat-doping

## 4.1 Introduction: The role of a P Cat-doped layer in the passivation of a c-Si surface

Cat-CVD promises potential applications in passivation technique for c-Si solar cells not only due to its benefit of forming high-quality film/c-Si interface property but also because of its ability to form doped a-Si films and shallow doped layers at low substrate temperature [1-6]. Cat-CVD can be used to form a shallow phosphorous (P)-doped layer, called P Cat-doped layer, at a low substrate temperature such as room temperature [4-6]. This shallow P Cat-doped layer has been found to be formed on a c-Si surface with a depth of <5 nm when a c-Si surface is exposed to radicals generated by decomposing $PH_3$ gas at a catalyzer temperature ($T_{cat}$) of more than 1100 $^oC$ [4]. It is also found that no etching damage is observed when $T_{cat}$ is sufficiently low. Figure 4.1 shows the secondary ion mass spectrometry (SIMS) profiles of P atoms in P Cat-doped layers formed at various substrate temperature ($T_{S\text{-}dope}$) and exposure time ($t_{dope}$) during doping process [4].

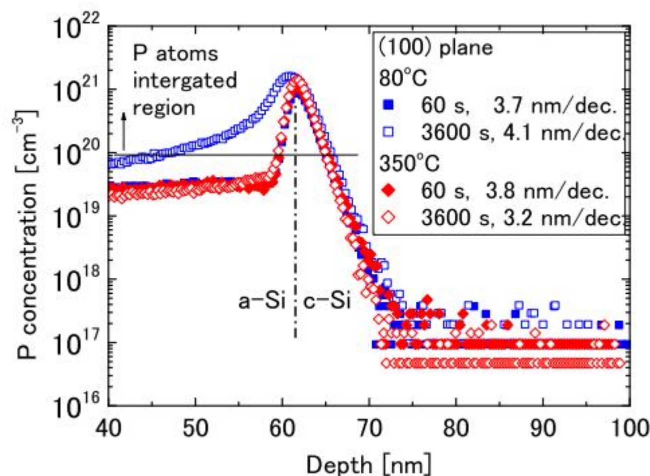


*Figure 4.1 SIMS profiles of P atoms in P Cat-doped layers deposited at various substrate temperature and exposure time [4].*

Although P concentration in a P Cat-doped layer is high, donor activation ratio is less than 2% [4]. The sheet carrier density of the P Cat-doped layer varies from $5\times10^{11}$ to $5\times10^{12}$ cm$^{-2}$ depending on $T_{S\text{-}dope}$ and $t_{dope}$. The shallow P doped layer with suitable sheet carrier density can therefore induce field-effect passivation, which can significantly suppress the recombination of minority carriers on a c-Si surface. Although the shallow doping can also be realized by other techniques such as plasma doping, atomic layer deposition of dopants, and molecular beam epitaxy [7-11], Cat-doping can significantly avoid damage onto a c-Si surface induced by energetic ions since gas molecules are decomposed on a heated wire by catalytic reaction. It has been demonstrated that there is no serious damage from generated radicals onto a c-Si surface at $T_{cat}$ of 1300 $^{o}$C, at which P Cat-doped layer is formed with high sheet carrier density [2]. This advantage makes Cat-doping become a favorable method for the formation of field-effect passivation layers for c-Si. Regarding the application of P Cat-doped layers to passivation technique, it has been already reported that the addition of P Cat-doped layers can reduce the $SRV_{max}$ of n-type c-Si passivated with an a-Si film from 5 to 3 cm/s [12]. In the previous chapter, I have optimized the preparation conditions of $SiN_x$ passivation films with a refractive index of ~2.0 at a wavelength of 630 nm prepared by Cat-CVD for n-type c-Si wafers. The highest $\tau_{eff}$ of 3 ms, corresponding to a low $SRV_{max}$ of 5 cm/s, can be obtained for n-type c-Si passivated with Cat-CVD $SiN_x$ films deposited at a low substrate temperature (~100 °C) and post annealing. The use of $SiN_x$ films, whose refractive indexes are adjusted to be 2.0 even after decreasing the substrate temperatures, can avoid optical loss due to parasitic absorption in a-Si for $SiN_x$/a-Si stacked passivation system. The Cat-CVD $SiN_x$ films with high passivation quality and high transparency are suitable for application to c-Si solar cells. As I mentioned above, a P Cat-doped layer can induce field-effect passivation, which is effective in suppressing surface recombination by sending electrons away from the c-Si surface. In this chapter, in order to obtain even lower $SRV_{max}$ on a c-Si surface passivated with a $SiN_x$ film, I attempt to apply P Cat-doping for field-effect passivation. The structure of a $SiN_x$/P Cat-doped layer is shown in Figure 4.2. The effects of sheet carrier density and annealing as well as H etching on the passivation quality of $SiN_x$/P Cat-doped layers on a c-Si surface are also investigated.

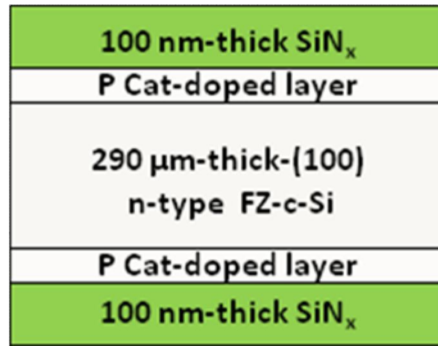


*Figure 4.2 Cross-sectional schematic of a c-Si passivated with $SiN_x$/P Cat-doped layers.*

## 4.2 Experimental procedure

*Table 4.1 Sample preparation conditions of P Cat-doping, a-Si, and $SiN_x$ films.*

| | Doping | a-Si | $SiN_x$ |
|---|---|---|---|
| Gas sources | $PH_3$ 20 sccm | $SiH_4$: 10 sccm | $SiH_4$: 8 sccm<br>$NH_3$: 150 sccm |
| Substrate Temperature ($T_{s\text{-}dope}$) | 80-300 °C | 90 °C | 100 °C |
| Pressure ($P$) | 1.0 Pa | 0.55 Pa | 10 Pa |
| Catalyzer temperature ($T_{cat}$) | 1300 °C | 1800 °C | 1800 °C |
| Catalyzer-substrate distance | 12 cm | 8 cm | 8 cm |
| Time ($t_{dope}$) | 30-120 s | 30 s | 184 s |

Sample preparation conditions are summarized in Table 4.1. All c-Si wafers were first cleaned in diluted (5%) HF solution for 10 s to remove native oxide. P Cat-doped layers, $SiN_x$ films and a-Si films were prepared in separate Cat-CVD chambers. 2.25% helium-diluted $PH_3$ was used as a gas source for doping process. A tungsten wire (W) with

a diameter of 0.5 mm and a length of 210 cm was used as a catalyzer in the P doping chamber. Distance between catalyzer and substrate was 12 cm to reduce heat radiation from the heated catalyzer. The schematic of a P Cat-doping chamber is described in Figure 4.3.

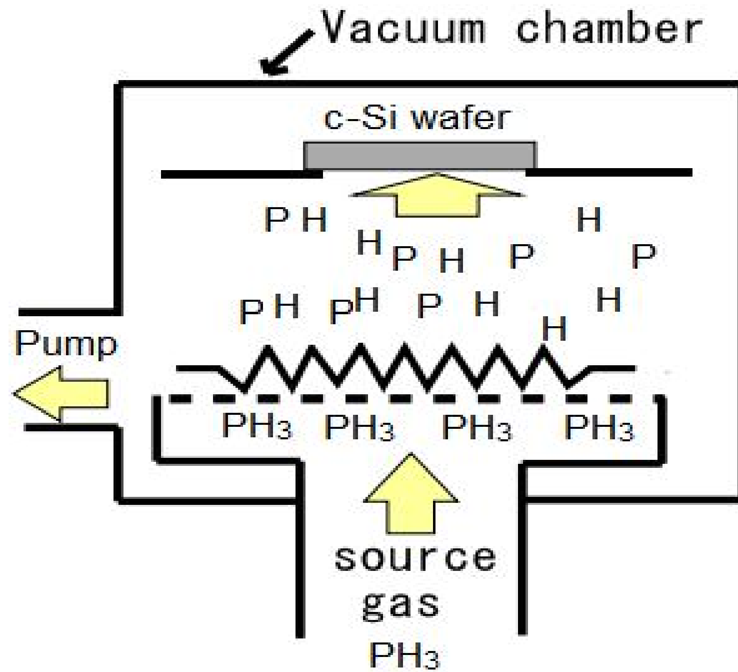


*Figure 4.3 Schematic of a P Cat-doping chamber.*

In this chapter, the properties of P Cat-doped layers were varied by changing doping substrate temperature ($T_{s\text{-}dope}$) and doping time ($t_{dope}$). The deposition condition of $SiN_x$ films and annealing conditions for the samples after depositing the $SiN_x$ films were the same as the optimized conditions, under which high $\tau_{eff}$ of 3 ms can be obtained for a $SiN_x$/c-Si structure, as reported in Chapter 3. 290-μm-thick n-type (100) FZ Si wafers with a resistivity of 2.5 Ωcm and a bulk minority carrier lifetime of >10 ms were used for the investigation of the passivation quality. The structure for $\tau_{eff}$ measurement is shown in Figure 4.2. In order to investigate the effect of annealing on passivation quality, the P Cat-doped samples were annealed before and after depositing $SiN_x$ films. In this paper, I refer them to "annealing A" and "annealing B", respectively. Annealing A and B were both conducted in a horizontal tubular furnace in nitrogen atmosphere. Two samples were prepared under the same P doping condition at the same batch; one is for a sample with only annealing B, and the other is for a sample with both annealing A and B. The samples

without annealing A were passivated with $SiN_x$ films immediately after P Cat-doping without air break, while the samples with annealing A were taken out from the P doping chamber, followed by furnace annealing and then $SiN_x$ deposition without any additional cleaning prior to the deposition. All the $SiN_x$-deposited samples were finally annealed at 350 $^oC$ for 30 min (annealing B). The $\tau_{eff}$ of the samples was measured by μ-PCD using a 904 nm wavelength pulse laser with a photon density of $5\times10^{13}$ $cm^{-2}$, as described in Chapter 2. I also measured excess-carrier-density- ($\Delta n$-) dependent $\tau_{eff}$ by quasi-steady-state photoconductance (QSSPC) (WCT-120, Sinton Instruments).

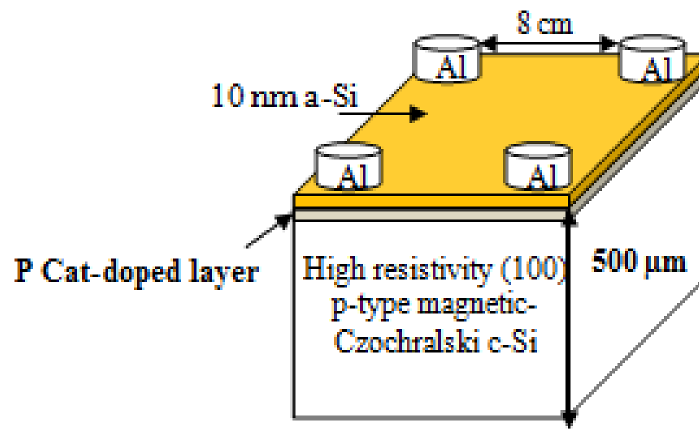


*Figure 4.4. Cross-sectional schematic of a sample for the Hall effect measurement.*

The Hall effect measurement and SIMS were employed to evaluate the sheet carrier density ($N_D$) of P Cat-doped samples and P concentration, respectively. The properties of c-Si wafers used for SIMS measurement are the same as those used for $\tau_{eff}$ measurement. The SIMS measurement was performed from the back side of the samples after removing most of Si wafers in order to avoid the effect of knock-on and resulting unintentional broadening of P profiles. I used 2900 Ωcm p-type FZ c-Si wafers for the Hall effect measurement. High resistivity samples are used for preventing leakage current from a P Cat-doped layer to a c-Si substrate. The reason of choosing p-type wafers here is to form a depletion layer, which is also to avoid current to a c-Si substrate. The capture of carriers at defects on a c-Si surface and oxidization may affect significantly the results of the Hall effect measurement [4,13,14]. In order to prevent these effects, a 10-nm-thick a-Si film was deposited on c-Si immediately after P Cat-doping without air exposure. In order to know the effect of annealing on $N_D$, samples were annealed at 350 $^oC$ before and after depositing a-Si films. Four Al electrodes were formed by evaporation through a metal hard

mask to form the van der Pauw configuration. The samples were annealed at 350 $^{o}$C for 1 min to make Ohmic contact between Al electrodes and a P Cat-doped layer. Figure 4.4 shows the cross-sectional schematic of a sample for the Hall effect measurement. The details of the measurement have been described in Ref. 3. More details of the Hall effect measurement is also summarized in Appendix A-6. The effect of H etching on the morphology of c-Si surface after P Cat-doping was evaluated by atomic force microscopy (AFM).

## 4.3 Results and discussion

### *4.3.1 The effect of annealing on P activation as donors and the passivation characteristic of $SiN_x$/P Cat-doped layer/c-Si structures*

Annealing plays an important role in improving the passivation quality of $SiN_x$/c-Si structures [15-20]. In this study, I first investigate the effect of annealing on the passivation properties of $SiN_x$/P Cat-doped layers. c-Si wafers received P Cat-doping at a $T_{s\text{-}dope}$ of 80 $^{o}$C for 1 min, followed by $SiN_x$ film deposition. The P doping and $SiN_x$ deposition condition are shown in Table 4.1. The samples were then annealed (annealing B) at various annealing temperature ($T_{aB}$) for 30 min.

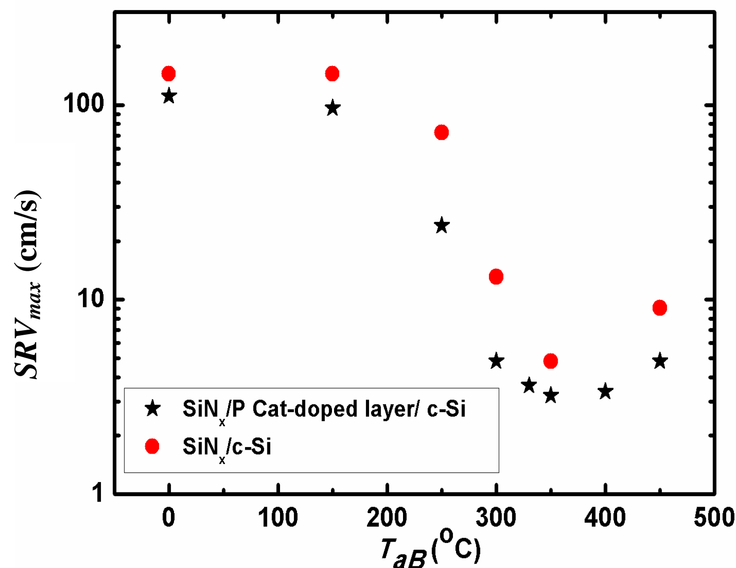


*Figure 4.5 $SRV_{max}$ of $SiN_x$/P Cat-doped layer/c-Si structures as a function of $T_{aB}$. The $SRV_{max}$ of $SiN_x$/c-Si structures as a function of $T_{aB}$ is also shown for comparison.*

Figure 4.5 shows the dependence of $SRV_{max}$ of a $SiN_x$/P Cat-doped layer/c-Si structures on $T_{aB}$. The $SRV_{max}$ of $SiN_x$/c-Si structures as a function of $T_{aB}$ is also shown for comparison. Before annealing, $SRV_{max}$ of two samples are high. $SRV_{max}$ starts to decrease when $T_{aB}$ exceeds 200 $^{o}$C for both structures. $SRV_{max}$ reaches the lowest value at a $T_{aB}$ of 350 $^{o}$C, and then increases with further increase in $T_{aB}$. In order to clarify passivation improvement mechanism of $SiN_x$/P Cat-doped layer, I firstly consider the effect of annealing on the distribution of P and H in P Cat-doped layer. The P and H profiles obtained by SIMS show that there is no significant change in P and H profiles in the P Cat-doped layer even after annealing at 350 $^{o}$C for 30 min, as shown in Fig. 4.6. In other words, annealing does not cause any diffusion of these atoms into c-Si as well as release of these atoms to ambient. A sample with H treatment was also examined. $H_2$ gas was used instead of $PH_3$ gas with the same flow rate of 20 sccm, other parameters were kept unchanged, such as a $T_{s\text{-}dope}$ of 80 $^{o}$C, $P$ of 1 Pa. $\tau_{eff}$ of the $SiN_x$/H treatment/c-Si structure after annealing is 3.0 ms, corresponding to a $SRV_{max}$ of 5.0 cm/s, does not differ from that of $\tau_{eff}$ of the $SiN_x$/c-Si structure. Therefore, I can confirm that reduction in $SRV_{max}$ of $SiN_x$/P Cat-doped layer/c-Si structure is related to $PH_3$ doping process.

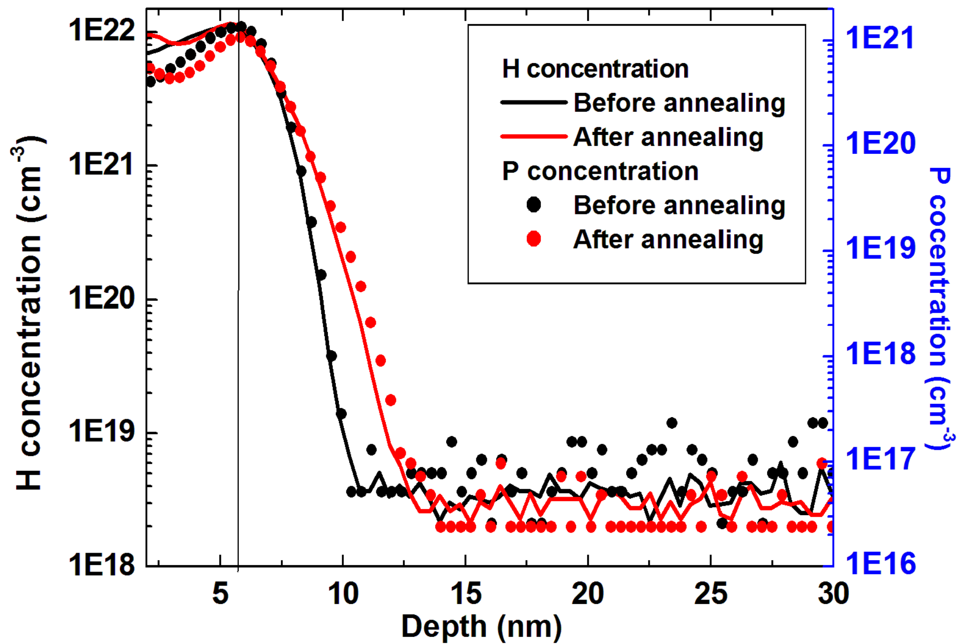


*Figure 4.6. P and H profiles in a P Cat-doped layer before and after annealing at 350 $^{o}$C for 30 min.*

The improvement in the passivation quality of the $SiN_x$/c-Si structure is supposed to be due to the effect of defect termination by H atoms during annealing [15-18]. For a $SiN_x$/P Cat-doped layer/c-Si structure, passivation quality relies not only on H defect termination but also on field-effect passivation, and increase in $T_{aB}$ might lead to increase in donor (activated P) concentration and resulting enhancement in field-effect passivation. Hayakawa *et al.* have reported that the most inactivated P atoms in a P Cat-doped layer exist in the forms of chemisorbed PH-, $PH_2$- and $PH_3$ (coordinate bond)-type bonds with Si atoms, denoted as $PH_x$ ($x$=1-3) [4]. It has been reported that P and H atoms are major products while PH- and $PH_2$- are minor products in the catalytic decomposition of $PH_3$ [22]. The $PH_x$ production mechanism inside P Cat-CVD chamber is described as below [2]:

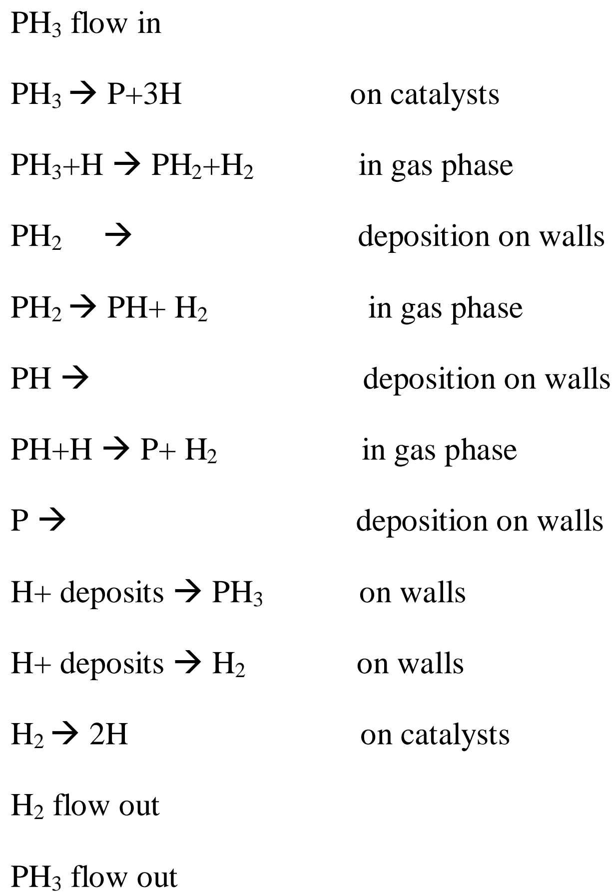

| | |
|---|---|
| $PH_3$ flow in | |
| $PH_3 \rightarrow P+3H$ | on catalysts |
| $PH_3+H \rightarrow PH_2+H_2$ | in gas phase |
| $PH_2 \rightarrow$ | deposition on walls |
| $PH_2 \rightarrow PH+H_2$ | in gas phase |
| $PH \rightarrow$ | deposition on walls |
| $PH+H \rightarrow P+H_2$ | in gas phase |
| $P \rightarrow$ | deposition on walls |
| H+ deposits $\rightarrow PH_3$ | on walls |
| H+ deposits $\rightarrow H_2$ | on walls |
| $H_2 \rightarrow 2H$ | on catalysts |
| $H_2$ flow out | |
| $PH_3$ flow out | |

I thus guess that the extraction of H atoms from $PH_3$ molecules by the formation of $H_2$ molecules or the addition of H atoms to P atoms on a c-Si surface is a possible mechanism of $PH_x$ production.

$PH_x$ may decompose at high temperature, resulting in the release of P and H atoms. The released H atoms can diffuse to a c-Si surface and terminate defects there, and the released P atoms act as donors and contribute to reinforcing field-effect passivation. There have been a number of literatures about the decomposition of P-H bonds using samples with $PH_3$ adsorbed on c-Si (100) [23-26]. Yu *et al.* have reported that $PH_3$ molecules are partially dissociated at an annealing temperature of 275 $^oC$ for $PH_3$ adsorbed samples [23]. Tsai *et al.* have reported that $PH_3$ species are converted to $PH_2$ species in an adsorbed layer at annealing temperature >317 $^oC$, and $PH_2$ species are converted to P atoms when an annealing temperature exceeds 377 $^oC$ [24]. The interesting results of two reports are shown in Figures 4.7 and 4.8. These facts indicate that $PH_2$ species are decomposed to P and H atoms at around 300 °C. I can guess that the released H atoms can make bonding with Si atoms and P atoms start to act as donors. In this study, as has been shown in Figure 4.5, the $SRV_{max}$ of a $SiN_x$/P Cat-doped layer/c-Si structure is much lower than that of a $SiN_x$/c-Si structure when $T_{aB}$ $\geq$250 $^oC$. This fact suggests that $PH_x$ starts to decompose efficiently at a $T_{aB}$ of 250 $^oC$. This temperature is quantitatively consistent with the values of the literatures shown above. A $T_{aB}$ of 350 $^oC$ is sufficiently high for both $PH_x$ bond breaking in a P Cat-doped layer and defect termination by H in $SiN_x$ films, and higher $T_{aB}$ leads to the desorption of H atoms to atmosphere and resulting increases in $SRV_{max}$. The lowest $SRV_{max}$ can thus be obtained at a $T_{aB}$ of 350 $^oC$ for both structures.

$D_{it}$ was evaluated for $SiN_x$/P Cat-doped c-Si samples after annealing. Figure 4.9 shows the $D_{it}$ of $SiN_x$/ P Cat-doped c-Si and $SiN_x$/c-Si samples after annealing at 350 $^oC$. $D_{it\text{-}average}$ at mid-gap region for the $SiN_x$/ P Cat-doped c-Si sample is $2.2\times10^{11}$ $eV^{-1}cm^{-2}$. This value is equivalent to that of the $SiN_x$/c-Si sample. We can thus guess that H atoms in a $SiN_x$ film contribute greatly to defect termination on a c-Si surface. The reason of slightly smaller $D_{it}$ for the $SiN_x$/P Cat-doped c-Si sample than the $SiN_x$/c-Si sample might be the effect of H atoms in a P Cat-doped layer.

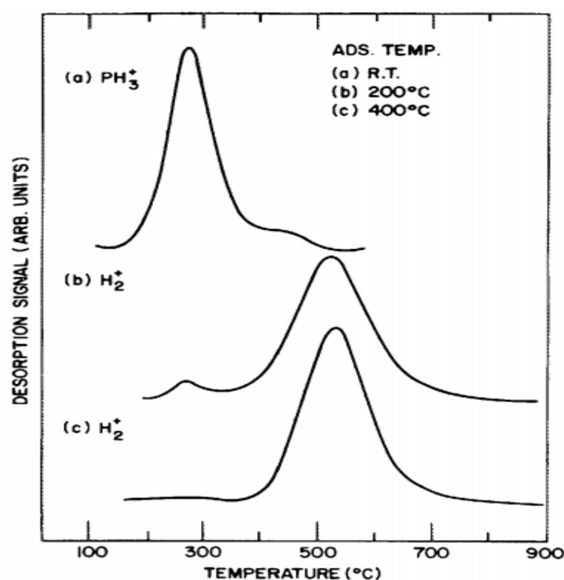


**FIG. 2. Thermal desorption spectra for $PH_3$ on Si(100). (a) shows the large $PH_3$ desorption peak at 275 °C from a room temperature adsorbed $PH_3$ layer on Si(100). (b) and (c) show the large $H_2$ desorption peak at 525 °C when $PH_3$ was adsorbed at 200 and 400 °C. The small feature at 275 °C in (b) is due to the cracking contribution from a small $PH_3$ desorption peak. All $PH_3$ exposures were 20 L. The temperature scale is a rough estimate only.**

*Figure 4.7 Desorption spectra of $PH_3$ adsorbed on Si(100) at various adsorption temperature. The peaks at 275 $^oC$ and 525 $^oC$ indicate $PH_3$ and $H_2$ desorption, respectively. The results are from ref. 23.*

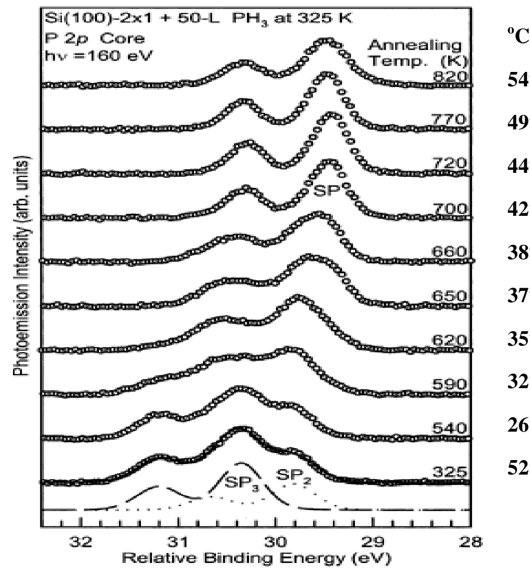


Fig. 2. Photoemission spectra (○) of the P 2p core levels for the Si(1 0 0)-2 × 1 surface saturated with a 50-L $PH_3$ dose at 325 K followed by progressive annealing to higher temperatures as indicated. The fit (—) and the decomposed individual $SP_2$ and $SP_3$ components for the bottom spectrum are also shown. The relative binding energy scale refers to the corresponding Si $2p_{3/2}$ line of the B component [10].

*Figure 4.8 The effect of annealing temperature on bonding components of $PH_3$ adsorbed on Si(100).One can clearly see the more significant conversion of $PH_3$ ($SP_3$) component to $PH_2$ ($SP_2$) component with increase in temperature. When annealing temperature is higher than 700K, $PH_2$ is converted into P atoms and $PH_3$ gas. [24]*

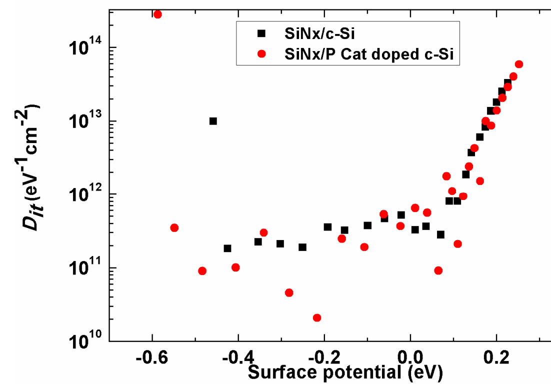


*Figure 4. 9. Calculated $D_{it}$ for the $SiN_x$/ P Cat-doped c-Si and $SiN_x$/c-Si samples after annealing at 350 °C for 30 min.*

On the other hand, contrary to our expectations, the results of the Hall effect measurement show that $N_D$ decreases by annealing. $N_D$ is $1.2\times10^{12}$ cm$^{-2}$ before annealing, while it reduces to $0.9\times10^{12}$ cm$^{-2}$ for the samples with annealing at 350 °C for 30 min after

depositing a-Si films, and to $0.7\times10^{12}$ $cm^{-2}$ for the samples with annealing under the same condition before depositing a-Si films, as shown in Figure 4.10. For the sample annealed after depositing an a-Si film, a possible reason for reduction in $N_D$ is the diffusion of H atoms from the a-Si film to the P Cat-doped layer, which can cause the formation of more $PH_x$ than $PH_x$ decomposition in a P Cat-doped layer and resulting reduction in $N_D$. Lower $N_D$ obtained in the sample annealed before depositing an a-Si film may be due to the oxidization of the c-Si surface. In order to conduct annealing process, I have to take out the samples to atmosphere. The oxidation can inactivate P on a c-Si surface and/or induce the formation of a thin Si oxide film containing P atoms on a c-Si surface, which affect the results of the Hall effect measurement. In order to clarify this effect, the samples for the Hall effect measurement after P Cat-doping at 350 $^{o}$C were put in air for 15 min before depositing a-Si films. By the additional air exposure, $N_D$ drops from $3\times10^{12}$ to $0.5\times10^{12}$ $cm^{-2}$, which is a clear evidence of oxidation-induced reduction in $N_D$. I actually confirmed the formation of a $SiO_x$ film with a thickness of 1.1 nm and a refractive index of 1.5 at a wavelength of 630 nm on a c-Si surface by using spectroscopic ellipsometry. In order to know the effect of addition of $SiO_x$ film on passivation quality of $SiN_x$/c-Si, I annealed bare c-Si before $SiN_x$ deposition. A comparison between $SiN_x$/c-Si and $SiN_x$/P Cat-doped layer/c-Si sample with and without annealing A and B is shown in Figure 4.11. Sample of $SiN_x$/c-Si with annealing A is $SiN_x$/$SiO_x$/c-Si sample. One can see that $SRV_{max}$ of samples with $SiO_x$ layer is lower than that of the $SiN_x$/c-Si sample but still lower than that of the $SiN_x$/P Cat-doped layer/c-Si sample. The results confirm that both oxidation and P Cat-doped layer can contribute in improvement passivation quality of $SiN_x$/c-Si, but the role of P Cat-doped layer is dominant.

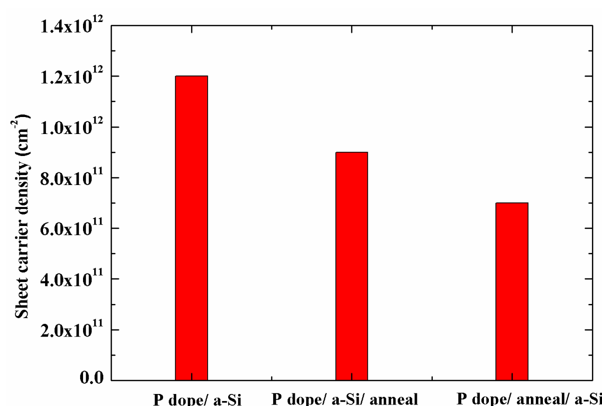


*Figure 4.10 Sheet carrier density of a P Cat-doped layer before and after annealing at 350 $^{o}$C for 30 min.*

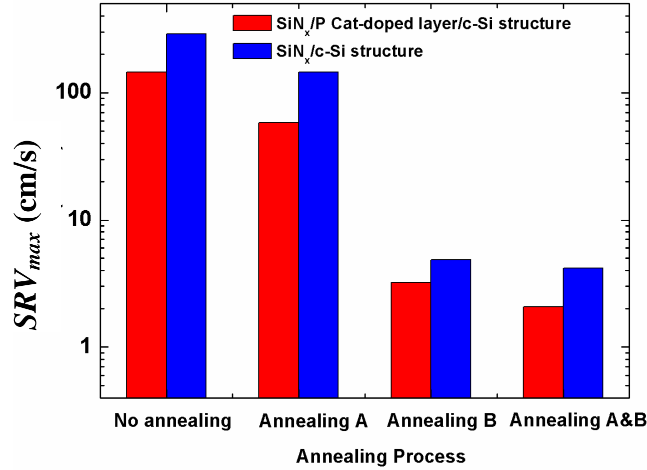


*Figure 4.11 $SRV_{max}$ of SiN$_x$/P Cat-doped layer/c-Si and SiN$_x$ /c-Si with and without annealing A and B*

On the other hand, as mentioned previously, $N_D$ obtained for an a-Si/P Cat-doped layer/c-Si structure is reduced by annealing at 350 $^o$C for 30 min. Cat-CVD SiN$_x$ films also contain high amount of H atoms, which can diffuse from SiN$_x$ films to c-Si surface and terminate defects or recombine with P atoms to form more PH$_x$ during annealing B. Assuming that reduction in $N_D$ for the SiN$_x$/P Cat-doped layer/c-Si structures is the same as the case of a-Si/P Cat-doped layer/c-Si after annealing B, $N_D$ of a SiN$_x$/P Cat-doped layer/c-Si structure decreases by 25%. The sample undergoing both annealing A and B has $N_D$ of ~ $5 \times 10^{11}$ cm$^{-2}$, which is due to the effect of oxidation by annealing A and H diffusion during annealing B. This value of $N_D$ might be high enough for field-effect passivation. The fact that the $N_D$ of the sample receiving both annealing A and B is less than that with only annealing B indicates less effective field-effect passivation. However, the benefit of defect termination by H atoms might overcome the deterioration of field effect and lead to better passivation quality for the sample with both annealing A and B.

To understand the effect of annealing A on the passivation quality of SiN$_x$/P Cat-doped layers, c-Si samples with Cat-doping at 80 $^o$C for 1 min were annealed (annealing A) at various annealing temperature ($T_{aA}$) for 30 min in the tubular furnace. Samples were then moved to the Cat-CVD system to deposit SiN$_x$ films. Finally, samples were annealed at 350 $^o$C for 30 min (annealing B). Figure 4.12 shows the $SRV_{max}$ of SiN$_x$/P Cat-doped layer/c-Si structures after annealing A and B as functions of $T_{aA}$ and annealing time ($t_{aA}$) for annealing A. $N_D$ as a function of $T_{aA}$ is also shown. One can clearly see that $SRV_{max}$

decreases with $T_{aA}$ for samples both with and without process B. $SRV_{max}$ decreases when $T_{aA}$ increases and decreases for $T_{aA} \geq 400$ °C. This is probably due to increase in $N_D$ at higher $T_{aA}$. The increase in $N_D$ is probably due to the decomposition of $PH_x$ at higher $T_{aA}$ and resulting activation of higher amount of P atoms. Additionally, the thermal oxidation of a c-Si surface for the samples annealed at high temperature and defect termination by H atoms by annealing might contribute to the formation of a high-quality $SiN_x/SiO_x$/P Cat-layer and c-Si interface, resulting improvement in passivation quality. Because the P Cat-doped layer is very shallow, too high $T_{aA}$ might lead to the desorption of H and P atoms to environment, which can result in increase in $SRV_{max}$ due to less effective defect termination and field-effect passivation. The complete thermal desorption of P atoms from $PH_3$ adsorbed c-Si surface at high temperature above 550 $^{o}$C were also reported in Ref. 24, in which desorption of H atoms at 400 $^{o}$C has also been observed. The same tendency is seen in the annealing time dependence for annealing A, as shown in Figure 4.12(b). $T_{aA}$ of 400 $^{o}$C and $t_{aA}$ of 30 min are thus optimum conditions for annealing A needed to activate P in P Cat-doped layer without H and P desorption, and the lowest $SRV_{max}$ obtained for $SiN_x$/P Cat-doped layer/c-Si structures under the conditions.

Another point which I should discuss is the effect of annealing at high $T_{aA}$ for low $t_{aA}$ on the passivation quality of the films. Annealing at high $T_{aA}$ such as 800 $^{o}$C may be able to activate P atoms as donors more effectively. If annealing time is short enough, the field effect passivation created by high donor concentration might be clarified. In order to investigate this idea, c-Si wafers were doped at 80 $^{o}$C for 60 s with different conditions from those shown in Table 4.1. c-Si samples with and without a P Cat-doped layer were then annealed at 800 $^{o}$C for 30 min, 5 min, 1 min. After that, $SiN_x$ were deposited and annealing B was conducted for all the samples. $SRV_{max}$ obtained for these samples is described in Figure 4.13. One can see that even at short time annealing, $SRV_{max}$ is very high not only for samples with P Cat-doping but also for the sample without P Cat-doping. Therefore, the high $SRV_{max}$ is mainly due to the deterioration of a c-Si wafer and high donor concentration of the structure has not been realized yet.

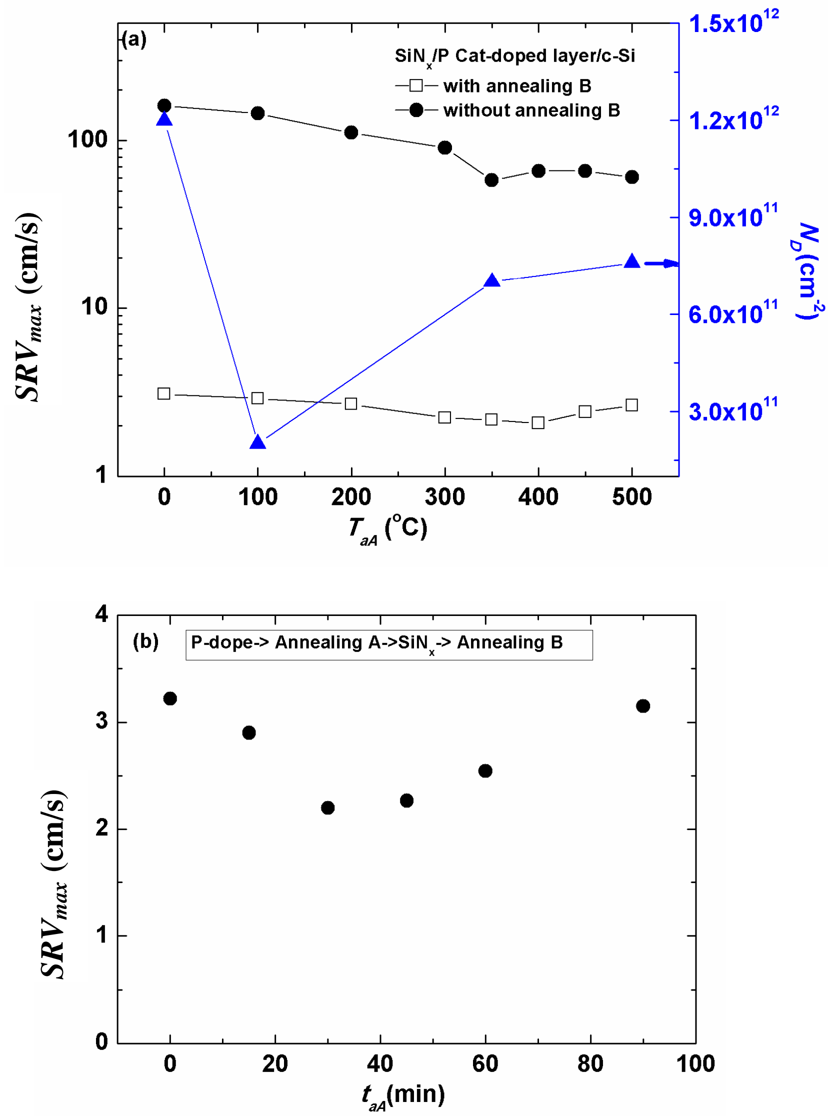


*Figure 4.12 SRV$_{max}$ of SiN$_x$/P Cat-doped layer/c-Si structures after annealing A at various $T_{aA}$ for 30 min and $t_{aA}$ at a $T_{aA}$ of 350 $^o$C. Annealing B was conducted at 350 $^o$C for 30 min.*

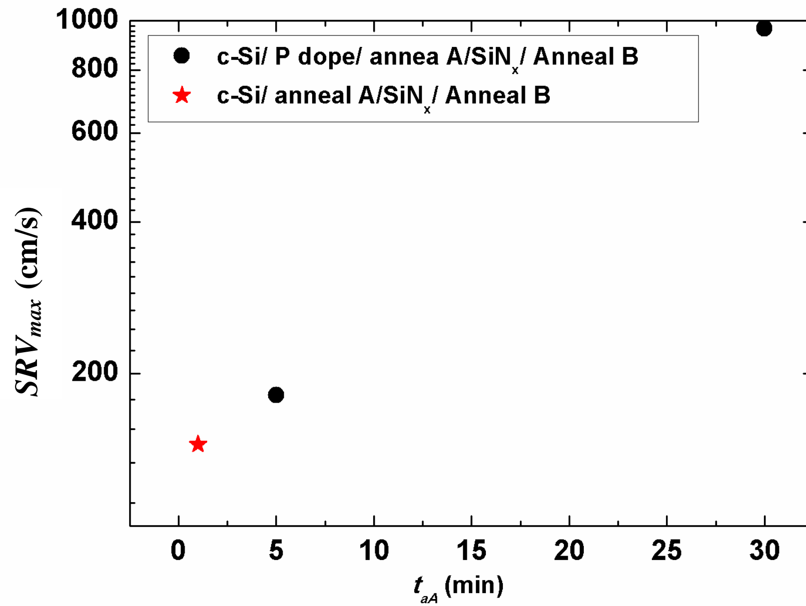


*Figure 4.13 $SRV_{max}$ of $SiN_x$/P Cat-doped layer/c-Si structures after annealing A at a $T_{aA}$ of 800 °C for various annealing time. Annealing B was conducted at 350 °C for 30 min.*

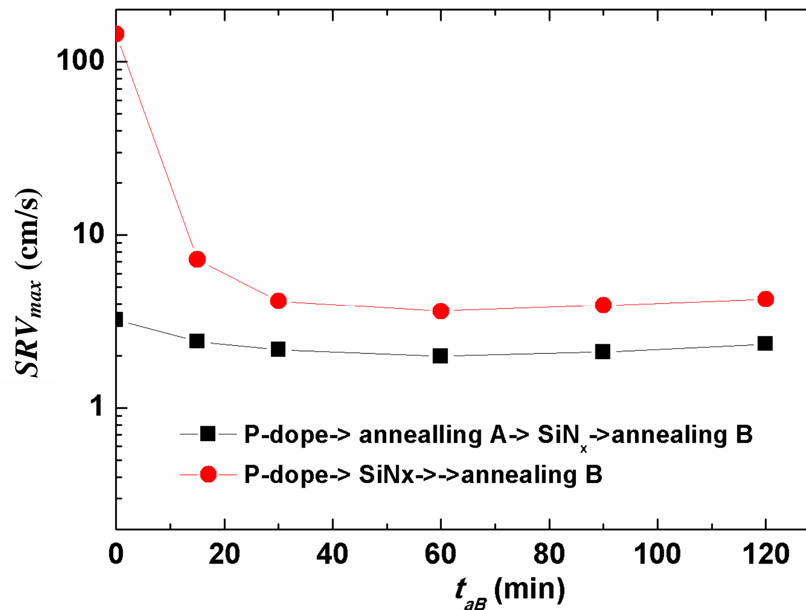


*Figure 4.14 $SRV_{max}$ of $SiN_x$/P Cat-doped layer/c-Si structures with and without annealing A as a functions of $t_{aB}$ at a $T_{aB}$ of 350 °C. Annealing A was conducted at 400 °C for 30 min.*

Figure 4.14 shows $SRV_{max}$ as a function of the duration of annealing B ($t_{aB}$). One can see that $SRV_{max}$ is still low for long $t_{aB}$. The tendencies of the variation of $SRV_{max}$ for both samples are the same. Annealing for 30 min is enough to obtain high passivation quality for the samples. Further increase in $t_{aB}$ does not enhance more the activation of P

atoms as well as defect termination. The instability of $SRV_{max}$ due to increase in $T_{aB}$ and $t_{aB}$ may raise a doubt of increase in $SRV_{max}$ after long time exposure to air even at room temperature. I have confirmed that $SRV_{max}$ of both $SiN_x$/c-Si and $SiN_x$/P Cat-doped layer/c-Si structures remain original values even after putting in air at room temperature for about 10 months.

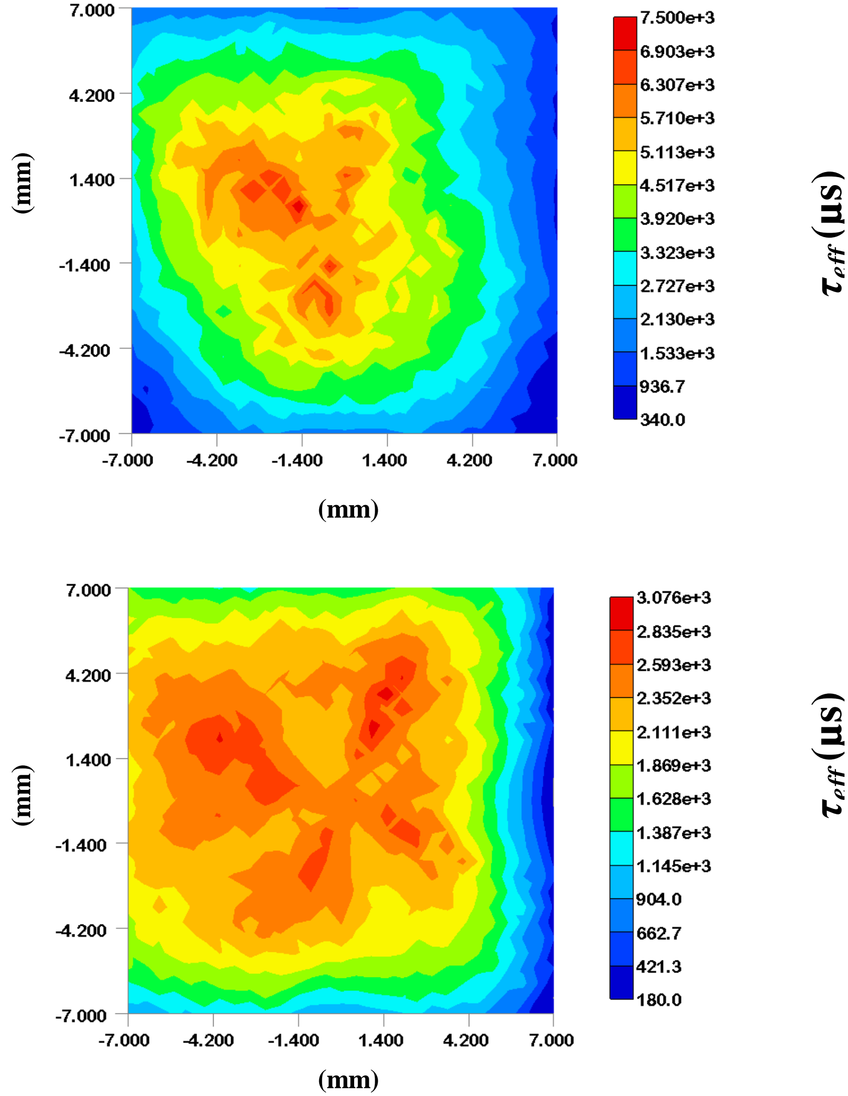


*Figure 4.15 $\tau_{eff}$ mapping data of $SiN_x$/P Cat-doped layer/c-Si structure (above) and a $SiN_x$/c-Si structure (bottom) measured by $\mu$-PCD in an area of 7×7 mm.*

In summary, a remarkably high $\tau_{eff}$ of ~7 ms, which corresponds to an $SRV_{max}$ of ~2 cm/s, can be achieved for $SiN_x$/P Cat-doped layer/c-Si samples after annealing B. Compared with a $SiN_x$/c-Si structure, the insertion of a P Cat-doped layer can reduce an $SRV_{max}$ from 5 cm/s to 2 cm/s. The mapping data of $\tau_{eff}$ for $SiN_x$/P Cat-doped layer/c-Si

sample and $SiN_x$/ c-Si sample are shown in Figure 4.15. Higher $\tau_{eff}$ at the center of the map may be due to ununiform thickness of films and/or the recombination of laterally diffused carriers on the sample edges and/or in an unpassivated region. A $SRV_{max}$ of 4 cm/s have also been achieved when nearly stoichiometric $SiN_x$ films were deposited by PECVD on 150-μm-thick 3-5 Ωcm n-type CZ Si wafers after annealed in an industrial firing process [30]. An $SRV_{max}$ of lower than 10 cm/s has been reported for 1.5 Ωcm p-type Si wafers passivated with stoichiometric $SiN_x$ films [31]. In these reports, they calculated $SRV_{max}$ through $\tau_{eff}$ obtained by a contactless photoconductance tester allowing both transient photoconductance decay (PCD) and QSSPC measurements at an $\Delta n$ of $1\times10^{15}$ $cm^{-3}$. Figure 4.16 shows $\tau_{eff}$ and corresponding $SRV_{max}$ of a $SiN_x$/P Cat-doped layer/c-Si structure and a $SiN_x$/c-Si structure measured by QSSPC in a transient mode. I observed $\tau_{eff}$ of ~7 ms for $SiN_x$/P Cat-doped layer/c-Si structure and ~3 ms for $SiN_x$/c-Si structure at a $\Delta n$ of $2.4\times10^{14}$ $cm^{-3}$. At a $\Delta n$ of $1\times10^{15}$ $cm^{-3}$, $\tau_{eff}$ is ~4 and 1.8 ms for $SiN_x$/P Cat-doped layer/c-Si and $SiN_x$/c-Si structures, corresponding to $SRV_{max}$ of 3.6 and 8 cm/s, respectively. Our $SRV_{max}$ obtained in this study is the lowest level for n-type c-Si passivated with $SiN_x$ films without firing process or with only low temperature process, which is acceptable for a-Si/c-Si heterojunction solar cells. The remarkable value of the $SRV_{max}$ obtained for $SiN_x$/P Cat-doped layer/c-Si structure highlights the promising application of Cat-CVD technique in high-efficiency n-type c-Si based solar cell fabrication.

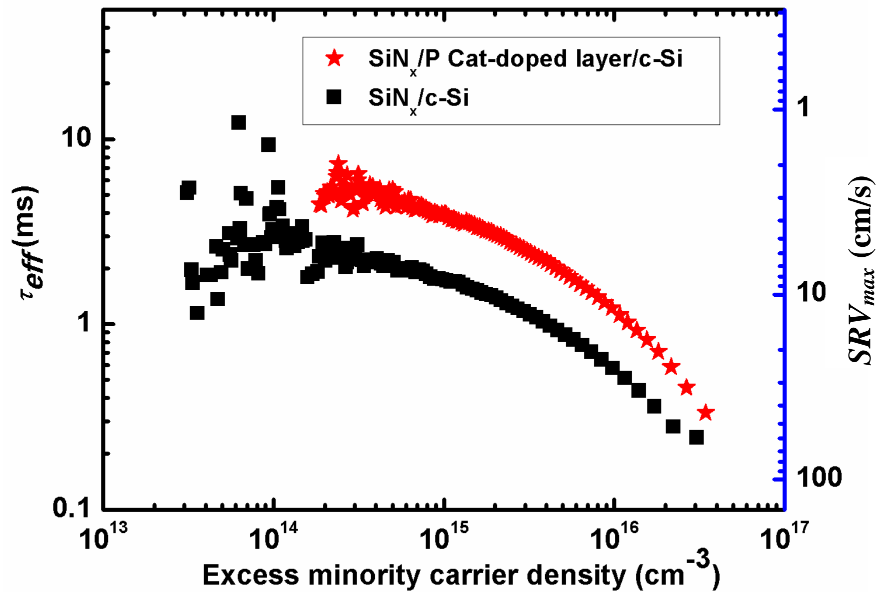


*Figure 4.16 $SRV_{max}$ and corresponding $\tau_{eff}$ as a functions of excess carrier density in a $SiN_x$/P Cat-doped layer/c-Si structure and a $SiN_x$/c-Si structure measured by QSSPC.*

### 4.3.2 Effect of $T_{s\text{-}dope}$ on the passivation characteristic of a $SiN_x$/P Cat-doped layer/c-Si structure

High $T_{s\text{-}dope}$ can activate P atoms as donors in a P Cat-doped layer [2,3]. This can contribute to improvement in field-effect passivation. In this investigation, I prepared P Cat-doped samples at various $T_{s\text{-}dope}$ for 1 min.

Figure 4.17 shows $SRV_{max}$ of $SiN_x$/P Cat-doped layer/c-Si samples as a function of $T_{s\text{-}dope}$ with and without annealing A. $N_D$ as a function of $T_{s\text{-}dope}$ before annealing is also shown. $N_D$ increases with increase in $T_{s\text{-}dope}$. This may suggest that H atoms desorb from a c-Si surface during P Cat-doping at high $T_{s\text{-}dope}$ due to the extraction of adsorbed H atoms on a c-Si surface by atomic H and/or $PH_3$ [2,32,33]. As I mentioned above, Umemoto *et al.* have reported that major products in the catalytic decomposition of $PH_3$ molecules on a heated tungsten catalyzer are P and H atoms [22]. Here, I suppose that the reaction of atomic H with adsorbed H and/or $PH_x$ on a c-Si surface and/or $PH_x$ bond breaking are possible mechanisms for H release at high $T_{s\text{-}dope}$. This process might assist P activation. I can see lower H concentration in a sample doped at a $T_{s\text{-}dope}$ of 300 $^{o}$C in a SIMS profile, as shown in Figure 4.18 later. The increase in $N_D$ makes small decrease in $SRV_{max}$ before annealing. It contributes significantly to improvement in passivation quality for the sample doped at high $T_{s\text{-}dope}$ when the samples were annealed with annealing B. The samples doped at a $T_{s\text{-}dope}$ of 300 $^{o}$C, which shows $N_D$ of ~ $2\times10^{12}$ cm$^{-2}$, can reach the highest $\tau_{eff}$ of ~6 ms, corresponding to $SRV_{max}$ of 2.4 cm/s. Figure 4.17 also shows $SRV_{max}$ of $SiN_x$/P Cat-doped layer/c-Si samples with annealing A and B as a function of $T_{s\text{-}dope}$. One can see that $\tau_{eff}$ does not depend on $T_{s\text{-}dope}$, and all the samples have constant and high $\tau_{eff}$ of ~7 ms corresponding to $SRV_{max}$ of 2 cm/s. This result suggests that P donor concentration is constant in all the samples with annealing before and after $SiN_x$ deposition. Figure 4.18 shows the SIMS profiles of samples with P Cat-doping at $T_{s\text{-}dope}$ of 80 and 300 $^{o}$C before annealing. I can see no significant difference in the two profiles, suggesting that the activation ratio of P atoms in the two samples is similar.

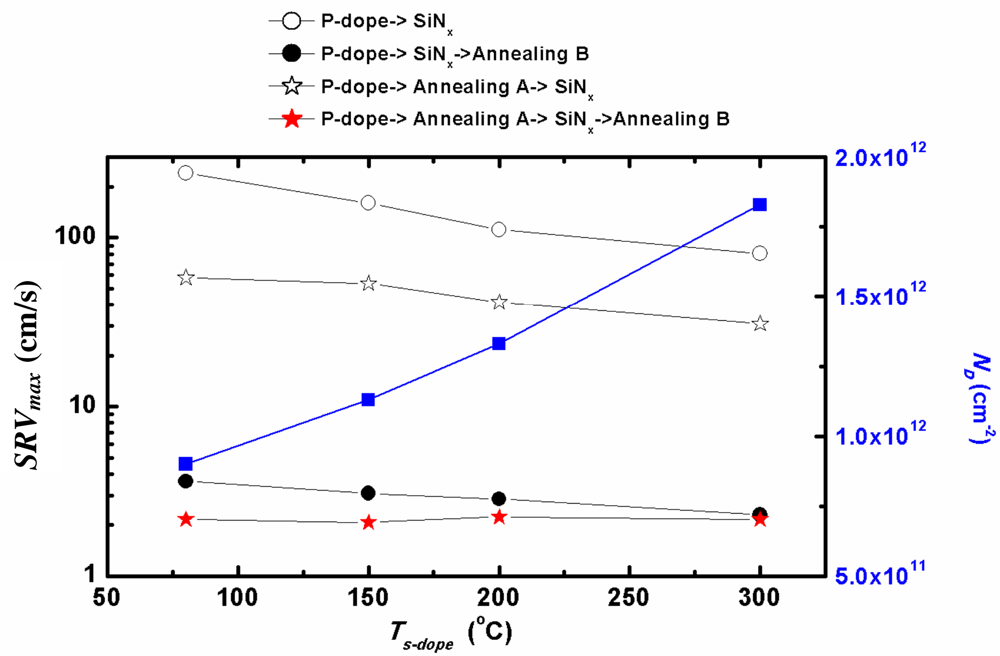


*Figure 4.17 $SRV_{max}$ of $SiN_x$/P Cat-doped layer/c-Si samples as a function of $T_{s\text{-}dope}$. $N_D$ as a function of $T_{s\text{-}dope}$ before annealing A is also shown. Annealing A was conducted at 400 °C for 30 min and Annealing B was conducted at 400 °C for 30 min.*

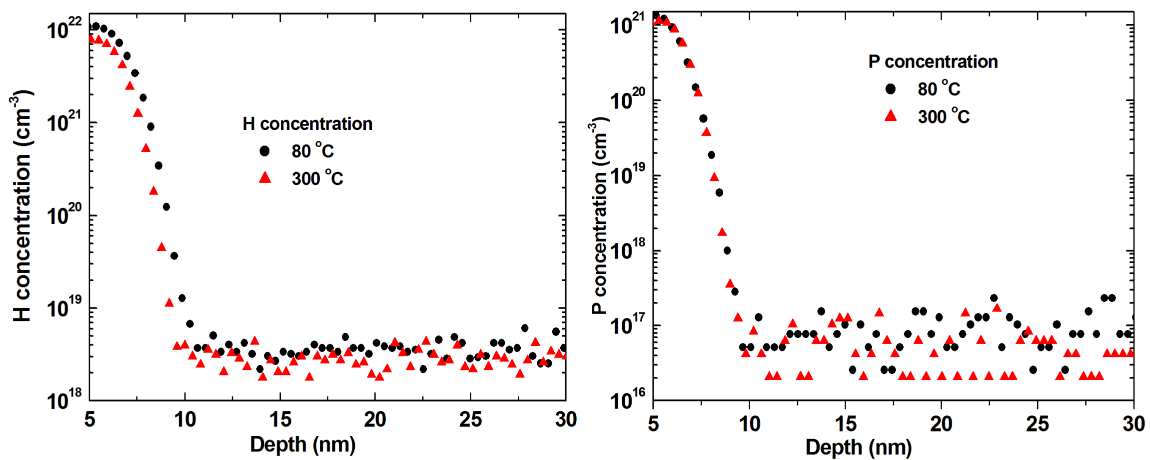


*Figure 4.18 SIMS profiles of P and H atoms in the samples doped at 80 °C and 300 °C without annealing.*

### 4.3.3 *Effect of $T_{s\text{-}dope}$ and doping duration on the passivation characteristic of $SiN_x$/P Cat-doped layer/c-Si structure*

$N_D$ of a P Cat-doped layer also increases with $t_{dope}$ [3]. I therefore concern the effect of $t_{dope}$ on $SRV_{max}$ of $SiN_x$/P Cat-doped layer/c-Si samples. The samples were doped at 80 $^oC$ for 30, 60, 90 and 120 s. The effect of annealing before depositing $SiN_x$ films was also investigated for these samples. Figure 4.19 shows the $SRV_{max}$ of $SiN_x$/P Cat-doped layer/c-Si samples as a function of $t_{dope}$ with and without annealing A. $N_D$ without annealing is also shown. Although $N_D$ increases with increase in $t_{dope}$, $SRV_{max}$ increases when $t_{dope} \geq 60$ s. For the sample doped for 30 s, $SRV_{max}$ is high due to low $N_D$. A possible reason for the high $SRV_{max}$ observed in the samples with $t_{dope} \geq 60$ s is the effect of surface etching by radical species during Cat-doping process.

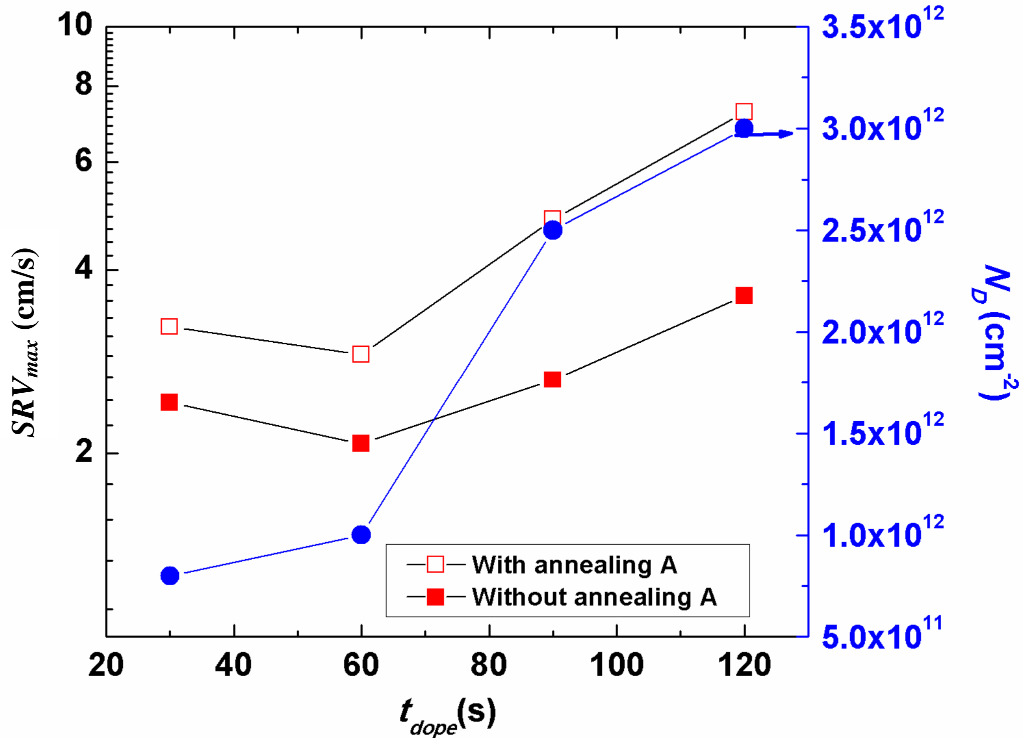


*Figure 4.19 $SRV_{max}$ of $SiN_x$/P Cat-doped layer/c-Si samples as a function of $t_{dope}$ with and without annealing A. $N_D$ before annealing is also shown. Annealing A was conducted at 400 $^oC$ for 30 min and Annealing B was conducted at 400 $^oC$ for 30 min.*

Figure 4.20 shows the surface AFM images of bare c-Si and c-Si doped for 60 and 90 s. The surface of bare c-Si has a root-mean-square roughness ($R_{rms}$) of ~0.09 nm with an average height of 0.3 nm. As shown in Figure 4.20 (b) and (c), the two P Cat-doped samples have more roughened surfaces, and the surface receiving longer Cat-doping is more seriously etched. The sample with a $t_{dope}$ of 90 s has a $R_{rms}$ of 0.24 nm and an average height is 0.9 nm, while they are 0.21 nm and 0.7 nm, respectively, for the sample doped at 60 s. Excess $t_{dope}$ thus rather deteriorates the interface quality, and an optimum $t_{dope}$ exists to obtain low *SRV* for $SiN_x$/P Cat-doped layer/c-Si structure.

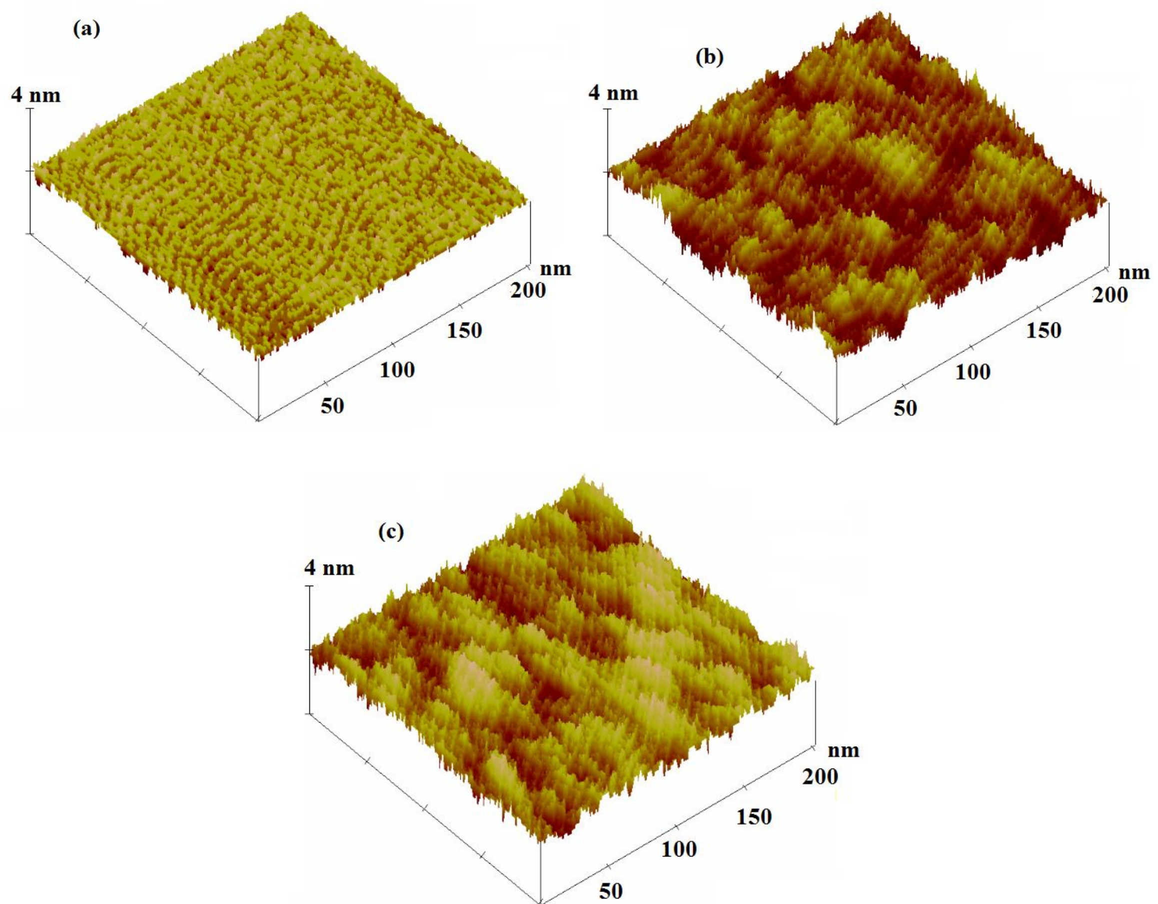


*Figure 4.19 Surface AFM images of (a) bare c-Si, and c-Si Cat-doped for (b) 60 s and (c) 90 s.*

### 4.3.4 *The effect of light soaking on $\tau_{eff}$ of $SiN_x$/P Cat-doped layer/c-Si structure.*

The effect of light soaking on the passivation quality of passivation layers is very important for actual solar cell operation. It has been reported that defects on a $SiN_x$/c-Si interface are strongly accumulated by light soaking [34-37]. In this study, I also found that the passivation quality of $SiN_x$/c-Si and $SiN_x$/P Cat-doped layer/c-Si structures was deteriorated after long-time light exposure.

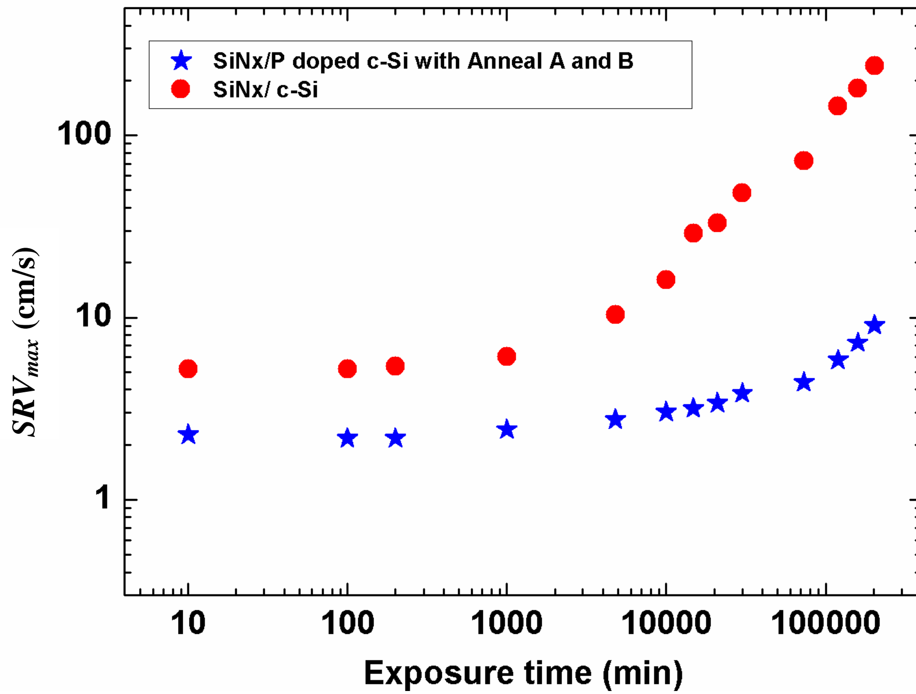


*Figure 4.21 $SRV_{max}$ of $SiN_x$/c-Si structure and $\tau_{eff}$ of $SiN_x$/P Cat-doped layer/c-Si structure (after anneal A and B) as a function of exposure time.*

Figure 4.21 shows the $SRV_{max}$ of $SiN_x$/c-Si structure and the $SRV_{max}$ of $SiN_x$/P Cat-doped layer/c-Si structure as a function of exposing time. One can see a increase in $SRV_{max}$ for both structures after long time light soaking, which might be related to light-induced defects in $SiN_x$ films. The evidence of photo-induced defects in amorphous $SiN_x$ films observed by ESR was firstly reported by Krick [34-37]. These defect centers are defects in $SiN_x$ films, which consist of a Si atom back-bonded to three N atoms whose configurations are shown in Figure 4.22. They were then named K centers, after Krick's name [35].

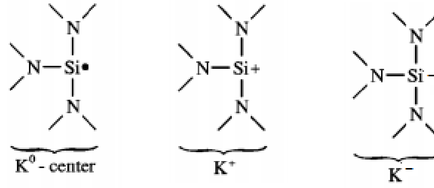


*Figure 4.22 Configurations of K centers and its states.*

By applying alternatively ultraviolet (UV) illumination and positive or negative bias, he found that UV illumination annihilates space charge and creates stable paramagnetic centers ($K^0$ centers) in $SiN_x$. This important result is shown in Figure 4.23. The paramagnetic defect is amphoteric, in other words, it can trap both holes and electrons. One can see in Figure 4.23 that defect density decreases after positive charging. It is explained that under positive bias, electrons tunnel from c-Si substrate to $SiN_x$ films, and they are trapped by these paramagnetic defects. These defects become negatively trapped centers ($K^-$ centers) and diamagnetic. After UV illumination, negative centers loss electrons and return to neutral in paramagnetic state as original. The behavior of C-V and ESR signal for the sample after negative bias and third illumination is explained by the same mechanism. After negative charging, positively trapped centers ($K^+$ centers) are formed.

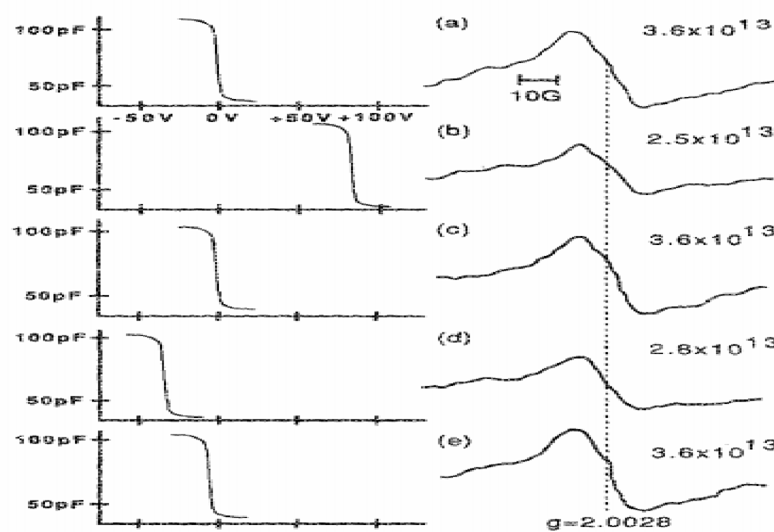


*Figure 4.23 CV curve and ESR signal with corresponding defect density (unit of $cm^{-3}$) of $SiN_x$/c-Si sample (in cycle): (a) after UV illumination, (b) after positive corona biasing, (c) second UV illumination, (d) after negative corona biasing, (e) after third UV illumination [35].*

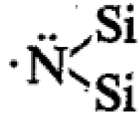


*Figure 4.24 Configuration of a N center.*

Warren *et.al* have reported that there are nitrogen (N) dangling bond defects existing in amorphous $SiN_x$ films [37]. They are two-coordinated N atoms with configuration shown in Figure 4.24. These defect centers are found in both as-deposited stoichiometric and N-rich $SiN_x$ films and after UV illumination. However, in my study, no signal of N dangling bond is observed, see Figures 4.25 and 4.26.

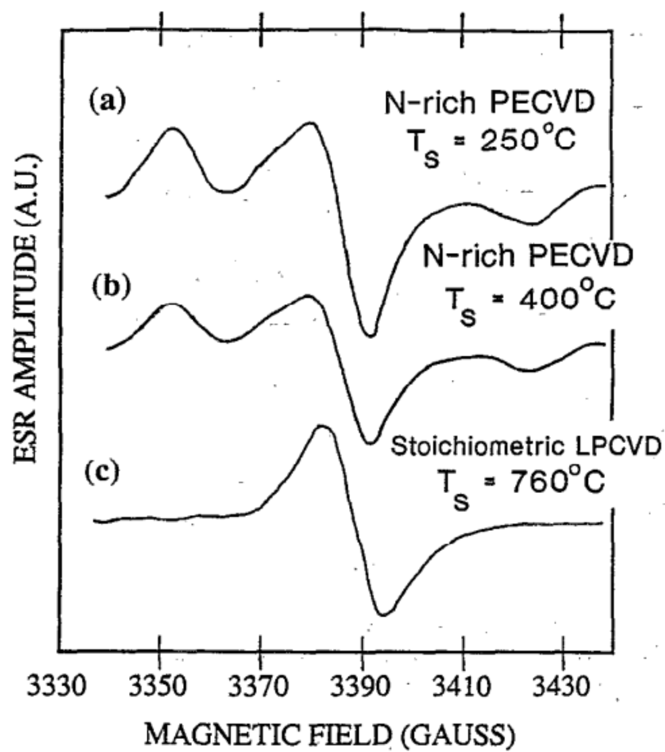


*Figure 4.25. The appearance of N dangling in $SiN_x$ films in ESR spectra: (a) and (b). N dangling bond signal (c) No N dangling bond [37].*

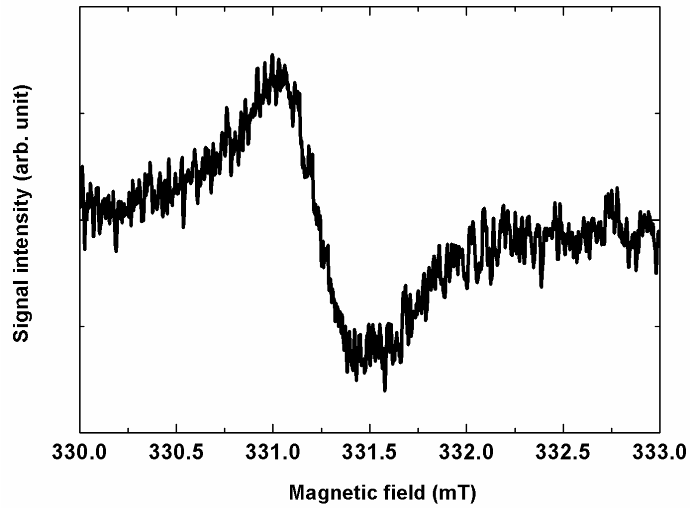


*Figure 4.26. A ESR signal obtained for $SiN_x$/glass in my study.*

Defect density related to Si dangling bonds in $SiN_x$ films increases with increase in light exposure time, as shown in Figure 4.27. Increase in defect density in $SiN_x$ films is probably accompanied with increase in defect density at $SiN_x$/c-Si, where photo-generated carriers in c-Si are easily trapped, and resulting increase in $SRV_{max}$. This fact is in agreement with previous reports [38-39].

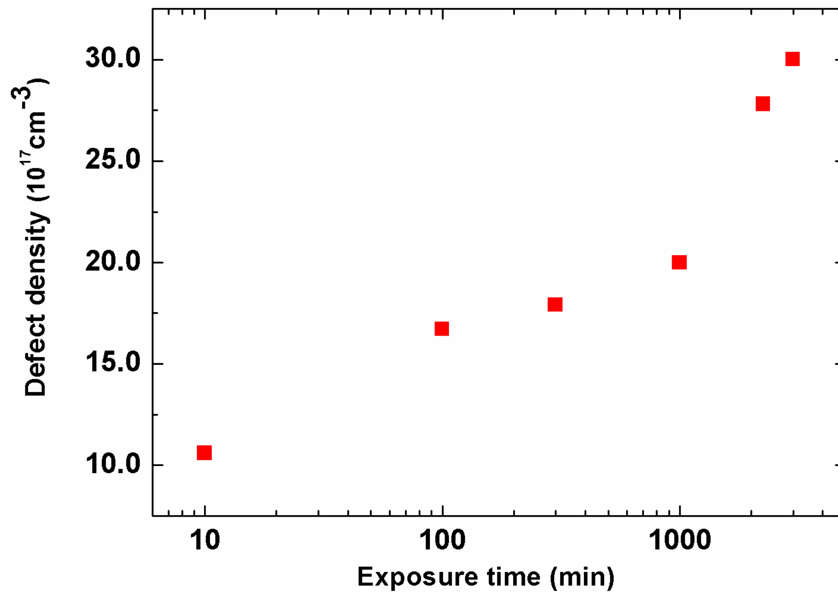


*Figure 4.27 Defect density of $SiN_x$ films as a function of exposure time.*

The recovery of the passivation quality of $SiN_x$ films by annealing has been reported by some lectures [38-40]. In my study, $SRV_{max}$ of $SiN_x$/c-Si sample, after light soaking to a stable value tends to recover to the original value of 5 cm/s when sample was annealing at 350 $^oC$ for 30 min. I also confirmed that the defect densities of the sample receiving light-soaking and annealing are nearly the same to that of the original sample before light soaking. This fact means that the properties of $SiN_x$ films are fully recovered after annealing. The effect of annealing process on $SRV_{max}$ of $SiN_x$/P Cat-doped layer/c-Si sample has not investigated yet because after light exposure for 5 months, $SRV_{max}$ of the sample is still increasing at present. The effect of annealing on $SRV_{max}$ of $SiN_x$/P Cat-doped layer/c-Si sample will be reported when $SRV_{max}$ reaches a stable value.

## 4.4 Conclusion

In conclusion, an extremely low $SRV_{max}$ of 2 cm/s can be obtained for the $SiN_x$/P Cat-doped layer/n-c-Si structure. Annealing plays important roles for improving the passivation quality of $SiN_x$ films and enhancing field-effect passivation. Additional annealing, before depositing $SiN_x$ films (annealing A) enhances the activation of P dopants in a P Cat-doped layer and improves passivation quality. Increase in $T_{s\text{-}dope}$ increases $N_D$, resulting in reduction in $SRV_{max}$. $SRV_{max}$ of the $SiN_x$/P Cat-doped/c-Si sample decreases with excessive $t_{dope}$ due to etching effect by radical species during P Cat-doping. An $SRV_{max}$ of 2 cm/s is obtained under optimum Cat-doping and annealing conditions for $SiN_x$ films on n-type c-Si wafers, indicating the potential application of Cat-CVD in producing high-efficiency c-Si solar cells. I emphasize that the use of a highly transparent $SiN_x$ passivation layer with a P Cat-doped layer can enhance the performance of n-type c-Si solar cells, particularly of back-contact solar cells.

**References**


[1] H. Matsumura, *J. Appl. Phys.* **65** (1989) 4396.

[2] K. Koyama, K. Ohdaira and H. Matsumura, *Appl. Phys. Lett.* **97** (2010) 082108.

[3] Trinh Cham Thi, K. Koyama, K. Ohdaira, and H. Matsumura, *Sol. Energy Mater. Sol. Cells* **93** (2012) 169.

[4] T. Hayakawa, Y. Nakashima, K. Koyama, K. Ohdaira, and H. Matsumura, *Jpn. J. Appl. Phys.* ***51*** (2012) 061301.

[5] T. Hayakawa, T. Ohta, Y. Nakashima, K. Koyama, K. Ohdaira, and H. Matsumura, *Jpn. J. Appl. Phys.* **51** (2012) 101301.

[6] T. Hayakawa, Y. Nakashima, M. Miyamoto, K. Koyama, K. Ohdaira, and H. Matsumura, *Jpn. J. Appl. Phys.* **50** (2011) 121301.

[7] H. J. Gossmann and F. C. Unterwald, *Phys. Rev. B* **47** (1993) 12618.

[8] F. J. Ruess, L. Oberbeck, M. Y. Simmons, K. E. J. Goh, A. R. Hamilton, T. Hallam, S. R. Schofield, N. J. Curson, and R. G. Clark, *Nano Lett.* **4** (2004) 1969.

[9] Y. Shimamune, M. Sakuraba, J. Murota, and B. Tillack, *Appl. Surf. Sci*. **224** (2002) 202.

[10] N. L. Mattey, M. G. Dowsett, E. H. C. Parker, T. E. Whall, S. Taylor, and J. F. Zhang, *Appl. Phys. Lett*. **57** (1990) 1648.

[11] H. P. Zeindl, T. Wegehaupt, I. Eisele, H. Oppolzer, H. Reisinger, G. Tempel, and F. Koch, *Appl. Phys. Lett.* **50** (1987) 1164.

[12] H. Matsumura M. Miyamoto, K. Koyama and K. Ohdaira, *Sol. Energy Mater. Sol. Cells* **95** (2011) 797.

[13] W. Clarke, X. Zhou, A. Fuhrer, T. Reusch, and M. Simmons, *Physica E* **40** (2008) 1566.

[14] H. Luth, *Solid Surfaces, Interfaces and Thin Films*, (Springer, Heidelberg, 2010), p.323.

[15] V. Yelundur, A. Rohatgi, J.I. Hanoka, R. Reedy, Proc. 19th European Photovoltaic Solar Energy Conference, Paris, France, June 2004, p. 951.

[16] B. Sopori, Y. Zhang, R. Reedy, K. Jones, Y. Yan, M. A. Jassim, B. Bathey and J. Kalejs, Proc. 31st Photovoltaic Specialists Conference, Orlando, USA, January 2005, p. 1039.

[17] F. Duerinckx and J. Szulfcik, *Sol. Energy Mater. Sol. Cells* **72** (2002) 231.

[18] T. Lauinger, A.G. Aberle, R. Hezel, Proc. 14th European Photovoltaic Solar Energy Conf., 1997, p. 853.

[19] V. Yelundur, A. Rohatgi, J.I. Hanoka, R. Reedy, Proc. 19th European Photovoltaic Solar Energy Conf., 2004, p. 951.

[20] Y. Larionova, V. Mertens, N. Harder, and R. Brendel, *Appl. Phys. Lett.* **101** (2012) 201601.

[21] J. Hong, W. M. M. Kessels, W. J. Soppe, A. W. Weeber, W. M. Arnolbik and M. C. M van de Sande, *J. Vac. Sci. Technol. B* **21** (2003) 2123.

[22] H. Umemoto, Y. Nishihara, T. Ishikawa and S. Yamamoto, *Jpn. J. Appl. Phys.* **51** (2012) 086501.

[23] M. L. Yu, J. J. Vitkavage and B. S. Meyerson, *J. Appl. Phys.* **59** (1986) 4032.

[24] M. L. Yu and B. S. Meyerson, *J. Vac. Sci. Technol. A* **2** (1984) 446.

[25] H. W. Tsai and D. S. Lin, *Surf. Sci.* **482-485** (2001) 654.

[26] S. R. Schofield, N. J. Curson, O. Warschkow, N. A. Marks, H. F. Wilson, M. Y. Simmons, P. V. Smith, M. W. Radny, D. R. McKenzie and R. G. Clark, *J. Phys. Chem. B* **110** (2006) 3173.

[27] H. Nagayoshi, M. Ikeda, M. Yamaguchi, T. Uematsu, T. Saitoh and K. Kamisako, *Jpn. J. Appl. Phys.* **36** (1997) 5688.

[28] Y. Lee, W. Oh, V. A. Dao, S. W. Hussain and J. Yi, *Int. J. Photoenergy* **2012** (2012) 753456.

[29] S. W. Glunz, *Advanced optoelectronics* **2007** (2007) 97370.

[30] S. Duttagupta, B.Hoex, A. G. Aberle, in the 22nd International Photovoltaic Science and Engineering Conference, Hangzhou, China (November, 2012).

[31] J Schmidt and M. Kerr, *Sol. Energy Mater. Sol. Cells* **65** (2001) 585.

[32] F. Khanom, A. Aoki, F. Rahman and A. Namiki, *Surf. Sci.* **536** (2003) 191.

[33] Y. Narita, Y. Kihara, S. Inanaga, and A. Namiki, *Surf. Sci.* **603** (2009) 1168.

[34] D. T. Krick, P. M. Lenahan, and J. Kanicki, *J. Appl. Phys.* **64** (1988) 3558.

[35] P. M. Lenahan, D. T. Krick, and J. Kanicki, *Appl. Surf. Sci.* **39** (1989) 392.

[36] P. M. Lenahan and S. E. Curry, *Appl. Phys. Lett.* **56** (1990) 157.

[37] W. L. Warren and P. M. Lenahan, *Phys. Rev. B* **42** (1990) 1773.

[38] M. Tucci, L. Serenelli, S. De Iuliis, M. Izzi, P. Mangiapane, A. Cuevas, J. Mitchell, *Thin Solid Films* **515** (2007) 7625.

[39] J. Arumughan, J. Theobald, M. Wilson, L. Hildebrand, R. Peters, A. Savtchouk, J. Lahowski and R. Kopecek. Proc. 26th European Photovoltaic Solar Energy Conf., 2011, p. 1014.

[40] S. K. Colberg, N. Barkmann, C. Streicch, A. Schütt, D. Suwito, P. Schäfer, S. Müller, D. Borchert, Proc. 26th European Photovoltaic Solar Energy Conf., 2011, p.1770

# Chapter 5 Passivation quality of a Cat-CVD $SiN_x$ single layer and Cat-CVD $SiN_x$/ P Cat-doped layers on textured c-Si

## 5.1 Introduction

In the previous chapters, I have succeeded to obtain extremely low $SRV_{max}$ for c-Si passivated with a $SiN_x$ layer and $SiN_x$/P Cat-doped layers. The important fact is the realization of a sufficiently low $SRV_{max}$ with high-transparency $SiN_x$ films, which are very suitable for application in passivation technique for c-Si solar cells. In my study, I aim to apply these passivation layers for back-contact solar cells. The simple schematic structure of a back contact solar cell which I try to fabricate in my study is shown in Figure 5.1.

In order to achieve high solar cell efficiency, the utilization of textured c-Si wafers is essential because it can enhance light trapping and reduce reflectance [1, 2, 3]. A significant improvement in optical loss by light trapping and reflectance reduction is schematically described in Figure 5.2. Therefore, in this chapter, I will examine the passivation quality of $SiN_x$ and $SiN_x$/P Cat-doped layer structures on textured c-Si wafers.

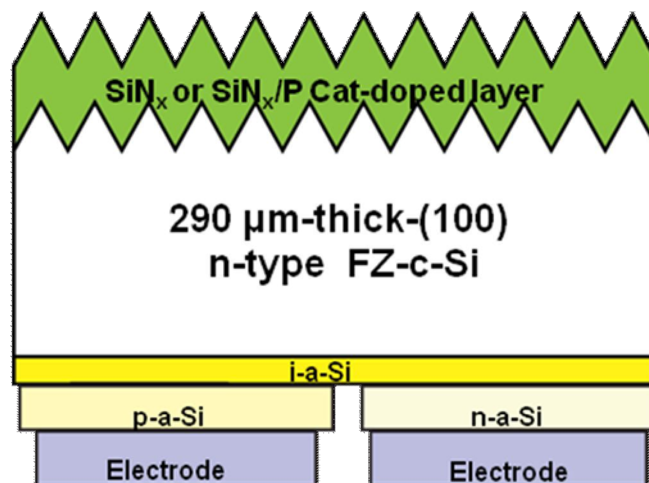


*Figure 5.1. Cross-sectional schematic of a back contact solar cell in my study.*

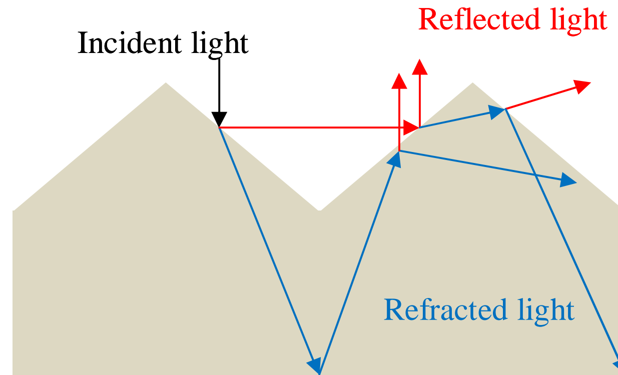


*Figure 5.2. light trapping inside a c-Si substrate and reflection on the Si surface*

## 5.2 c-Si texturing and cleaning processes

*Table 5.1. Etching rate of c-Si (μm/min) in KOH solution for different c-Si surface orientations at various KOH concentration at a temperature of 70 $^{o}$C. The values in bracket are relative values to (110) surface [5].*

| Crystallographic Orientation | Rates at different KOH Concentration | | |
|---|---|---|---|
| | 30% | 40% | 50% |
| (100) | 0.797 (0.548) | 0.599 (0.463) | 0.539 (0.619) |
| (110) | 1.455 (1.000) | 1.294 (1.000) | 0.870 (1.000) |
| (210) | 1.561 (1.072) | 1.233 (0.953) | 0.959 (1.103) |
| (211) | 1.319 (0.906) | 0.950 (0.734) | 0.621 (0.714) |
| (221) | 0.714 (0.491) | 0.544 (0.420) | 0.322 (0.371) |
| (310) | 1.456 (1.000) | 1.088 (0.841) | 0.757 (0.871) |
| (311) | 1.436 (0.987) | 1.067 (0.824) | 0.746 (0.858) |
| (320) | 1.543 (1.060) | 1.287 (0.995) | 1.013 (1.165) |
| (331) | 1.160 (0.797) | 0.800 (0.619) | 0.489 (0.563) |
| (530) | 1.556 (1.069) | 1.280 (0.989) | 1.033 (1.188) |
| (540) | 1.512 (1.039) | 1.287 (0.994) | 0.914 (1.051) |
| (111) | 0.005 (0.004) | 0.009 (0.007) | 0.009 (0.010) |

Textured c-Si wafers were prepared by dipping 290-μm-thick (100) n-type flat c-Si wafers (the same wafers for lifetime measurement in the previous chapters) into SUN-X 600 solution diluted with $H_2O$ with a ratio of 1:3. The etching process for some samples

was conducted in a stirring hot plate to make uniform surface morphology. SUN-X 600 is a product of Wako pure Chemical Co., Ltd., which contains alkali solution (ex. potassium hydroxide (KOH)) and other components [4]. Textured structure on c-Si was formed by orientation-dependent wet etching, as shown in Table 5.1 [5]. Alkali solution has high etching rate for Si (100) and (110) surfaces, while its etching rate for (111) surface is significantly low. This is the reason why pyramid structure is formed on alkali-etched c-Si (see Figure 5.3)

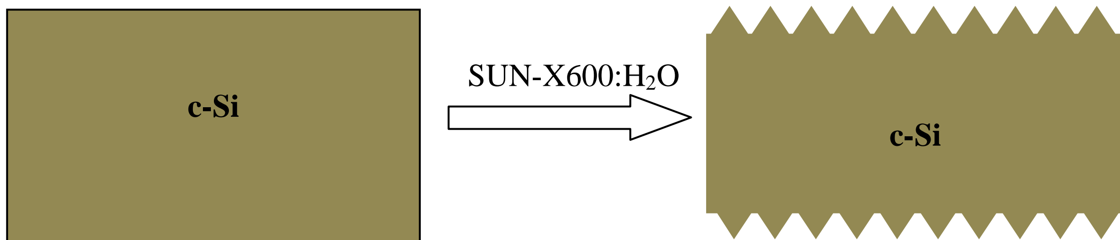


*Figure 5.3. Change of c-Si surface morphology after etching*

The detailed mechanism of c-Si etching by alkali solution is illustrated as below [6]:

$$4H_2O \rightarrow 4OH^- + 4h^+ + 2H_2$$

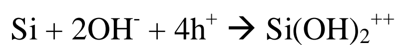

$$Si + 2OH^- + 4h^+ \rightarrow Si(OH)_2^{++}$$

Silicate reacts with hydroxyls to from a water soluble complex:

$$Si(OH)_2^{++} + 2H_2O \rightarrow SiO_2(OH)_2^{2-} + 2H_2$$

c-Si wafers after the alkali etching need careful cleaning process to remove all contaminations remaining on their surfaces. In this study, standard cleaning were employed to clean textured c-Si samples following the chart below:

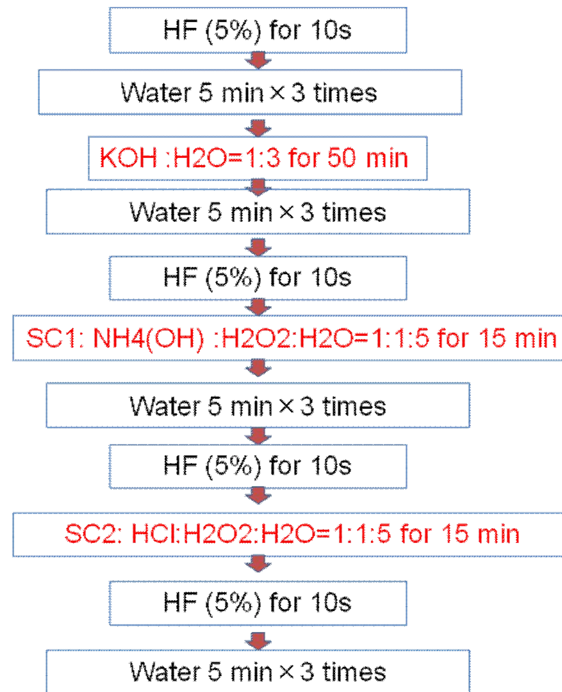


*Figure 5.4: c-Si etching and cleaning steps*

The first standard cleaning (SC-1) is for the removal of organic and particles. Boiling SC1 solution chemically attacks organic impurities, resulting in the removal of these impurities out of a c-Si surface. The mechanism of removing particles by SC-1 is clarified by Itano *et al.*, shown in Figure 5.5 [7]. Particles are lifted off by etching solution, and then electrically repelled from a c-Si surface. Samples were then put in water in ultrasonic cleaner for 5 min, which was repeated 3 times. Hydrofluoric acid in water (5%) is needed to trip oxide formed on a c-Si surface. The second standard cleaning (SC-2) is to dissolve ionic contaminations.

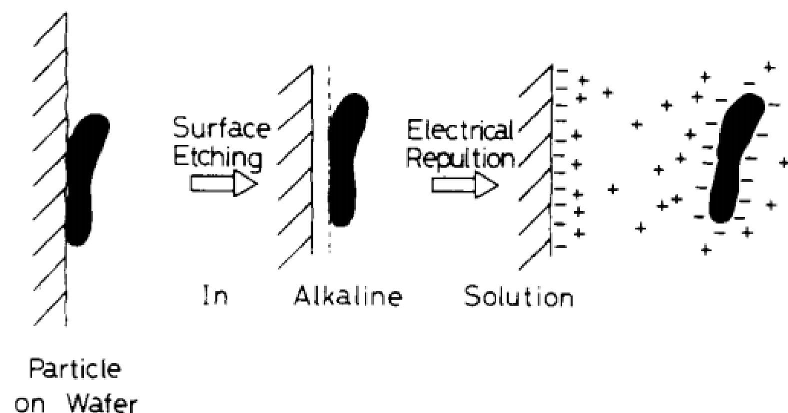


*Figure 5.5. Mechanism of removing particles on a c-Si surface by $NH_4(OH):H_2O_2:H_2O$*

*Table 5.2. Conditions of $SiN_x$ deposition and P Cat-doping.*

| | Doping | $SiN_x$ |
|---|---|---|
| Gas sources | $PH_3$ 20 sccm | $SiH_4$: 8 sccm<br>$NH_3$: 150 sccm |
| Substrate temperature ($T_{s\text{-}dope}$) | 80-300 $^{o}$C | 100 $^{o}$C |
| Pressure ($P$) | 1.0 Pa | 10 Pa |
| Catalyzer temperature ($T_{cat}$) | 1300 $^{o}$C | 1800 $^{o}$C |
| Catalyzer –substrate distance | 12 cm | 8 cm |
| Time ($t$) | 30-120 s | 184 s |

Textured c-Si samples were then passivated with $SiN_x$ films or $SiN_x$/P Cat-doped layers to investigate the passivation quality and reflectance of the samples. The conditions of $SiN_x$ deposition and P Cat-doping are the same with those at which the highest $\tau_{eff}$ is achieved on flat c-Si samples, as summarized in Table 5.2. The surface morphology of the samples was observed by scanning electron microscopy (SEM). The optical reflectance of the samples was measured by using UV-Vis spectroscopy.

## 5.3 Morphology of textured c-Si surfaces and their optical reflectance

Flat c-Si samples were etched for different duration in SUN-X/$H_2O$ solution (1:3) at various etching temperature. Figure 5.6 shows the SEM images of the samples etched at 65, 70 and 80 $^oC$ for 50 min.

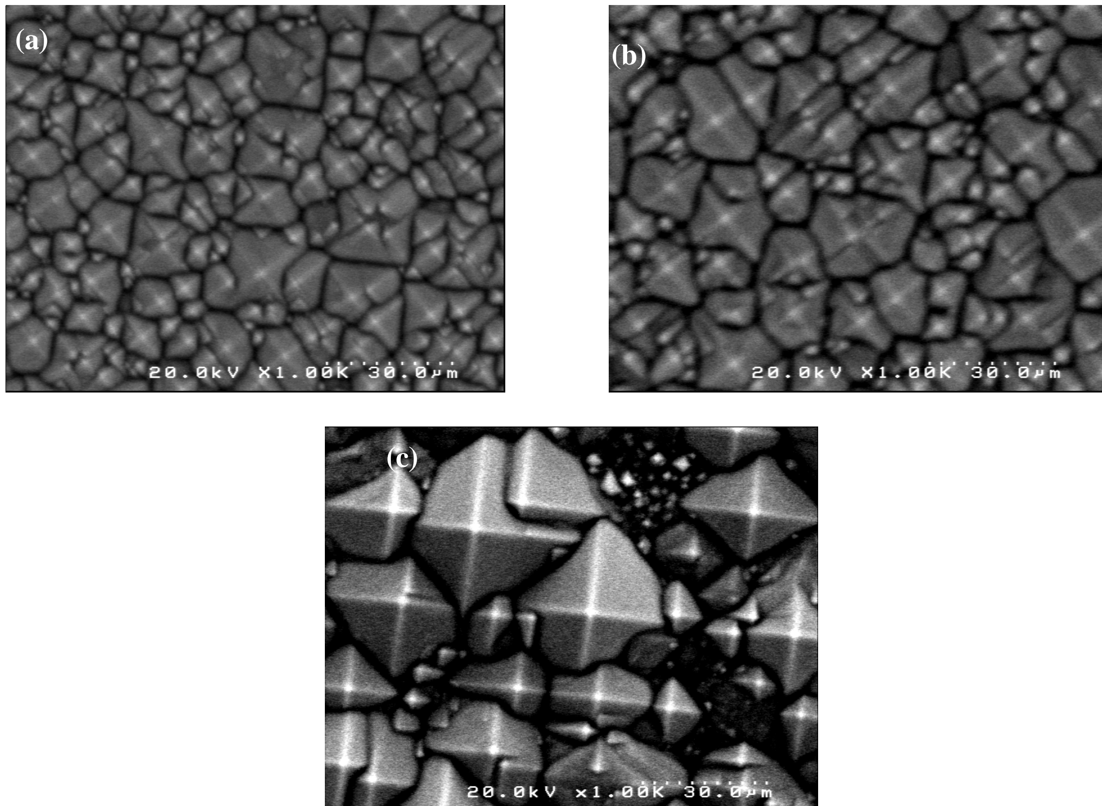


*Figure 5.6. SEM images of textured c-Si samples at (a) 65 $^oC$, (b) 70 $^oC$, (c) 80 $^oC$*

One can see that pyramid size depends strongly on etching temperature. The etching rate of c-Si by alkali solution usually increases with increase in etching temperature [10]. The sample etched at 70 $^oC$ shows more uniform morphology than others. Figure 5.7 describes an increase in the $SRV_{max}$ of the textured c-Si wafers passivated with $SiN_x$ films with increase in etching temperature. The increase in $SRV_{max}$ may be due to increase in surface area, un-coverage surface, and/or the emergence of (111) surface. Increase in surface area leads to increase in the probability of carrier trapping. A textured c-Si surface might also prevent the uniform deposition of $SiN_x$ films, resulting in the presence of unpassivated region. Difference in surface orientation may cause different

passivation property of $SiN_x$ films, resulting in high $SRV_{max}$. I have also confirmed that the passivation property of $SiN_x$ films and $SiN_x$/P Cat-doped layers on (111) surface is less significant than that on (100) surface. Figure 5.8 demonstrates that $SRV_{max}$ of (111)-oriented mirror-polished wafers passivated with $SiN_x$ films and $SiN_x$/P Cat-doped layers are 6.6 cm/s and 3.2 cm/s, respectively. These values are smaller than those in the case of the (100)-oriented c-Si samples.

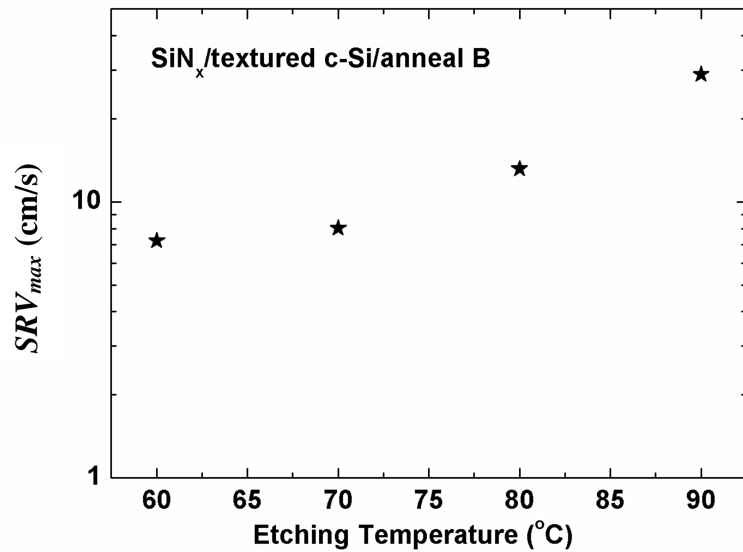


*Figure 5.7. $SRV_{max}$ of textured c-Si wafers passivated with $SiN_x$ films as a function of etching temperature.*

Figure 5.9 shows the optical reflectance spectra of textured c-Si and $SiN_x$/textured c-Si samples after etching for 25 and 50 min at 70 °C. A significant reduction in optical reflectance can be obtained after long time etching. When textured c-Si wafers were covered with $SiN_x$ films, a drastic reduction in optical reflectance is observed. In a visible region, reflectance is suppressed to be less than 10%. The reduction is attributed by the anti-reflective $SiN_x$ coating layer and texturing structure.

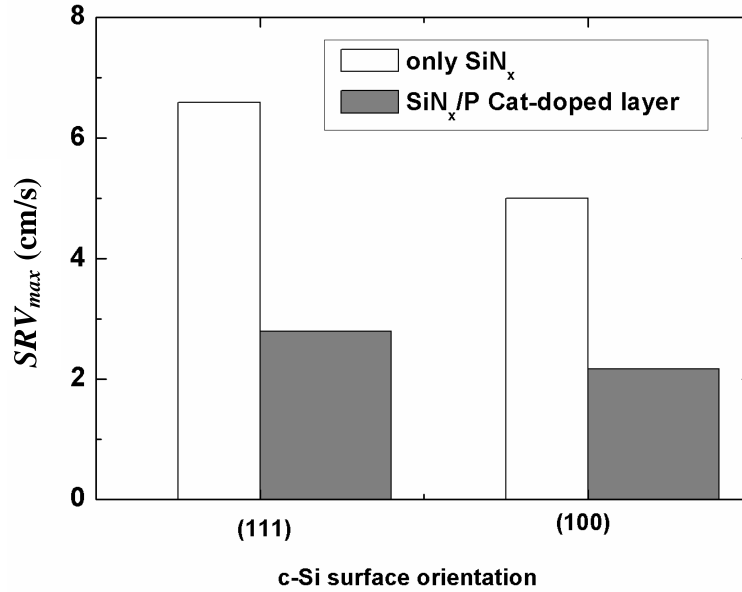


*Figure 5.8. $SRV_{max}$ of c-Si wafers passivated with $SiN_x$ and $SiN_x$/P Cat-doped layers with different surface orientation.*

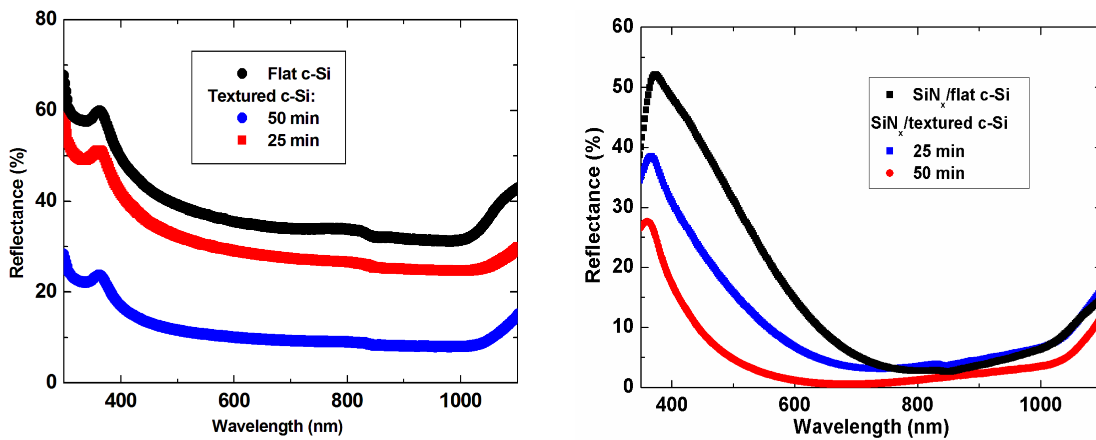


*Figure 5.10. Optical reflectance spectra of bare c-Si and $SiN_x$/c-Si surfaces before and after texturing at 70 $^oC$ for 25 and 50 min.*

However, $SRV_{max}$ increases with increase in etching time, as shown in Figure 5.11. The reason of $SRV_{max}$ increase is probably the same as the case of $SRV_{max}$ increase with increase in etching temperature discussed above. $\tau_{eff}$ obtained for the sample etched for 50 min is 1.8 ms, corresponding to a $SRV_{max}$ of 8.2 cm/s. It is low enough to apply to surface passivation for high-efficiency back-contact c-Si solar cell fabrication, as discussion in Chapter 1.

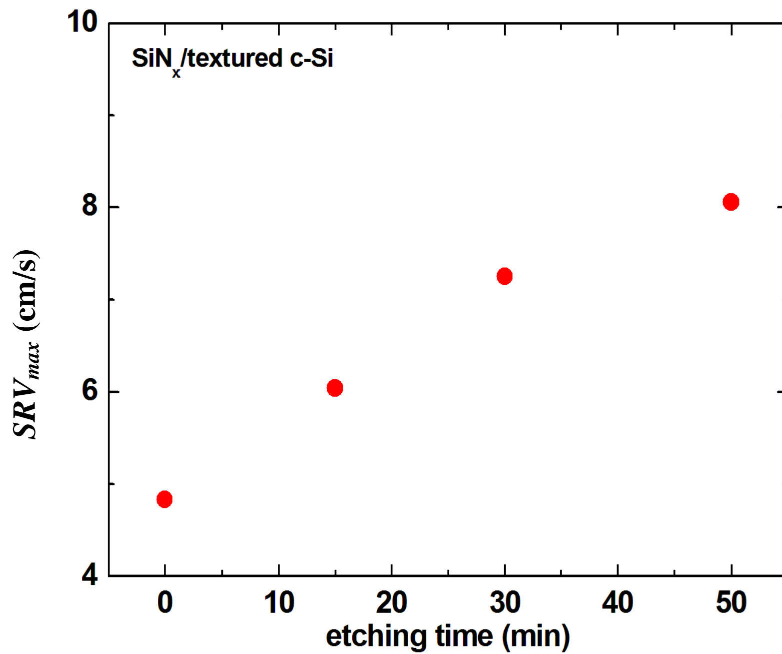


*Figure 5.11. $SRV_{max}$ of c-Si wafers passivated with $SiN_x$ as a function of etching time.*

The use of a stirring water bath during the etching of c-Si wafers can improve the uniformity of the surface morphology of textured c-Si wafers because of more uniform heat distribution. Some samples were etched at 70 °C for 50 min at various stirring speeds. The rotation speed was set to be 100 rpm or less because samples move more quickly at higher stirring speed during etching and the uniformity of the c-Si samples rather becomes worse. The result obtained shows that $SRV_{max}$ and reflectance are improved when the samples are etched at a stirring speed of 100 rpm, as shown in Figure 5.12. $\tau_{eff}$ obtained for the sample etched at a stirring speed of 100 rpm is 2.0 ms, corresponding to a $SRV_{max}$ of 8.0 cm/s. The surface SEM images of the samples etched with and without stirring are shown in Figure 5.13.

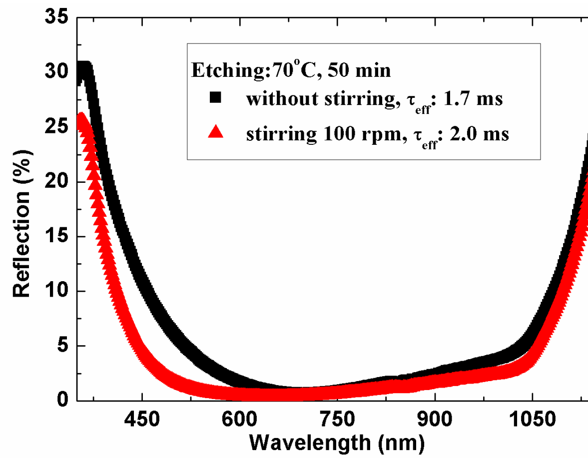


*Figure 5.12. Optical reflectance spectra of the samples etched with and without stirring. $\tau_{eff}$ of the samples are also shown.*

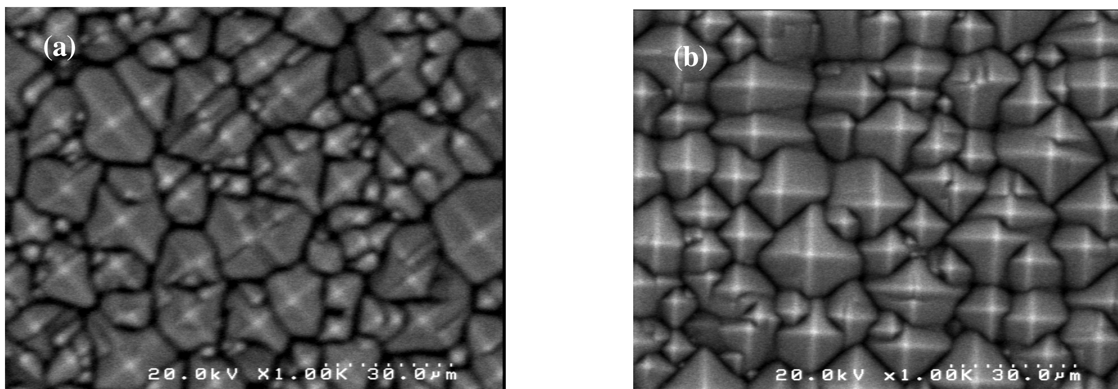


*Figure 5.13. Surface SEM images of the samples etched (a) without and (b) with stirring.*

For the sample etched at a stirring speed of 30 rpm, alike the sample without stirring, non-uniform surface morphology can be seen. Furthermore, the two surfaces on the sample show different optical reflectance, as shown in Figure 5.14, which is another indication of insufficient uniformity.

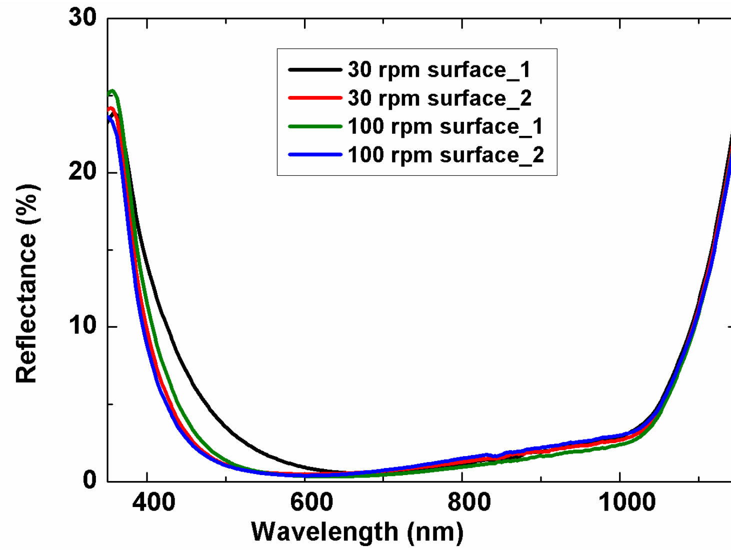


*Figure 5.14. Optical reflectance spectra of the samples etched with stirring at a speed of 100 and 30 rpm.*

I performed P Cat-doping on textured c-Si surfaces formed under the conditions by which $\tau_{eff}$ reaches the highest value (2 ms) when $SiN_x$ films are deposited. $\tau_{eff}$ of 2.5 ms, corresponding to a $SRV_{max}$ of 6.7 cm/s, can be obtained for the $SiN_x$/P Cat-doped layer/c-Si structure. P doping can considerably suppress the surface recombination of minority carriers on a textured c-Si surface but not as significantly as in the case on a flat surface. This fact implies that a textured surface might be more difficult to uniformly form a P Cat-doped layer, that is, some area cannot be covered with a P Cat-doped layer. A comparison between $SRV_{max}$ of samples passivated with $SiN_x$ and $SiN_x$/P Cat-doped layers on flat and textured c-Si is illustrated in Figure 5.15.

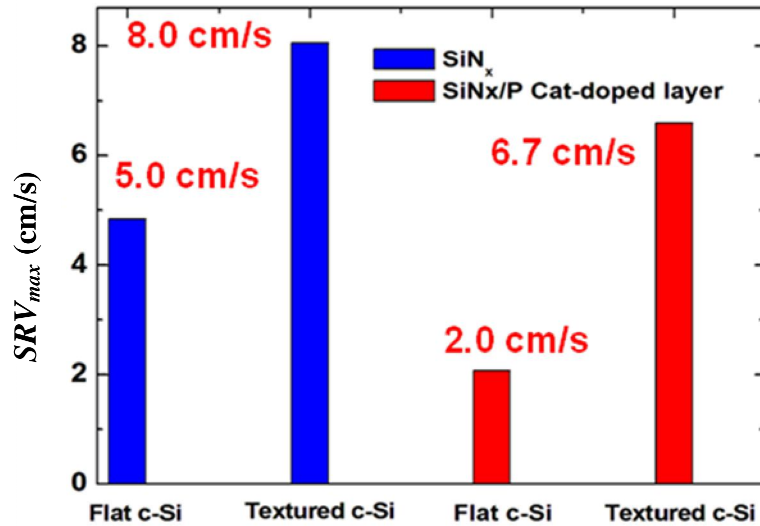


*Figure 5.15. $SRV_{max}$ of flat and textured c-Si samples passivated with $SiN_x$ and $SiN_x$/P Cat-doped layers.*

## 5.4 Conclusion

$SiN_x$ films and $SiN_x$/P Cat-doped layers demonstrate high passivation ability on textured c-Si wafers, which are essential for high-performance solar cells due to its ability of lowering optical reflectance and enhancing light trapping inside c-Si absorber. P Cat-doping is not only effective on flat c-Si but also on textured c-Si surface. A $SRV_{max}$ of 8.0 cm/s is obtained for the $SiN_x$/textured c-Si structure. $SRV_{max}$ decreases to 6.7 cm/s when P Cat-doping is applied. Low optical reflectance less than 10% in visible range can be achieved for these structures. This demonstrates that $SiN_x$/P Cat-doped layers can be used as a favorable passivation layer in producing high-efficiency n-type back-junction solar cells.

**References**

[1] M. A. Green, *Prog. Photovolt*: Res. Appl. **10** (2002) 235.

[2] P. Campbell and M. A. Green, *J. Appl. Phys.* **62**, (1987) 243.

[3] B. G. Lee, Y. T. Lin, M. J. Sher, E. Mazur and H. M. Branz, The 38th IEEE Photovoltaic Specialists conference, Austin, Texas, June 3-8, 2012, p. 001606.

[4] http://www.docin.com/p-33590019.html

[5] http://www.virginiasemi.com/pdf/siliconetchingandcleaning.pdf

[6] H. Seidel, L. Csepregi, A. Heuberger, H. Baumgärtel, *Electrochem. Soc.* **137** (1990) 3612.

[7] M. Itano, F. W. Kern, Jr., M. Miyashita and T. Ohmi, *IEEE Trans. Semicond. Manuf.* **6** (1993) 258.

[8] W. Kern, *J. Electrochem. Soc.* **137** (1990) 1889.

[9] http://www.microtechprocess.com/pdf/MTS_RCA.pdf

[10] P. A. Alvi, V. S. Meel, K. Sarita, J. Akhtar, K. M. Lai, A. Azam, and S. A. H. Naqvi, *Int. J. Chem. Sci.* **63** (2008) 1168.

# Chapter 6 Application of Cat-CVD $SiN_x$ and $SiN_x$/ P Cat-doped layers on back contact back junction solar cells

## 6.1. Introduction

In the previous chapters, I have succeeded to obtain low SRVs for both flat and textured c-Si by passivating Cat-CVD $SiN_x$ and $SiN_x$/P Cat-doped layers. A low $SRV_{max}$ of 2 and 6.7 cm/s can be obtained for flat and textured c-Si surface passivated by $SiN_x$/P Cat-doped layer, respectively. By using high transparency Cat-CVD $SiN_x$ and textured surface, a low optical reflection of less than 10% for visible region can be realized. These important results indicate potential application of these passivation layers to actual solar cells. In order to elucidate the promising features, in this chapter, I would like to apply these passivation layers to back-contact solar cells. Back contact solar cells have many advantages, due to their structure with no contact on the front side, such as no shading loss, no trade-off between series resistance and reflection, easier and simpler module process than conventional cells. By applying high transparency and passivation quality Cat-CVD $SiN_x$/ P Cat-doped layers, high solar cell efficiency would be expected.

## 6.2. Theory of solar cell and its characteristics

### *6.2.1. Working principle of solar cell*

In the first part of this chapter, I would like to briefly introduce solar cell and its characteristics.

Solar cell is an electronic device which directly converts sun-light into electricity based on photovoltaic effect. When light with sufficient energy comes to absorber material, an electron in material absorbs photon energy is exited to conduction band. A pair of a free electron and a hole is generated. “Light with sufficient energy” means that photon energy is equal or higher than material’s band gap so that electron can jump from valence band to conductance band to become free electron. For p/n junction solar cell, under illumination, free electrons generated in p-type region flow into n-type region through the p/n junction

to reach an electrode and are collected there. Free holes generated in n-type region travel in the opposite direction, flow into p-type region through p/n junction to reach electrode, and are collected there. If electrodes are connected to a load, electrons flow around electrical circuit, create an electric current and recombine with hole at the contact. An illustration of the process is shown in Figure 6.1.

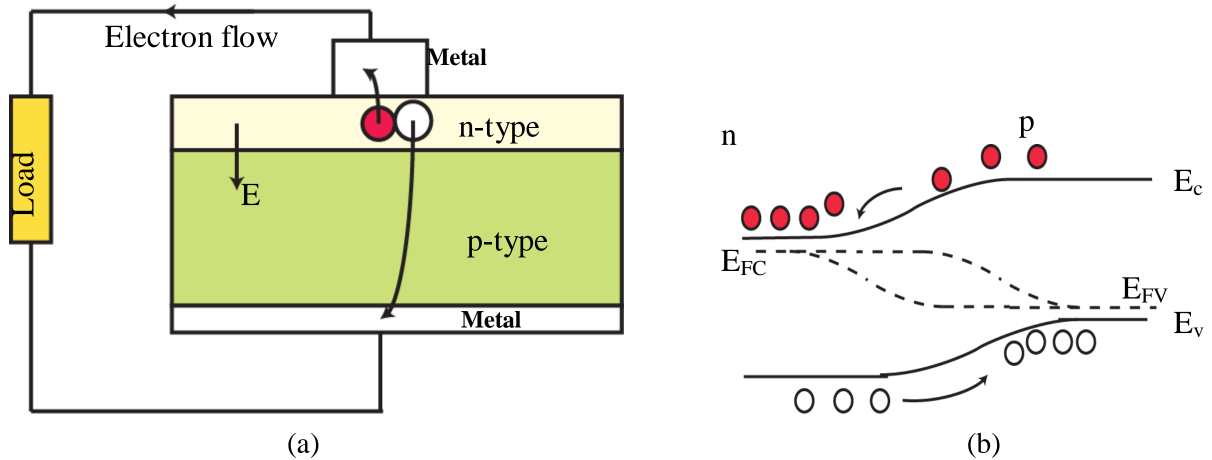


*Figure 6.1. (a) Electron (pink circle) and hole (white circle) flow through p/n junction of solar cell and (b) energy band under illumination*

The collection probability of photo-generated carriers depends on surface properties and distance that carriers have to travel to reach electrodes. The travelling distance must be sufficiently smaller than base and emitter diffusion length. For a conventional solar cell structure as shown in Figure 6.1, base is p-type and emitter is n-type. Surface of device should be good so that photo-generated carriers are not frequently trapped on surface states. The parameter to evaluate surface property is surface recombination velocity (SRV), which indicate how fast or slow carriers will recombine on the surface. In my study, a low $SRV_{max}$ of 2 cm/s is obtained for n-type c-Si passivated with $SiN_x$/P Cat-doped layers, as I mentioned in the previous chapters.

### *6.2.2.* Solar cell parameters

A solar cell can be represented as an equivalent circuit shown in Figure 6.2. $I_{ph}$ is photo-generated current. $R_s$ is series resistance which originates from the resistance of the metal contact, contact between electrodes and cell, impurity concentration, and junction depth [1]. $R_{sh}$ is shunt resistance, which is caused by a parallel current path along the edge of the cell and/or crystal defects.

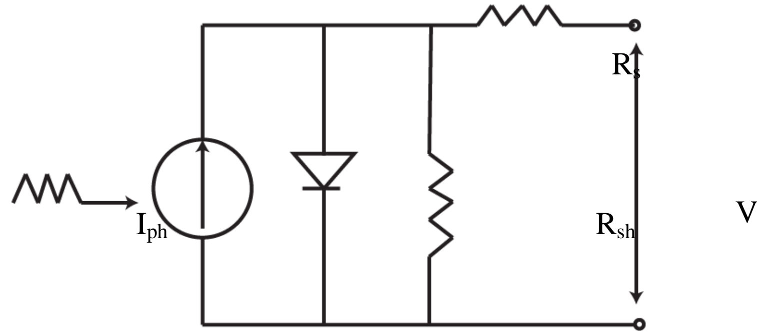


*Figure 6.2. Equivalent circuit of a solar cell.*

In dark, the solar cell behaves as a diode. When voltage is applied, current flows in the solar cell. Ideal dark current of the cell is drawn in Figure 6.3 and described as:

$$I = I_s\left(\exp(\frac{qV}{nkT}) - 1\right),$$

where $I_s$ is saturation current of diode and $V$ is voltage across the cell.

Under illumination, photo-carriers are generated and current flows out of the cell. Photo-current of the cell in the ideal case is described as:

$$I = I_{ph} + I_s\left(\exp(\frac{qV}{nkT}) - 1\right).$$

In the actual case with $R_s$ and $R_{sh}$, photo-current is:

$$I = -I_{ph} + I_s \exp(\frac{q(V - IR_s)}{nkT}) + \frac{V - IR_s}{R_{sh}}$$

In order to evaluate solar cell efficiency, there are three important parameters: short circuit current ($I_{sc}$), open circuit voltage ($V_{oc}$) and fill factor ($FF$). Solar cell efficiency is calculated as below:

$$\eta = \frac{P_{max}}{P_{in}} = \frac{V_{oc} I_{sc} FF}{P_{in}},$$

where $P_{max}$ is maximum power, that is, the maximum product of photocurrent and voltage, and $P_{in}$ is input power.

$V_{oc}$ is a voltage at which $I$ =0. Therefore, $V_{oc}$ is

$$V_{oc} = \frac{nkT}{q} \ln\left( \frac{I_{ph}}{I_s} + 1 \right)$$

Because $I_s$ depends on the amount of carrier recombination in the device, $V_{oc}$ also depends on the recombination. Therefore, $V_{oc}$ is affected by some factors such as material quality, material doping, and surface passivation quality. $V_{oc}$ can also be determined from carrier concentration as [3]:

$$V_{oc} = \frac{kT}{q} \ln\left( \frac{(N_A + \Delta n)\Delta n}{n_i^2} \right)$$

$V_{oc}$ calculated from this equation can be called as implied $V_{oc}$.

The equation shows relationship between $V_{oc}$ and recombination as below:

$$V_{oc} = \frac{kT}{q} \ln\left( \frac{J_{sc} N_D \tau_{eff}}{q n_i^2} \right)$$

Where, $\frac{1}{\tau_{eff}} = \frac{1}{\tau_{bulk}} + \frac{2SRV}{W}$

Where, $W$ is thickness of cell, SRV is surface recombination velocity and $\tau_{bulk}$ is bulk lifetime.

$I_{sc}$ is photo-current when voltage is equal to 0. $I_{sc}$ depends on the factors such as the area of a solar cell, number of photons, the spectrum of the incident light, the optical properties and the collection probability. To remove the effect of area, current density is usually used instead of current. The maximum short circuit current produced by the absorbed photo-current and is calculated by [4]:

$$J_{sc} = -e \int_0^\infty \alpha(\hbar\omega) dJ_{\gamma,sun}(\hbar\omega) = -e \int_{E_g}^\infty dJ_{\gamma,sun}(\hbar\omega),$$

where $E_g$ is band energy gap and $\alpha(\hbar\omega)$ is absorptivity. For a cell with large thickness and large diffusion length, if $\hbar\omega > E_g$, $\alpha(\hbar\omega)$ equal to 1; $J_{\gamma,sun}$ is photo-current density.

$J_{sc}$ is also calculated as sum of current from depletion region $J_{dr}$, hole current from n-type region $J_p$ and electron current from p-type region $J_n$ as below:

$$J_p = \left[ q\phi(1-R)\frac{\alpha L_p}{\alpha^2 L_p^2 - 1} \right] \times \left[ \frac{\left( \frac{S_p L_p}{D_p} + L_p \right) - \exp(-\alpha x_j)\left( \frac{S_p L_p}{D_p}\cosh\frac{x_j}{L_p} + \sinh\frac{x_j}{L_p} \right)}{\frac{S_p D_p}{D_n}\sinh\frac{xj}{L_p} + \cos\frac{xj}{L_p}} \right] - \alpha L_p \exp(-\alpha x_j)$$

$$J_p = \left[ q\phi(1-R)\frac{\alpha L_n}{\alpha^2 L_n^2 - 1} \right] \times$$

$$\left[ \frac{\left( \frac{S_n L_n}{D_n}\left( \cosh\frac{H^{'}}{L_n} - \exp(-\alpha H^{'}) \right) + \sinh\frac{H^{'}}{L_n} + \alpha L_n \exp(-\alpha H^{'}) \right)}{\frac{S_n L_n}{D_n}\sinh\frac{H^{'}}{L_n} + \cosh\frac{H^{'}}{L_n}} \right] \times \alpha L_n \exp(-\alpha(x_j + W_D))$$

$$J_{dr} = q\phi(1-R)\exp(-\alpha x_j)[1-\exp(\alpha W_D)]$$

Where, $\phi$ is incident photo flux density.

R is surface reflectance

$\alpha$ is absorption coefficient.

$S_p$, $S_n$: surface recombination velocity for hole and electron

$L_p$, $L_n$, $D_p$, $D_n$ is bulk diffusion length and diffusion coefficient for hole and electron, respectively.

$x_j$ is p/n junction position from surface

$W_D$ is depletion width.

$H^{'}$ is distance from edge of depletion region to back side of cell.

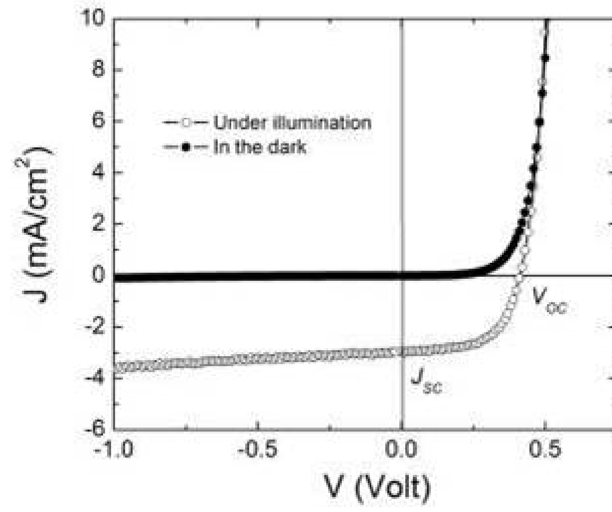


*Figure 6.3. Current-Voltage characteristic of a solar cell in dark and under illumination [2].*

## 6.3. Application of $SiN_x$ and $SiN_x$/P Cat-doped layers on back contact solar cells

### *6.3.1.* Simulation data

In this study, I firstly used simulation method to characterize the properties of back- contact solar cell using two well-know software solar cell simulation: PC1D and PC2D [5-7].

*a. Cell structure and electrical properties*

The cross-sectional schematic of a simulation cell structure is shown in Figure 6.4. A 150-µm-thick Si wafer with a bulk lifetime of 10 ms and a resistivity of 1 Ωcm, corresponding to a donor carrier concentration ($N_D$) of $5\times10^{15}$ $cm^{-3}$, was used for the calculation. Cell area was set to be 1 $cm^2$. Basic structure and electrical parameters are shown in Figure 6.5.

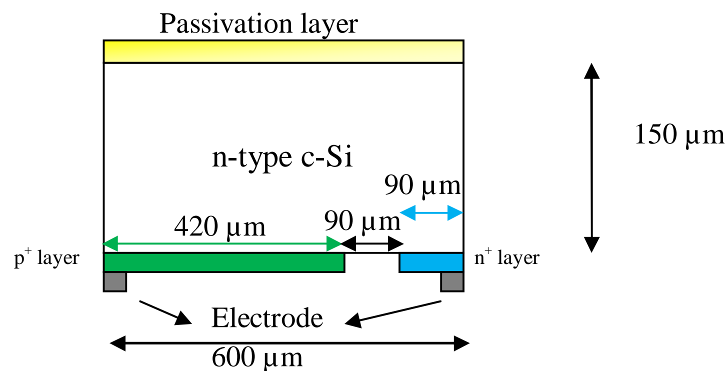


*Figure 6.4. The cross-sectional schematic of a simulation cell structure.*

| A | B | C | D | E | F | G | H | I | J | K | L | M | N | O | P | Q | R | S | T | U | V | W |
|---|---|---|---|---|---|---|---|---|---|---|---|---|---|---|---|---|---|---|---|---|---|---|
| STRUCTURAL | Recalculate Photogeneration after any change to the Structural parameters | | | | | | | | | | | | | | | | | | | | | |
| | delta X: | 3.00E-03 | cm | delta Y: | 7.50E-04 | cm | delta Z: | 1.67E+01 | cm | Y/X: | 0.2500 | aspect ratio | | | Size: | 20 | Rows&Columns | | | | | |
| | Width: | 6.00E-02 | cm | Height | 1.50E-02 | cm | Depth: | 1.67E+01 | cm | Area: | 1.00E+00 | (Width*Depth) cm^2 | | | Sides | -1 | -1=reflecting, +1=repeating | | | | | |
| ELECTRICAL | | | | | | | | | | | | | | | | | | | | | | |
| | N: | -5.00E+15 | cm-3 | Rho: | 1.11 | ohm-cm | Dp: | 11.0 | cm2/s | Vt: | 0.02569 | V | | Auger coefficient: | 8.30E-31 | cm6/s | | | | | | |
| | | | | | | | Dn: | 29.0 | cm2/s | q: | 1.60E-19 | coulombs | | | | | | | | | | |
| | tau: | 1.00E-02 | seconds | L/H: | 22.11 | | ni | 8.56E+09 | cm-3 | | 2.93E-12 | ni^2/N^2 | | | | | | | | | | |
| Sheet Rho (ohms/sq) | | | 0 = undoped | | negative = n-type | | positive = p-type | | | | | | | | | | | | | | | |
| Top: | -200 | -200 | -200 | -200 | -200 | -200 | -200 | -200 | -200 | -200 | -200 | -200 | -200 | -200 | -200 | -200 | -200 | -200 | -200 | -200 | -200 | -200 |
| Bottom: | 50 | 50 | 50 | 50 | 50 | 50 | 50 | 50 | 50 | 50 | 50 | 50 | 50 | 50 | 50 | 0 | 0 | 0 | -50 | -50 | -50 | -50 |
| CIRCUIT | | | | | | | | | | | | | | | | | | | | | | |
| | | | | | | Additional Rs: | 0.00E+00 | ohms | | Additional Gsh: | 0.00E+00 | siemens | | | | | | | | | | |
| Contacts: | 0 = no contact | | 1 = contact | | | | | | | | | | | | | | | | | | | |
| Top: | 0 | 0 | 0 | 0 | 0 | 0 | 0 | 0 | 0 | 0 | 0 | 0 | 0 | 0 | 0 | 0 | 0 | 0 | 0 | 0 | 0 | 0 |
| Bottom: | 1 | 1 | 0 | 0 | 0 | 0 | 0 | 0 | 0 | 0 | 0 | 0 | 0 | 0 | 0 | 0 | 0 | 0 | 0 | 0 | 1 | 1 |
| Shunt conductance (siemens): | | | 0.00E+00 | | | Shunt node branches: | 0 | | | Shunt conductance per branch: | | 0.00E+00 | siemens | | Central node potential: | | 0.000 | *Vt = | 0.000 | V | | |
| Top: | 0 | 0 | 0 | 0 | 0 | 0 | 0 | 0 | 0 | 0 | 0 | 0 | 0 | 0 | 0 | 0 | 0 | 0 | 0 | 0 | 0 | 0 |
| Bottom: | 0 | 0 | 0 | 0 | 0 | 0 | 0 | 0 | 0 | 0 | 0 | 0 | 0 | 0 | 0 | 0 | 0 | 0 | 0 | 0 | 0 | 0 |

*Figure 6.5. Basic parameters used for solar cell simulation.*

*b. Recombination*

A two diode model are used for the solar cell simulation. The first diode represents p-n junction with recombination outside a depletion region [8]. The second diode describes the p-n junction governed by recombination in a depletion region. Figure 6.6 describes two diode model of a solar cell.

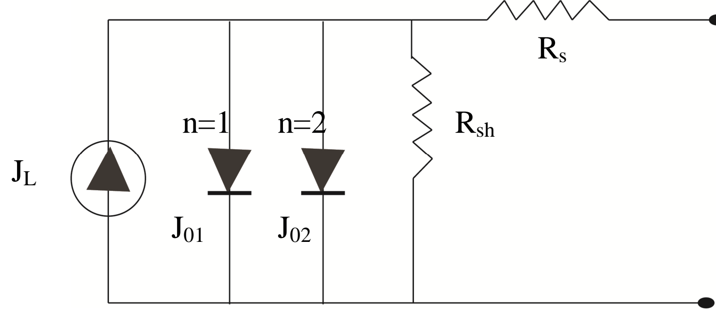


*Figure 6.6 : Two diodes model of a solar cell*

Dark current equation:

$$J = J_{01}\exp(\frac{q(V-JR_s)}{kT}) + J_{02}\exp(\frac{q(V-JR_s)}{2kT}) + \frac{V-JR_s}{R_{sh}}$$

Under illumination:

$$J = J_L - J_{01}\exp(\frac{q(V+JR_s)}{kT}) - J_{02}\exp(\frac{q(V+JR_s)}{2kT}) - \frac{V+JR_s}{R_{sh}}$$

Where, $J_{01}$ is the saturation current due to recombination in the quasi-neutral regions, $J_{02}$ is the saturation current due to recombination in the depletion region.

In order to calculate surface saturation current $J_{01_front}$, I used a formula to determine surface saturation current under low injection (excess carrier density ($\Delta n$) $<N_D$) [9]:

$$J_{01_front} = \frac{S_{eff}qn_i^2}{(N_D + \Delta n)},$$

where $S_{eff}$ is SRV at $\Delta n$. In my study, the value $\Delta n$ is $1.7\times10^{15}$cm$^{-3}$ corresponding to injection carrier concentration for μ-PCD measurement. Therefore, $J_{01_front}$ is calculated by using this value of $\Delta n$. The value of SRV taken for calculation is $SRV_{max}$ in this study. The values of calculated $J_{01_front}$ for the passivation layers are summarized in Table 6.3 later.

*c. Optical properties*

The effects of texturing and the transmission of passivation layers should be taken into account for the cell simulation.

In order to calculate external quantum efficiency, reflectance data of $SiN_x$/c-Si and $SiN_x$/textured c-Si should be used. Instead of using texture function available in PC1D software, in this calculation, I used the experimental reflectance data measured by using an UV-Vis spectrometer, and is plotted in Figure 6.7. Thickness of $SiN_x$ films used is 80 nm. The raw data is converted to a text file and input into calculation as front external reflectance as shown in Figure 6.8.

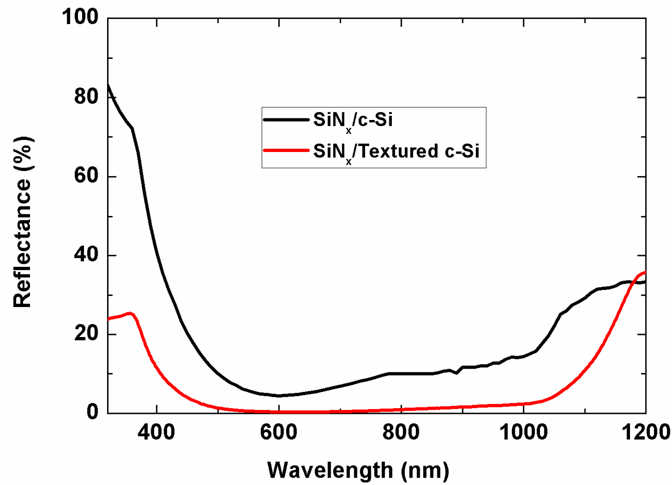


*Figure 6.7. Reflectance spectra of $SiN_x$ film on flat and textured c-Si*

Parameters used for the calculation is described in Figure 6.8. Obtained quantum efficiency is plotted in Figure 6.9. "Wavelength multiplier" in PC2D is external quantum efficiency in PC1D for wavelength less than 600 nm. It is 100% minus the reflectance for wavelength larger than 600 nm. The obtained value is assigned for front surface transmission (Trans, top) in PC2D. Other optical parameters are summarized in Table 6.1.

**DEVICE**
Device area: 1 $cm^2$
*No surface texturing*
*No surface charge*
Front reflectance from d:\set up\pc1d5\refsinx.ref
*No Exterior Rear Reflectance*
*No internal optical reflectance*
Emitter contact enabled
Base contact enabled
*No internal shunt elements*

**REGION 1**
Thickness: 150 µm
Material from si.mat
  Carrier mobilities from internal model
  Dielectric constant: 11.9
  Band gap: 1.124 eV
  Intrinsic conc. at 300 K: $1\times10^{10}$ $cm^{-3}$
  Refractive index from si.inr
  Absorption coeff. from si300.abs
  Free carrier absorption enabled
N-type background doping: $5\times10^{15}$ $cm^{-3}$
  *No front diffusion*
  1st rear diff.: P-type, $1\times10^{18}$ $cm^{-3}$ peak
  *No 2nd rear diffusion*
Bulk recombination: $\tau_n = \tau_p$ = 10000 µs
  Front-surface recom.: S model, $S_n = S_p$ = 5 cm/s
  *No Rear-surface recombination*

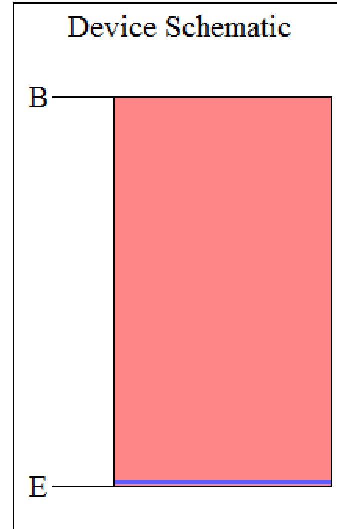


*Figure 6.8. Device structure and input parameters for PC1D simulation to obtain quantum efficiency.*

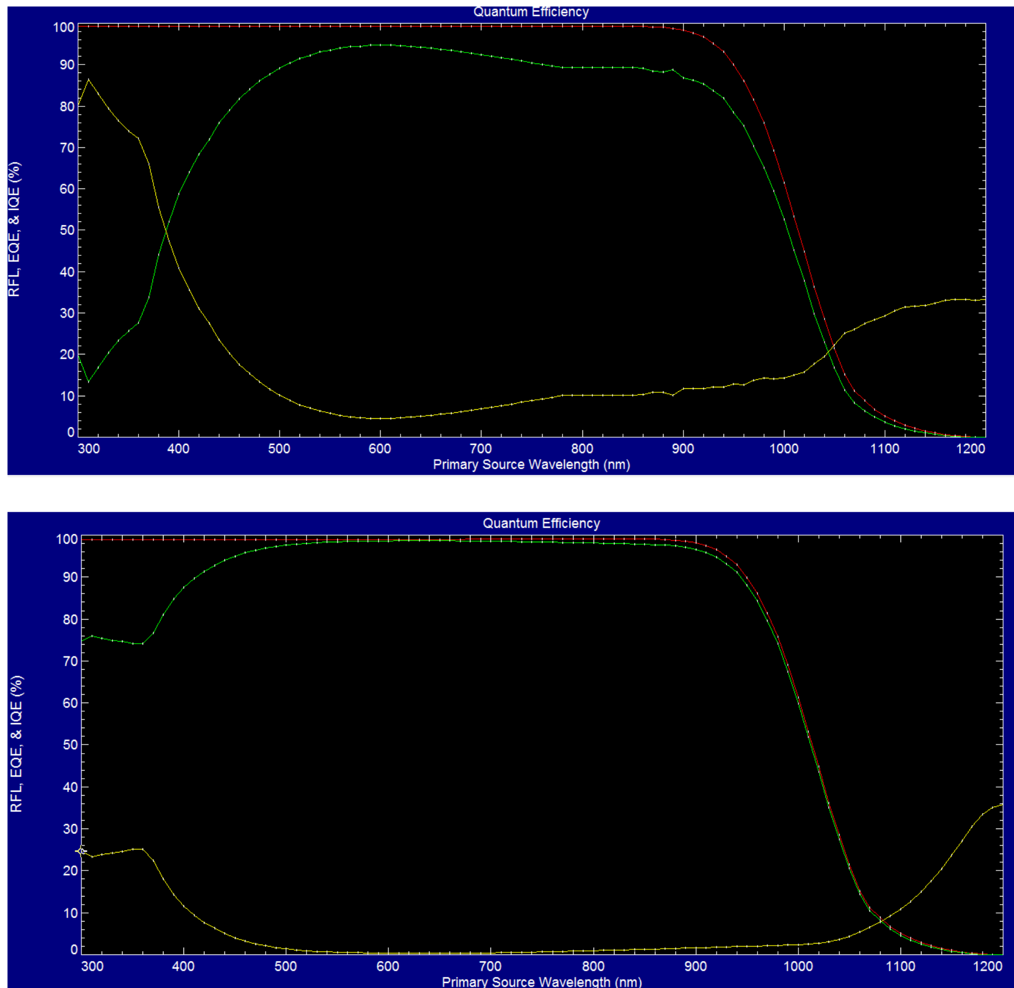


*Figure 6.9. Quantum efficiency obtained by PC1D for flat (top) and textured (bottom) c-Si covered with a $SiN_x$ film: Red: internal quantum efficiency; Blue: External quantum efficiency; Yellow: total reflectance.*

For the $SiN_x$/a-Si passivation layer, optical absorption in a-Si is should be taken into account. For PC2D calculation, 10 monochromatic lights with wavelength in range of 300 nm to 1200 nm are used. Transmission in a-Si at each wavelength is multiplied with power density to obtain light power density in case of $SiN_x$/a-Si passivation. Figure 6.10 shows incident peak flux density as a function of calculating wavelength. The values used in case of $SiN_x$/a-Si passivation are also shown.

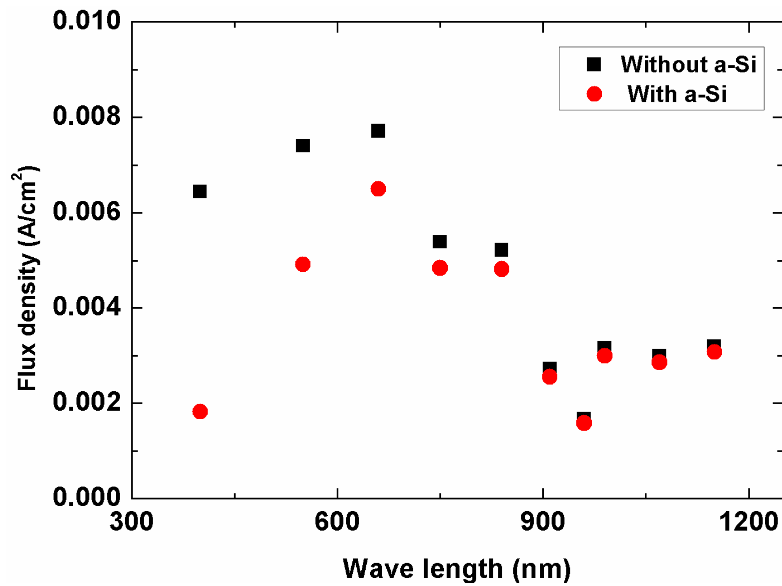


*Figure 6.10. Incident peak flux density as a function wavelength used for cell simulation in case of with and without a-Si used as passivation layers.*

*d. Results and discussion*

In order to quantitatively clarify the degree of improvement in cell efficiency achieved by reduction in SRV and optical properties by using the passivation layers in my study, I firstly simulated the performance of an ideal cell. For this cell, the effect of reflectance, SRV on front and back surfaces were set to be negligible. The parameters using for this simulation is listed in Table 6.1. The I-V curve obtained for the ideal cell in shown in Figure 6.11. Simulated characteristics are given in Table 6.2. The efficiency of the cell is 29.17%, which is in good agreement with the reported value as the maximum c-Si cell performance [10]. This result clearly indicates the reliability of the software used here.

| | Parameter | | | Value |
|---|---|---|---|---|
| **Electrical properties** | Base concentration | | | $5\times10^{15}$ $cm^{-3}$ |
| | Emitter doping | | | 50 Ω/sq |
| | Bulk lifetime | | | 10 ms |
| | Diffusivity constant for holes | | | 11 $cm^2/s$ |
| | Diffusivity constant for electrons | | | 29 $cm^2/s$ |
| | Area | | | 1 $cm^2$ |
| | Thickness | | | 150 µm |
| | External series resistance | | | 0 |
| | External shunt conductance | | | 0 |
| **Optical properties** | Spatial multiplier | Trans(top) | | 100% |
| | | Haze(top) | | 100% |
| | | Rspec(top) | | 100% |
| | | Rdiff(top) | | 100% |
| | | Haze(bot) | At $n^+$, $p^+$ and gap region | 50% |
| | | | At metal contact region | 100% |
| | | Rspec(bot) | At $n^+$, $p^+$ and gap region | 100% |
| | | | At metal contact region | 80% |
| | | Rdiff(bot) | At $n^+$, $p^+$ and gap region | 100% |
| | | | At metal contact region | 70% |
| | Top surface transmission | | | 100% |
| | Top-surface haze | | | 100% |
| | Top internal specular reflectance | | | 5% |
| | Top internal diffuse reflectance | | | 100% |
| | Bottom specular reflectance | | | 100% |
| | Bottom specular reflectance | | | 100% |
| | Bottom -surface haze | | | 100% |
| | Wavelength multiplier | Trans(top) | | 100% |
| | | Haze(top) | | 100% |
| | | Rspec(top) | | 100% |
| | | Rdiff(top) | | 100% |
| | | Haze(bot) | | 100% |
| | | Rspec(bot) | | 100% |
| | | Rdiff(bot) | | 100% |
| **Recombination** | $J_{01}$ | Top | | 0 |
| | | Bottom | | 0 |
| | $J_{02}$ | Top | | 0 |
| | | Bottom | | 0 |

*Table 6.1. Optical parameters used for PC2D simulation*

| Parameters | Value |
|---|---|
| $V_{oc}$ (V) | 0.757 |
| $I_{sc}$ (mA) | 44.10 |
| Efficiency (%) | 29.17 |
| Fill factor | 0.874 |

*Table 6.2. Simulated characteristics of an ideal solar cell.*

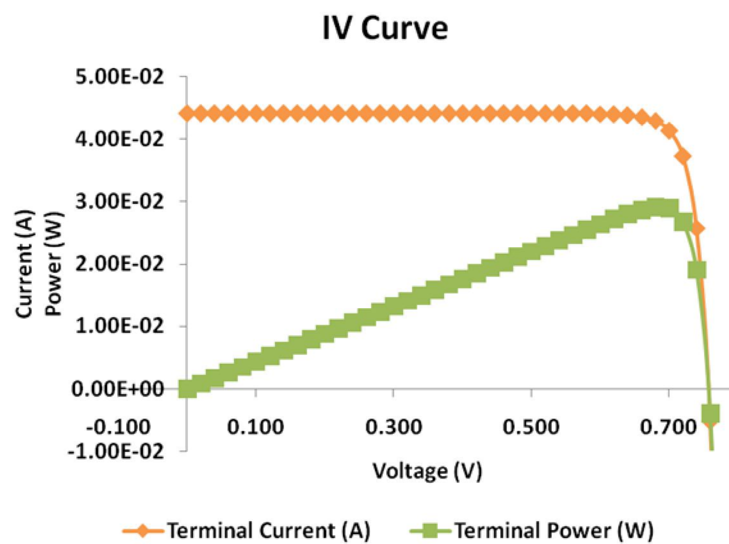


*Figure 6.11. I-V curve of a simulated ideal solar cell obtained by PC2D.*

In the next step, I simulated the performances of solar cells which have front surfaces passivated with the passivation layers in my study. Front SRV and $J_{01}$_front are summarized in Table 6.3. In order to consider the ideal case except for the front-surface SRV and optical reflection, $J_{02}$ was set to be zero. For optical properties, front surface transmission (Trans, top) at each wavelength (exported from Figure 6.10) for each surface passivation is also taken into account.

Simulated $V_{oc}$, $I_{sc}$ and efficiency of the cells are summarized in Table 6.3. $SiN_x$ films and $SiN_x$/P Cat-doped layers show significant improvement in solar cell efficiency. Although $SiN_x$/a-Si stacked layers show extremely low SRV, parasitic absorption in a-Si films strongly reduces $I_{sc}$ and efficiency. The efficiency of the cell passivated with this staked layer is lower than that of a cell passivated with only a $SiN_x$ film. The efficiency is 23.14 and 23.82% for cell passivated with only $SiN_x$ films and $SiN_x$/P Cat-doped layer, respectively. Decrease in SRV from 5 cm/s to 2cm/s can increase cell efficiency. It should be emphasized that the highest $V_{oc}$ obtained of 0.744 V for the $SiN_x$/P Cat-doped layer is larger than that of Panasonic record solar cell (0.740 V) [11]. Increase in SRV leads to decrease in $V_{oc}$ and fill factor for texture surface cell. However, the benefit of low reflectance can enhance cell efficiency to 26.09%. Solar cell with using textured c-Si passivated with $SiN_x$/P Cat-doped layer can thus improve significantly c-Si solar cell efficiency.

| Passivation layer | Surface | SRV (cm/s) | $J_{01_front}$ (fA/cm$^2$) | $V_{oc}$ (V) | $I_{sc}$ (mA) | Fill factor | Efficiency (%) |
|---|---|---|---|---|---|---|---|
| $SiN_x$/a-Si | flat | 1.5 | 2.6 | 0.742 | 29.69 | 0.860 | 18.94 |
| $SiN_x$ | flat | 5 | 8.7 | 0.734 | 37.08 | 0.850 | 23.14 |
| $SiN_x$/P dope | flat | 2 | 3.5 | 0.744 | 37.26 | 0.859 | 23.82 |
| $SiN_x$/P dope | texture | 7 | 11.7 | 0.733 | 41.96 | 0.848 | 26.09 |

*Table 6.3. Solar cell characteristics at various passivation layers.*

The simulation results indicate that improvement in cell efficiency is strongly affected by SRV and optical properties of passivation layers. Back-contact c-Si solar cell which has advantages of low reflectance by using texture structure and low SRV by using excellent Cat-CVD $SiN_x$/P Cat-doped layer demonstrate the highest efficiency of 26.09%, higher than the best experimental efficiency of 25.6%[11]. This result indicates the availability of Cat-CVD $SiN_x$/P Cat-doped layers in passivation technique for high efficiency solar cells.

### *6.3.2. Back contact solar cell fabrication*

*a. Fabrication process*

The design of the back contact solar cell in my studdy is shown in Figure 6.12. Energy band of a $n^+/n/p$ cell structure is drawn in Figure 6.13.

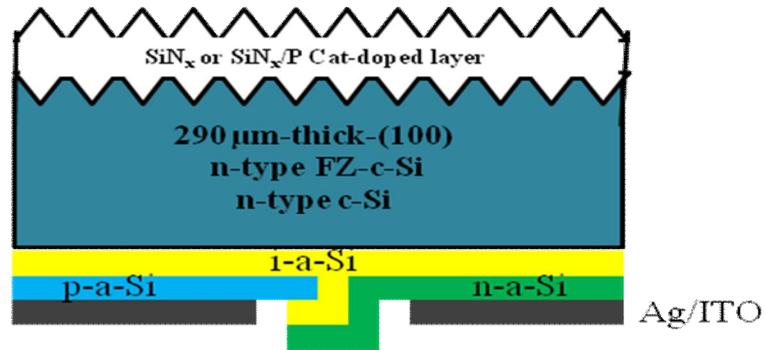


*Figure 6.12. A schematic of a back-contact solar cell of my study*

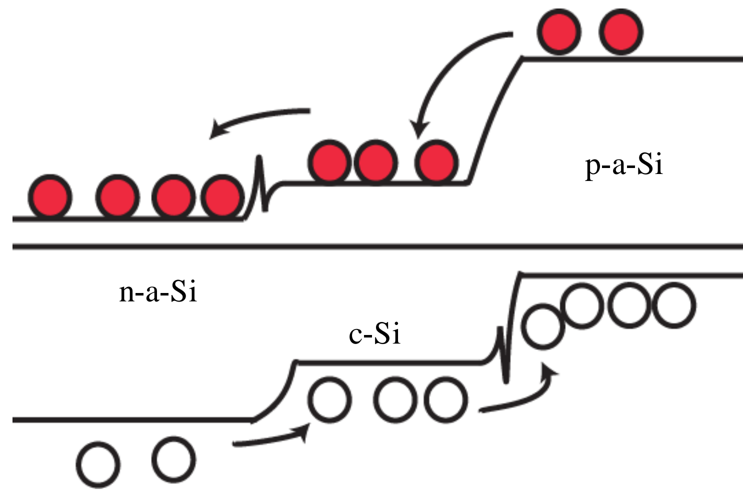


*Figure 6.13. Energy band of a $n^+/n/p^+$ structure. Band offset exists due to difference of band gap between a-Si and c-Si.*

In order to investigate the effect of the passivation quality of $SiN_x$, $SiN_x$/P Cat-doped layers and c-Si surface morphology on cell efficiency, I fabricated solar cells with textured and flat c-Si surfaces passivated with these passivation layers.

For textured c-Si cells, texturing process was conducted as described in Chapter 5. For some cells, c-Si wafers with a textured front side surface and a flat rear side surface is

prepared. To meet this purpose, one side of the surface was covered with $SiN_x$ films to protect surface from SUN-X600 etching. After that, $SiN_x$ film was removed by dipping in 20% water diluted HF solution. Samples are divided into three groups according to surface morphology; one group includes samples which have two flat surfaces, one group includes samples which have two textured surfaces, and the other includes samples which have a flat and a textured surface. Fabrication process of the cell is described in the steps below:

**Step 1:**

Deposition of a passivation layer: $SiN_x$ or $SiN_x$/P Cat-doped layer and annealing.

*The cross-sectional view of c-Si passivated by $SiN_x$ film. Sample size is $2\times2$ $cm^2$*

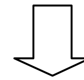

**Step 2:**

Aluminum markers: evaporation and photolithography

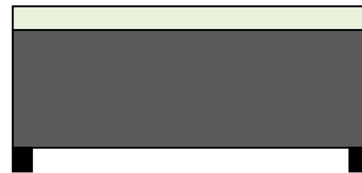

*The cross-sectional view of sample with Al marker*

**tep 3:**

Deposition of i-a-Si and p-type a-Si by Cat-CVD and the removal of p-a-Si formed on an unexpected part by photolithography

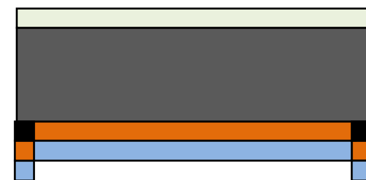

*The cross-sectional view of sample after deposition of i-a-Si and p-a-Si films*

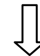

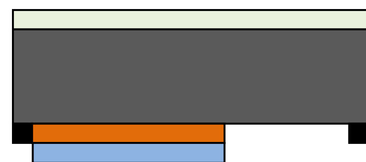

Rear side

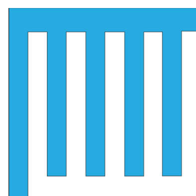

*The cross-sectional view of sample after removal of unexpected i –a-Si and p-a-Si films*

**Step 4:**

Deposition of i-a-Si and n-type a-Si by Cat-CVD and the removal of a-Si formed on an unexpected part by photolithography

Rear side

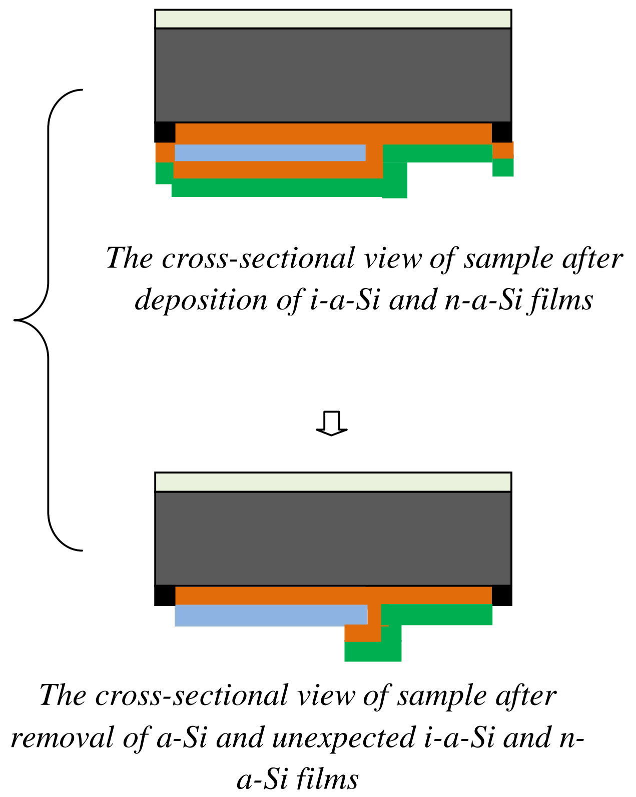

*The cross-sectional view of sample after deposition of i-a-Si and n-a-Si films*

*The cross-sectional view of sample after removal of a-Si and unexpected i-a-Si and n-a-Si films*

**Step 5:**

Electrode formation: ITO (sputtering) and Ag (evaporation)

Rear side

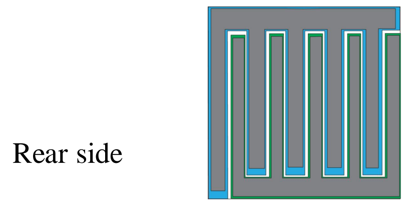

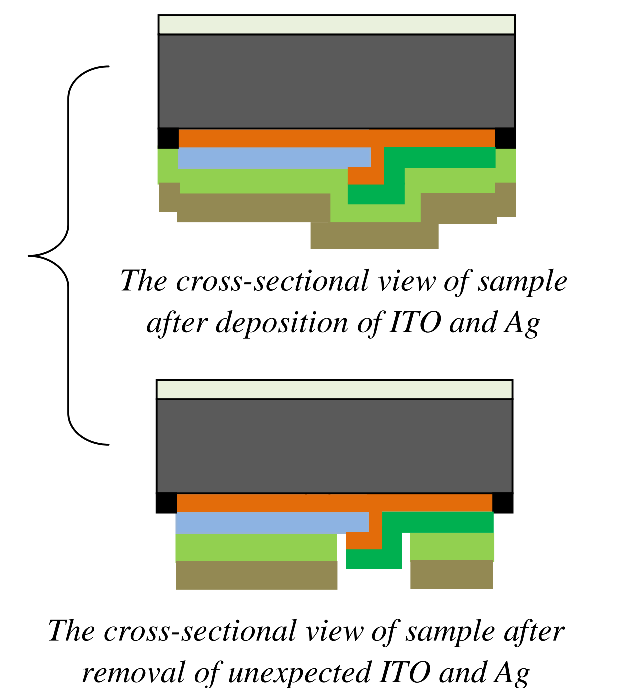

*The cross-sectional view of sample after deposition of ITO and Ag*

*The cross-sectional view of sample after removal of unexpected ITO and Ag*

**Step 6:**

Cutting to remove markers and un-working region

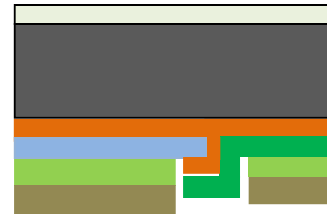

*The cross-sectional view of solar cell after cutting (sample size is 1×1 cm²)*

**Color chart:**

c-Si: ■  $SiN_x$ or $SiN_x$/P Cat-doped layer: ■

i-a-Si: ■  p-a-Si: ■  n-a-Si: ■

ITO: ■  Ag : ■

$SiN_x$ films or $SiN_x$/P Cat-doped layers were prepared on one side of c-Si samples. For $SiN_x$/c-Si samples, annealing B was conducted. For samples receiving P Cat-doping, both annealing A and B were performed. Annealing A and B were conducted at 350 $^oC$ for 30 min in $N_2$ ambient. The condition of $SiN_x$ and P doping are the same with condition at which the highest $\tau_{eff}$ is obtained.

For i-a-Si, p-a-Si, and n-a-Si films, the deposition conditions used are the same with condition at which the highest heterojunction solar cell efficiency obtained when using Cat-CVD technique in my lab [11]. Thickness of i-a-Si films for the first time and second time is 6 and 15 nm, respectively. Thickness of p-type and n-type a-Si is around 10 nm. Deposition conditions of these layers are listed in Table 6.3. 77 nm-thick ITO was prepared by sputtering. 100 nm-thick Ag electrodes were formed by evaporation. Table 6.5 summarizes etching condition for these films to form the interdigitated emitter/electrode shape.

After cutting, 1 $cm^2$ square samples were tested under 1-sun (AM 1.5, 100 $mWcm^{-2}$) for photocurrent-voltage measurement.

| | $T_s$ (°C) | $T_{cat}$ (°C) | Gas flow rate (sccm) | | | | | Pressure (Pa) | Process time (s) |
|---|---|---|---|---|---|---|---|---|---|
| | | | $SiH_4$ | $NH_3$ | $H_2$ | $PH_3$ | $B_2H_6$ | | |
| P doping | 80 | 1300 | | 20 | | | | 1 | 60 |
| $SiN_x$ | 100 | 1800 | 8 | 150 | | | | 10 | 210 |
| i-a-Si (1) | 160 | 1800 | 10 | | | | | 1 | 12 |
| p-a-Si | 250 | 1900 | 10 | | 20 | | 8 | 1 | 45 |
| i-a-Si (2) | 160 | 1800 | 10 | | | | | 1 | 30 |
| n-a-Si | 200 | 1900 | 20 | | 50 | 4.4 | | 2 | 12 |

*Table 6.4. Conditions of i-a-Si, n-a-Si, p-a-Si, $SiN_x$ deposition and P Cat-doping.*

| | Solution | Temperature | Time |
|---|---|---|---|
| Al marker | $H_3PO_4$:$CH_3COOH$:$HNO_3$:$H_2O$=3:1:3:1 | 50 °C | 1 min |
| p-a-Si | $HNO_3$ :HF: $H_2O$=1:1:2 | RT | 30 s |
| n-a-Si | KOH:$H_2O$=1:2 | RT | 15s |
| ITO and Ag | $HNO_3$: $H_2O$=1:2 | RT | 2 min |

*Table 6.5. Etching condition for some of films using in my study.*

*b. Solar cell characteristics*

The results obtained from the fabricated solar cells are not so good until now. Solar cell efficiency is less than 1% for all the cells. J-V curves of a cell in dark and under illumination are shown in Figures 6.14 and 6.15.

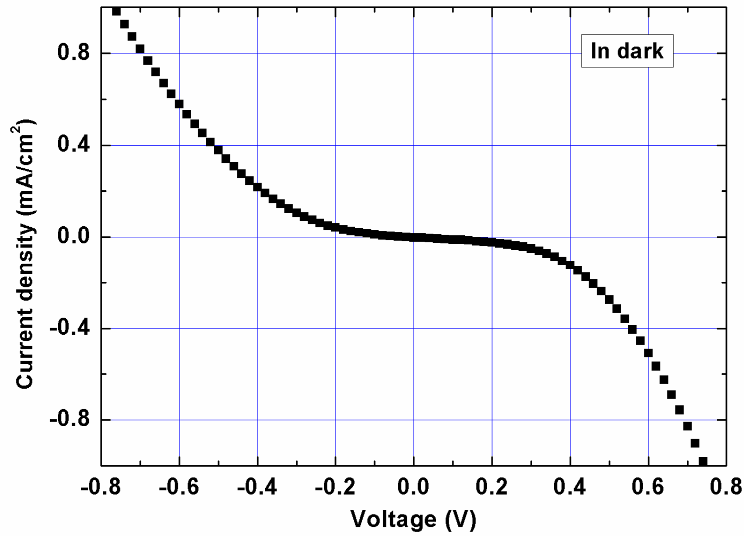


*Figure 6.14. J-V curve of a cell in dark*

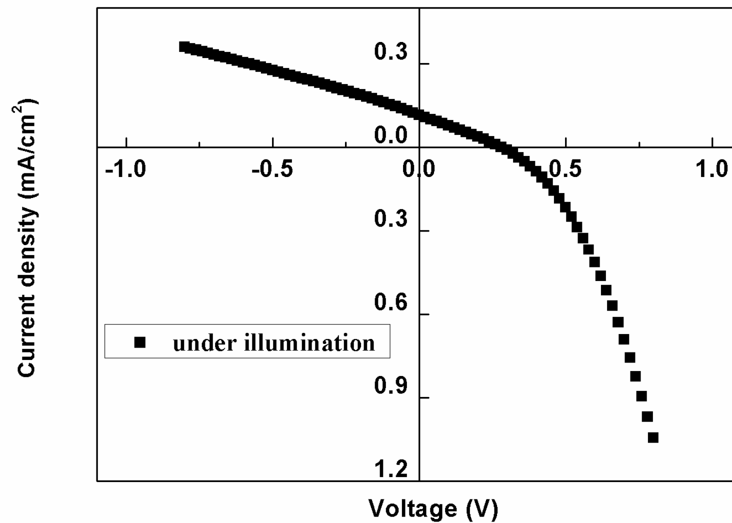


*Figure 6.15. J-V curve of a cell under illumination*

The reason for low efficiency obtained may be due to unmatured fabrication process. $\tau_{eff}$ obtained for samples after n-a-Si film deposition is less than 100 µs. After etching to remove un-expected part of some layers such as p-a-Si and n-type a-Si, interface properties of these layers are not good due to un-optimized cleaning process. The damage after Ag etching is shown in Figure 6.16.

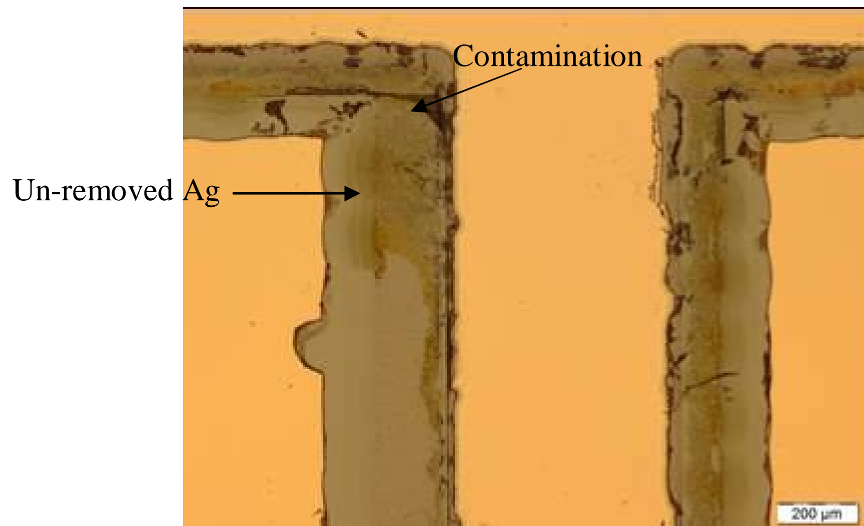


*Figure 6.16. Contamination and un-removed Ag after etching Ag.*

In summary, fabrication process for the solar cell has not been optimized yet. Additional steps such as cleaning and the optimization of etching time will become future work.

### 6.4. Conclusion

I fabricated back-contact back-junction solar cells with $SiN_x$ and $SiN_x$/P Cat-doped layer structures. However, their efficiency is very low at present. It might be due to un-optimized fabrication process. The simulation results indicate that using $SiN_x$/ P Cat-doped layer can improve significantly cell efficiency compared to using $SiN_x$/a-Si stacked layer. Parasitic absorption of a-Si decrease drastically cell efficiency. $SiN_x$/P Cat-doped layer demonstrates low SRV of 6.7 cm/s on textured c-Si. The benefit of low SRV and low surface reflectance by using texture surface can enhance cell efficiency to 26.09%. This result shows promising application of Cat-CVD $SiN_x$/P Cat-doped layer in back-contact solar cell fabrication.

## References

[1] http://pveducation.org/pvcdrom/solar-cell-operation/open-circuit-voltage

[2] http://depts.washington.edu/cmditr/modules/opv/physics_of_solar_cells.html

[3] R.A. Sinton, A. Cuevas, *Appl. Phys. Lett.* **68** (1996) 2510.

[4] P. Würfel, Physics of solar cells: From principle to new concepts, Willey-VCH VerlagGmbH&Co.KGaA (2005) p.139

[5] P. A. Basore, *PC-1D Installation maula and user's guide*, 1991.

[6] P. A. Basore and K. C. Holmen, *IEEE J. Photovolt.* **1** (2011) 72.

[7] K. C. Holmen and P. A. Basore, Proc. 27th European photovoltaic solar energy conference, (Frankfurt, Sept. 2012), 2BV.5.42

[8]http://www.tf.unikiel.de/matwis/amat/semitech_en/kap_8/backbone/r8_1_2.html

[9] W. Shockley, H. J. Queisser, *J. Appl. Phys.* **32** (1961) 510.

[10] F. Granek, C. Reichel, M. Hermle, D. Huljié, O. Schultz, S. W. Glunz, Proc. 22nd European photovoltaic solar energy conference, (Milan, Sept. 2007) p. 816

[11] S. Tsuzaki, JAIST Master thesis, 2014

# Chapter 7 General conclusion

I have succeeded to obtain Cat-CVD high-transparency $SiN_x$ films with high-passivation quality on n-type c-Si surfaces. I have also significantly improved the passivation quality by doping P atoms on n-type c-Si surfaces by exposing to P-related radicals generated by the catalytic cracking of $PH_3$ (Cat-doping), called P Cat-doped layer, before passivated with the Cat-CVD $SiN_x$ single layer. The main results of the passivation properties are summarized as bellow:

- A $SRV_{max}$ of as low as 5 cm/s can be achieved for n-type c-Si passivated by a single Cat-CVD $SiN_x$ films, which is prepared at low deposition substrate temperature as low as 100 $^oC$, and then annealed at 350 $^oC$ for 30 min in $N_2$ atmosphere. Annealing contributes substantially to improvement in the passivation quality by anneal-enhanced H defect termination.
- A drastic reduction in $SRV_{max}$ from 5 to 2 cm/s can be obtained when the n-type c-Si surface is doped to form a P Cat-doped layer before a Cat-CVD $SiN_x$ single layer is deposited. The P Cat-doped layer is a shallow layer (<5 nm) with suitable sheet carrier density, which can induce field-effect passivation to reduce SRV.
- The P Cat-doping is also effective for textured c-Si surfaces. By using $SiN_x$/P Cat-doped layers, an extremely low $SRV_{max}$ obtained of 6.7 cm/s for textured c-Si wafers, which are essential for high-performance solar cells due to its ability of lowering optical reflectance and enhancing light trapping inside c-Si absorber. For $SiN_x$/P Cat-doped layer/c-Si textured samples, optical reflectance less than 10% in visible range can be achieved.
- Simulation data for back-contact solar cell using these passivation layers shows the highest cell efficiency of 26.09% for textured c-Si passivated with $SiN_x$/P Cat-doped layer. The high efficiency is the result of low $SRV_{max}$ and low reflectance by using $SiN_x$/ P Cat-doped layer and texturing structure.

The obtained results indicate that Cat-CVD have potential application in passivation technique for high-efficiency solar cells, particularly for n-type back-junction solar cells. Based on the remarkable results for the passivation of n-type c-Si surfaces, I will investigate the application of these passivation layers to n-type back-contact solar

cells. The solar cells which will be realized in my research have some advantages as below:

- High transparency and high passivation quality by using $SiN_x$/P Cat-doped layers.
- No shading loss by metal grids on the front side.
- Fabrication processes at low temperature (< 200 °C).

The simulation result indicates that back-contact c-Si solar cell which has advantages of low reflectance by using texture structure and low SRV by using excellent Cat-CVD $SiN_x$/P Cat-doped layer demonstrate high efficiency of 26.1%. I have fabricated back-contact back junction solar cell using these excellent passivation layers. However, solar cell efficiency is very low at present, less than 1%. This is because fabrication processes have not been optimized yet. Solar cell with completely optimized fabrication processes will be reported in the near future.

# Appendix

## A-1. Spectroscopic ellipsometry

### *A-1-1. Working principle of ellipsometry*

Ellipsometry measures a change in polarization as light reflects (or transmits) from a material structure to determine thickness and optical properties of material. The polarization change is represented as an amplitude ratio (Ψ) and a phase difference (Δ) between s- and p-polarized light, as described below.

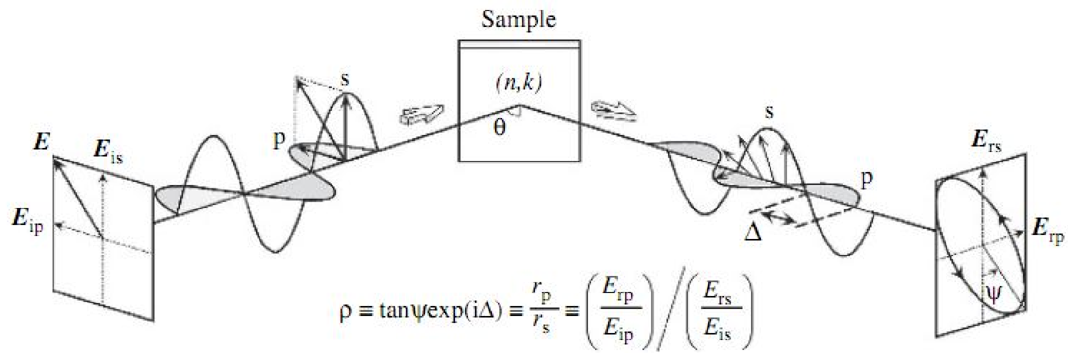


*Figure A-1.1. The change of polarization when light is reflected on the surface of material [1]*

The change in polarization in the ellipsometry measurement is commonly written as:

$$\rho = \tan(\psi)e^{j\Delta} = \frac{r_p}{r_s}$$

Fresnel equation:

$$r_s = \left(\frac{E_{rs}}{E_{is}}\right)_s = \frac{n_i\cos(\phi_i) - n_t\cos(\phi_t)}{n_i\cos(\phi_i) - n_t\cos(\phi_t)}$$

$$r_p = \left(\frac{E_{rp}}{E_{ip}}\right)_p = \frac{n_i\cos(\phi_i) - n_t\cos(\phi_t)}{n_i\cos(\phi_i) - n_t\cos(\phi_t)},$$

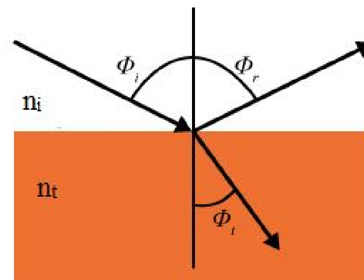


*Figure A-1.2 . Illustration of incident light, reflected light and refracted light.*

where s and p are denoted for s- and p-polarization as described later. $n_i$ and $n_t$ are refractive indices of incoming environment and materials.

In order to understand the working principle of ellipsometry, I firstly introduce light polarization.

There are three typical light polarizations: linear, elliptical and circular, describing shape of end point of electrical field vector marking on a plane which is perpendicular to

light wave travelling direction. In ellipsometry, incident light with linear polarization reflects on a sample surface and the reflected light generally becomes elliptical polarization, which is the origin of the name "ellipsometry".

Light is an electromagnetic wave, in which electric field and magnetic field are perpendicular to each other and perpendicular to wave vector. The relationship between electric field and magnetic field follows Maxwell equation. Therefore, one can choose electric field to describe light polarization behavior. (Magnetic field will be deduced by using Maxwell equation).

### *1. Light polarization*

Electric field can be divided into two components as below:

$$E_x = A_x \cos(\omega t - kz + \phi_x),$$

$$E_y = A_y \cos(\omega t - kz + \phi_y),$$

where $A_x$ and $A_y$ is wave amplitude in $x$ and $y$ axis, respectively; $z$ is light propagation direction; $k$ is wave vector (number of wave from 0 to 2π); $\omega$ is angular frequency and $\phi_x$ and $\phi_y$ is initial phase angle in $x$ and $y$ axis, respectively.

- In order to form linear polarization, points of sum electric field must be on a straight line. That means:

$$\tan(\varphi) = \frac{E_y}{E_x} = \frac{A_x \cos(\omega t - kz - \phi_x)}{A_y \cos(\omega t - kz - \phi_y)} = \pm \frac{A_x}{A_y} = const$$

$$\Leftrightarrow \cos(\omega t - kz - \phi_x) = \pm \cos(\omega t - kz - \phi_y)$$

$$\phi_x - \phi_y = k\pi$$

($k$=0,±1, ±2…)

- In order to form circular polarization, points of sum electric field must be on a circle. Consider boundary conditions: $A_x$=$A_y$, at $E_x$=0, $E_y$=$A_y$, we can find the condition for circular polarization is:

$$\phi_x - \phi_y = k\frac{\pi}{2} \qquad (k=\pm 1, \pm 3, \pm 5\ldots)$$

$$E_x^2 + E_y^2 = A_x^2 = A_y^2$$

- In order to form elliptical polarization, points of sum electric field must be on a circle. That means:

$$\phi_x - \phi_y = k\frac{\pi}{2}$$
$$\frac{E_x^2}{A_x^2} + \frac{E_y^2}{A_y^2} = 1 \quad (k=\pm1, \pm3, \pm5\ldots),\ A_x \neq A_y$$

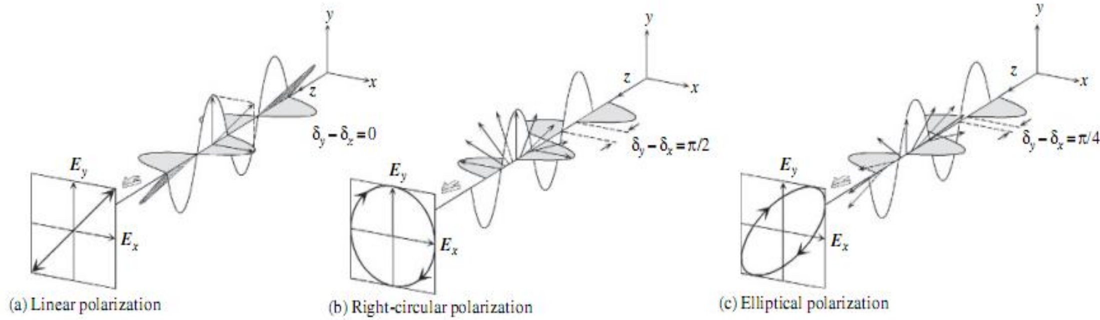


*Figure A-1.3. Examples of linear, circular, and elliptical Polarization [1].*

2. *Definition of ellipsometry parameter*

As I mentioned above, ellipsometry measures the change of polarization, which is defined as:

$$\rho = \tan\psi \exp(j\Delta)$$

In this part, I will explain what are ψ and Δ.

In ellipsometry, when linear incident light comes to surface, it is reflected and the reflected light is elliptically polarized, as shown in Figure A-1.1.

Dividing polarized light electric field into two conponent direction, called p (paralell) and s (Senkrecht) polarization. In p polarization, the electric field of both incident and reflected light are in the incident plane. In s polarizarion, the electric field of both incident and reflected light are normal to the incident plane.

When light changes polarization, amplitude and mutual phase are changed. The change in two components between incident and reflected light is:

$$\frac{\chi_i}{\chi_r} = \frac{\frac{E_{iy}}{E_{ix}}}{\frac{E_{ty}}{E_{rx}}} = \frac{E_{iy}}{E_{ry}}\frac{E_{rx}}{E_{ix}} = \frac{\frac{E_{rx}}{E_{ix}}}{\frac{E_{iy}}{E_{ry}}} = \frac{r_p}{r_s}$$

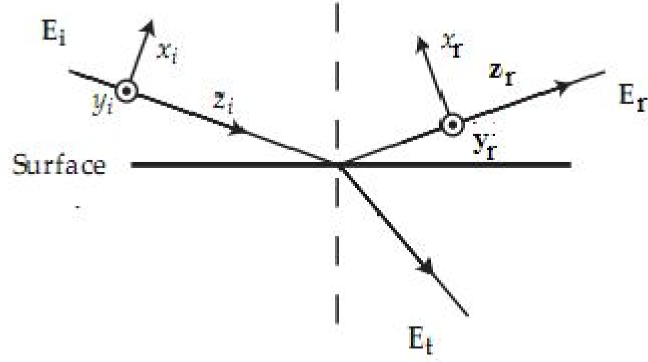


*Figure A-1.4. Electric field of incident and reflected light. y is normal to incident plane and x is parallel to incident plane[2]*

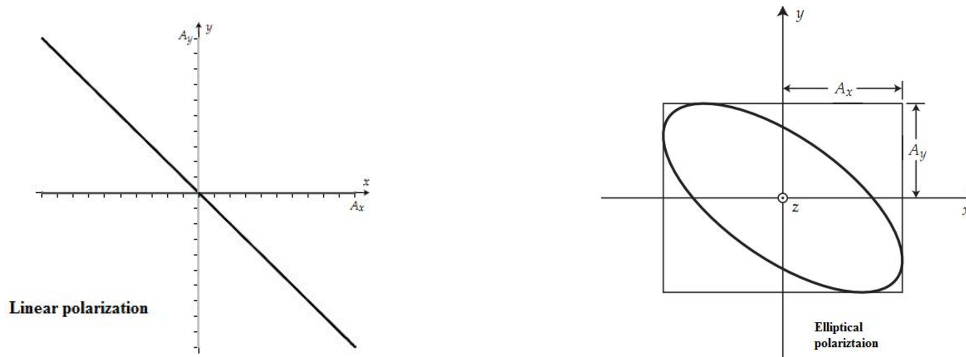


*Figure A-1.5. Linear and eliptical polarization.[2]*

$$\frac{\chi_i}{\chi_r} = \frac{A_{iy}\exp(j\phi_{iy})}{A_{ix}\exp(j\phi_{ix})}\frac{A_{ry}\exp(j\phi_{ry})}{A_{rx}\exp(j\phi_{rx})} = \frac{A_{iy}}{A_{ix}}\exp(j(\phi_{iy}-\phi_{ix}))\frac{A_{ry}}{A_{rx}}\exp(j(\phi_{ry}-\phi_{rx}))$$

If incident light is linearly polarized with $\phi_i$=0 and $A_{ix}$=$A_{iy}$, we have:

$$\frac{\chi_i}{\chi_r} = \frac{A_{ry}}{A_{rx}}\exp(j(\phi_{ry}-\phi_{rx}))$$

The parameter Δ and ψ are defined as below:

$$\tan\psi = \frac{A_{ox}}{A_{oy}} \text{ and } \Delta = \phi_{rx} - \phi_{ry}$$

Then, we obtain: $$\frac{\chi_i}{\chi_r} = \frac{r_p}{r_s} = \tan\psi \exp(j\Delta) = \rho$$

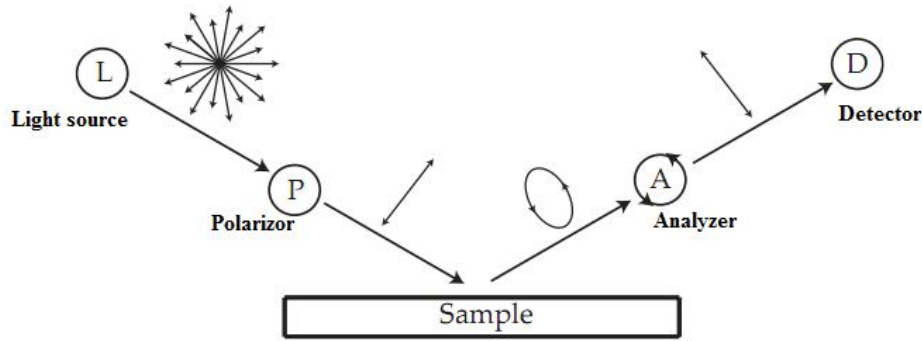


*Figure A-1.5. Schematic of spectroscopic ellipsometry[2].*

Usually, in order to obtain high accuracy, incident angle is set to be Brewster angle, at which the difference between $r_s$ and $r_p$ is maximum. At Brewster angle, for p polarization light, the direction of dielectric dipole oscilattion is the same as that of reflected light. Because light is transverse wave and the oscilation of electric field is perpendicular to wave vector, no light is radiated as reflected light. Therefore, p component of electric field approaches to zero.

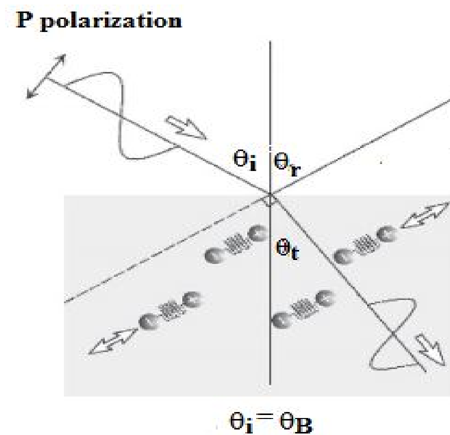


*Figure A-1.6. Incident p-polarized light at Brewster angle [1]*

Brewster angle is defined as:

$$\tan\theta_B = \frac{n_t}{n_i}$$

For c-Si, with $n_t$= 4.3, Brewster angle is ~75 °.

### *A-1-2. Cauchy model for data analysis*

The wavelength (λ) dependent refractive indices $n(\lambda)$ of $SiN_x$ films were measured on J. A. Woollam Co., HS-190$^{TM}$ spectroscopic ellipsometer, using Cauchy model for data analysis. In this model, $n(\lambda)$ and extinction coefficients $k(\lambda)$ are approximately expressed as:

$$n(\lambda) = A + \frac{B}{\lambda^2} + \frac{C}{\lambda^4}$$

$$k(\lambda) = \alpha e^{\beta(12400(\frac{1}{\lambda} - \frac{1}{\gamma}))}$$

The six fitting parameters in this dispersion model are *A*, *B*, *C*, the extinction coefficient amplitude $\alpha$, the exponent factor $\beta$, and the band edge $\gamma$.

***A-2. X-ray photoelectron spectroscopy***

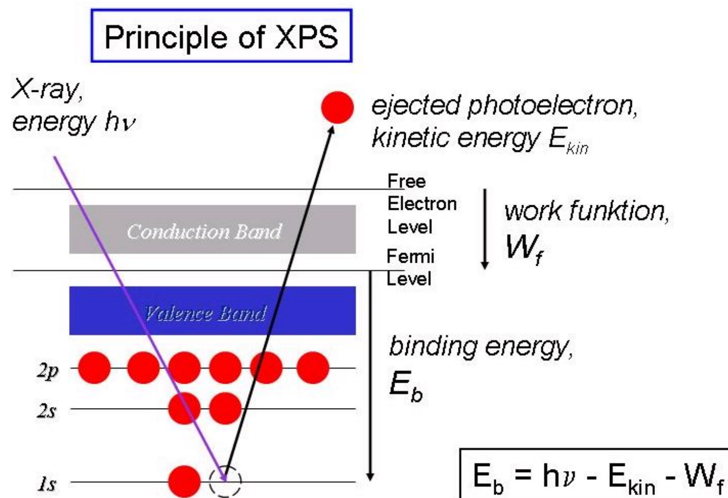


*Figure A-2.1. Principle of XPS [3]*

XPS is a quantitative spectroscopic technique that measures the elemental composition, empirical formula, chemical state and electronic state of the elements (except for H and He) existing in a material.

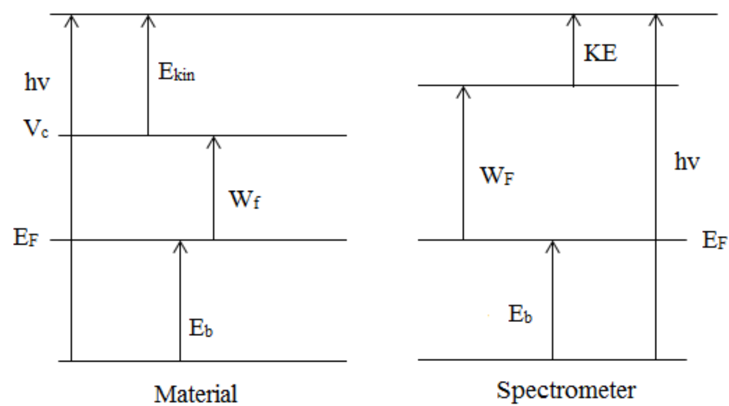


*Figure A-2.3. Energy diagram*

XPS works by irradiating X-Ray photons to atoms on a surface of any solid material, causing the ejection of electrons. Core electrons locating close to the nucleus have binding energies (BE), which is determined by the attraction of the electrons to the nucleus. The core electrons have high probability to be excited by the X-Ray. Therefore, XPS can identify element through binding energy of its core electrons.

A cylindrical mirror analyzer (CMA) is usually used to measure the KE of emitted photoelectrons. A detector counts how many photoelectrons have the same KE and a computer calculates BE from the obtained KE.

$$KE = hv - E_b - \emptyset$$

KE -Kinetic Energy (measure in the XPS spectrometer)

$hv$- photon energy from the X-Ray source (controlled)

$\emptyset$ - Spectrometer work function. It has an order of a few eV, and gets more complicated because the materials in the instrument will affect it. $E_b$ is an unknown variable.

A spectrum is plotted from the analyzer signal. The binding energies can be determined from the peak positions and the elements present in the sample identified.

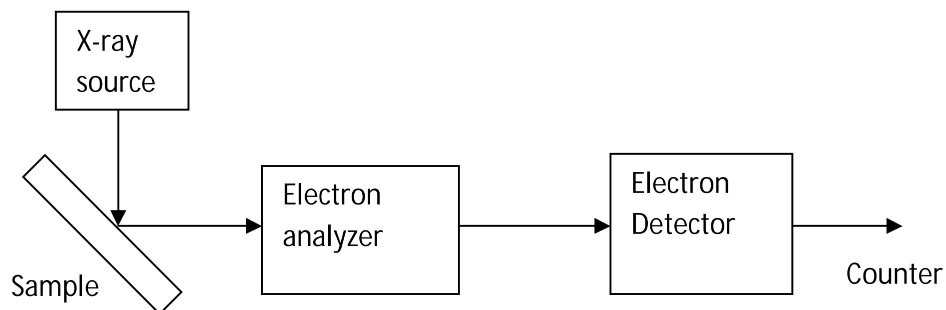


*Figure A-2.4. Schematic of XPS*

XPS spectra are obtained by exposing a material to X-ray, while simultaneously measuring the kinetic energy of electrons that escape from the top 1 to 10 nm of the material. XPS requires an ultra-high vacuum condition of $<10^{-7}$ Pa. XPS spectra express binding energy versus number of electrons recorded (Intensity).

*A-3. Ultraviolet-visible-near infrared spectrophotometry*

Light coming into a material can be reflected, absorbed, or transmitted. Spectrophotometer measures the relative intensity of transmitted light. An ultraviolet-visible-near infrared spectrophotometer uses light in in the visible and adjacent (near UV and near infrared) ranges (300 to 2000 nm) to obtain spectra.

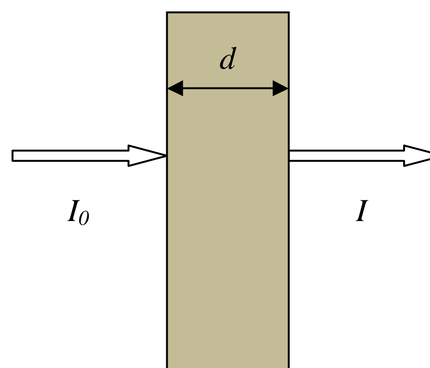


*Figure A-3.1. Diagram of Beer–Lambert absorption of a beam of light*

Principle of the spectrophotometer is based on Beer's law as below:

$$I = I_0 \exp(-\alpha d),$$

where $I_0$ and $I$ are the incident and transmitted light intensities, respectively, $d$ is the absorption path length, and α is absorption coefficient that depends on wavelength.

In order to measure transmission of light, intensity of incident light and transmitted light are determined on photo-resistors, photodiodes or photomultipliers.

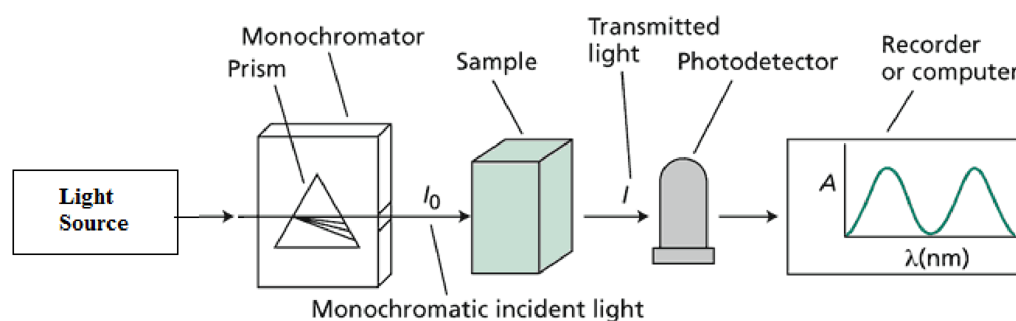


*Figure A-3.2. Schematic diagram of a spectrophotometer[4]*

## A-4. Lifetime measurement

### A-4.1. Microwave photoconductivity decay method (μ-PCD)

μ-PCD method provides a contactless measurement for effective minority carrier lifetime ($\tau_{eff}$) in semiconductor using a laser pulse for the optical excitation of minority carriers.

The generation of excess carriers in a silicon sample increases its conductivity, and hence, causes a change in the microwave reflectivity of the sample. This change in resistivity can be measured by means of the reflection of microwaves.

The excess carrier density is related to the excess conductivity via:

$$\Delta\sigma = q(\mu_n + \mu_p)\Delta n,$$

where $\mu_n$ and $\mu_p$ are electron and hole mobilities, respectively. The conductance and the incident light intensity are converted to electric signal measured by instruments. $\mu_n$ and $\mu_p$ are well known and their dependence on both the sample material and injection level can be found in literatures.

In order to measure $\tau_{eff}$, we use the continuity equation of minority carriers:

$$\frac{d\Delta n}{dt} = G(t) - \frac{\Delta n}{\tau_{eff}},$$

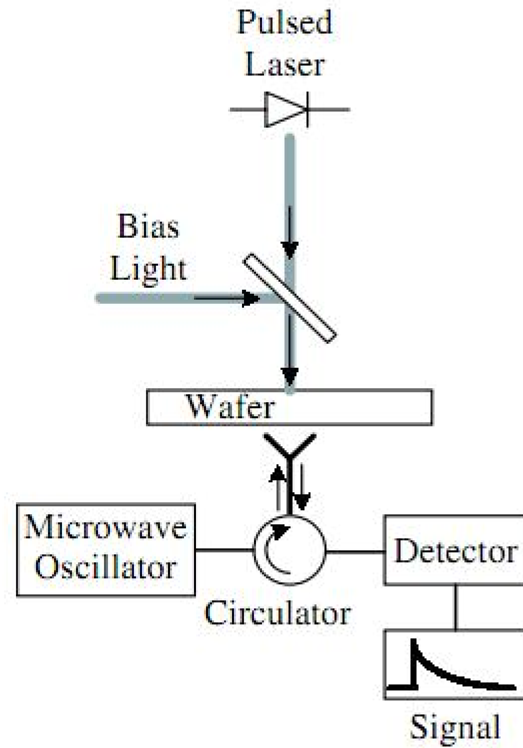


*Figure A-4.1. Schematic of μ-PCD measurement[5]*

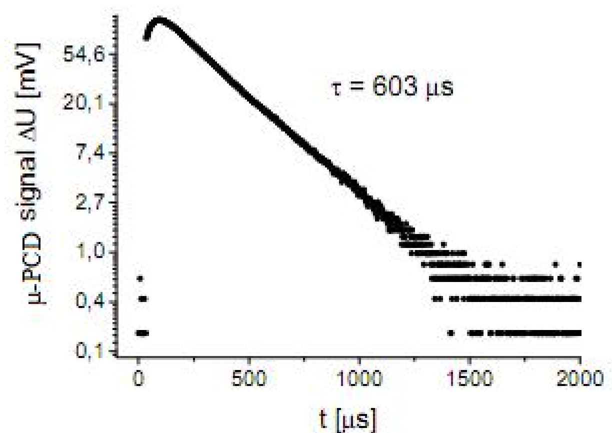


Figure A-4.2. μ-PCD signal as function of time for $SiN_x$ passivated on c-Si wafer [5]

where G(t) is the generation rate.

This mode is based on analyzing photoconductance decay transients after very short light pulse, that is, G($t$)=0 in $t$>0. The equation above is thus easily solved to be

$$\Delta n = A\exp(-t/\tau_{eff}),$$

where A is an arbitrary constant, and $\tau_{eff}$ is obtained from the slope of the decay curve, as shown in Figure A-4.2.

### *A-4.2 Quasi-steady state photoconductance decay method*

In quasi-steady state photoconductance (QSSPC) method, lifetime measurement is performed under quasi-steady-state illumination. That means excited light (usually flash light with a whole light spectrum) is tuned slowly so that $\frac{d\Delta n}{dt} \approx 0$. Light decay time is usually several milliseconds. In the steady state, the generation of electron hole-pairs must be balanced with their recombination. Therefore, generation current is equal to recombination current:

$$J_{photogeneration} = J_{recombination}$$

When sample is illuminated, excess carries are generated, resulting in an increase of wafer conductance:

$$\Delta\sigma = q(\Delta n\mu_n + \Delta p\mu_p)W = q\Delta n(\mu_n + \mu_p)W,$$

where $\Delta$n and $\Delta$p are excess electron and hole densities, respectively, $\mu_n$ and $\mu_p$ are the mobilities of electrons and holes, and $W$ is wafer thickness.

$$J_{ph} = \Delta nqW/\tau_{eff}$$

$$\tau_{eff} = \frac{\Delta nqW}{J_{ph}} = \frac{\Delta n}{G(t)}$$

In order to obtain $\tau_{eff}$, $\Delta n$ and $G(t)$ should be known.

$\Delta n$ can be converted from carrier density measured through a radio frequency (RF) coil inductively coupled to the sample. $\Delta n$ is the calculated as below:

$$\Delta n = \frac{\Delta\sigma}{qW(\mu_n + \mu_p)}$$

Photo-generation rate is converted from flash intensity measured by the calibrated light sensor for each moment time. An estimate of fraction of incident light absorbed in the sample (optical constant) is required.

### *A-5. Electron spin resonance*

Electron spin resonance (ESR) is a tool to find out how many un-paired electrons exist in a sample. The method is based on the phenomenon that, when an un-paired electron is placed in a strong magnetic field, the spin of un-paired electron splits into two states, $m_s=\pm 1/2$.

Electron has two kinds of movements. One is traveling around nucleus, causing orbital magnetic moment and the other is moving around its one axis, causing spin magnetic moment. If species, such as molecule, radicals… have un-paired electrons, it exhibits paramagnetism. When the species is put in a magnetic field, magnetic potential energy is supplied to split the un-paired electron into two spin states $m_s=\pm 1/2$, called Zeeman effect. Magnetic potential energy of electron spin in magnetic field:

$$E_{\pm\frac{1}{2}} = \pm\frac{1}{2} g\mu_B B$$

$B$: strength of the magnetic field

$g$: g factor

$\mu_B$: Bohr magneton.

Transitions of electrons between the two spin states can be induced by supplying electromagnetic energy (usually using microwave radiation):

$$\Delta E = g\mu_B B$$

During experiment, we can continuously change the intensity of the external magnetic field or microwave radiation. ESR spectrum is the derivative of the absorption of microwave frequency radiation vs magnetic field strength or microwave frequency.

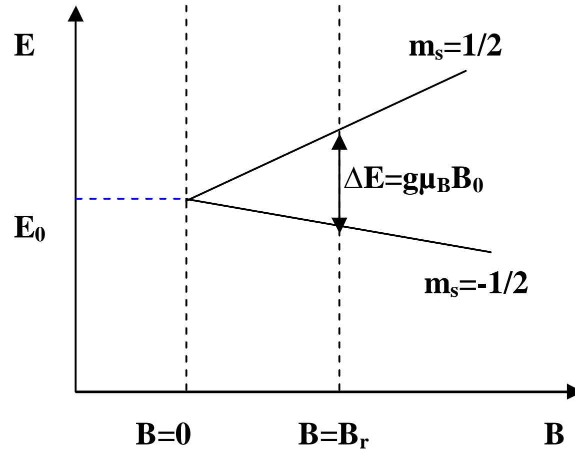


*Figure A-5.1. The split of electron spin states.*

Because defect density in a measured film is proportional to the microwave absorption, in order to calculate defect density from ESR signal, a reference sample whose defect density has been known is needed.

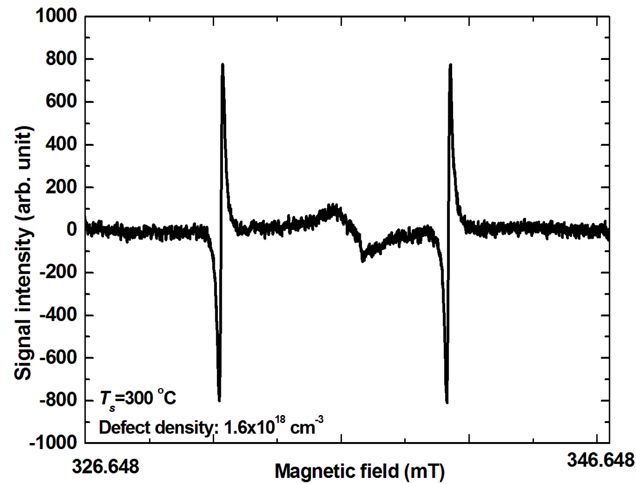


*Figure A-5.2. A ESR signal obtained for $SiN_x$/glass*

We can obtain defect density as:

$$N_{samp} = N_{ref} \times \frac{A_{samp}}{A_{ref}},$$

where $N_{samp}$ and $N_{ref}$ are the defect densities of measured and reference samples, and $A_{samp}$ and $A_{ref}$ are the areas of absorption peak of measured and reference samples.

*A-6. Hall effect measurement*

In order to understand doping concentration measurement, I firstly introduce Hall effect. When a conductive solid with a current flowing through is put in a magnetic field applied perpendicular to the current, magnetic will apply Lorentz force on charge carriers, by which the current flow is curved. I assume that there are carriers with a density of $n$ and an elementary charge of $q$ moving with speed $v_x$ creating current $I_x$ with $x$ direction as Figure A-6-1.

Current $I_x$ equals to:

$I_x = n.q.w.t.v_x$

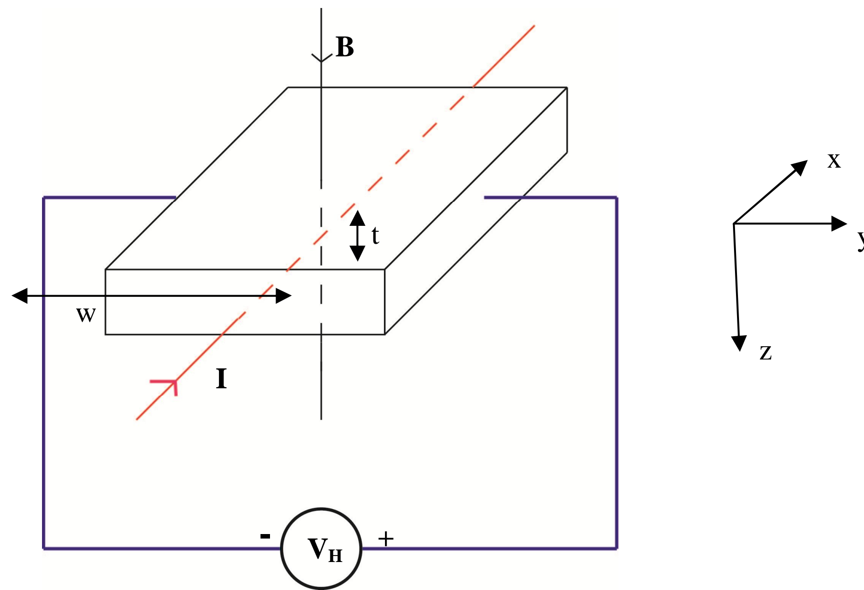


*Figure A-6.1. Hall effect measurement. B is electric field, I is current, $V_H$ is Hall voltage, w and t are width and thickness of a thin film respectively.*

Lorentz force on a carrier:

$$F_y = q.v_x.B_z$$

Carriers pushed toward $y$ direction cause electric field $E_y$. Electric force applied on carriers is:

$F_{Ey} = E_y.q$

where $E_y$ is electric field in $y$ direction.

In steady condition, there is no current flow in $y$ direction. Therefore,

$q.v_x.B_z = E_y.q$

then, $E_y = v_x.B$

Voltage crossing the sample in y direction is Hall voltage, and is determined as:

$$V_H = -\int_0^w E_y dy = E_y.w = v_x.B_z.w$$

Since $v_x = \frac{I_x}{nqwt}$, we have $V_H = -\frac{I_x B_z}{qnt} = \frac{I_x B_z}{R_H}$, where $R_H$ is Hall coefficient.

$$R_H = -\frac{1}{|q|n_s} \text{ for n-type}$$

$$R_H = \frac{1}{|q|n_s} \text{ for p-type}$$

In this study, I used Van der Pauw method to calculate carrier concentration of P Cat-doped layers. A configuration of my sample for Hall measurement is shown in Figure A-6-2. Van der Pauw method is very convenient to determine resistivity of uniform samples.

Sheet resistance $R_s$ is determined through Van der Pauw equation:

$$\exp\left(\frac{-\pi R_A}{R_S}\right) + \exp\left(\frac{-\pi R_B}{R_S}\right) = 1,$$

where $R_A$ and $R_B$ is determined by:

$$R_A = \frac{R_{12,43} + R_{43,12} + R_{21,34} + R_{34,21}}{4}$$

and

$$R_B = \frac{R_{23,14} + R_{14,23} + R_{32,41} + R_{41,32}}{4}$$

$R_{21,34} = V_{34}/I_{21}$, $R_{12,43} = V_{43}/I_{12}$,

$R_{32,41} = V_{41}/I_{32}$, $R_{23,14} = V_{14}/I_{23}$,

$R_{43,12} = V_{12}/I_{43}$, $R_{34,21} = V_{21}/I_{34}$,

$R_{14,23} = V_{23}/I_{14}$, $R_{41,32} = V_{32}/I_{41}$.

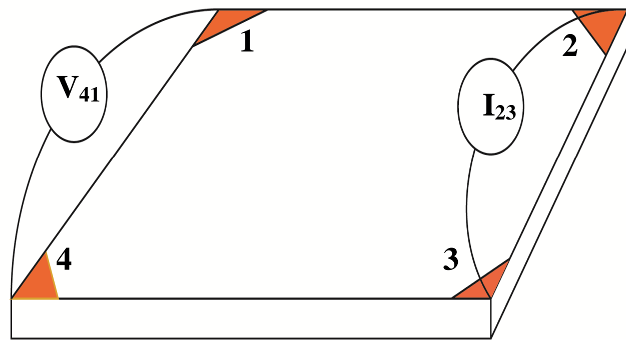


Figure A-6.2 Van der Pawn configuration for Hall measurement.

To conduct the measurement, firstly positive magnetic field is applied. After that, $I_{24}$ is applied and $V_{13}$ is measured, and then repeated for $I_{13}$ and $V_{42}$.

These processes are performed again for negative magnetic field.

Hall voltage is sum of difference voltage at positive and negative magnetic field between two points:

$$V_H = \frac{V_{13} + V_{31} + V_{24} + V_{42}}{8}$$

We can calculate sheet carrier density as:

$$n_s = \frac{IB}{q|V_H|}$$

### *A-7. X-ray reflectivity*

When an electromagnetic light impinges to material surface, electrons in material will oscillate and a new electromagnetic wave is created. The new radiation wave is resonant of electron vibration around atoms and incoming wave. The different phase of the incoming light and new radiation determines what the index of refraction is.

The real part of refractive index is written as:

$$n = 1 + \frac{q^2 N}{2\varepsilon_0 m\left(\omega_0^2 - \omega^2\right)} \quad \text{(A-7.1)}$$

For electromagnetic light with large wavelength, such as visible region, wave oscillation is relatively slow. When this light impinges on a material, electrons in material can oscillate following the wave and vibrate around their equilibrium position. The vibrations cause new radiation waves, which have a frequency less than that of incoming light. Therefore, refractive index of these wavelength is larger than 1.

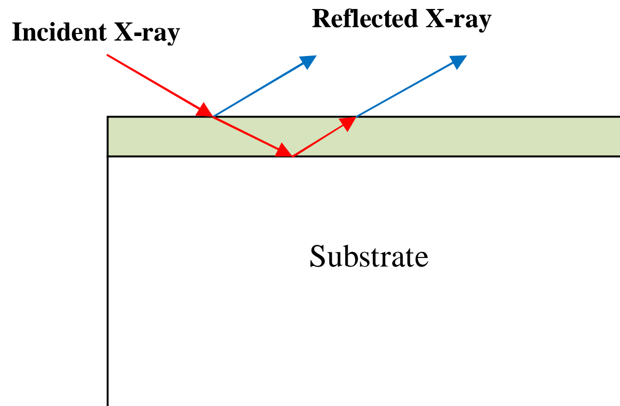


*Figure A-7.1. Sketch of a X-ray reflectivity*

X-ray is an electromagnetic wave with wavelength of 0.1-10 nm. Its wave frequency is very high. When X-ray comes to a material surface, the electron cannot follow the wave oscillation. The wave radiated by electrons has a phase lower than that of incoming light. Therefore, refractive index of material at X-ray wavelength is less than 1. Notice that refractive index of less than 1 here does not mean that velocity of light in material is higher than velocity of light in vaccum (which is proved as the highest velocity).

Typical reflectivity of X-ray on a material is shown in Figure A-7-2. X-ray is totally reflected on material surface at a grazing angle is smaller than the critical angle for total reflection $\theta_c$ .

Refractive index is complex number:

$$n = 1 - \delta - i\beta \qquad \text{(A-7.2)}$$

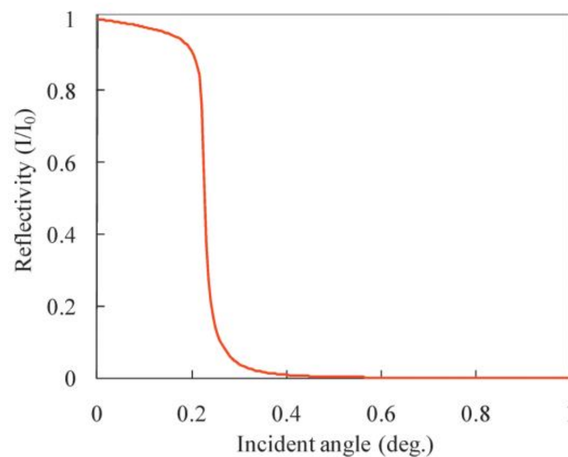


*Figure A-7.2. Reflectivity as a function of incident angle [6]*

where

$$\delta = \frac{r_e \lambda^2}{2\pi} N_A \rho \frac{\sum_i x_i (Z_i + f_i^{'})}{\sum_i x_i M_i} \qquad \text{(A-7.3)}$$

$$\beta = \frac{r_e \lambda^2}{2\pi} N_A \rho \frac{\sum_i x_i (Z_i + f_i^{''})}{\sum_i x_i M_i} \qquad \text{(A-7.4)}$$

$r_e$ :classical radius of an electron ($2.8\times10^{-15}$ m)

$N_A$ :Avogadro number

$\lambda$: X-ray wavelength

$\rho$: film density (g/cm$^3$)

$Z_i$: Atomic number of the i-th atom.

$M_i$: Atomic weight of the i-th atom.

$f_i^{'}, f_i^{''}$: Atomic scattering factors.

Density of polished bulk material or thin films can be calculated by using simplification of equation (*):

$$\delta \approx \frac{r_e}{2\pi} \rho_e \lambda^2 \qquad \text{(A-7.5)}$$

A simple equation describing the relationship between real part of refractive index and electron density of film was found as below [7]:

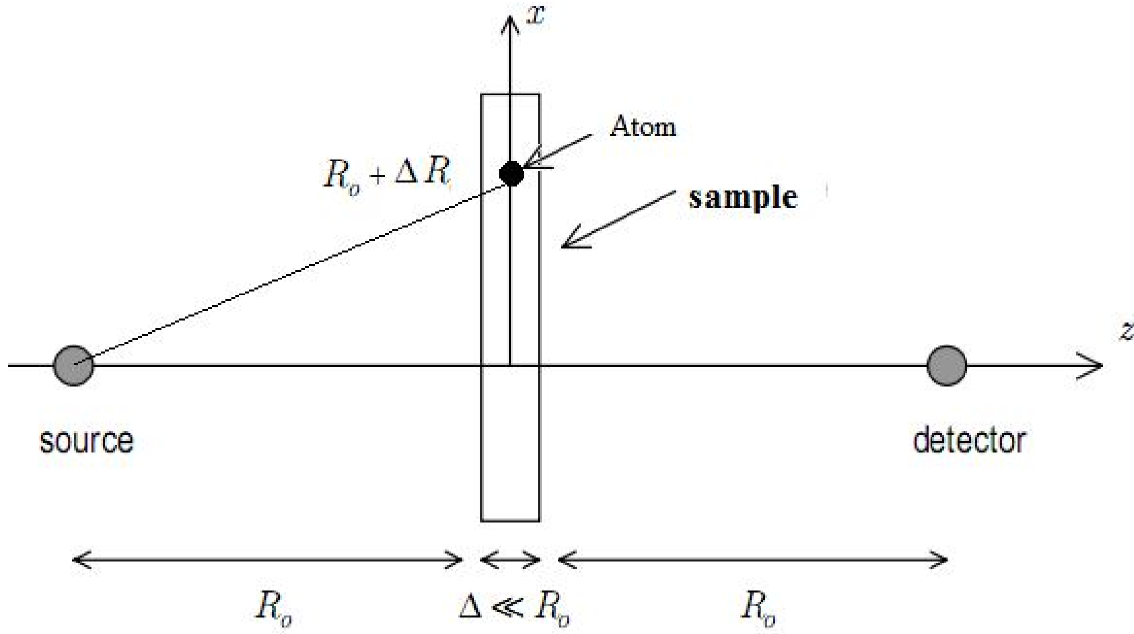


*Figure A-7.3. Illustration of light propagation from a source to a detector [7].*

Assume that there is electric field wave at source $E_0$ coming to sample and $E_d$ is electric field detected by detector, as shown in Figure A-7.3.

$$E_d \approx E_0 \frac{e^{i2kR_0}}{2R_0} \underbrace{e^{i(n-1)k\Delta}} \approx E_0 \frac{e^{i2kR_0}}{2R_0}(1 + i(n-1)k\Delta) \qquad \text{(A-7.6)},$$

Phase shift of wave inside sample.

where $k$ is wave vector, $n$ is refractive index of medium and $R_0$ is distance from source to sample and sample to detector.

Consider scattering of X-rays from individual atoms, we have wave scattered by atom at $R$+$\Delta R$ picked up by detector is:

$$E_{scatt} = -E_{in} \frac{e^{ik(R_0+\Delta R)}}{R_0} r_0 f(\overline{Q}) \qquad \text{(A-7.7)}$$

With $E_{in} = -E_0 \frac{e^{ik(R_0+\Delta R)}}{R_0}$ (A-7.8)

$$\Delta R = \sqrt{R_0^2 + x^2 + y^2} \approx R_0 \left(1 + \frac{x^2 + y^2}{2R_0^2}\right) \qquad \text{(A-7.9)}$$

$$\rho_{atom} z = \rho_e \text{ (electron density)} \qquad \text{(A-7.10)}$$

Integrate over all atoms in sample:

$$\begin{aligned} E_{scatt} &= -E_0 \frac{e^{2ikR_0}}{R^2{}_0} \int_{-\infty}^{\infty} \rho_{atom} \Delta r_e Z e^{ik\frac{x^2+y^2}{R_0}} dxdy \\ &= -E_0 \frac{e^{2ikR_0}}{kR^2{}_0} \rho_e \Delta r_e \int_{-\infty}^{\infty} Z e^{ik(x_*^2+y_*^2)} dx_* dy_* \end{aligned} \qquad \text{(A-7.11)}$$

where $x_* = \sqrt{\frac{k}{R_0}} x$, $y_* = \sqrt{\frac{k}{R_0}} y$.

Using $\int_{-\infty}^{+\aleph} e^{-x^2} dx = \sqrt{\pi}$ , we obtain:

$$E_{scatt} = -E_0 \frac{e^{2ikR_0}}{R^2{}_0} \rho_e \Delta r_e \pi \quad \text{(A-7.12).}$$

Total electric field at detector equals to sum of unscattered wave and sum of all waves scattered by atoms in sample, we have:

$$E_d = E_0 \frac{e^{2ikR_0}}{2R^2{}_0} \left[ 1 - \frac{2\rho_e \Delta r_e \pi}{k} \right] \quad \text{(A-7.13)}$$

From (A-7.6) and (A-7.13), we obtain:

$$\delta = \frac{2\pi r_e \rho_e}{k^2} = \frac{r_e}{2\pi} \rho_e \lambda^2 \qquad \text{(A-7.14)}$$

From electron density, we can easily calculate film density using this below equation:

$$\rho = \frac{M_A \rho_e}{N_A \mathrm{Z}} \qquad \text{(A-7.15),}$$

where $M_A$ is atomic mass; $Z$ is atomic number.

The real component of refractive index is related to critical angle:

$$\theta_c = \cos^{-1}(1-\delta) \qquad \text{(A-7.16)}$$

Or

$$\delta = \frac{\theta^2{}_c}{2} \qquad \text{(A-7.17)}$$

Once critical angle is known, film density can be calculated.

### *A-8. Secondary ion mass spectrometry*

Secondary ion mass spectrometry (SIMS) is a method to analyze the concentration and profile of a particular element in a solid by identifying and counting the number of secondary ions ejected from the sample surface when it is bombarded by a primary beam of heavy ions. The schematic of a SIMS system is shown in Figure A-8.1.

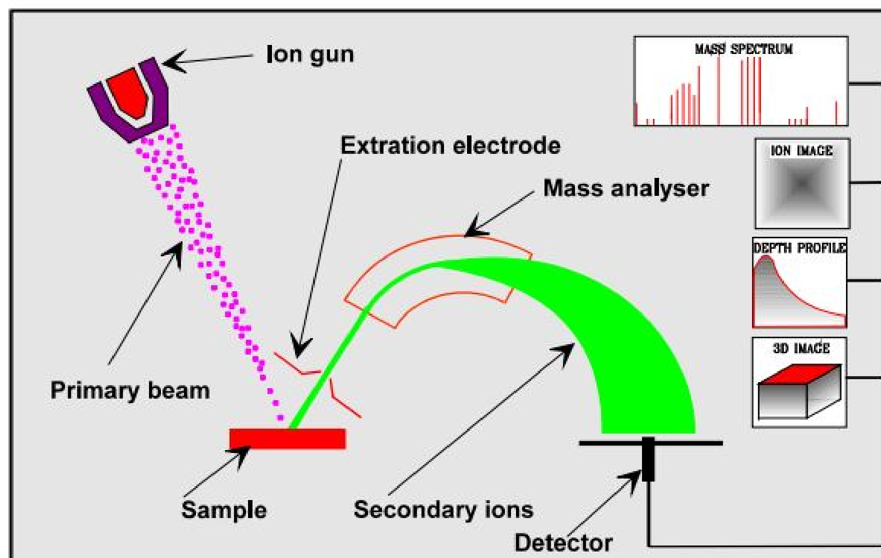


*Figure A-8.1. Schematic of a SIMS measurement [8].*

Primary ions come to a surface with high speed, sputter the surface of the surface, and secondary ions (from sample) are formed. These secondary ions are immediately trapped by using extraction electrode and driven to an ion energy analyzer. Depending on the polarity of the sample, positive or negative secondary ions may be extracted.

Secondary ions include molecular species with low energy and mono-atomic species with high energy. By adjusting position window energy to detector, mono atomic

species are selectively collected. In order to identify the component, there are three basic analyzers: sector, quadrupole and time of flight.

❖ A sector field mass spectrometer uses electrostatic and a magnetic analyzer to obtain mass to charge ratio of secondary ion. When ions pass through magnetic field, Lorentz force acts as a centripetal force. Since the radius of ion movement is proportional to the mass of species, desired species can be selectively detected if a slit with a proper width is set in front of the detector.

❖ A quadrupole mass analyzer using resonant electric field to collect selected mass ions. A quadrupole consists of two couples of opposite rods having an applied opposite potential, as shown in figure A-8.3. Voltage applied affects the trajectory of ions traveling through the rods. For given dc and ac voltages, only ions of a certain mass-to-charge ratio can pass through and reach a detector.

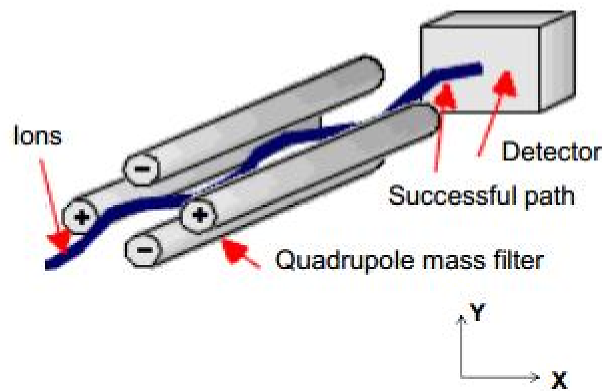


*Figure A-8.2. Schematic of a quadrupole[9]*

Ions with low and high mass-to-charge ratio are separated by effect of ac and dc component. Low mass-to-charge ratio ions are able to follow ac component and are discharged by striking X electrode. Only high mass-to-charge ratio ions are collected at the end of quadrupole. In contrast, only low mass-to-charge ratio ions are collected at the end of quadrupole in Y direction because high mass to charge ratio ions are defocused by dc component. By choose RF/DC ratio, selected mass ions can be obtained.

The relationship between mass-to-charge ratio, voltage and ac frequency is described as below:

$$\frac{d^2x}{dt^2} = -\left(\frac{q}{m}\right)\frac{U + V\cos(wt)}{r_0^2}x$$

$$\frac{d^2y}{dt^2} = \left(\frac{q}{m}\right)\frac{U + V\cos(wt)}{r_0^2}y$$

$$\frac{d^2z}{dt^2} = 0$$

- ❖ A time-of-flight mass analyzer is based on the velocity of ions to separate the ions in field-free drift path. Ions are accelerated by an electric field. Ions with the same charge will have the same kinetic energy $E_k$. However, the velocity of ions depends on mass-to-charge ratio.

$$E_k = qU = \frac{1}{2}mv^2$$

$$v = \frac{d}{t}$$

$$\rightarrow t = \frac{d}{2U}\sqrt{\frac{m}{q}}$$

Here, $d$ is length of path. $U$ is voltage applied to accelerate ions.

By measure the time for ions to reach a detector, we can find mass-to-charge ratio of the ions.

### *A-9. Scanning electron microscopy*

Scanning electron microscope is a tool to examine and analysis microstructural morphology of samples by using electron beam. Electron beam scan on a sample surface from left to right and top to down. During the scanning, electrons such as secondary electrons and back scattering electrons are rejected and extracted by their own detectors. The signal obtained will be visualized as an image.

A stream of electrons is formed in an electron gun and the electrons are accelerated toward specimen using a positive electrical potential. An electron lens is used to focus the electron beam on a sample.

When an electron beam hits the sample surface, secondary electrons and back scattering electrons are ejected. Secondary electrons are ejected from the sample surface. These electrons are collected on a detector which has positive charges on it. The detector collects information of these electrons and forms image depending on the number of collected electrons. Surface morphology such as difference of height, edge or groove gives a difference of the number of secondary electrons emitted. Using the signal from secondary electrons, image resolution less than 0.5 nm is possible.

Back scattering electrons consist of high energy electron from electron beam that are reflected and back-scattered out of specimen by elastic scattering reactions with specimen atoms. Because back scatter electrons with heavy element are more strongly than light ones, a sample consisting of heavier element shows brighter image. Therefore, the signal from back scattering electrons indicates information of areas with different chemical composition.

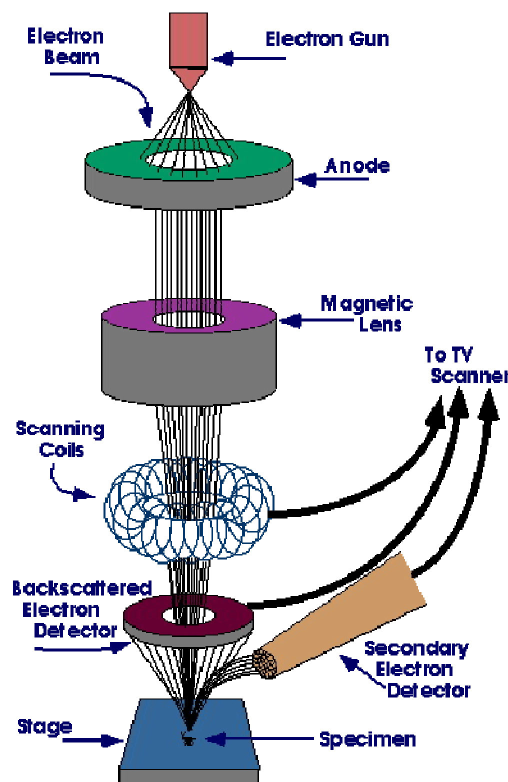


*Figure A-9.1. Schematic of a SEM system [10]*

## *A-10. $D_{it}$ Calculation*

### *A-10.1.* C-V curve of MIS structure

In order to understand the method to calculate defect density on a film/c-Si interface using C-V curve, I firstly introduce the C-V curve of MIS structure.

A MIS structure is shown in Figure A-10.1, which was also used in my study.

For n-type c-Si, electrons are the majority carriers and holes are minority carriers. I firstly assume that an insulator layer is ideal, that is, there is no charge or defect in insulator layer and at the interface. When no voltage is applied, because of the difference of the work functions of metal and semiconductor, energy levels near semiconductor surface bend. Energy diagrams of MIS structure when no voltage applied are illustrated in Figure A-10.2. In order to make a flat band condition, a voltage called flat band voltage ($V_{FB}$) need to be supplied:

$$V_{FB} = \phi_M - \phi_S ,$$

where $\phi_M$ and $\phi_S$ is work function of metal and semiconductor, respectively.

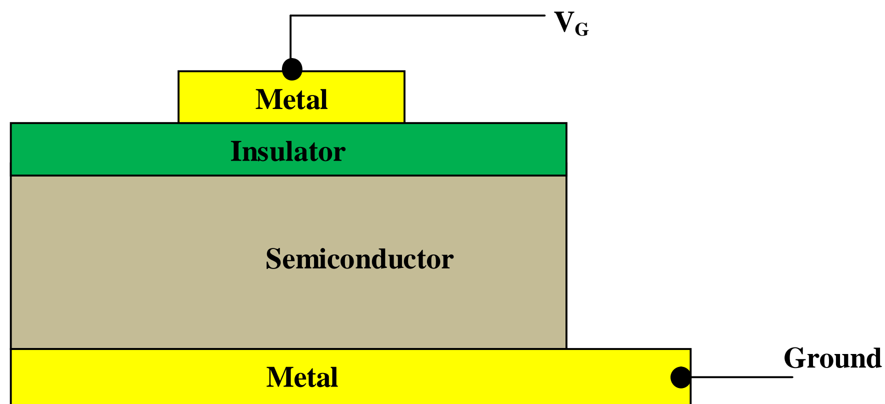


*Figure A-10.1. Configuration of MIS structure for C-V measurement.*

Figure A-10.3 shows energy diagram of MIS structure under flat band condition for n-type and p-type.

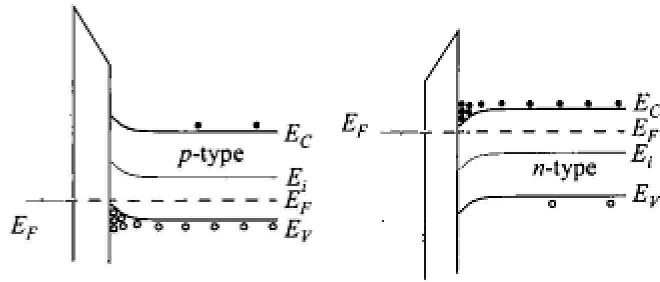


*Figure A-10.2. Energy diagrams of MIS structures using n-type and p-type semiconductors. If No voltage is applied, band bends due to the difference of work function between metal and semiconductor[11]*

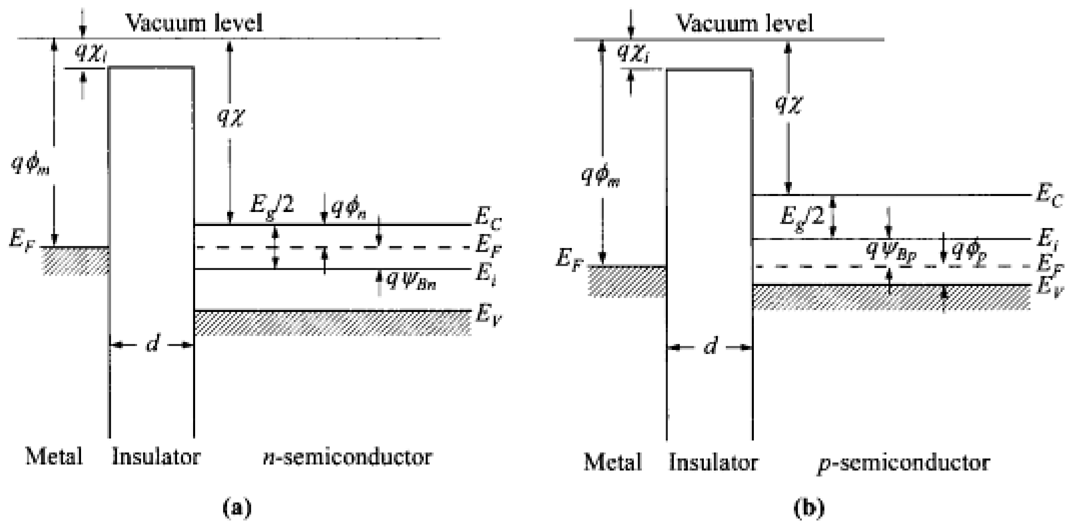


*Figure A-10.3. Energy diagram of MIS structure under flat band condition for (a) n-type and (b) p-type [11]*

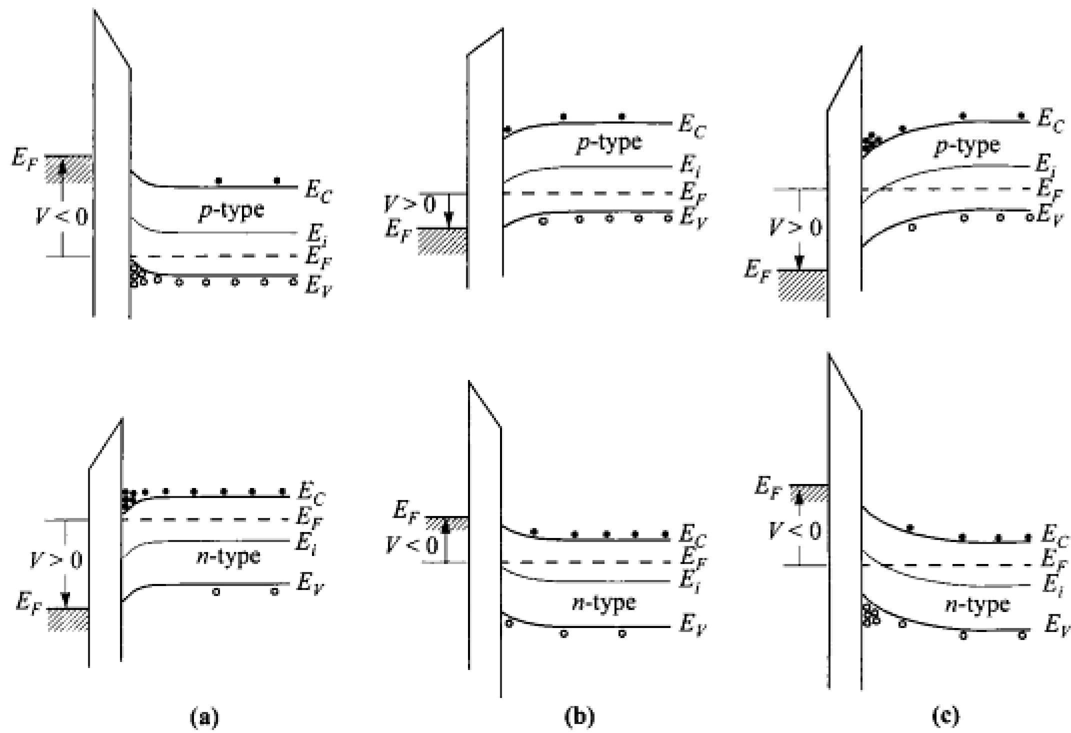


*Figure A-10.4. Energy band diagrams for ideal MIS capacitors under (a) accumulation, (b) depletion and (c) inversion. [11]*

When voltage is applied, energy band of c-Si bends depending on applied voltage, as shown in Figure *A-10.4*. For example, in the case of n-type semiconductor, when positive charge voltage applied, negative charges in c-Si are induced on a c-Si surface. Electron density near the surface of c-Si is calculated by:

$$n_s = N_D \exp(\frac{q\psi_s}{kT}) \quad \text{(A-10.1)},$$

where $\psi_s$ called band bending is energy difference between surface and bulk potential:

$$\psi_s = \phi_s - \phi_b \quad \text{(A-10.2)},$$

as illustrated in Fig. A-10.5.

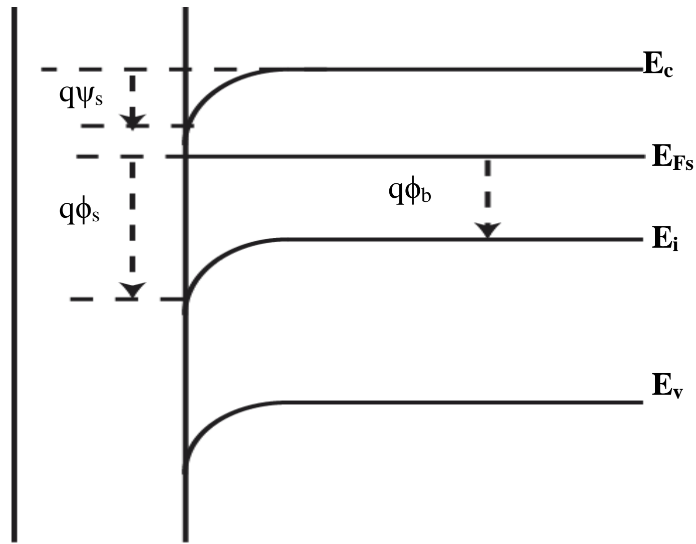


*Figure A-10.5. Illustration of $\psi_s$, $\phi_s$ and $\phi_b$ in energy band for a n-type c-Si.*

Figure A-10.6 shows carrier density and charge density under various conditions of MIS structures for both n-type and p-type Si. For n-type Si, when $n_s$ is larger than $N_D$, $\phi_s > \phi_b$ and band bends down. This condition is accumulation. In this condition, large electron charge density near the surface contribute to a large differential capacitance, thus $C_s >> C_i$ and $C = C_i$.

When $n_s = N_D$, applied voltage is equal to flat band voltage, and band is flat.

When negative bias is applied to the gate electrode, electrons are pushed away from the surface, and $n_s$ is less than $n_d$, $\phi_s < \phi_b$, and band bends up. This condition is depletion.

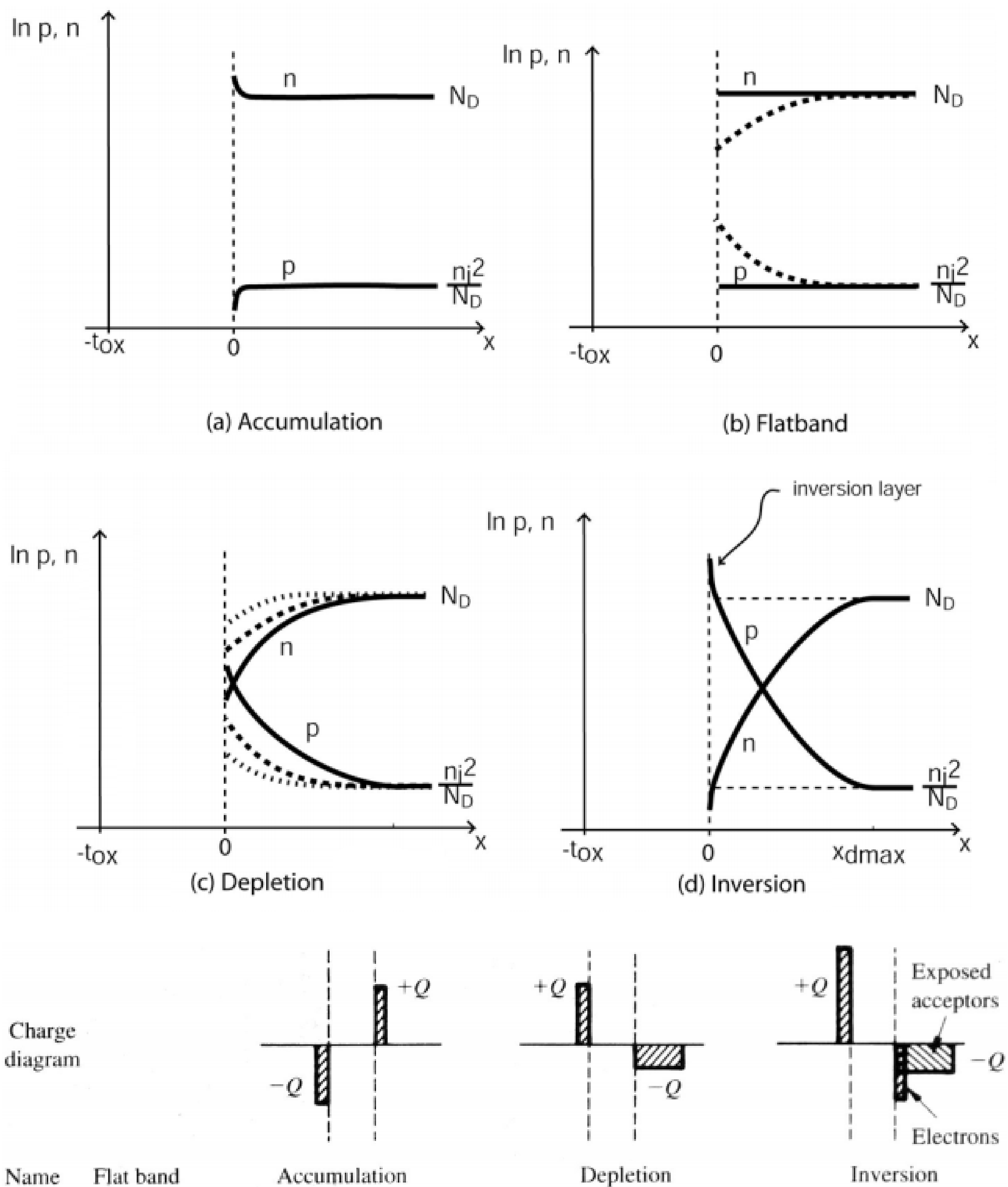


*Figure A-10.6. Carrier density and charge density under various conditions of MIS structures [11].*

In the depletion condition, the MIS capacitance at low frequency and high frequency ($C_{LF}$ and $C_{HF}$) is obtained from the series connection of the insulator capacitance ($C_i$) and the capacitance of the depletion layer, or:

$$C_{LF} = C_{HF} = \frac{1}{\frac{1}{C_i} + \frac{x_d}{\varepsilon_s}} \qquad \text{(A-10.3)},$$

where $\varepsilon_i$ is permittivity of semiconductor. $x_d$ is the depletion layer width which is calculated from:

$$x_d = \sqrt{\frac{2\varepsilon_S \phi_s}{qN_D}} \qquad \text{(A-10.4)}$$

In order to find the capacitance corresponding to a specific value of the gate voltage, we also need to use the relation between the potential across the depletion region and the gate voltage, given by:

$$V_G = V_{FB} + \phi_s + \frac{\sqrt{2\varepsilon_s qN_D \phi_s}}{C_i} \quad \text{for } 0 \le \phi_s \le 2\phi_b \qquad \text{(A-10.5)}.$$

When negative voltage is very high, hole concentration near the c-Si surface is comparable to $N_D$. This condition is inversion. In the inversion condition, the capacitance becomes independent of the gate voltage. The low frequency capacitance equals to the insulator capacitance since charge is added to and is removed from the inversion layer. The high frequency capacitance is obtained from the series connection of the insulator capacitance, and the capacitance of the depletion layer having its maximum width ($x_{dmax}$). The capacitances are given by:

$$C_{HF} = \frac{1}{\frac{1}{C_i} + \frac{x_{d\max}}{\varepsilon_s}} \qquad \text{(A-10.6)}$$

### *A-10.2.* Theoretical C-V curve

In this method, we need to calculate theoretical C-V curve at high frequency. The method to calculate C-V theoretical curve is described below.

For n-type semiconductor, electron density at a position $x$ is:

$$n(x) = N_D \exp\frac{q\psi(x)}{kT} \qquad \text{(A-10.7)},$$

where $N_D$ is donor concentration.

For convenient, I denote potential and band bending in unit of $kq/T$ as below:

$$n(x) = \frac{q\phi(x)}{kT} \qquad \text{(A-10.8)}$$

$$v(x) = \frac{q\psi(x)}{kT} \qquad \text{(A-10.9)}$$

In equilibrium condition, product of mobile hole and electron concentration in sample at any position is equal to square of intrinsic carrier concentration.

$$pn = n_i^2 \qquad \text{(A-10.10)}$$

Then, $n(x) = n_i \exp(u(x)) = N_D \exp(v(x))$ (A-10.11)

For carrier concentration at the surface, we have:

$$n_s = n(x=0) = n_i \exp(u_s) = N_D \exp(v_s) \qquad \text{(A-10.12)}$$

$$p_s = p = n_i \exp(-u_s) = N_A \exp(-v_s) \qquad \text{(A-10.13)}$$

By solving poison equation, we have:

$$\frac{d^2\phi(x)}{dx^2} = -\frac{\rho(x)}{\varepsilon_s} \qquad \text{(A-10.14)},$$

where $\varepsilon_s$ is permittivity of silicon.

$$\rho(x) = q[p(x) - n(x) + N_D - N_A] \qquad \text{(A-10.15)}$$

$$\frac{d^2\phi(x)}{dx^2} = -\frac{q[p(x) - n(x) + N_D - N_A]}{\varepsilon_s} \qquad \text{(A-10.16)}$$

Because $N_A$ and $N_D$ are the concentration of acceptor and donor in bulk of c-Si so we have:

$$N_D - N_A = n(\infty) - p(\infty) \quad \text{or} \quad N_D - N_A = n_i(\exp(u_B) - \exp(-u_B)) \qquad \text{(A-10.17)}$$

$$\frac{d^2\phi(x)}{dx^2} = -\frac{ni(\exp(u_B) - \exp(u(x)) - ni(\exp(-u_B) - \exp(-u(x)))}{\varepsilon_s} \qquad \text{(A-10.18)}$$

$$v(x) = u(x) - u_B \qquad \text{(A-10.19)}$$

$$\rightarrow \frac{d^2\phi(x)}{dx^2} = -\frac{N_D(1-\exp(v(x)) - \frac{ni^2}{N_D}(1-\exp(-v(x))}{\varepsilon_s} \quad \text{(A-10.20)}$$

$$\frac{d^2\phi(x)}{dx^2} = \frac{kT}{q}\frac{d^2u(x)}{dx^2} \text{ (21)}$$

We have: $\frac{d}{dx}\left(\frac{du(x)}{dx}\right)^2 = 2\frac{du}{dx}\frac{d^2u}{dx^2}$ (A-10.22)

$$2\int_{\frac{du_s}{dx}}^{0} \frac{d^2u}{dx^2} = \int_{u_s}^{u_b}\left(\frac{du(x)}{dx}\right)^2 \quad \text{(A-10.23)}$$

where $\frac{du_s}{dx} = E = \frac{q}{kT}Fs$ is electric field at c-Si surface.

By integrating above equation, we obtain:

$$E^2 = \left(\frac{2kT}{q}\right)^2\left(\frac{qN_Dq}{2\varepsilon_s kT}\right)\left(\frac{n_i^2}{N_D^2}[\exp(-us)+us-1]+[\exp(us)-us-1]\right) \quad \text{(A-10.24)}$$

Electric field at the surface:

$$E_s^{\ 2} = \left(\frac{2kT}{q}\right)^2\left(\frac{qN_Dq}{2\varepsilon_s kT}\right)\left(\frac{n_i^2}{N_D^2}[\exp(-vs)+vs-1]+[\exp(vs)-vs-1]\right) \quad \text{(A-10.25)}$$

$$Fs = \left(\frac{n_i^2}{N_D^2}[\exp(-us)+us-1]+[\exp(us)-us-1]\right) \quad \text{(A-10.26)}$$

Total charge per unit area is $Q_s = \varepsilon_s E$

$$Qs = \text{sgn}(-vs)\frac{\varepsilon_s}{\lambda_n}\left(\frac{kT}{q}\right)Fs \quad \text{(A-10.27)}$$

Debye length $\lambda_n$ is defined as:

$$\lambda_n = \left(\frac{\varepsilon_s kT}{2q^2\ N_D}\right)^{\frac{1}{2}} \quad \text{(A-10.28)}$$

At low-frequency capacitance, semiconductor capacitance is calculated as:

$$Cs = \frac{dQ_s}{dv_s} = \frac{\frac{n_i^2}{N_D^2}(1-\exp(-vs)) - (\exp(vs)-1)}{Fs} \quad \text{(A-10.29)}$$

At flat band condition, $v_s$=0, capacitance of semiconductor is

$$C_{FBS} = \frac{\varepsilon_s}{\lambda_n} \quad \text{(A-10.30)}$$

Total capacitance is:

$$C = \frac{Cs * Ci}{Cs + Ci} \quad \text{(A-10.31)}$$

Next, we will find applied gate voltage. Applied voltage is equal to sum of insulator voltage and voltage drop through semiconductor or:

$$Vg = Vi + Vs + V_{Fb} = Vi + \phi s + V_{Fb} \quad \text{(A-10.32)}$$

$$Vox = -sign(vs)\frac{Qs}{Ci} \quad \text{(A-10.33)}$$

$\Phi s$ is surface potential calculated through $v_s$. $V_{Fb}$ is calculated by the difference of work function between metal and semiconductor.

For example here, I use Al and 1.5Ωcm n-type c-Si surface. Work function of Al is 4.1 eV [12]. For n-type c-Si with resistivity of 1.5 Ωcm, donor concentration is $1.87\times10^{17}$ $cm^{-3}$. Gap energy between conduction band and valence band of c-Si is 1.12 eV.

$$-(E_C - E_F) = 0.026\ln\frac{N_D}{ni} = 0.43eV$$

$$\phi_{ms} \equiv \phi_m - \left(\chi + \frac{E_g}{2q} - \psi_B\right) = \phi_m - (\chi + E_F - E_C) = 4.1 - 4.05 - 0.43 = -0.48$$

$V_{Fb}$=-0.48 V

The big difference between high and low frequency capacitance is from weak to strong inversion region. In this region, minority carriers play a critical role. Surface charge density is a sum of inversion charges and depletion charges. At low frequency of AC voltage, the change of voltage is not so fast that minority carriers can follow the AC signal. That means minority carriers can neutralize AC charge in depletion region. Minority

carrier density increases exceeds ionized bulk concentration, and capacitance of inversion layer becomes comparable to and then exceeds $C_i$, and total capacitance approaches $C_i$.

On the other hand, in case of high-frequency, AC voltage changes very quickly. Minority carrier generation does not follow the ac voltage, and minority carrier density does not change with change in AC voltage. In order to make charge neutralization for AC charge in depletion layers, majority carriers flow in and out of the boundary between the depletion layer and bulk silicon. Depletion layer edge move with the variation of AC voltage. Because depletion layer width does not change when increase gate voltage more than limitation of depletion region voltage, capacitance in depletion does not change. Total capacitance is lowest capacitance in depletion for inversion region.

To draw a high-frequency C-V curve, a simple way is: firstly make a low-frequency curve and then, take the lowest value of capacitance as value of higher applied voltage. However, minority carrier density does change spatially with increase in applied voltage. This fact can induce the error of inversion region of high-frequency C-V curve.

To eliminate this error, we consider the change of Fermi level when majority carriers flow in and out, causing small change in depletion layer width. The new Fermi level is called quasi Fermi level. Electron and hole concentrations become:

$$p(x,t) = n_i \exp(-v(x,t) - u_{Fp}(t)) \quad \text{(A-10.34)}$$

In which, $u_{Fp} = -\dfrac{E_{Fp} - Ei}{kT}$ (A-10.35)

For n-type, charge density per unit volume is

$$\rho = -q(p - n + N_D) = -n_i\left(\exp(u_B)[1 - \exp(v)]\right) - \exp(-v - u_{Fp}) \quad \text{(A-10.36)}$$

Poisson equation becomes:

$$\frac{d^2 v}{dx^2} = \lambda_n^{-2}\left[1 - \exp(v) + \exp(-v - u_{Fn} - u_B)\right] \quad \text{(A-10.37)}$$

$$\left|\frac{dv}{dx}\right|_{x=0} = 2^{1/2}\lambda_n^{-1}\left(-vs + \exp(vs) - 1\right) + \exp(-u_B - u_{Fp})\left[\exp(-vs) - 1\right]^{1/2} = \lambda_n^{-1} Fs \quad \text{(A-10.38)}$$

The small-signal quantities defined as

$$u_{Fp} = u_B + \delta u_{Fp} \quad \text{(A-10.39)}$$

$vs = vso + \delta vs$   (A-10.40)

Silicon surface capacitance is calculated as

$$Cs = \varepsilon_s \frac{\delta}{\delta vs}\left(\frac{dv}{dx}\right)_{x=0} \quad \text{(A-10.41)}$$

Therefore, for n-type c-Si, for $vs<-u_B$ , we have:

$$Cs = C_{FBS}\left\{1-\exp(-vs)+\left(\frac{ni}{N_D}\right)^2\left[\left(\exp(-vs)-1\right)\left(1-\frac{\delta u_{Fp}}{\delta vs}\right)\right]\right\}Fs^{-1} \quad \text{(A-10.42)}$$

In order to find $\frac{\delta u_{Fb}}{\delta vs}$, we use the condition that excess carrier density at surface caused by AC voltage and applied voltage must equal to excess carrier density caused by applied voltage only.

That means:

$$\begin{aligned} Q_p &= q\int_0^\infty p(x) - N_A \\ &= qni\int_0^\infty \{\exp(-vx-u_{Fn})-\exp(-u_B)\} \quad \text{(A-10.43)} \\ &= qni\int_0^\infty \{\exp(-vx-u_B)-\exp(-u_B)\} \end{aligned}$$

Solve the above equation, we find: $\frac{\delta u_{Fn}}{\delta vs} = \frac{1}{1+\Delta}$   (A-10.44),

where

$$\Delta = \frac{Fs(vs0)}{\exp(-vso)+1}\left\{\int dvs\left[\frac{\exp(-vs+\exp(vs)+2vs}{F^3(vs)}\right]+1\right\} \quad \text{(A-10.45)}$$

Finally we have:

$$Cs = 2C_{FBS}\left\{1-\exp(v_{s0})+\left(\frac{ni}{N_D}\right)^2\left[\frac{\Delta}{1+\Delta}\exp(-v_{s0})+1\right]\right\}F^{-1}\left(v_{s0}\right) \quad \text{(A-10.46)}$$

Equation to find applied voltage corresponding to each value of $v_{so}$ is similar to low-frequency case, which is described above. A theoretical C-V curve at high frequency simulated by this method is shown in Figure A-10.7.

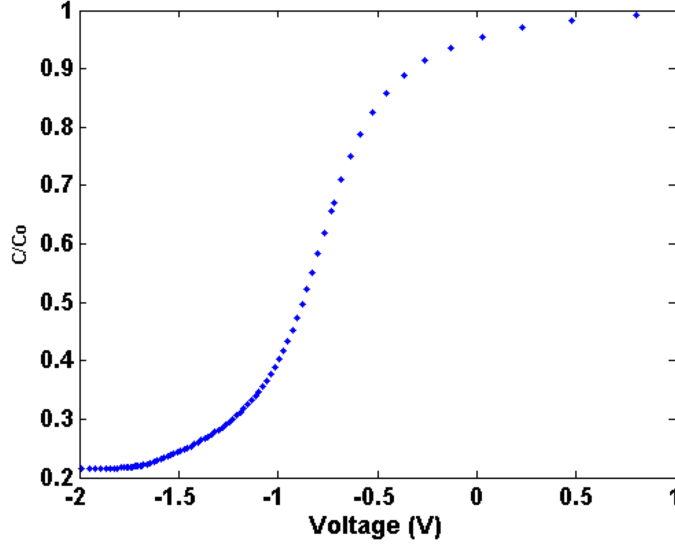


*Figure A-10.7. A theoretical C-V curve at high frequency simulated by this method.*

### A-10.3. Calculation of $D_{it}$ using Terman method

The idea of calculating $D_{it}$ is based on the distortion of high frequency experimental C-V curve compared to theoretical curve [11, 13]. Under high-frequency condition, interface traps cannot respond to AC signal, and do not contribute to measured capacitance. However, interface traps do follow very slow changes in gate bias, causing the C-V curve stretching out along applied gate voltage. Therefore, the change in two curves must give information of interface trap density.

In this method, first, a theoretical curve at high frequency is calculated. At the same capacitance (experimental and theoretical value), we find theoretical surface potential and experimental applied gate voltage. An example of theoretical and experimental curves is shown in Figure A-10.8. Surface potentials and corresponding applied voltages extracted from Figure A-10.8 are plotted in Figure A-10.9.

Then, interface trap capacitance is calculated as:

$$C_{it}(\psi_s) = Ci\left(\left(\frac{d\psi_s}{dV_G}\right)^{-1}\right) - C_s(\psi_s) \qquad \text{(A-10.47)}$$

Interface trap density is calculated through $C_{it}$ as: $D_{it}(\phi_s) = \dfrac{C_{it}(\psi_s)}{q}$ (A-10.48)

where $C_{it}$ is interface trap capacitance, $\frac{d\psi_s}{dV_G}$ is differential of surface potential ($\psi_s$) with respect to gate voltage ($V_G$), $C_i$ is insulator capacitance, and $C_s$ is semiconductor capacitance.

$D_{it}$ calculated as function of surface potential is shown in Figure A-10.10.

However, this method has some limitation of applicability and accuracy [14]. To use this method, we must assume that insular is an ideal layer. That means no traps exiting in it. In fact, insulator layer may contain traps, which can affect distortion in shape of C-V curves. Exact value of surface doping density is also very important to simulate theoretical C-V curve. Figure A-10.11 shows theoretical CV curves at various doped concentration of c-Si. One can see that small change in $N_d$ leads to significant change in CV curve shape. The second problem is insulator capacitance. Like $N_d$, insulator capacitance affects greatly on CV shape, as shown in Figure A-10.12. It is usually to take accumulation capacitance as insulator capacitance. However, the value depends on AC frequency and measurement technique limitation. Accumulation capacitance depends not only on AC frequency but also on voltage step. The obtained result is thus influenced by measurement frequency and applied voltage step.

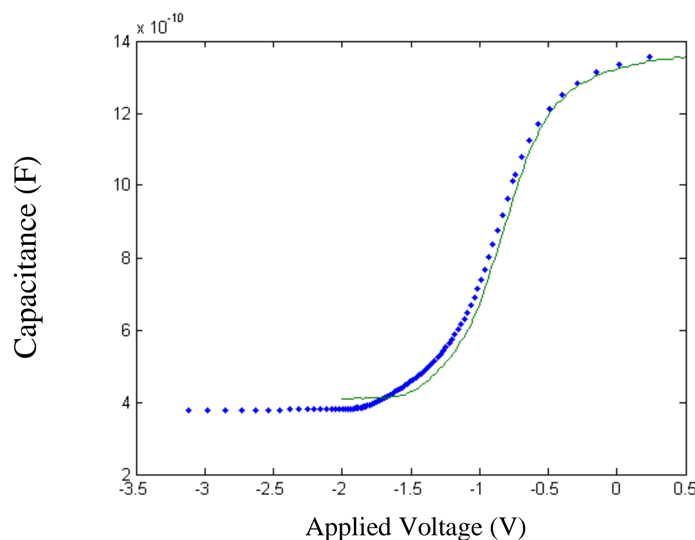


*Figure A-10.8. A theoretical (dot line) and experimental (solid line) high-frequency C-V curve of an Al/SiN$_x$/c-Si sample*

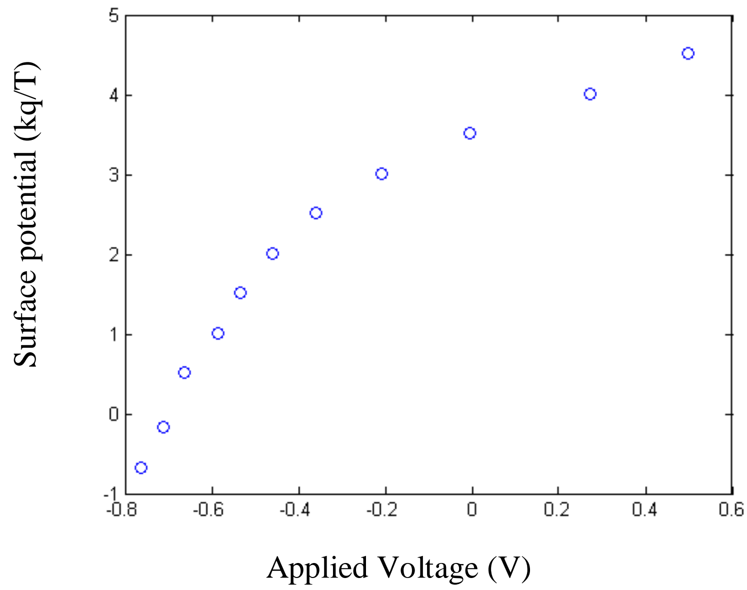


*Figure A-10.9 Capacitance as a function of surface potential and applied voltage*

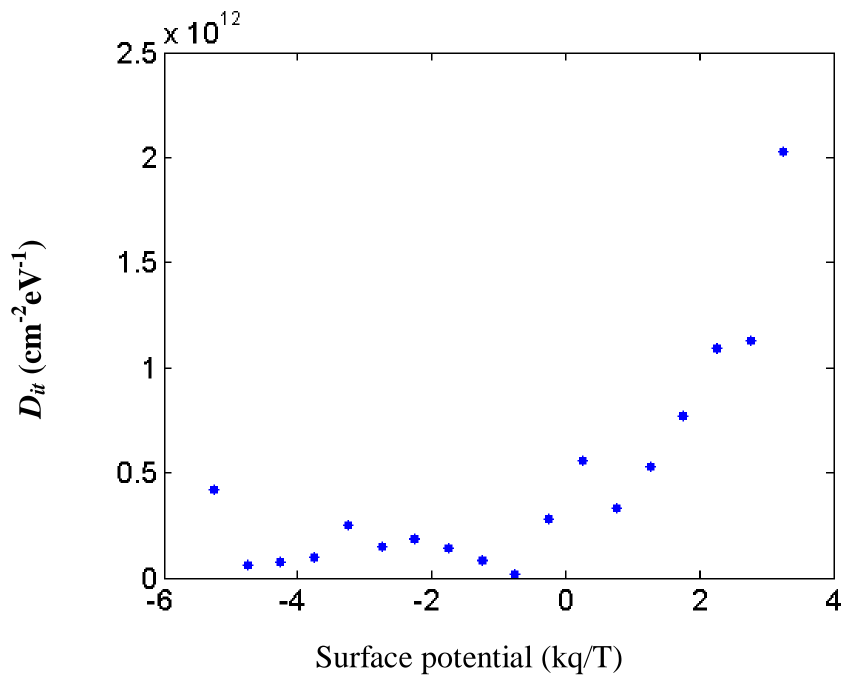


*Figure A-10.10. $D_{it}$ as a function of surface potential using Terman method.*

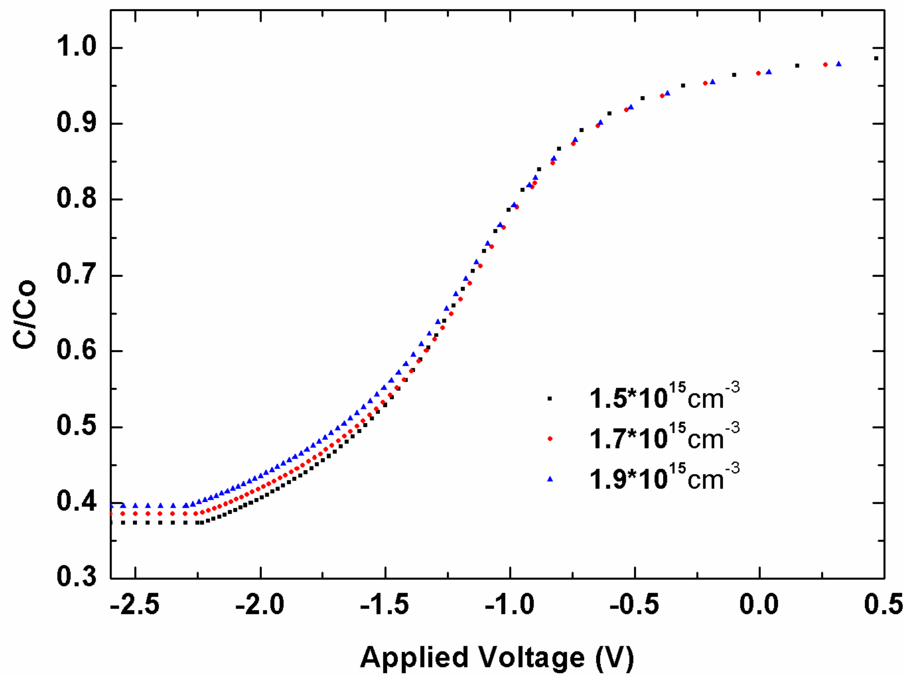


*Figure A-10.11. Theoretical C-V curves at various c-Si doped concentrations.*

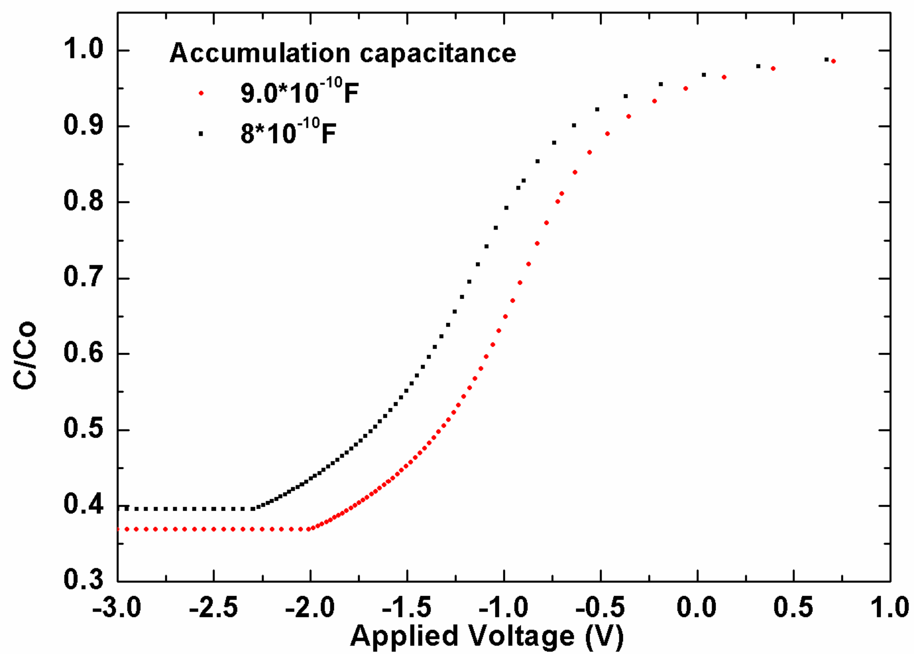


*Figure A-10.12. Theoretical C-V curves at various c-Si accumulation capacitance input.*

Since series resistance can make change in C-V curve, corrected *C* and *G* should be taken into account [11]. One possible origin of series resistance is imperfect contact between back contact and gate probe [12]. Series resistance is calculated as:

$$R_s = \frac{G_{ma}}{G_{ma}^2 + \omega^2 C_{ma}^2} \quad \text{(A-10.49)}$$

Where, $C_{ma}$, $G_{ma}$ is capacitance and conductance at accumulation condition.

The corrected capacitance and conductance are:

$$C_c = \frac{G_m^2 + \omega^2 C_m^2}{a^2 + \omega^2 C_m^2} C_m \quad \text{(A-10.50)}$$

$$G_c = \frac{G_m^2 + \omega^2 C_m^2}{a^2 + \omega^2 C_m^2} a, \quad \text{(A-10.51)}$$

where

$$a = G_m - (G_m^2 + \omega^2 C_m^2) R_s \quad \text{(A-10.52)}$$

C-V curves and calculated $D_{it}$ with and without correction are shown in Figures A-10.13 and 14. $R_s$ calculated here is around 60 Ω.

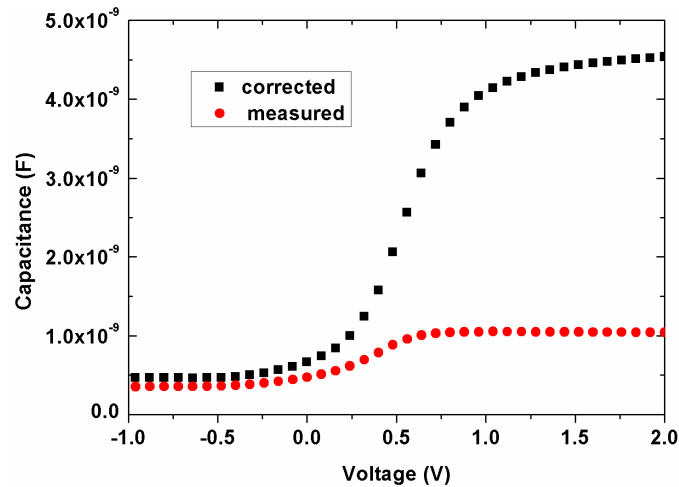


*Figure A-10.13 C-V curves before and after correction. $R_s$ calculated here is around 60 Ω.*

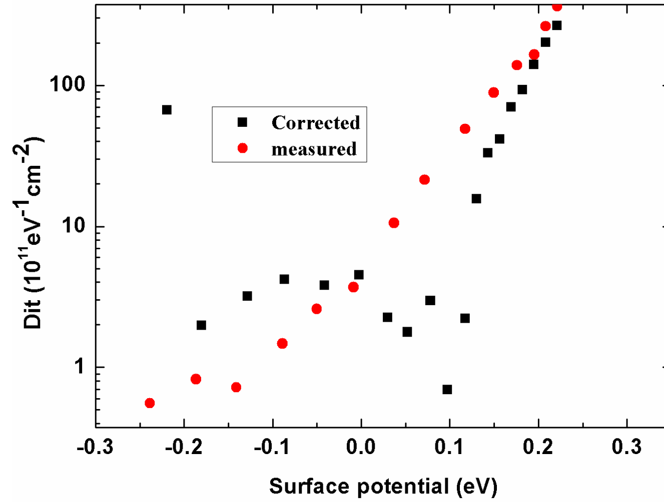


*Figure A-10.14 Comparison between $D_{it}$ from measured and corrected data.*

One can see in Figure 10-A.14 that there is a difference between $D_{it}$ values obtained from measured and corrected C-V data. However, at mid-gap, $D_{it}$ is the same for both curves. In Chapter 3, I just show the C-V curve obtained from measurement data.

$D_{it}$ calculated from Terman method is easy and convenient. However, the problem of this method is that $D_{it}$ value sometimes becomes negative. It may be related to an error occurring from approximation during calculation. Therefore, in my calculation, absolute values are taken for negative values.

### *A-10.4.* Calculation of $D_{it}$ using low frequency method

As I mentioned above, Terman method has some disadvantages related to high frequency C-V curve calculation. To meet high accuracy, exact $N_d$ and $C_i$ value is required. In order to solve these problems, Berglund developed low frequency method [15]. The main ideal is based on the fact that, at a frequency low enough, sample is under equilibrium condition. That means surface state is in equilibrium at all time during measurement. Surface state can follow both variation of DC signal and ac signal.

Under the equilibrium condition, the relationship between surface potential and applied voltage is expressed as below:

$$\frac{d\psi_s}{dV_i} = \frac{\frac{\varepsilon_i}{d}}{\left[\frac{dQ_D(\psi_s)}{d\psi_s} + qD_{it}(\psi_s)\right]} \qquad \text{(A-10.53)}$$

$$\frac{d\psi_s}{dV_i} = \frac{C_i}{C} - 1, \qquad \text{(A-10.54)}$$

where $Q_D$ is the net charge in the silicon at surface potential $\psi_s$

$$Q_D(\psi_s) = 5.82 \times 10^{-6} \left( \frac{N_D}{\beta} \right)^{1/2} \left( \exp(\beta\psi_s) - \beta\psi_s - 1 \right)^{1/2} \qquad \text{(A-10.55)}$$

$$\frac{dQ_D(\psi_s)}{d\psi_s} = \frac{1}{2} 5.82 \times 10^{-6} \left( \frac{N_D}{\beta} \right)^{1/2} \left( \exp(\beta\psi_s) - \beta\psi_s - 1 \right)^{-1/2} \left( \beta \exp(\beta\psi_s) - \beta \right) \qquad \text{(A-10.56)}$$

$$\beta = \frac{q}{kT}$$

Steps of the method are described as below:

- Measurement of C-V curve of a sample at low frequency (ex. 50 Hz)
- Calculation of surface potential vs. applied voltage.

$$\overline{\psi_s}(V) = \int_{V_A}^{V} \left( 1 - \frac{c_m}{c_i} \right) dV + \overline{\psi_{s0}} \quad , \qquad \text{(A-10.57)}$$

where $C_{om}$ is measured capacitance.

$C_{ox}$ is oxide capacitance, $V$ is applied voltage, and $V_a$ is oxide voltage (voltage at accumulation condition). $\overline{\psi}_{s0}$ is determined at accumulation voltage as:

$$V_a = \frac{Qsi(\overline{\psi_{s0}})}{c_i} + \overline{\psi_{s0}} \qquad \text{(A-10.58)}$$

$$\frac{V_a}{t_i} = \frac{1}{\varepsilon_{ox}} \frac{Qsi(\overline{\psi_{s0}})}{c_i} + \overline{\psi_{s0}} c_i \qquad \text{(A-10.59)}$$

$$Q_{si}(\overline{\psi_{so}}) = 5.82 \times 10^{-6} \left( \frac{Nd}{\beta} \right)^{1/2} \left( \exp(\beta\overline{\psi_{s0}}) - \beta\psi_{s0} - 1 \right)^{1/2} \qquad \text{(A-10.60)}$$

Solve the equation using Newton-Raphson method to find $\overline{\psi}_{s0}$ by changing value $\overline{\psi}_{s0}$ and calculate right side of equation until cross-point is found.

- Calculation of $d\psi_s / dV_i$ from measurement $C_i$ and C.
- Calculation of $dQ_D / d\psi_s$ at each $\psi_s$

- Calculation of $D_{it}$

Figure A-10.15 shows CV curve of Al/$SiN_x$/c-Si sample before and after annealing measured at 50 Hz. Corresponding $D_{it}$ calculated using low frequency method are plotted in Figure A-10.16.

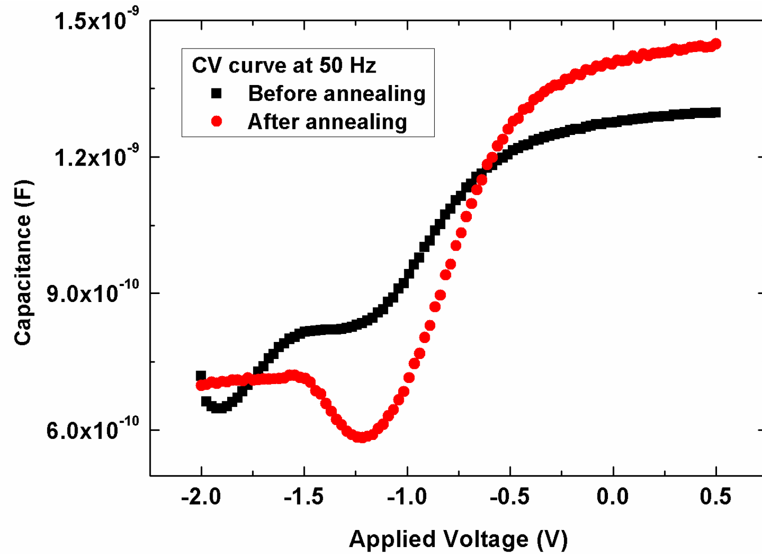


*Figure A-10.15 C-V curves before and after annealing measured at 50 Hz*

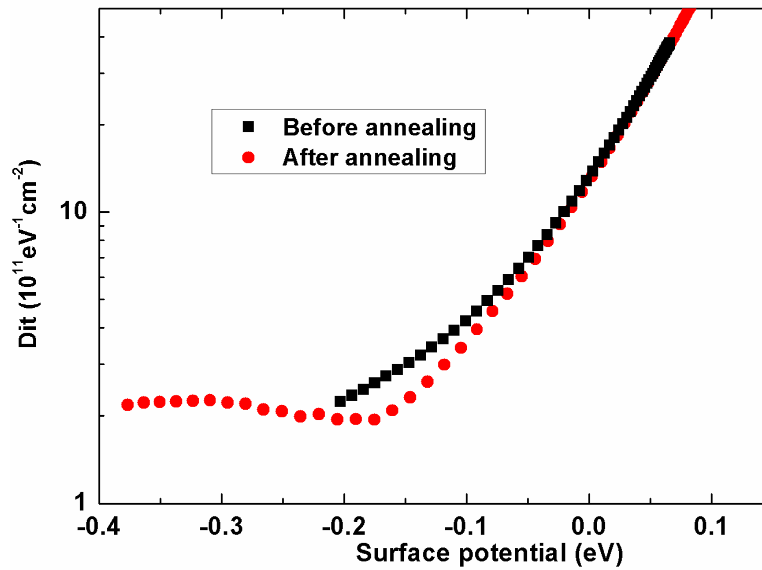


*Figure A-10.16 $D_{it}$ as a function of surface potential before and after annealing calculated using low frequency method.*

### *A-10.5.* Calculation of $D_{it}$ using conductance method

This method is based on the loss of energy associated with capture and emission of electrons at interface traps on both halves of the AC cycle. The loss is taken into account as equivalent parallel conductance $G_P$.

There are two steps to obtain interface trap density and capture probability as a function of Si band gap energy in the conductance method:

- Measurement of C-V at low frequency, at which equilibrium conditions are satisfied to extract surface band bending as a function of gate voltage.
- Measurement of admittance as a function of gate bias and frequency.

Equivalent circuit of MOS structure can be illustrated as Figure A-10.17. $D_{it}$ is calculated using the relationship between conductance of parallel equivalent circuit and surface potential as below:

$$\frac{G_p}{\omega} = \frac{1}{2} q D_{it} \left(2\pi\sigma^2\right)^{-1/2} \left(\frac{c_p N_D}{\omega}\right) \int_{-\infty}^{\infty} \exp\left(\frac{-(u_s - \overline{u_s})^2}{2\sigma^2}\right) \exp(-u_s) \ln\left[1 + \omega^2 \left(c_p N_D\right)^{-2} e^{2u_s}\right] du_s$$

(A-10.61)

Or $$\frac{G_p}{\omega} = \frac{1}{2} q D_{it} \left(2\pi\sigma^2\right)^{-1/2} \int_{-\infty}^{\infty} \exp\left(\frac{-(u_s - \overline{u_s})^2}{2\sigma^2}\right) \frac{1}{\omega\tau_m} \ln\left[1 + \omega^2 \tau_m^{\ 2} e^{2u_s}\right] du_s \quad \text{(A-10.62)}$$

where $u_s$ - surface bending, $\bar{u}_s$ - mean value of $u_s$, $C_p$ - capture probability, $\sigma$ - standard deviation of $u_s$ are unknown parameters.

For impedance system measurement, I use carbon tape to stick a sample on a holder. This may affect series resistance during impedance measurement. Therefore, capacitance and conductance correction is necessary. Calculated corrected $C$ and $G$ are described in Terman method above. Equivalent parallel conductance is calculated as below:

$$\left\langle G_p \right\rangle = \frac{\omega^2 C_{ox}^2 G_{mc}}{G_{mc}^2 + \omega^2 (C_{ox} - C_m)} \quad \text{(A-10.63)}$$

$$G_{mc} = \frac{\omega^2 C_c^2 R_s}{1 + \omega^2 C_c^2 R^2{}_s} \quad \text{(A-10.64)}$$

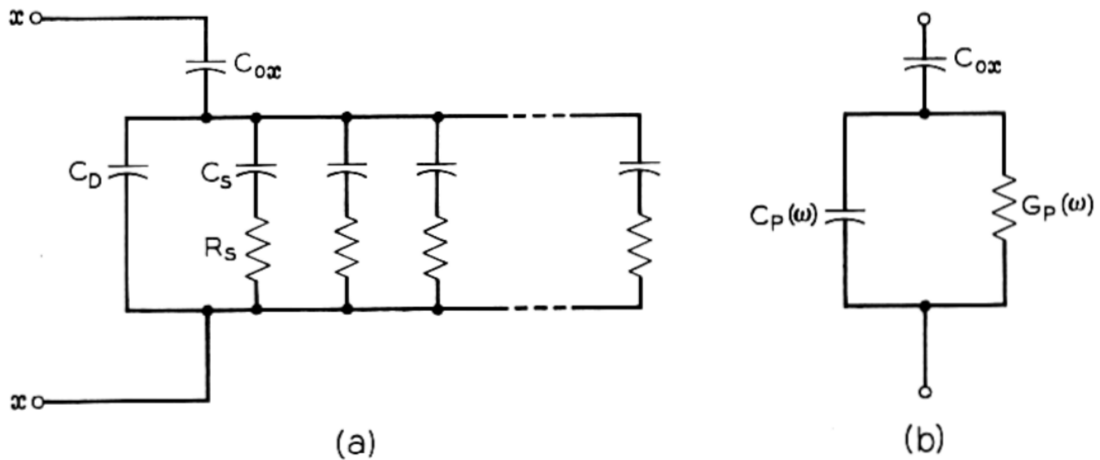


Fig. 8 — (a) Equivalent circuit for depletion region showing time constant dispersion caused primarily by statistical fluctuations of surface potential. $C_{ox}$ is the oxide capacitance per unit area, and $C_D$ the depletion layer capacitance per unit area. Each subnetwork consisting of $C_s$ and $R_s$ in series represents time constant of the continuum of interface states in a characteristic area. Bulk generation-recombination is zero. (b) Simplified version of (a) useful when extracting $C_{ox}$ from the measured admittance. $C_p(\omega)$ is the capacitance per unit area at a given bias and frequency of the distributed network in parallel with $C_D$. $G_p(\omega)$ is the equivalent parallel conductance per unit area.

*Figure A-10.17. Equivalent circuit for depletion of MOS structure in depletion region [11]*

Calculation of $D_{it}$ using conductance method is described as these steps below:

*A. Calculation of $\bar{u}_s$ at each applied voltage (as described in low-frequency method)*

For example, in my study, we measure C-V curve of Al/$SiN_x$/c-Si structure. C-V curve of Al/$SiN_x$/c-Si structure at low frequency are shown in Figure A-10. 18a. Frequency of 50 Hz is chosen to calculate. At each applied voltage, $\bar{u}_s$ (unit of kq/T) is calculate by using equation A-10.57-60. $\bar{u}_s$ as function of applied voltage are drawn in Figure A-10.18b.

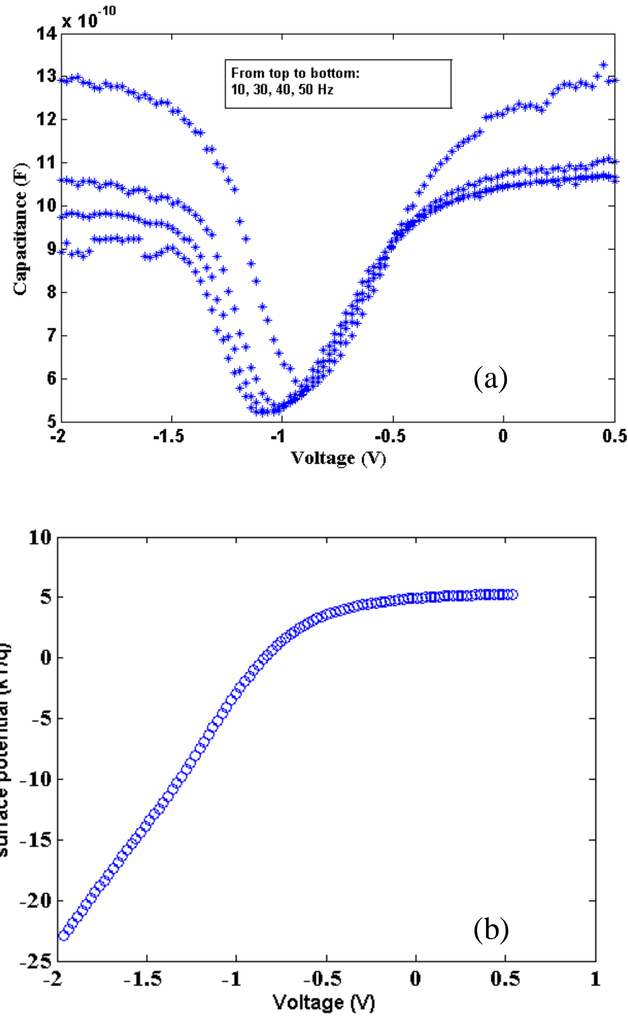


*Figure A-10.18. Figures of steps for calculating surface potential.*

*B. Standard deviation σ*

In order to find $\sigma$, we use the two symmetric frequency values as shown in Figure A-10.19 and the equation above:

$$\frac{(G_p/\omega)_{\omega_A}}{(G_p/\omega)_{\omega_B}} = \frac{\omega_B}{\omega_A} \frac{\int_{-\infty}^{\infty} \exp\left(\frac{-(u_s-\overline{u_s})^2}{2\sigma^2}\right)\exp(-u_s)\ln\left[1+\omega_A{}^2\left(c_pN_D\right)^{-2}e^{2u_s}\right]du_s}{\int_{-\infty}^{\infty} \exp\left(\frac{-(u_s-\overline{u_s})^2}{2\sigma^2}\right)\exp(-u_s)\ln\left[1+\omega_B{}^2\left(c_pN_D\right)^{-2}e^{2u_s}\right]} \quad \text{(A-10.65)}$$

The limitation of the integrate is from (-2$u_B$, 2$u_B$), where $u_B$ is bulk potential in unit of kq/T:

$$u_B = \ln\left(\frac{Nd}{ni}\right)(kT/q) \quad \text{(A-10.66)}$$

Right side equation is theoretical value at fixed $c_p$ with various $\sigma$, we obtain Figure A-10.20. The suitable value of σ is the same values of two curves.

*C. Calculation of $C_p$ at each ūs and corresponding $D_{it}$.*

At fixed σ, we substitute it into equation (55) above, and change value of $C_p$. Left side is experimental value and right side is theoretical value. We can find $C_p$ at each ūs by using Newton-Raphson method. When we can find $C_p$ at each ūs (or $V_g$ voltage), we substitute these parameters into equation (A-10.49), we can calculate $D_{it}$.

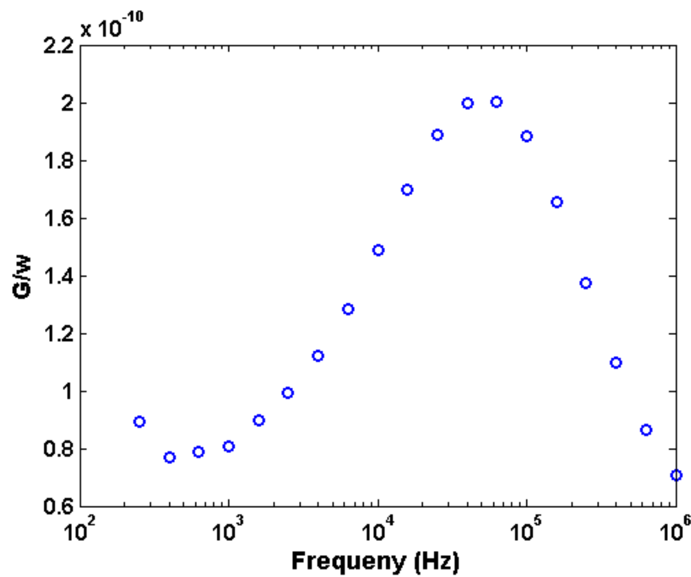


*Figure A-10.19. Conductance to frequency ratio as a function of frequency.*

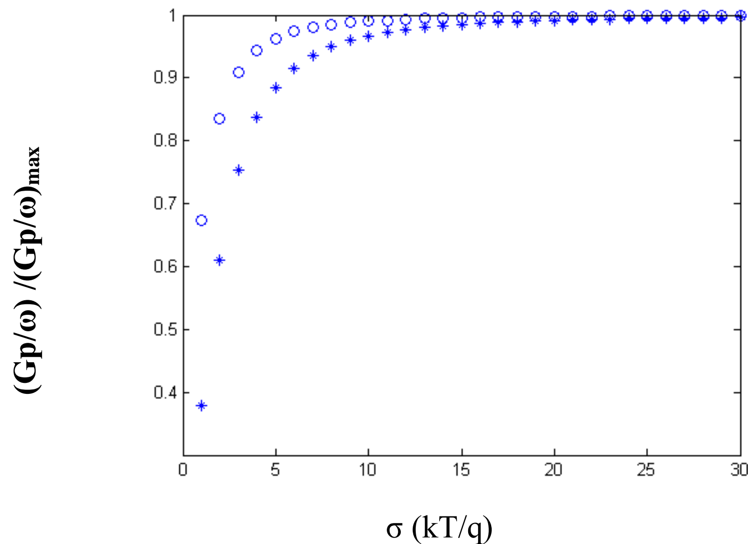


*Figure A-10.20. $(Gp/\omega) /(Gp/\omega)_{max}$ vs. standard deviation at two frequencies taken as symmetric frequency in Figure A-10.19*

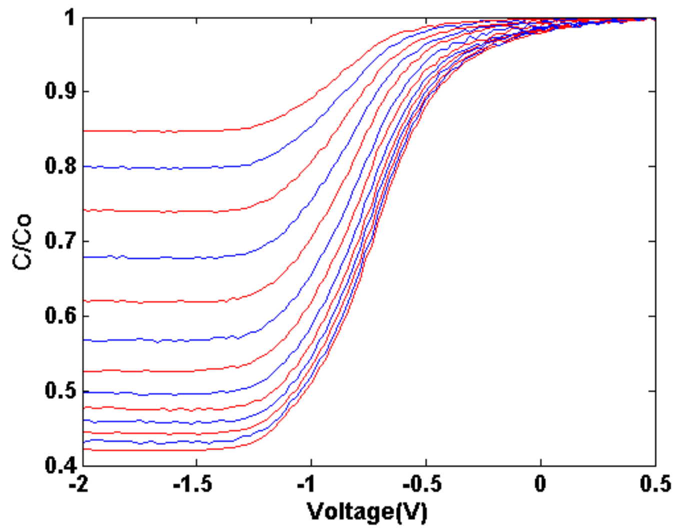


*Figure A-10.21. C-V curve of a $SiN_x$/c-Si sample at various frequencies: From top to bottom is from high frequency to low frequency.*

There are some problems occurring during my calculation. First is the variation of accumulation capacitance when frequency changes as shown in Figure A-10.21. I suppose the change of accumulation capacitance is due to the property of $SiN_x$ films itself. The second problem is related to applied voltage chosen two symmetric frequencies to find σ. Figure A-10.22 shows that peak position frequency changes with applied voltage. The third problem is that σ value obtained from my calculation is too big, as shown in Figure A-10.19. Although I took small $\sigma$ for my calculation, the result of $D_{it}$ is still unreasonable for sample before annealing. $D_{it}$ is too small compared to normal value at which minority carrier lifetime is on the order of several μs.

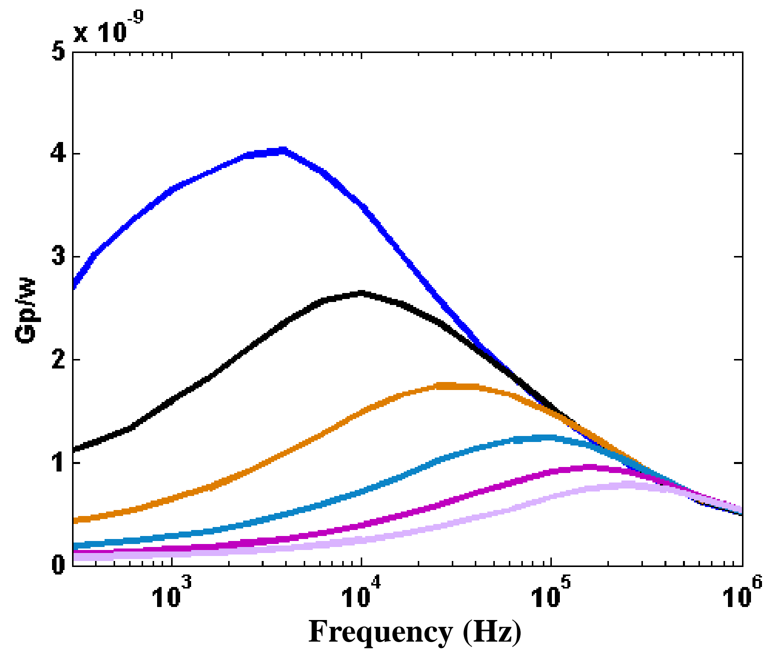


*Figure A-10.22.* $G_p/\omega$ *as functions of frequency of a SiN$_x$/c-Si sample at various bias voltage.*

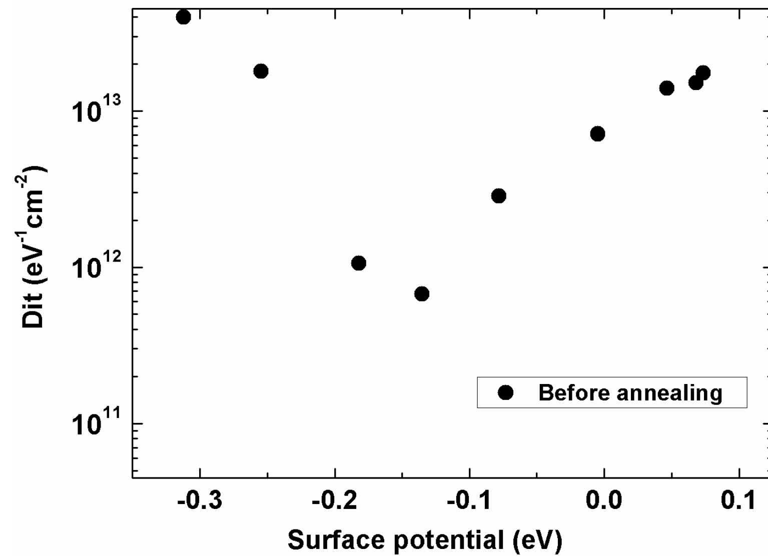


*Figure A-10.23. $D_{it}$ as a function of surface potential calculated using Conductance method.*

*A-11. Deviation of equation of $J_{sc}$ and $V_{oc}$*

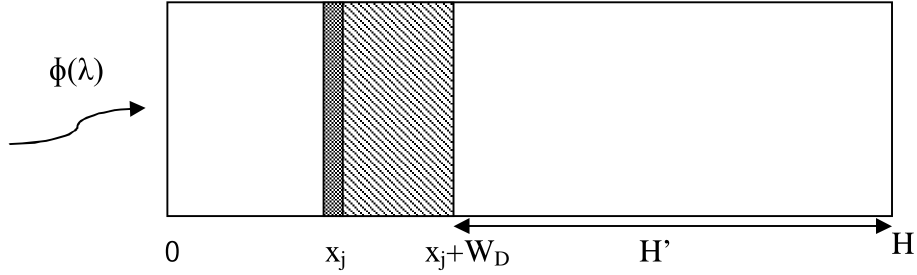


Assuming that there is incident photon flux coming to cell as shown in Figure 1. Photons going into cell for each wavelength λ equal to:

$(1-R(\lambda))\phi(\lambda)$ at surface of cell

$(1-R(\lambda))\phi(\lambda)\exp(-\alpha(\lambda)x)$ at position x:

$(1-R(\lambda))\phi(\lambda)\exp(-\alpha(\lambda)(x+dx))$ at position x+dx

Generation rate of electron-hole pairs:

$$G(\lambda,x)dx = (1-R(\lambda))\phi(\lambda)\exp(-\alpha(\lambda)x) - (1-R(\lambda))\phi(\lambda)\exp(-\alpha(\lambda)(x+dx))$$
$$= (1-R(\lambda))\phi(\lambda)\exp(-\alpha(\lambda)x)(1-\exp(-\alpha(\lambda)dx))$$
$$= (1-R(\lambda))\phi(\lambda)\exp(-\alpha(\lambda)x)\alpha(\lambda)dx$$

Current generated through cell is divided into three components: hole current, electron current and space charge region current.

In order to obtain hole current, we firstly consider steady-state continuity equation:

$$G_p - \frac{p_n - p_{n0}}{\tau_p} - \frac{1}{q}\frac{dJ_p}{dx} = 0 \qquad (1)$$

Where, Gp is generation current:

$$G(\lambda,x) = \phi(\lambda)\alpha(\lambda)(1-R(\lambda))\exp(-\alpha(\lambda)x) \qquad (2)$$

Current density equation:

$$J_p = q\mu_p p_n E - qD_p\left(\frac{dp_n}{dx}\right) \qquad (3)$$

Substitute (2) and (3) into (1), we obtain:

$$D_p \frac{d^2 p_n}{dx^2} + \alpha\phi(1-R)\exp(-\alpha x) - \frac{p_n - p_{n0}}{\tau_p} = 0$$

$$p_n - p_{n0} = A\cosh\frac{x}{L_p} + B\sinh\frac{x}{L_p} - \frac{\alpha\phi(1-R)\tau_p}{\alpha^2 L_p^2 - 1}\exp(-\alpha x)$$

Boundary conditions:

Surface recombination:

$$D_p \frac{d(p_n - p_{n0})}{dx} = S_p(p_n - p_{n0}) \text{ at x=0}$$

No excess carrier at the depletion region edge:

$$p_n - p_{n0} \approx 0 \text{ at x=xj}$$

Hole density:

$$p_n - p_{n0} = \left[\phi(1-R)\frac{\tau_p}{\alpha^2 L_p^2 - 1}\right] \times$$
$$\left[\frac{\left(\frac{S_p L_p}{D_p} + L_p\right)\sinh\frac{x_j - x}{L_p} + \exp(-\alpha x_j)\left(\frac{S_p L_p}{D_p}\sinh\frac{x_j}{L_p} + \cosh\frac{x_j}{L_p}\right)}{\frac{S_p D_p}{D_n}\sinh\frac{xj}{L_p} + \cos\frac{xj}{L_p}}\right] - \exp(-\alpha x_j)$$

$$J_p = -qD_p\left(\frac{dp_n}{dx}\right)_{xj} = \left[q\phi(1-R)\frac{\alpha L_p}{\alpha^2 L_p^2 - 1}\right] \times$$
$$\left[\frac{\left(\frac{S_p L_p}{D_p} + L_p\right) - \exp(-\alpha x_j)\left(\frac{S_p L_p}{D_p}\cosh\frac{x_j}{L_p} + \sinh\frac{x_j}{L_p}\right)}{\frac{S_p D_p}{D_n}\sinh\frac{xj}{L_p} + \cos\frac{xj}{L_p}}\right] - \alpha L_p \exp(-\alpha x_j)$$

Similarly, we solve the steady-state continuity equation for electron:

$$G_n - \frac{n_p - n_{p0}}{\tau_n} - \frac{1}{q}\frac{dJ_n}{dx} = 0$$

Current density equation:

$$Jn_p = q\mu_n n_p E - qD_n\left(\frac{dn_p}{dx}\right)$$

And using the boundary conditions:

Surface recombination:

$$-D_n \frac{dn_p}{dx} = S_n\left(n_p - n_{p0}\right) \text{ at x=H}$$

No excess carrier at the depletion region edge:

$$n_p - n_{p0} \approx 0 \text{ at x=xj+W}_D$$

We obtain:

$$J_n = \left[q\phi(1-R)\frac{\alpha L_n}{\alpha^2 L_n^2 - 1}\right]\times$$

$$\left[\frac{\left(\frac{S_n L_n}{D_n}\left(\cosh\frac{H'}{L_n} - \exp\left(-\alpha H'\right)\right) + \sinh\frac{H'}{L_n} + \alpha L_n \exp\left(-\alpha H'\right)\right)}{\frac{S_n L_n}{D_n}\sinh\frac{H'}{L_n} + \cosh\frac{H'}{L_n}}\right] \times \alpha L_n \exp\left(-\alpha\left(x_j + W_D\right)\right)$$

In space charge region:

$$J_{dr} = q\phi(1-R)\exp(-\alpha x_j)\left[1-\exp(\alpha W_D)\right],$$

**References**

[1] Hiroyuki Fujiwara, Spectroscopic ellipsometry-principle and application, John Wiley & Sons, Ltd, 2007.

[2] J. Jung, J. Bork, T. Holmgaard, N. A. Kortbek and K. Pedersen, Ellipsometry, 2001

[3]https://www.ifw-dresden.de/de/institute/institut-fuer-komplexe materialien/abteilungen/mikro-und-nanostrukturen/available-methods/xps/

[4] http://5e.plantphys.net/article.php?ch=t&id=66

[5] http://article.sapub.org/10.5923.j.ijoe.20120202.02.html

[6] M. Yasaka, *The Rigaku Journal* **26 -2** (2010) 1

[7] http://cxc.cfa.harvard.edu/xrayschool/talks/optics.pdf

[8] http://www.geos.ed.ac.uk/facilities/ionprobe/SIMS4.pdf

[9]http://instructor.physics.lsa.umich.edu/adv-labs/Mass_Spectrometer/MassSpecQMS.pdf

[10] http://www.purdue.edu/ehps/rem/rs/sem.htm

[11] E.H. Nicollian, J. R. Brews, MOS physic and technology, John Wiley &Sons, 1982.

[12] S.M. Sze, Semiconductor devices physics and technology, John Wiley&Son, inc. (2001) p.179

[13] E.H. Nicollian, A. Goetzberger and A. D. Lopez, *Solid-State Electron.* **12** (1968) 937.

[14] K. H. Zaininger, member, IEEE and G. Warfield, *IEEE Trans. Electron Dev.*, **ED-12** (1965) 179.

[15] C. N. Berglund, *IEEE Trans. Electron Dev.*, **ED-13** (1966) 701.

**Matlab code**

1. **For Terman method**

```
clc; close all; clear all;
%f=input('please input measurement frequency')
f=1000000;
AA=xlsread ('datafilename');
% some constants
ni=1e10;
eps=11.7*8.85e-14;
T=300;
k=1.38e-23;
q=1.6e-19;
Nd=1.87e15;
%electrode area A
Ar=0.0314;
% data in AA: voltage capacitance dissipation factor Vg Cf cf- D+ D-
% uncomment if you want to calculate Dit using corrected data
% w=f*2*pi;
% Cma=max(AA(:,2));
% for i=1:length(AA);
%     Gm(i)=AA(i,2)*w*AA(i,4);
% end
% Gma=max(Gm);
% Rs=Gma/(Gma^2+(w*Cma)^2);
% Co=Cma*(1+(Gma/w/Cma)^2);
% for k=1:length(AA)
```

```
%     t(k)=(Gm(k)^2+(w*AA(k,2))^2);
%     a(k)=Gm(k)-t(k)*Rs;
%     Cc(k)=t(k)*AA(k,2)/(a(k)^2+(w*AA(k,2))^2);
%     Gc(k)=t(k)*a(k)/(a(k)^2+(w*AA(k,2))^2);
%     A(k,2)=Cc(k);
% end
%if you use corrected data please comment (%) two codes below
A(:,2)=AA(:,2);
A(:,1)=AA(:,1);
% tinh c min
ca=max(A(:,2));
w=2*sqrt(eps*k*T*(log(Nd/ni))/Nd/q^2);
csmin=eps*Ar/w;
cmin=csmin*ca/(csmin+ca);
cmmin=min(A(:,2));
vd=log(ni/Nd);
% find Vfb
cfb=sqrt(eps*((q)^2)*Nd/k/T);;
cf=Ar*cfb*ca/(cfb*Ar+ca);
for i=1:length(A)
   delc(i)=abs(cf-A(i,2));
end
mdelc=min(delc);
for i=1:length(delc)
   if mdelc==delc(i)
       Vfb=A(i,1);
```

```
    end
end
%calculate theoretical high frequency CV curve
% positive region from Va to flat band condition
% choose maximum of surface potential in kq/T unit
de=0.5;
vvs1=0.01:de:10;
f1=sqrt(((ni/Nd)^2)*(exp(-vvs1)-1)+exp(vvs1)-vvs1-1);
hs=sqrt(2*eps*k*T*Nd);
q1=hs*f1;
cd1=cfb.*Ar*(((ni/Nd)^2)*(1-exp(-vvs1))+((exp(vvs1)-1)))./f1/sqrt(2);
c1=(cd1.*ca)./(cd1+ca);
vox1=-1*sign(vvs1).*q1./(ca/Ar);
phis1=vvs1*k*T/q;
vg1=phis1-vox1+Vfb;
%negative region 1 from flat band condition to band bending equal to vd
vvs2=vd:de:-0.01;
f2=sqrt(abs(((ni/Nd)^2)*(exp(-vvs2)+vvs2-1)+exp(vvs2)-vvs2-1));
q2=hs*f2;
cd2=abs(cfb.*Ar*(((ni/Nd)^2)*(1-exp(-vvs2))+((exp(vvs2)-1)))./f2/sqrt(2));
c2=(cd2.*ca)./(cd2+ca);
vox2=-1*q2./(ca/Ar);
phis2=vvs2*k*T/q;
vg2=phis2+vox2+Vfb;
% negative region 2: MOS physic and technology simulation
```

```
fx=inline('(exp(-x)-exp(x)+2.*x)./((sqrt(2*(-x+exp(x)-
1+((9.65e9/1.87e15)^2).*(exp(-x)-1)))).^3)');
vvs3=2*vd+1:1:vd;
for  kk=1:length(vvs3);
 vs3=vvs3(kk);
 I3=quad(fx,vs3,vs3/1000);
 f3=sqrt(2*(exp(vs3)-vs3-1+((ni/Nd)^(2))*(-1+exp(-vs3))));
 q3=hs*f3/sqrt(2);
 vox3=-1*q3/(ca/Ar);
 del3=f3*(I3-1)/(-1+exp(-vs3));
 k3=(1-exp(vs3)+((ni/Nd)^2)*(((-1+exp(-vs3))*del3/(del3+1)+1)))/f3;
 cs3=cfb*k3*Ar;
 cn3=cs3*ca/(cs3+ca);
 c3(kk)=cn3;
 phisn3=vs3*T*k/q;
 vgn3=phisn3+vox3+Vfb;
 vg3(kk)=vgn3;
 phis3(kk)=phisn3;
end
vss4=-34:1:2*vd;
for  nn=1:length(vss4);
 vs4=vss4(nn);
 I4=quad(fx,vs4,vs4/1000);
 f4=sqrt(2*(-vs4+exp(vs4)-1+((ni/Nd)^(2))*(-1+exp(-vs4))));
 q4=sign(vs4)*hs*f4/sqrt(2);
 vox4=1*q4/(ca/Ar);
```

```
 del4=f4*(I4-1)/(-1+exp(-vs4));
 k4=(1-exp(vs4)+((ni/Nd)^2)*(((-1+exp(-vs4))*del4/(del4+1)+1)))/f4;
 cs4=cfb*k4*Ar;
 cn4=cs4*ca/(cs4+ca);
 phisn4=vs4*k*T/q;
 vgg4=phisn4+vox4+Vfb;
 c4(nn)=cn4;
 vg4(nn)=vgg4;
phis4(nn)=phisn4;
end

phis=[phis1 phis2 phis3 phis4];
Vgg=[vg1 vg2 vg3 vg4];
c=[c1 c2 c3 c4];
cc=[c1 c2];
n=max(c)/Co;
for i=1:length(A(:,2))
   mca(i)=abs(0.9*max(c)-A(i,2));
end
mcaa=min(mca)
for i=1:length(A(:,2))
   mca(i)=abs(0.9*max(c)-A(i,2));
   if mca(i)==mcaa
       va=A(i,1)
   end
end
```

```
Va=min(va)
vssa=[phis1  phis2];
vgg=[vg1 vg2];
tll(:,1)=Vgg';
tll(:,2)=c';
tll(:,3)=phis;
tl(:,1)=[vg1 vg2 vg3];
tl(:,2)=1e9*[c1 c2 c3];
tl(:,3)=[phis1 phis2 phis3];
plot(tll(:,1),tll(:,2),'.',A(:,1),A(:,2),'*');
k1=ginput(1);
hold off
% Chose range to calculate Dit
j=1
for jj=1:length(A)
   if A(jj,1)>min((vg3))&A(jj,1)<Va
     D(j,:)=A(jj,:);
     j=j+1;
   end
end
D(:,3)=D(:,2)*1e9
% at the same capacitance, choose other value
for i=1:1:length(D)
          for j=1:1:length(tl);
           qq(j)=abs(D(i,3)-tl(j,2));
          end
```

```
        qmn(i)=min(qq)
        for j=1:1:length(tl);
          q1(j)=abs(D(i,3)-tl(j,2));
          if q1(j)==qmn(i)
              cx(i)=D(i,3)
              vga(i)=D(i,1);
              phi(i)=tl(j,3);
              vglt(i)=tl(j,1); %theoretical voltage


           end
        end
end
 B(:,1)=vga;
 B(:,2)=phi;
 B(:,3)=cx;
 B(:,4)=vglt;
 B(:,5)=-vga+vglt;
 %flit same phi
 B=round(B*1e4)/1e4;
[tmp,INDEX]=unique(B(:,2),'rows');
for i2=1:length(tmp)
kq(i2,:)=B(INDEX(i2),:);
end
kq;
%subplot(3,1,2)
%subplot(2,1,1)
```

```
%plot(kq(:,1),kq(:,2),'.',kq(:,4),kq(:,2),'.');
%plot(kq(:,1),kq(:,2),'o');
%k2=ginput(1);
%hold off
% find Dit
i=1;
for d1=1:length(kq)-1
   ddv(i)=(kq(d1,5)-kq(d1+1,5))
   dphis(i)=(kq(d1,2)-kq(d1+1,2))
   dphiss(i)=(kq(d1,2)+kq(d1+1,2))/2
   del(i)=(ddv(i)/(dphis(i)))
   ditt(i)=ca*(del(i))/q/Ar
   kqVg(i)=kq(d1,1)
   i=i+1
end

   kqq(:,1)=(dphiss);
   kqq(:,3)=kqVg;
   kqq(:,2)=1e-12*abs(ditt);
   kqq;

%flit same Vg
kqq=round(kqq*1e4)/1e4;
[tmp1,chiso]=unique(kqq(:,3),'rows');
for i3=1:length(tmp1)
kqo(i3,:)=kqq(chiso(i3),:);
```

```
end
kqo;
ke(:,1)=kqo(:,1)
ke(:,2)=kqo(:,2)
%subplot(3,1,3)
%subplot(2,1,2)
plot(kqo(:,1),1e12*kqo(:,2),'O');
%save Dit_sample.xls ke -ascii
%save datafilename_corrected.xls B -ascii
```

## 2. Calculation of $D_{it}$ using low frequency method

### 2.1. Find surface potential as a function of applied voltage

(measured data obtained from impedance systems)

```
function P=findps
clc;close all; clear all;
beta=1.6e-19/(1.38e-23*300);
q=1.6e-19;
Nd=1.87e15;
%tim Vo, Co
B=xlsread('50f_a');
%find capacitance and voltage of SiNx
  Co=max(B(:,12))
  k=1;
  for i=1:(length(B))
    if Co==B(i,12)
      Va(k)=B(i,7);
```

```
        k=k+1;
      end
    end

%find flat band voltage va flat band capacitance
cfbs=0.0314*sqrt(11.7*8.85e-14*((1.6e-19)^2)*1.9e15/1.38e-23/300);
cfb=(cfbs*Co)/(cfbs+Co);
for i=1:(length(B))
    xx(i)=abs(cfb-B(i,12));
end
    xxmin=min(xx);
for i=1:(length(xx))
    if xx(i)==min(xx)
        vfb=B(i,12);
    end
end
A=[B(:,7)-vfb B(:,12)];
n=(5.82e-16*sqrt(Nd/beta))/(Co/0.0314);
m=min(Va)-vfb;

%finding Va position
for i=1:(length(A))
      if m==A(i,1)
          tt=i;
       end
    end
```

```
t=gpt(n,m);
avphi=t(1)/beta;
% calculate phi vs. Vg
   ii=1;
   for i=2:(length(A))
   ar0=0;
   for k=1:i-1
   area=abs((A(k+1,1)-A(k,1))*(A(k+1,2)+A(k,2))/2);
   ar0=ar0+area;
   end
   a(ii)=ar0;
   phii(ii)=(A(i,1)-m)+ar0/Co+avphi;
   Vgg(ii)=A(i,1);
   ii=ii+1;
     end
phi=beta*[avphi phii];
Vg=[m Vgg];
A(:,3)=phi;
P=A;
plot(Vg, phi,'o')
save phiV.xls A -ascii
%save Dit100aa.xls ke -ascii
```

### 2.2. Function for calculation of $D_{it}$

```
clc;clear all;close all;
%50f_a is data file in excel xls form.
```

```
%Note to change file name in findps function
AA=xlsread('50f_a');
% data measured from impedance systems
Nd=1.875e15;
ni=1e10;
vd=-log(9.65e9/Nd);
q=1.6e-19;
k=1.38e-23;
T=300;
b=q/k*T;
P=findps;
w=50*2*pi;
Ar=0.0314;
epsi=11.7*8.85e-14;
 hs=sqrt(2*epsi*k*T*Nd);
 cfb=sqrt(epsi*((q)^2)*Nd/k/T);;
 % uncomment if you want to calculate Dit using corrected data
%       Cma=max(AA(:,12));
%       for i=1:length(AA);
%           Gm(i)=AA(i,14);
%       end
%       Gma=max(Gm);
%       Rs=Gma/(Gma^2+(w*Cma)^2);
%       Co=Cma*(1+(Gma/w/Cma)^2);
%       for k1=1:length(AA)
%           t(k1)=(Gm(k1)^2+(w*AA(k1,12))^2);
```

```
%           a(k1)=Gm(k1)-t(k1)*Rs;
%           Cc(k1)=t(k1)*AA(k1,12)/(a(k1)^2+(w*AA(k1,12))^2);
%           Gc(k1)=t(k1)*a(k1)/(a(k1)^2+(w*AA(k1,12))^2);
%           A(k1,2)=Cc(k1);
%       end
%if you use corrected data please comment (%) two codes below
A(:,1)=AA(:,7);
A(:,2)=AA(:,12);
Ci=max(A(:,2))
for i =1:length(A)
   delCi(i)=abs(A(i,2)-Ci)
end
delCimin=min(delCi)
ii=1
for i =1:length(A)
   delCi(i)=abs(A(i,2)-Ci)
   if delCimin==delCi(i)
      vaa(ii)=A(i,1)
      ii=ii+1
   end
end
Va=min(vaa)


for i=1:length(P)
   for kk=1:length(A)
```

```
        delVg(kk)=abs(A(kk,1)-P(i,1));
    end
    mdelVg(i)=min(delVg);
    for k2=1:1:length(A)
        delVg(k2)=abs(A(k2,1)-P(i,1));
        if delVg(k2)==mdelVg(i)
            Vg(i)=A(k2,1);
            C(i)=A(k2,2);
            Phi(i)=P(i,3);


        end
    end
end
 B(:,1)=Vg;
 B(:,2)=Phi;
 B(:,3)=C;
 plot(Vg,C);
 nsd=ginput(1);
 hold off


 kk=1
for k3=1:length(B)
    if (B(k3,1) > -2) & (B(k3,1) < Va)
        if B(k3,2)>0
            vvs1(kk)=B(k3,2)
            % here I choose formula of si capacitance following MOS physics
```

```
        % and technology book
        %the result obtained is the same for dQ and cd1
        f1(kk)=sqrt(abs((9.65e9/1.87e15)^2)*(exp(-vvs1(kk))+vvs1(kk)-
1)+exp(vvs1(kk))-vvs1(kk)-1);
        q1(kk)=hs*f1(kk);
        cd1(kk)=abs(cfb*0.0314*(((9.65e9/1.87e15)^2)*(1-exp(-
vvs1(kk)))+((exp(vvs1(kk))-1)))/f1(kk)/sqrt(2));
        D1(kk)=Phi(k3)*k*T/q
        deVi(kk)=1/(Ci/B(k3,3)-1)
        dQ(kk)=sign(B(k3,2))*5.82e-16*(Nd/b)*(exp(B(k3,2))-
((ni/Nd)^2)*exp(-B(k3,2))-1)*((exp(B(k3,2))-    B(k3,2)-1+((ni/Nd)^2)*exp(-
B(k3,2)))^(-1/2))/2;
        %D2(kk)=1e-11*abs((Ci/deVi(kk)/Ar)-dQ(kk))/q
        D2(kk)=abs((Ci/deVi(kk)/Ar)-cd1(kk)/Ar)/q;


    end
    if B(k3,2)<0
        vvs1(kk)=B(k3,2)
        f1(kk)=sqrt(abs(((ni/Nd)^2)*(exp(-vvs1(kk))+vvs1(kk)-
1)+exp(vvs1(kk))-vvs1(kk)-1));
        q1(kk)=hs*f1(kk);
        cd1(kk)=abs(cfb*Ar*(((ni/Nd)^2)*(1-exp(-vvs1(kk)))+((exp(vvs1(kk))-
1)))/f1(kk)/sqrt(2));
        D1(kk)=Phi(k3)*k*T/q
        deVi(kk)=1/(Ci/B(k3,3)-1)
        dQ(kk)=sign(B(k3,2))*5.82e-16*(Nd/b)*(exp(B(k3,2))-
((ni/Nd)^2)*exp(-B(k3,2))-1)*((exp(B(k3,2))-    B(k3,2)-1+((ni/Nd)^2)*exp(-
B(k3,2)))^(-1/2))/2;
```

```
        %D2(kk)=1e-11*abs((Ci/deVi(kk)/Ar)-dQ(kk))/q;

        D2(kk)=1e-11*abs((Ci/deVi(kk)/Ar)-cd1(kk)/Ar)/q;


      end

        kk=kk+1;

   vvs1%

  end


end

plot(D1,D2,'*')

%plot(D(:,1),dQ,'*')

%save Ditlf_ba_100.xls D -ascii
```

## 3. Conductance method

### 3.1. Find surface potential as function of applied voltage (shown in 2.1)

```
function P=findphis
clc;close all; clear all;
beta=1.6e-19/(1.38e-23*300);
q=1.6e-19;
Nd=1.87e15;

%tim Vo, Co
B=xlsread('50f');
%find capacitance and voltage of SiNx
  Co=max(B(:,2))
  k=1;
  for i=1:(length(B))
    if Co==B(i,2)
      Va(k)=B(i,1);
      k=k+1;
    end
  end

%find flat band voltage va flat band capacitance
cfbs=0.0314*sqrt(11.7*8.85e-14*((1.6e-19)^2)*1.9e15/1.38e-23/300);
cfb=(cfbs*Co)/(cfbs+Co);
for i=1:(length(B))
  xx(i)=abs(cfb-B(i,2));
```

```
end
    xxmin=min(xx);
for i=1:(length(xx))
    if xx(i)==min(xx)
        vfb=B(i,1);
    end
end
A=[B(:,1)-vfb B(:,2)];
n=(5.82e-16*sqrt(Nd/beta))/(Co/0.0314);
m=min(Va)-vfb;

%finding Va position
for i=1:(length(A))
        if m==A(i,1)
            tt=i;
         end
    end
t=gpt(n,m);
avphi=t(1)/beta;
% calculate phi vs. Vg
    ii=1;
    for i=2:(length(A))
    ar0=0;
    for k=1:i-1
    area=abs((A(k+1,1)-A(k,1))*(A(k+1,2)+A(k,2))/2);
    ar0=ar0+area;
```

```
    end
    a(ii)=ar0;
    phii(ii)=(A(i,1)-m)+ar0/Co+avphi;
    Vgg(ii)=A(i,1);
    ii=ii+1;
     end
phi=beta*[avphi phii];
Vg=[m Vgg];
A(:,3)=phi;
P=A;
plot(Vg, phi,'o')
```

### 3.2. Find standard deviation

```
clc;close all; clear all
% read data file
%file=input('data file name   ')
A=xlsread('decade');
l=1;
 Vgmax=max(A(:,7));
 Vgmin=min(A(:,7));
 for x=1:length(A)
     if Vgmin==A(x,7)
         minn=A(x,3);


     end
     if Vgmax==A(x,7)
         maxx=A(x,3);
```

```
    end
 end
 mi=minn-40;
 ma=maxx+39;
l=1;
%chose any ll in range of ma to mi to built symetric frequency-conductance
%per w curve
% choose range ll:=mi:ma to see how the curve change with change applied
% voltage and then remove to continue calculation
%for ll=ma:mi
 for ll=ma
     i1=1;
         for i=3:max(A(:,2));
             ii=1;
             for k=1:length(A)
               if i==A(k,2)
               w1(ii)=A(k,5)*pi*2;
               f1(ii)=A(k,5);
               Vg(ii)=A(k,7);
               gm(ii)=A(k,13);
               cm(ii)=A(k,12);
               ii=ii+1;
               end
             end
              w(i1)=w1(1);
```

```
 f(i1)=f1(1);
 cma(i1)=max(cm);
for h=1:length(cm)
    if cm(h)==cma(i1)
     gma(i1)=gm(h);
     Yma(i1)=sqrt((cm(h)*w(i1))^2+gm(h)^2);
     cox(i1)=cma(i1)*(1+(gma(i1)/(cma(i1)*w(i1)))^2);
    end
end
Rs(i1)=gma(i1)/Yma(i1)/Yma(i1);
for h=1:length(cm)
  Ym(h)=sqrt((cm(h)*w(i1))^2+gm(h)^2);
  a(h)=((gm(h)-Ym(h)*Ym(h)*Rs(i1)));
  cc(h)=Ym(h)*Ym(h)*cm(h)/(a(h)*a(h)+(cm(h)*w(i1))^2);
  gc(h)=Ym(h)*Ym(h)*a(h)/(a(h)*a(h)+(cm(h)*w(i1))^2);
  %gpw(h)=w(l)*cox*cox*gc(h)/(gc(h)*gc(h)-(w(l)*(cox-cc(h)))^2);

gmc(h)=w(i1)*w(i1)*Rs(i1)*cc(h)*cc(h)/(1+w(i1)*w(i1)*Rs(i1)*Rs(i1)*cc(h)*
cc(h));

gpw(h)=w(i1)*w(i1)*cox(i1)*cox(i1)*gmc(h)/(gmc(h)*gmc(h)+(w(i1)*(cox(i1
)-cc(h)))^2);
end

  M(i1,1)=gpw(ll)/w(i1);
  vgg(i1)=Vg(ll);
  M(i1,3)=f(i1);
```

```
            M(i1,4)=log10(f(i1));
            M(i1,5)=f(i1);


            i1=i1+1;
        end
        plot(M(:,4),M(:,1),'o')
        peak(l)=max(M(:,1))
        hold on
        kr=ginput(1);
        %hold off
        l=l+1;

end

     p=1
      for f=1:length(M)
          if M(f,1)==peak
             po(p)=M(f,4);
             pmax=M(f,1);
             fo=f;
             fmaxx=M(f,5);
             display('fo')
             plot(fmaxx,pmax,'*')
             hold off
          end
          p=p+1;
```

```
        end


deltaf1=input('please choose range1 to find f max')
    deltaf2=input('please choose range to find f min')
    ffmax=fo+deltaf1;
    ffmin=fo-deltaf2;
    for ff=1:length(M)
            if ff==ffmax
              wmax=2*pi*M(ffmax,5);
              fmax=M(ffmax,5);
            end
            if ff==ffmin
              wmin=2*pi*(M(ffmin,5));
              fmin=M(ffmin,5);
            end


    end
    AA=findphis;
    m=AA(:,3);
    mm=ma;
    for mi=1:length(mm)
       ji=m(mi);
    xxx=1:2:30;
       for ki=1:length(xxx)
          xx=xxx(ki);
       Rmax(ki,1)=xxx(ki);
```

```
    Rmax(ki,1)=xxx(ki);
    Rmax(ki,2)=hc(fmax,xx,ji);
    Rmin(ki,2)=hc(fmin,xx,ji);
    Rpeak(ki,2)=hc(fmaxx,xx,ji);
    ki=ki+1;
    end
    for ik=1:length(Rmax);
    xmax(ik,1)=Rmax(ik,1);
    xmax(ik,2)=1/(Rmax(ik,2)*fmaxx/Rpeak(ik,2)/fmax);
    xmin(ik,2)=((Rmin(ik,2)*fmaxx/Rpeak(ik,2)/fmin));
    xmin(ik,1)=Rmin(ik,1);
    end
plot(xmax(:,1),xmax(:,2),'o')
hold on
plot(xmax(:,1),xmin(:,2),'*')
hold on
mi=mi+1;
end
```

### 3.3. Calculation of $D_{it}$ based on standard deviation found in part 3.2

```
clc;close all; clear all
syms v
sigma=5;
q=1.6e-19;
Nd=1.87e15;
% read data file
%file=input('data file name   ')
A=xlsread('100aa');
 AA=findphis;
 m=AA(:,3);
 Vg=AA(:,1);
 l=1;
 for i=15:1:16;
      ss=1;
        for s=1:length(A)
             if i==A(s,2)
                A(s,2);
                A1(ss,:)=A(s,:);
                ss=ss+1;
             end


        end


      w(l)=A1(1,5)*2*pi;
      f(l)=A1(1,5)
```

```
 cm=A1(:,12);
 gm=A1(:,13);
 cma(l)=max(cm);
for h=1:length(A1)
      if cm(h)==cma(l)
       gma(l)=gm(h);
       Yma(l)=sqrt((cm(h)*w(l))^2+gm(h)^2)
       cox(l)=cma(l)*(1+(gma(l)/(cma(l)*w(l)))^2);
      end
end
Rs(l)=gma(l)/Yma(l)/Yma(l);
       for h=1:length(cm)
           Ym(h,l)=sqrt((cm(h)*w(l))^2+gm(h)^2);
           a(h,l)=((gm(h)-Ym(h)*Ym(h)*Rs(l)));
           cc(h,l)=Ym(h)*Ym(h)*cm(h)/(a(h)*a(h)+(cm(h)*w(l))^2);
           gc(h,l)=Ym(h)*Ym(h)*a(h)/(a(h)*a(h)+(cm(h)*w(l))^2);
           %gpw(h)=w(l)*cox*cox*gc(h)/(gc(h)*gc(h)-(w(l)*(cox-cc(h)))^2);

gmc(h,l)=w(l)*w(l)*Rs(l)*cc(h)*cc(h)/(1+w(l)*w(l)*Rs(l)*Rs(l)*cc(h)*cc(h));

gpw(h,l)=w(l)*w(l)*cox(l)*cox(l)*gmc(h)/(gmc(h)*gmc(h)+(w(l)*(cox(l)-
cc(h)))^2);
       end


    l=l+1;
 end
 h=1
```

```
for ki=28:2:60
    uav(h)=m(ki);
    vgg(h)=Vg(ki);
    gmr(h)=gm(ki);
        cc=1;
        for ci=1:2:24
                ji(cc)=1*10^(-(ci+1));
               Rmin(cc,1)= uav(h);
               Rmax(cc,1)= uav(h);
               Rmax(cc,2)=hcc2(f(1),ji(cc),uav(h));
               Rmin(cc,2)=hcc2(f(2),ji(cc),uav(h));
               R(cc,2)=Rmax(cc,2)*f(2)/Rmin(cc,2)/f(1);
               R(cc,1)= ji(cc);
               cc=cc+1;
        end
         vt(h)=gpw(ki,1)/gpw(ki,2)
        % this comment part is to show cp-R curve
        %plot(log10(R(:,1)),R(:,2));
        %hold on
        %ezplot(v,vt(h),[-24 0])
        %kkk=ginput(1)
        %hold off
        for tx=1:length(ji)
               calz(tx)=abs(vt(h)-R(tx,2));
               tx=tx+1;
        end
```

```
        mincal(h)=min(calz);
      for txx=1:1:length(ji)
          calzt(txx)=abs(vt(h)-R(txx,2));
              if mincal(h)==calzt(txx)
              cpr(h)=ji(txx);
              Rkq(h)=R(txx,2);
              end
              txx=txx+1;
      end

       h=h+1
 end
  for kk=1:1:length(cpr)
     kk
     Rmaxr(kk,1)=hcc2(f(1),cpr(kk),uav(kk));
     Vgate(kk)=vgg(kk);
     phiss(kk)=uav(kk);
     hss(kk)=q*((2*pi*sigma^2)^(-1/2))*cpr(kk)*Nd/2;
     Nss(kk)=gpw(kk,1)/Rmaxr(kk)/hss(kk)/0.0314
     M(kk,1)=vgg(kk);
     M(kk,2)=0.026*phiss(kk);
     M(kk,3)=Nss(kk);
  end
save Ditcd_aa_100.xls M -ascii
plot(M(:,2),Nss,'o')
```

# List of publications

***Papers:***

1. **Trinh Cham Thi**, K. Koyama, K. Ohdaira, and H. Matsumura, “Effect of hydrogen on passivation quality of $SiN_x$/Si-rich $SiN_x$ stacked layers deposited by catalytic chemical vapor deposition on c-Si wafers”, Thin Solid Film (in press).
2. H. Matsumura, T. Hayakawa, T. Ohta, Y. Nakashima, M. Miyamoto**, Trinh Cham Thi**, K. Koyama, and K. Ohdaira, “Cat-Doping: Novel Method for Phosphorus and Boron Shallow Doping in Crystalline Silicon at 80 $^{o}$C”, Journal of Applied Physics 116, 114502-1-10 (2014).
3. **Trinh Cham Thi**, K. Koyama, K. Ohdaira, and H. Matsumura, “Drastic reduction in the surface velocity of crystalline silicon passivated with Cat-CVD $SiN_x$ films by introducing phosphorus Cat-doped layer”, Journal of Applied Physics 116, 044510-1-7 (2014).
4. **Trinh Cham Thi**, K. Koyama, K. Ohdaira, and H. Matsumura, “Passivation quality of a stoichiometric $SiN_x$ single passivation layer on crystalline silicon prepared by Cat-CVD and successive annealing”, Japanese Journal of Applied Physics 53, 022301-1-6 (2014).
5. **Trinh Cham Thi**, K. Koyama, K. Ohdaira, and H. Matsumura, “Passivation characteristics of $SiN_x$/a-Si and $SiN_x$/Si-rich $SiN_x$ stacked layers on crystalline silicon”, Solar Energy Mater and Solar Cells 93, 169-173 (2012).

***Proceedings***

1. **Trinh Cham Thi**, K. Koyama, K. Ohdaira, and H. Matsumura, “Passivation quality of Car-CVD $SiN_x$ and $SiN_x$/P Cat-doped layers on textured c-Si wafers”, Technical Digest of the 6$^{th}$ world conference on photovoltaic energy conversion, November 23-27, 2014.
2. H. Matsumura, S. Tsuzaki, **Trinh Cham Thi**, K. Koyama and K. Ohdaira, “A novel low temperature doping technology, Cat-doping, and its application to solar cells”, Technical Digest of the 6$^{th}$ world conference on photovoltaic energy conversion, November 23-27, 2014.

3. K. Ohdaira, **Trinh Cham Thi**, S. Tsuzaki and H. Matsumura, “Activation of Cat-doped phosphorus atoms by flash lamp annealing”, Technical Digest of the 6th world conference on photovoltaic energy conversion, November 23-27, 2014.
4. K. Koyama, **Trinh Cham Thi**, K. Ohdaira, and H. Matsumura, “Requirement for achieving extremely low surface recombination velocity and negligible optical loss in Cat-CVD $SiN_x$/a-Si stacked passivation”, Proc. 39th IEEE Photovoltaic Specialists conference, June 8-13, 2014.
5. **Trinh Cham Thi**, K. Koyama, K. Ohdaira, and H. Matsumura "Extremely Low Surface Recombination Velocity of Crystalline silicon Realized by Low Temperature Phosphorus Cat-Doping and Successive Deposition of Cat-CVD Silicon-Nitride Films", Technical Digest of the 23rd International Photovoltaic Science and Engineering Conference (PVSEC-23), 1-O-24, 2013.

***International conference:***

1. **Trinh Cham Thi**, K. Koyama, K. Ohdaira, and H. Matsumura, “Passivation quality of Car-CVD $SiN_x$ and $SiN_x$/P Cat-doped layers on textured c-Si wafers”, Technical Digest of the 6th world conference on photovoltaic energy conversion (WCPEC-6) (Kyoto, Japan), November 23-27, 2014.
2. H. Matsumura, S. Tsuzaki, **Trinh Cham Thi**, K. Koyama and K. Ohdaira, A novel low temperature doping technology, Cat-doping, and its application to solar cells, Technical Digest of the 6th world conference on photovoltaic conversion (WCPEC-6) (Kyoto, Japan), November 23-27, 2014.
3. K. Ohdaira, **Trinh Cham Thi**, S. Tsuzaki and H. Matsumura, “Activation of Cat-doped phosphorus atoms by flash lamp annealing”, Technical Digest of the 6th world conference on photovoltaic energy conversion (WCPEC-6) (Kyoto, Japan), November 23-27, 2014.
4. **Trinh Cham Thi**, K. Koyama, K. Ohdaira, and H. Matsumura, "Significant improvement in the passivation property of Cat-CVD $SiN_x$/c-Si structure by applying P Cat-doping", The 8th Hot-Wire (Cat) Chemical Vapor Deposition (HWCVD-8) (Braunschweig, Germany), October 13-16, 2014.
5. H. Matsumura, D. H. Chi, **Trinh Cham Thi**, S. Tsuzaki, K. Koyama, and K. Ohdaira, "Cat-doping: a novel low temperature impurity doping technology using

hot catalyzing wires", The 8th Hot-Wire (Cat) Chemical Vapor Deposition (HWCVD-8) (Braunschweig, Germany), October 13-16, 2014.

6. K. Koyama, **Trinh Cham Thi**, K. Higashimine, K. Ohdaira, and H. Matsumura, "Optical loss in Cat-CVD $SiN_x$/a-Si passivation with low surface recombination velocity",
The 8th Hot-Wire (Cat) Chemical Vapor Deposition (HWCVD-8) (Braunschweig, Germany), October 13-16, 2014.
7. K. Koyama, **Trinh Cham Thi**, K. Ohdaira, and H. Matsumura, "Requirement for achieving extremely low surface recombination velocity and negligible optical loss in Cat-CVD $SiN_x$/a-Si stacked passivation", The 39$^{th}$ IEEE Photovoltaic Specialists conference, (Colorado Convention Center, United State), June 8-13, 2014.
8. **Trinh Cham Thi**, K. Koyama, K. Ohdaira, and H. Matsumura "Extremely Low Surface Recombination Velocity of Crystalline Silicon Realized by Low Temperature Phosphorus Cat-Doping and Successive Deposition of Cat-CVD Silicon-Nitride Films", 23rd International Photovoltaic Science and Engineering Conference (PVSEC-23) (Taipei, Taiwan), October 28-November 1, 2013.
9. **Trinh Cham Thi**, K. Koyama, K. Ohdaira, and H. Matsumura, "High Passivation Quality on c-Si Surface Realized by a Stoichiometric $SiN_x$ Single Layer Prepared by Cat-CVD and Successive Annealing", 2013 JSAP-MRS Joint Symposia (Doshisha University, Kyoto), September 16-20, 2013.
10. **Trinh Cham Thi**, K. Koyama, K. Ohdaira, and H. Matsumura, Passivation quality of a $SiN_x$ single passivation layer on crystalline-Si Prepared by Cat-CVD, JAIST International School Cat-CVD (Hot-wire CVD) and Related Technologies (Kanazawa) March 4-8, 2013.
11. **Trinh Cham Thi**, K. Koyama, K. Ohdaira, and H. Matsumura , Surface passivation of c-Si wafers using Cat-CVD $SiN_x$/Si-rich $SiN_x$ stacked films, 7$^{th}$ International conference on Hot-wire Chemical Vapor Deposition (Osaka) October 8-12, 2012.

***Domestic conference:***

1. **Trinh Cham Thi**, K. Koyama, K. Ohdaira, and H. Matsumura, "Defect termination at the interfaces of Cat-CVD $SiN_x$/c-Si and $SiN_x$/P Cat-doped layer/c-

Si structure", the 62nd JSAP Spring Meeting (Shonan Campus, Tokai University) March 11-14, 2015.

2. **Trinh Cham Thi**, K. Koyama, K. Ohdaira, and H. Matsumura, "A low surface recombination velocity realized on textured c-Si by Cat-CVD $SiN_x$/P Cat-doped layers", the 75th JSAP Autumn Meeting (Sapporo Campus, Hokkaido University) September17-20, 2014.

3. **Trinh Cham Thi**, K. Koyama, K. Ohdaira, and H. Matsumura, "High Passivation Quality for Textured Crystalline Silicon Realized by Low Temperature Phosphorus Cat-Doping and Cat-CVD Silicon-Nitride Passivation Films", Catalytic Chemical Vapor Deposition (Cat-CVD) 11th Conference (Sendai) June 12-13, 2014.

4. 松村英樹、小山晃一、東嶺孝一、**Trinh Cham Thi**、大平圭介, "Cat-CVD 法による最大表面再結合速度 2 cm/s 以下の透明パシベーション膜低温形成", 第 61 回応用物理学会春季学術講演会（青山学院大）、2014 年 3 月 17-20 日 (招待講演).

5. **Trinh Cham Thi**, K. Koyama, K. Ohdaira, and H. Matsumura, "Drastic reduction in surface recombination velocity of Cat-CVD $SiN_x$/c-Si structures by phosphorus (P) Cat-doping", 61st JSAP Spring Meeting (Kanagawa) March 17-20, 2014.

6. **Trinh Cham Thi**, K. Koyama, K. Ohdaira, H. Matsumura, "Passivation Quality of A $SiN_x$ Single Passivation Layer on Crystalline-Si Prepared by Cat-CVD", 日本学術振興会第175委員会 第10回「次世代の太陽光発電システム」シンポジウム（石川県立音楽堂）、2013年5月23-24日

7. **Trinh Cham Thi**, K. Koyama, K. Ohdaira, and H. Matsumura, "Passivation quality of a $SiN_x$ single passivation layer on crystalline-Si Prepared by Cat-CVD", 60th JSAP Spring Meeting (Kanagawa) March 27-30, 2013.

8. **Trinh Cham Thi**, K. Koyama, K. Ohdaira, and H. Matsumura, "Surface passivation of crystalline silicon by $SiN_x$/Si-rich $SiN_x$ stacked layers", 73rd JSAP Autumn Meeting (Ehime) September 11-16, 2012.

9. **Trinh Cham Thi**, K. Koyama, K. Ohdaira, and H. Matsumura, "Investigation of the passivation property of $SiN_x$/Si-rich $SiN_x$ stacked layers on crystalline silicon wafers", Catalytic-Chemical Vapor Deposition (Cat-CVD) 8th Conference

(Kanazawa) June 2011.

*Award:*

1. **Innovative Photovolatic Young Researcher's Award** for

**Trinh Cham Thi**, K. Koyama, K. Ohdaira, H. Matsumura, "Passivation Quality of A $SiN_x$ Single Passivation Layer on Crystalline-Si Prepared by Cat-CVD", at the 10th Symposium of the 175th Committee on Innovative Photovoltaic Power Generating Systems, Japan Society for the Promotion of Science, Kanazawa, Japan, 23-24 May, 2013.